



UNIVERSITÀ
DEGLI STUDI
DI PADOVA

Head Office: Università degli Studi di Padova

CISAS – Centre of Studies and Activities for Space “G. Colombo”

Ph.D. COURSE IN: Space Sciences, Technologies and Measurements

CURRICULUM: Sciences and Technologies for Aeronautics and Satellite Applications (STASA)

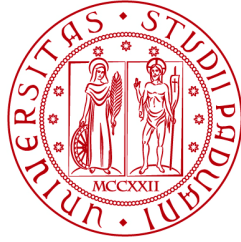
XXX SERIES

SPACECRAFT RENDEZVOUS AND DOCKING USING ELECTROMAGNETIC INTERACTIONS

Coordinator: Prof. Giampiero Naletto

Supervisor: Prof. Alessandro Francesconi

Ph.D. student: Matteo Duzzi



**UNIVERSITÀ
DEGLI STUDI
DI PADOVA**

SEDE AMMINISTRATIVA: UNIVERSITÀ DEGLI STUDI DI PADOVA
CISAS – CENTRO D’ATENEIO DI STUDI ED ATTIVITÀ SPAZIALI “G. COLOMBO”

CORSO DI DOTTORATO DI RICERCA IN: Scienze Tecnologie e Misure Spaziali
CURRICOLO: Scienze e Tecnologie per Applicazioni Satellitari e Aeronautiche
CICLO XXX

SPACECRAFT RENDEZVOUS AND DOCKING USING ELECTROMAGNETIC INTERACTIONS

Coordinatore: Ch.mo Prof. Giampiero Naletto

Supervisore: Ch.mo Prof. Alessandro Francesconi

Dottorando: Matteo Duzzi

Humans are allergic to change. They love to say “we’ve always done it this way”. I try to fight that. That’s why I have a clock on my wall that runs counter-clockwise.

- Grace Brewster Murray Hopper

Science, my lad, is made up of mistakes, but they are mistakes which it is useful to make, because they lead little by little to the truth.

- Jules Verne, A Journey to the Center of the Earth

Abstract

On-orbit operations such as refuelling, payload updating, inspection, maintenance, material and crew transfer, modular structures assemblies and in general all those processes requiring the participation of two or more collaborative vehicles are acquiring growing importance in the space-related field, since they allow the development of longer-lifetime missions.

To successfully accomplish all these on-orbit servicing operations, the ability to approach and mate with another vehicle is fundamental. Rendezvous strategies, proximity procedures and docking manoeuvres between spacecraft are of utmost importance and new, effective, standard and reliable solutions are needed to ensure further technological developments.

Presently, the possibility to create low-cost clusters of vehicles able to share their resources may be exploited thanks to the broadening advent of CubeSat-sized spacecraft, which are conditioning the space market nowadays.

In this context, this thesis aims at presenting viable strategies for spacecraft Rendezvous and Docking (RVD) manoeuvres exploiting electro-magnetic interactions. Two perspective concepts have been investigated and developed, linked together by the use of CubeSat-size testing platforms.

The idea behind the first one, PACMAN (Position and Attitude Control with MAgnetic Navigation) experiment, is to actively exploit magnetic interactions for relative position and attitude control during rendezvous and proximity operations between small-scale spacecraft. PACMAN experiment has been developed within ESA Education *Fly Your Thesis!* 2017 programme and will be tested in low-gravity conditions during the 68th ESA Parabolic Flight Campaign (PFC) in December 2017. The experiment validation is accomplished by launching a miniature spacecraft mock-up (1 U CubeSat, the CUBE) and a Free-Floating Target (1 U CubeSat, the FFT) that generate static magnetic fields towards each other; a set of actively-controlled magnetic coils on board the CUBE, assisted by dedicated localization sensors, are used to control the CUBE attitude and relative position, assuring in this way the accomplishment of the soft-docking manoeuvre.

The second one, TED (Tethered Electromagnetic Docking), concerns a novel docking strategy in which a tethered electromagnetic probe is expected to be ejected by a chaser toward a receiving electromagnetic interface mounted on a target spacecraft. The generated magnetic field drives the probe to the target and realizes an automatic alignment between the two interfaces, thus reducing control requirements for close approach manoeuvres as well as the fuel consumption necessary for them. After that, hard-docking can be accomplished by retracting the tether and bringing the two spacecraft in contact.

Summary

In the last years, international space-related companies and agencies are manifesting great interest in on-orbit servicing [1–10]. Innovative solutions to perform on-orbit operations such as refuelling, payload updating and maintenance, subsystems repairing and inspection are under study, influencing considerably the aerospace market to reduce the manufacturing costs, obtain more reliable and long-lasting complex systems. All the new ideas and technologies under development to succeed in on-orbit operations are perceived as extremely functional and cost-effective, capable of increasing the operational lifetime of a satellite and decreasing the costs related to its complete replacement.

For this reason, the development of an automatic, standard and reliable docking system would allow the accomplishment of on-orbit servicing procedures. As of today, all the docking systems are characterized by high alignment and attitude control requirements and particular procedures have to be carefully supervised to guarantee a safe connection between two spacecraft that are performing a docking manoeuvre. This is due to the fact that docking operations have been developed mainly exclusively for crew and cargo transfer [11–14] and no similar technique was designed for commercial or scientific spacecraft.

Recently, the advent of CubeSat modules has greatly encouraged international aerospace companies and agencies to invest in the development of technological demonstrators or scientific payloads using these platforms, thanks to their reduced cost for accessing space. The main drawback of CubeSats is related to the very limited available resources. However, this limitation has been overcome thanks to the possibility of scaling the results obtained with these small platforms to bigger systems, preserving the effectiveness of the outcomes. Various technologies have been already tested in space using CubeSats, but only few experiments have been performed on docking systems [15–22], even if the development of such mechanisms could expand enormously the possible mission scenarios. Modular assemblies built in space with multiple CubeSat modules would be able to share resources more efficiently, reorganize and update autonomously.

The objective of this research is to present a novel soft-docking system demanding lower requirements and a less-accurate attitude control with respect to the current systems. The innovative idea behind the study is to exploit the self-alignment capability and the mutual attractive force generated by the magnetic interaction between two electromagnetic interfaces to ease the proximity and docking manoeuvres. In details, the objectives of this work are:

- to briefly analyse the rendezvous and docking manoeuvre, focusing on already developed or under development systems for both large and small satellites (Chapter 1);

- to develop and experimentally verify, in relevant environment (i.e. in low-gravity conditions), soft-docking interfaces able to exploit electromagnetic interactions (Chapters 2,3,4,5,6);
- to develop a dynamical model to simulate tethered rendezvous and soft-docking manoeuvres exploiting electromagnetic interactions (Chapter 7).

To be more precise, Chapter 1 presents the typical phases of a rendezvous and docking manoeuvre, focusing on the docking description. Docking mechanisms for both large and small satellites are presented in this chapter, giving strong emphasis to electromagnetic systems. The objectives and the thesis structure are explained at the end of this introductory chapter.

In the first part of the dissertation (Chapters 2-6), PACMAN (Position and Attitude Control with MAGnetic Navigation) experiment is presented. PACMAN is a technological demonstrator concerning a docking system that features actively-controlled electromagnetic actuators used for relative position and attitude control during rendezvous and proximity operations between small-scale spacecraft. PACMAN has been developed within the ESA Education *Fly Your Thesis!* 2017 programme and will be tested in low-gravity conditions during the 68th Parabolic Flight Campaign this December. In the second part of the work (Chapter 7), the focus is on the TED (Tethered Electromagnetic Docking) concept, in which a tethered electromagnetic probe is designed to be ejected by a chaser toward a receiving electromagnetic interface mounted on a target spacecraft. The generated magnetic field drives the probe to the target and realizes an automatic alignment between the two interfaces. After that, hard-docking is accomplished by retracting the tether and bringing the two spacecraft in contact.

In details, Chapter 2 presents a brief introduction about PACMAN experiment, its scientific objectives and the gravity-related research systems used to simulate the low-gravity environment. The chapter concludes with the motivation about the choice of the parabolic flight as testing platform.

In Chapter 3, ESA Education *Fly Your Thesis!* 2017 is introduced with the description of both the Airbus A310 Zero-G and the parabolic flight manoeuvre, paying special attention to the disturbances aboard the plane and the different phases during the parabolic trajectory: the hyper-gravity (2g) phase during the pull-up and pull-out manoeuvres and the low-gravity ($10^{-2} - 10^{-3}g$) phase during the peak of the parabola.

The fourth chapter describes PACMAN design in detail, from the original idea presented at the proposal of the *Fly Your Thesis!* programme to the final design. The main objective of PACMAN is to validate, in low-gravity conditions, a soft-docking system for small satellites based on electromagnetic actuators and an integrated sensor system for proximity navigation. The magnetic actuators are used to perform the attitude control

of the system and ensure the satellite connection. To achieve its objectives, PACMAN flight configuration is designed for the launch, through a linear guide, of a small-scale spacecraft (CUBE) towards a Free-Floating Target (FFT) that generates a static magnetic field. The coils aboard the CUBE, together with the integrated sensor system, are used to control its position and relative attitude with respect to the FFT. Various modifications to the design have been realized during the development of the project, following the results obtained from the dynamic simulations performed to study the CubeSat motion inside the Airbus A310 Zero-G. The model implemented for the analysis considers the parabolic trajectory of the A310 Zero-G and the Near-field magnetic model used to develop the algorithm control of the CUBE. In parallel, a list of requirements have been drawn to perform effectively the test in low-gravity conditions and achieve the scientific goals.

Part of the tests performed on ground before the Parabolic Flight Campaign (PFC) are presented in Chapter 5. The validation of the Near-field magnetic model is proposed in this chapter, along with the test done on the CUBE vision system and the temperature tests carried out to evaluate the temperature trend of the two modules during the operative low-gravity phase. The hold & launch system, used to hold the CubeSats during the hyper-gravity phases and release them during low-gravity conditions, was checked in the laboratory. Finally, the driver circuit developed to power the CUBE was tested to verify its functioning before manufacturing the Printed Circuit Board (PCB).

Chapter 6 introduces the procedures to be adopted during the parabolic flights: from the earliest initialization of the CUBE and the FFT before the first parabola, through the description of the low-gravity operative phase, to the module recovery and their repositioning on the launch systems. All the operations are regulated through the interchange of the typical ($2g - 0g - 2g$) phases of each parabola.

As for the second part of this thesis, the TED concept is presented and described in Chapter 7. The idea behind the TED concept is the ejection of a tethered electromagnetic probe from a chaser spacecraft towards an electromagnetic interface mounted aboard a target. The generated magnetic field drives the probe to the target and realizes an automatic alignment between the two interfaces, thus reducing the control requirements for close-range approach manoeuvres. After that, hard-docking is accomplished by retracting the tether and bringing the two spacecraft in contact. Standard rendezvous manoeuvres are simulated in Matlab[®] and preliminary TED simulations are then presented as possible alternative to standard traditional approach through the implementation of a simplified magnetic field model (Far-field) and a tether model to study the dynamical behaviour of the tether in space. Finally, one section is dedicated to the technologies developed for this innovative docking procedure, in perspective of a possible future test in orbit.

In Chapter 8 the whole work is briefly summarized and the conclusions with the main

results are presented. Finally, the roadmap with the future activities foreseen is introduced.

Sommario

La capacità di eseguire operazioni di servizio su veicoli in orbita ha riscontrato, negli ultimi anni, un enorme interesse da parte delle maggiori compagnie e agenzie spaziali internazionali [1–10]. La necessità di ridurre i costi di produzione, assieme alla possibilità di ottenere sistemi complessi più affidabili e duraturi, ha indirizzato marcatamente il mercato dell'ingegneria aerospaziale verso lo studio di soluzioni innovative per eseguire in orbita operazioni quali rifornimento, aggiornamento e manutenzione di sottosistemi, riparazioni di componenti non funzionanti e ispezioni. Le nuove idee e tecnologie in via di sviluppo per eseguire queste operazioni sono percepite come estremamente funzionali e efficienti in termini di costo, in grado di estendere la vita operativa di un satellite e diminuire i costi connessi alla sua completa sostituzione.

Attualmente, il tassello mancante per poter procedere efficacemente con questo tipo di procedure, è un sistema automatico di docking che possa costituire un nuovo standard semplice ed affidabile. Gli odierni sistemi di docking, infatti, sono caratterizzati da elevati requisiti di puntamento e necessitano dell'attuazione di precise azioni sul controllo d'assetto in modo da garantire un aggancio sicuro tra i due veicoli coinvolti nella manovra. Questo è dovuto al fatto che tali sistemi di aggancio sono stati progettati quasi unicamente per il trasferimento di equipaggio o di materiali [11–14] mentre nessuna progettazione, finora, è mai stata prevista per i satelliti commerciali e scientifici.

Recentemente, l'avvento dei CubeSat ha fortemente incoraggiato aziende e agenzie del settore aerospaziale ad investire nello sviluppo di dimostratori tecnologici e payload scientifici, grazie alla notevole riduzione nel costo necessario per lanciare in orbita tali veicoli. Lo svantaggio nell'utilizzare questo tipo di piattaforme è principalmente legato ai limiti tecnici intrinseci degli stessi, rappresentati dalle ridotte risorse a disposizione. Ciononostante, gran parte di queste limitazioni sono state superate grazie alla possibilità di scalare i risultati ottenuti ed applicarli a sistemi più grandi. Numerose tecnologie sono già state testate e caratterizzate nello spazio usando moduli CubeSat, ma solo esperimenti marginali sono stati condotti sino ad oggi su sistemi di docking, anche se si sta percependo un cambio di tendenza [15–22]. Tali sistemi, infatti, permetterebbero l'esecuzione di operazioni di aggancio e sgancio, ampliando enormemente i possibili scenari di missione: sistemi modulari formati da molteplici unità CubeSat potrebbero interagire tra loro creando agglomerati più grandi in grado di condividere le risorse più efficacemente, riorganizzarsi e aggiornarsi autonomamente.

Lo scopo di questa ricerca è quello di proporre un nuovo sistema di soft-docking caratterizzato da requisiti meno stringenti per quanto concerne l'accuratezza nel puntamento e nel controllo d'assetto rispetto ai sistemi esistenti. L'idea innovativa alla base dello studio è quella di sfruttare la capacità di auto-allineamento e reciproca attrazione garantita dall'interazione magnetica che si instaura tra due interfacce elettromagnetiche, in

modo da facilitare le manovre di prossimità ed aggancio.

Entrando nel dettaglio, gli obiettivi di questo lavoro sono:

- analizzare brevemente la manovre di rendezvous e docking, con particolare focus ai sistemi sviluppati o in via di sviluppo per grandi e piccoli satelliti (Capitolo 1);
- sviluppare e verificare sperimentalmente, in ambiente caratteristico (gravità ridotta), interfacce per sistemi di soft-docking che sfruttino le interazioni elettromagnetiche (Capitoli 2,3,4,5,6);
- sviluppare un modello dinamico per simulare manovre di rendezvous e soft-docking alternative a quelle esistenti che sfruttino le interazioni elettromagnetiche integrate in un sistema di docking a filo (Capitolo 7).

Più precisamente, il Capitolo 1 presenta le fasi caratteristiche eseguite durante una manovra di rendezvous e docking, soffermandosi in modo particolare nella descrizione della fase di aggancio. In questo capitolo vengono poi presentati i meccanismi di docking esistenti per grandi satelliti ed un breve excursus sulle tecnologie sviluppate o in via di sviluppo per piccoli satelliti, con particolare riguardo ai sistemi caratterizzati da interfacce elettromagnetiche. Gli obiettivi della ricerca e la struttura della tesi vengono introdotti alla fine del capitolo.

La trattazione viene poi suddivisa in due parti principali. Nella prima parte viene presentato l'esperimento PACMAN (Position and Attitude Control with MAGnetic Navigation) il quale rappresenta un dimostratore tecnologico di un sistema di docking per piccoli satelliti basato su attuatori magnetici. Tale sistema, sviluppato all'interno del programma ESA Education *Fly Your Thesis!* 2017, verrà testato in gravità ridotta durante la 68th campagna di voli parabolici ESA questo dicembre. La seconda parte si focalizza invece su un nuovo concept, TED (Tethered Electromagnetic Docking), secondo il quale le manovre di close-range rendezvous e docking possono essere realizzate lanciando una sonda elettromagnetica collegata ad un filo da un satellite chaser verso un'interfaccia elettromagnetica montata su di un satellite target. Stabilito il collegamento, tramite il recupero del filo, i due veicoli sono connessi rigidamente concludendo la manovra.

Nello specifico, il Capitolo 2 presenta una breve introduzione dell'esperimento PACMAN e dei suoi obiettivi scientifici, con un accenno alle piattaforme esistenti sulla terra usate per poter simulare la gravità ridotta e la motivazione della scelta dei voli parabolici come setup sperimentale.

Nel Capitolo 3 viene introdotto il programma ESA Education *Fly Your Thesis!* 2017, presentando l'Airbus A310 ZERO-G, illustrando la manovra eseguita durante il volo parabolico e i disturbi presenti a bordo dell'aereo. L'attenzione è rivolta soprattutto alla

spiegazione delle differenti fasi della traiettoria parabolica, durante la quale è possibile sperimentare diversi livelli di gravità: iper-gravità (fino a 2g) durante le fasi ascendenti e discendenti e gravità ridotta ($10^{-2} - 10^{-3}$ g) nei 22 s di picco della parabola.

Il quarto capitolo descrive nel dettaglio il design dell'esperimento PACMAN, dall'idea iniziale presentata alla proposal del programma *Fly Your Thesis!* alla progettazione finale. Lo scopo principale di PACMAN è validare, in condizioni di gravità ridotta, un sistema di docking per piccoli satelliti basato su attuatori magnetici. Tali dispositivi, integrati con sensori per la navigazione di prossimità, hanno la duplice funzione di garantire il controllo d'assetto e assicurare l'aggancio del satellite. La configurazione di volo di PACMAN prevede il lancio tramite una guida lineare di un piccolo satellite miniaturizzato (CUBE) verso un target mobile (FFT) in grado di generare un campo elettromagnetico; una serie di solenoidi montati all'interno del satellite, coadiuvati da sensori di localizzazione, sono utilizzati per controllarne la posizione e l'assetto relativo al target. Numerose modifiche alla configurazione finale di volo sono state realizzate durante lo sviluppo del progetto a seguito dei risultati ottenuti dalle analisi dinamiche eseguite per studiare il moto dei due CubeSat all'interno dell'Airbus A310 Zero-G. Tali analisi sono state realizzate considerando il moto dell'aereo durante la traiettoria parabolica ed implementando il modello di campo magnetico (Near-field) utilizzato per sviluppare il controllore del CUBE. L'accuratezza del modello è stata accertata tramite test sperimentali in laboratorio. Parallelamente, i requisiti del progetto sono stati stilati in modo da poter eseguire efficacemente i test in gravità ridotta e raggiungere gli obiettivi scientifici.

Nel Capitolo 5 sono presentati una parte dei test eseguiti a terra prima della campagna di volo. La validazione del modello di campo magnetico è proposta in questo capitolo, assieme ai test compiuti sul sistema di visione del CUBE e ad alcuni test realizzati per valutare l'andamento della temperatura dei due moduli durante la fase operativa in gravità ridotta. Il sistema di sgancio, responsabile del rilascio dei moduli durante la fase a 0 g e del loro mantenimento in posizione durante le fasi di iper-gravità, è stato collaudato in laboratorio. Infine, test sul sistema di alimentazione del CUBE sono stati effettuati per verificare il funzionamento del circuito prima di procedere con la produzione del circuito stampato.

Il Capitolo 6 contiene le procedure pensate per essere eseguite durante il volo parabolico: dall'inizializzazione dei moduli all'inizio del volo, alla descrizione della fase operativa durante il periodo di gravità ridotta, fino al recupero dei moduli e alla loro ricollocazione sul sistema di lancio. Tutte le operazioni sono scandite dall'alternarsi delle varie fasi (2g - 0g - 2g) caratteristiche di ogni parabola.

La seconda parte della tesi, nella quale viene presentato il concetto di TED, è contenuta nel Capitolo 7. L'idea alla base di TED prevede il lancio di una sonda elettromagnetica,

collegata tramite un filo, da parte di un satellite chaser verso un'interfaccia elettromagnetica a bordo di un satellite target. L'influenza reciproca dovuta all'interazione generata dai campi magnetici guida la sonda verso l'interfaccia del satellite target e ne permette l'auto-allineamento, riducendo i requisiti del sistema di controllo d'assetto per eseguire la manovra di prossimità. Conclusa l'operazione di soft-docking, la connessione rigida tra i due satelliti è garantita dal recupero del filo. Alcune manovre standard di rendezvous sono trattate nel capitolo tramite simulazioni in Matlab[®]. La procedura di docking a filo è poi simulata in modo preliminare e presentata come possibile alternativa agli approcci tradizionali attraverso l'implementazione di un modello semplificato di campo magnetico (Far-field) e di un modello per l'analisi dinamica del filo nello spazio. Infine, un paragrafo è dedicato alle tecnologie sviluppate per questo innovativo sistema di aggancio, in previsione di un possibile test in orbita.

Nel Capitolo 8 sono riportate le conclusioni e l'intero lavoro riassunto brevemente con i principali risultati ottenuti e la roadmap prevista per le future attività.

Acknowledgements

In these three years, a lot of things happened in my life: I met a lot of people and new friends from all over the world, I am finishing my PhD and I completed an important project, I grew both personally and professionally... but all these achievements were possible thanks to all the people I had the fortune to encounter. I do apologize from the beginning if I missed someone: it could be due to my proverbial absent-minded trait or to the fact that I am writing these lines just the evening before delivering this dissertation.

First of all, I want to thank all my colleagues: Livia for helping me during my first year of PhD, Fren, Franz and Francesco for the precious advices and the support whenever I needed, Andrea... for the funny dinners/parties in his house! Chiodo and Mirco for the cheerful lunches and the coffe breaks at “ex Fiat” and of course Riccardo for the unexpected evenings!

I really want to thank my friend/colleague Laura for her daily patience with me, especially during our recurring dialogues in which I in general do not pay much attention: now you know me quite well and unfortunately you can recognise when I am pretending to listen to you. I really enjoyed our stupid conversations and discussions about “how to select a good conference” but also the serious ones about work and life. Thank you for having shared with me the craziest PhD’s moments (that were quite a lot, if I have to say the truth).

I truly want to thank my Friends Giovanni and Alessandra: even if we do not see frequently I deeply know that I can rely on you whenever I need. I would like to thank you for all the recommendations about my personal life you gave me during the past years and I am quite sure I will need many more in the near future. I am very proud of having been your best man.

I want to thank my friend Curling aka Lorenzo for the funny moments, the parties, the beers, the dinners, the lunches, the conferences. I want to thank you for all the advices and the support throughout the whole PhD. It was the far 2006 when we started to study at University, more than 10 years ago by now, and I definetly can say that you are a trustworthy Friend.

My PhD would not be the same without my friends Giulia & Daniele. I would like to thank Giulia for the support during the last craziest months of my PhD, the “try-to-relax” walking after the lunches but especially for being always present whenever I needed. Oh, and of course for all the postcards you always send me from around the world, even when I travel with you... and the re-read of this dissertation. I wish the best to Daniele for his future in Thailand (next time I will visit you we must go to the beach!) and thank him for his take-it-easy teachings and advices: remember to write a book about your life!

I would like to thank all my old friends Andrea, Monica, Giuliano, Besso, Angelica, Debbie, Alberto for their support and the funny weekends, especially the snowtrips: remember, winter is coming!

I would like to thank all the “GoodFellows” members Beatrice, Debora, Sara, Giulia, Matteo, Milly: I will always remember all the good moments spent together and I will carry in my heart our croatian holiday. I particularly want to thank Debora for all her support (not quantifiable) and patience (probably even more not quantifiable) in the last 5 years: you know you are my personal “psychologist” even if you are not a psychologist. A heartfelt thanksgiving goes also to the RotarAct family for all the fun and evenings spent together. In particular, I would like to thank Elisa (you are a really wonderful person), Eleonora and Gabriele (parties would not be the same without you two).

Special thanks goes to the “Toccata & Sushiatà” members Eleonora, Filippo, Mara, Marta, Mattia, Alessia for organizing the sushi-time events. I also really enjoyed waiting with you the advent of the New Year (again) the evening of the 5th of January!

My “mercoledì universitari” would not have been so lively without the members of the “A.A. Team” Paola, Nicola, Beppe, Anna, Enrico: thank you for the aperitives and the evenings spent together.

I particularly want to thank all the team members of PACMAN team: Matteo, Fabrizio, Riccardo, Luca, Filippo, Mattia. The project would not be the same without you and your contribution has been fundamental (in driving me crazy). I especially want to thank Mattia that shared with me both the PhD and the PACMAN adventures: your support was essential for the development of the project and for preserving my mental health conditions. I take the chance to thank also the European Space Agency Education Office coordinator Dr. Nigel D. L. Savage, the trainees Lukas Pfeiffer, Maximilian Nürnberger and Antonino Campolo and our supervisor Thomas Villatte from NoveSpace for their support during the whole *Fly Your Thesis!* programme and the Parabolic Flight Campaign: it has been an astonishing experience in ZERO-G.

A particular mention goes to the peculiar members of “Operazione marmellata” Alex, Matteo, Alberto, Enrico and Gilberto. Thank you all for the funny moments spent together, the wonderful holidays in Sicily and your attempts to distract me from PACMAN project. I remember with particular affection and gratitude Gilberto’s call during PACMAN integration in Bordeaux.

I want to thank all the SCRAT Team members, just because SCRAT Team is SCRAT Team, what else?

I would like to thank all the secretaries at CISAS Federica, Luciana, Novella, Chiara, Federica, Marika for helping me in dealing with bureaucracy and orders. A special thank goes to Novella for the deadline notes, her patience and of course for the chocolate candies during the hardest moments.

I also want to thank my supervisor Prof. Alessandro Francesconi for giving me the

opportunity of putting myself to test, teaching me how to face new challenges with confidence and persistence.

Finally, I want to thank my entire family for the continuous support: you believed in me even more I believed in myself and you strongly encouraged me in pursuing my dreams during the hardest moments. This thesis is entirely dedicated to you.

Contents

Abstract	i
Summary	ii
Sommario	vi
Acknowledgements	x
List of Figures	xvii
List of Tables	xxv
Abbreviations	xxvii
1 Introduction	1
1.1 Spacecraft rendezvous and docking manoeuvres	3
1.1.1 Launch	3
1.1.2 Phasing	3
1.1.3 Far range rendezvous	4
1.1.4 Close range rendezvous	5
1.1.5 Docking	6
1.1.6 Departure	7
1.2 Docking mechanisms for large spacecraft	8
1.3 Docking mechanisms for small satellites	11
1.4 Research objectives, thesis structure & work logic	14
PART 1	
PACMAN EXPERIMENT	
(Position and Attitude Control with MAgnetic Navigation)	20
2 PACMAN Experiment & Gravity-related Research Systems	21
2.1 Introduction to PACMAN experiment	21
2.1.1 PACMAN experiment scientific objectives	22
2.2 Gravity-related research systems	23
2.2.1 Ground-based facilities	23
2.2.2 Relevant environment: why is micro-gravity needed for PACMAN experiment?	26

3	ESA Education <i>Fly Your Thesis!</i> Programme	31
3.1	ESA Education <i>Fly Your Thesis!</i> programme:	
	parabolic flights	31
3.1.1	Parabolic flight manoeuvre	32
3.1.2	Disturbances during a parabolic flight: g-jittering effects and vibrations	33
3.1.3	The Airbus A310 Zero-G as low-gravity test platform	34
4	PACMAN Experiment Design Evolution	37
4.1	PACMAN proposal for the <i>Fly Your Thesis!</i> programme	37
4.2	Dynamic analysis of the CUBE motion during a parabola	42
	4.2.1 Identification of the ideal launch window	44
	4.2.2 Analysis of the CUBE motion inside the Airbus A310 ZERO-G	47
4.3	PACMAN experiment requirements	52
	4.3.1 Functional requirements	53
	4.3.2 Performance requirements	53
	4.3.3 Design requirements	56
	4.3.4 Interface requirements	57
	4.3.5 Operational requirements	57
	4.3.6 Human factor requirements	58
4.4	Magnetic field model for PACMAN experiment	59
	4.4.1 Near-Field model based on Lorentz approach	60
	4.4.2 PACMAN simulation	63
4.5	PACMAN Experiment final design	65
	4.5.1 System 1: CHAMBER	65
	4.5.1.1 Structure of the CHAMBER	67
	4.5.1.2 Hold & launch subsystems	69
	4.5.1.3 Vision subsystem	71
	4.5.2 System 2: CUBE	72
	4.5.2.1 Navigation subsystem	72
	4.5.2.2 Data handling & communication subsystem	76
	4.5.2.3 Power subsystem	78
	4.5.2.4 Hold & launch system interface	83
	4.5.3 System 3: FFT	83
	4.5.3.1 Docking interface	84
	4.5.3.2 Microcontroller board	86
	4.5.3.3 Power subsystem	87
	4.5.4 Supporting electronics	89
5	Ground Tests	91
5.1	Validation of PACMAN dynamic model: coil test	91
	5.1.1 Methodology	91
	5.1.2 Experimental setup	92
	5.1.3 Experimental results	93
5.2	CUBE camera test	94
	5.2.1 Methodology	94
	5.2.2 Experimental setup	95

5.2.3	Experimental results	97
5.3	Temperature tests	98
5.3.1	Testing conditions and experimental setup for the CUBE	99
5.3.2	Testing conditions and experimental setup for the FFT	101
5.4	CUBE driver circuit test	102
5.4.1	Experimental setup	102
5.4.2	Experimental results	103
5.5	Static load test for the hold system	104
5.5.1	“Plug ‘n’ play” interface	104
5.5.2	Orienting release interface	105
6	PACMAN Parabolic Flight Procedures	107
6.1	Procedures during the parabolas	108
PART 2		
TED		
(Tethered Electromagnetic Docking)		
7	TED: Tethered Electromagnetic Docking	113
7.1	Reference system and model	114
7.2	Rendezvous manoeuvres description	116
7.2.1	Hohmann transfer as reference for the <i>R-bar</i> approach	117
7.2.2	Phasing manoeuvre as reference for the <i>V-bar</i> approach	118
7.2.3	Continuous thrust manoeuvres	119
7.2.3.1	<i>R-bar</i> approach	119
7.2.3.2	<i>V-bar</i> approach	120
7.2.4	Glideslope algorithms	121
7.2.4.1	<i>R-bar</i> approach	123
7.2.4.2	<i>V-bar</i> approach	124
7.3	ΔV budget and propellant consumption	124
7.4	TED manoeuvre	125
7.4.1	Technological developments for TED	126
7.4.1.1	Launch mechanism	126
7.4.1.2	Controlled tether deployment and retrieval	130
7.4.1.3	Passive probe design	133
7.4.2	Tether model for TED application	135
7.4.2.1	Tether deployment	136
7.4.2.2	Tether retrieval	137
7.4.3	Magnetic field model for TED application	138
7.4.3.1	Dipoles equations of dynamics	140
7.4.3.2	Dipole dynamic simulations	141
7.4.3.3	Laboratory test	143
7.4.3.4	Experimental results	144
7.4.4	Real in-space manoeuvre	146
7.4.4.1	<i>R-bar</i> approach	146
7.4.4.2	<i>V-bar</i> approach	148
8	Conclusions & Future Works	151

8.1	Results and discussion	151
8.2	PACMAN & TED correlation and future works	154
8.3	Conclusions	156
A	CUBE Driver Circuit Evolution	159
A.1	Introduction	159
A.2	Custom driver circuit	159
A.3	Alternatives to the custom driver circuit	162
B	PACMAN project management	165
B.1	Work Breakdown Packages	165
B.2	Project timeline	169
C	Clohessy-Wiltshire Formulation	171
C.1	CW matrices formulation	171
C.2	Initial velocity calculation for the R-bar approach	172
D	Validation of PACMAN launch system	175
E	Procedures for ground and in-flight operations	179
E.1	Preparation before each flight	179
E.2	Procedures during the flight before first parabola	182
E.3	Procedures during the pauses between parabolas	183
E.4	Preparation after each flight	183
	Bibliography	185

List of Figures

1.1	Earth-centred inertial frame and phase angle definition.	4
1.2	Target local frame: the coordinate system is centred at the target and it moves with it along its orbit. The direction of motion is defined with a straight line and named as $V - bar$ while the direction toward the centre of the Earth is named $R - bar$. The orbital angular momentum vector H complete the reference system.	5
1.3	$V - bar$ (a) and $R - bar$ (b,c,d) close range rendezvous approaches. . . .	6
1.4	Standard rendezvous and docking manoeuvre. Usually, the close range rendezvous is the most critical phase due to the strict navigation and safety requirements.	8
1.5	Photo of the Agena Target Vehicle taken from the Gemini 8 (courtesy of NASA).	8
1.6	Apollo probe-drogue docking system (courtesy of NASA).	9
1.7	American and Soviet docking interfaces (left) for the Apollo-Soyuz Test Project and the improved Androgynous Peripheral Docking System (right) (courtesy of NASA).	10
1.8	NASA Docking System (NDS): active androgynous variant (top) and passive interface (bottom) (courtesy of NASA).	10
1.9	(September 4 th , 2013) ESA astronaut Luca Parmitano conducting an experiment with a pair of SPHERES (courtesy of NASA).	11
1.10	ARCADE probe-drogue system. The conical probe is captured by an electromagnet placed at the end of the drogue. The rigid connection is realized by pulling the probe towards the drogue and securing it with three latches.	12
1.11	SPHERES satellites equipped with the RINGS floating in the ISS (courtesy of NASA).	12
1.12	A SPHERES satellite with the connecting interface, the Universal Docking Port (courtesy of NASA).	14
1.13	Investigated perspective applications: PACMAN Experiment & TED. . . .	15
1.14	Work Breakdown Structure.	16
2.1	Electromagnetic soft-docking. The CUBE and the FFT will be launched towards each other. The controller will power separately the coils aboard the CUBE allowing to control its attitude and position.	21
2.2	Sketch of the control algorithm of the closed-loop system.	22
2.3	ESA astronaut Samantha Cristoforetti wearing a training version of her Extravehicular Mobility Unit (EMU) spacesuit in preparation for a spacewalk training session at the Neutral Buoyancy Laboratory (NBL) near NASA's Johnson Space Center (courtesy of NASA).	24

2.4	ESA Maser launched from the Esrange facility near Kiruna, Sweden (©SSC Id 213859).	25
2.5	ZARM drop tower in Bremen (courtesy of ZARM).	25
2.6	ESA Airbus A310 ZERO-G aircraft performing a parabola (©ESA Id 330758).	26
2.7	Comparison among different activities performed during parabolic flights and drop towers.	29
3.1	Parabolic flight manoeuvre. Different gravity levels are achieved during the manoeuvre. The low-gravity phase lasts about 22 s and it is reached at the peak of the parabola (©NoveSpace/CNES/DLR/ESA Id 324324).	32
3.2	Phases of the parabolic flight manoeuvre (©ESA Id 330758).	33
3.3	Extrapolation of the central part of the accelerations profiles of the 16 th parabola (parabolic flight #22, 19 th May 20015, ©NoveSpace).	34
3.4	Top view of the cabin section (©NoveSpace).	34
3.5	Cross-section of the Airbus A310 ZERO-G testing area (©NoveSpace).	35
4.1	PACMAN experiment layout and main elements (left), detail of the CUBE (right).	38
4.2	The microcontroller board would have acquired and processed the data from the IMU, the on-board camera, the temperature sensors and the coils. The laptop would have collected data from the external reference cameras, the load cells, the accelerometers in proximity of the docking interface and those in the bottom wall of the CHAMBER. If necessary, useful telemetry data would have been processed and sent to the CUBE via the wireless board for the close-control loop.	41
4.3	NED reference system of the Airbus A310 ZERO-G (©NoveSpace).	43
4.4	Reference systems: CUBE reference system 'xyz', docking interface reference system 'xyz', Airbus A310 ZERO-G reference system 'XYZ'. The CHAMBER lays horizontally along the aircraft wingspan.	44
4.5	Best launch time windows for each parabola. Combined effect of the g-jitter along z (a), along x (b) and along y (c) with the aircraft pitch. Combined effect of the g-jitter along z (d), along x (e) and along y (f) with the aircraft roll.	46
4.6	Reference systems used in the simulations. The three reference frames at the moment of launch ($T = 0$, left) and the same reference frames during the low-gravity phase ($T > 0$, right).	47
4.7	The graphs represent the maximum displacements of the CUBE inside the Airbus A310 ZERO-G. The axis of the abscissae represents the launch instant, the ordinates axis the maximum displacement for each parabola. The duration of the free-floating phase was set to 4.5 s.	49
4.8	The graphs represent the maximum displacements of the CUBE inside the Airbus A310 ZERO-G along each axis at the best launch instants: 7, 8 and 11 s. The axis of the abscissae represents the considered parabola, the ordinate axis the maximum displacement for each parabola. The mean value and the standard deviation 's' are plotted as reference.	52

4.9	Two arbitrary current loops. The magnetic field produced by the current flowing in the blue coil interacts with the magnetic field produced in the red one. The interaction generates an electromagnetic force which acts on both coils in opposite directions.	60
4.10	Two arbitrary circular coils. The magnetic field produced by the primary coil interacts with the one generated by the secondary coil. The result is an electromagnetic force acting on both the coils.	61
4.11	Block diagram of the Simulink model implemented.	63
4.12	Axial force acting on the CUBE with no initial rotation/angular velocity.	64
4.13	Relative misalignment of 15° around the x -axis between the CUBE and the FFT.	65
4.14	Torque acting on the CUBE with initial rotation of 15° around the x -axis.	65
4.15	CHAMBER sensors. The data collected by these sensors will be processed by the Supporting Electronics outside the CHAMBER (laptop).	66
4.16	Electrical block diagram of PACMAN experiment text.	66
4.17	CHAMBER structure. The CUBE and the FFT will be launched towards each other. The CHAMBER will be surrounded by a net (not showed in the figure).	67
4.18	Top view of cabin layout with the main dimensions (right) and zoom of the baseplate with the distances of the fixing holes highlighted (left). All the measures are in [mm].	68
4.19	Photo of the rack structure and its main elements.	69
4.20	Hold system design (left) and final assembly (right). The launch plate is directly connected to the Bosch profile on the linear guide, while the release interface can be oriented simply by screwing and unscrewing the orienting screw.	70
4.21	Linear guide used to launch the CUBE and the FFT during the low-gravity phase.	70
4.22	DUO MC stereo-camera used as the external reference camera to acquire images of the CUBE and the FFT during the floating phase.	72
4.23	Photo of the complete CUBE in aluminium (left) and electronic boards stacking (right).	72
4.24	The CUBE magnetic actuators. The coils are the actuators of the rendezvous/attitude control system.	73
4.25	TMP36GZ thermal sensor used to monitor the coil temperature.	73
4.26	Raspberry Pi NoIR Camera V2 module. The camera aboard the CUBE is used for visual relative pose (position/attitude) determination.	74
4.27	IMU board. The IMU board is powered at system start-up and acquires data for the whole duration of the floating phase.	75
4.28	Phidget Spatial Precision 3/3/3 High Resolution IMU board.	76
4.29	Data Handling & Communication Subsystem. Raspberry Pi 3 model B is used to manage the video data obtained from the Raspberry Pi NoIR Camera V2 module and process the attitude and position information coming from the IMU board. Arduino UNO uses these pieces of information for the feedback control loop to correctly power the magnetic actuators.	76
4.30	PID control algorithm. The scheme presents an anti-windup that allows a faster response to the feedback loop. Several constant parameters were tested during the simulations. As a result, the P gain selected is bigger than the D and I gains.	77

4.31	PID control algorithm and current inversion. Two different PID controls command the pitch and roll angle of the CUBE, powering in pairs the coils and summing the resulting control signal on each coil.	78
4.32	Power subsystem. Battery pack and buck converters highlighted inside the CUBE with the custom Printed Circuit Board (PCB) and the two Pololu A4990 dual motor drivers.	79
4.33	Driver circuit. Pololu A4990 Dual Motor Driver Shield boards connected to the microcontroller Arduino UNO.	80
4.34	Schematic of the A4990 Dual Motor Driver Shield board.	80
4.35	Block diagram of the driver circuit.	81
4.36	Schematic (top) and block diagram (bottom) of the electrical connection of the CUBE. The battery pack supplies both the Drock buck and the Eboot buck converters. The Drock buck converter lower the voltage to 7 V to supply the Pololu A4990 Dual Motor Driver Shield boards and Arduino UNO while the Eboot buck converter gives 5.1 V in input to the Raspberry Pi model B. The power supply to all the other devices is directly managed by the microcontrollers boards.	82
4.37	Hold & launch system interface. The small iron plate at the centre of the bottom face of the CUBE matches connect precisely to the holding electromagnet. The small incisions are used to align correctly the CubeSat after the recovery. The proximity sensor is used to trigger the data acquisition	83
4.38	Photo of the FFT. The mechanical structure of the CubeSat is the same used for the CUBE. An Arduino UNO is used as microcontroller to power the coil properly through the driver circuit.	84
4.39	Docking interface. The coil of the target is wrapped around the aluminium structural rod and powered by the driver circuit.	84
4.40	OSRAM SFH 487 P LED.	85
4.41	Position of the five LEDs on the docking interface. Four LEDs are positioned on the surface (red circle) while the fifth one is on a different plane.	85
4.42	Microcontroller board. Arduino UNO is used as the microcontroller board of the FFT to power correctly both the docking interface (through the Boost buck converter) and the IMU. A micro SD card is used to store all the data.	86
4.43	SparkFun 9 Degrees of Freedom - Sensor Stick IMU board powered at system start-up.	86
4.44	The power subsystem of the FFT is composed of two different buck converters and the battery pack.	87
4.45	Block diagram of the electrical connection of the FFT. The battery pack supplies both the Eboot buck and the Boost buck converters. The Eboot buck converter lower the voltage to 5 V to supply Arduino UNO and the LEDs while the Boost buck converter gives 14.4 V in input to the docking interface.	88
5.1	Experimental setup. The repellent force between the two coils is measured as a weight variation.	92

5.2	Comparison between the experimental results obtained in laboratory conditions and the data obtained from the model. The green circles represent the measured force (in mN), while the blue cross represent the force obtained from the model (in mN) as a function of the distances (in mm) between the two coils. The red bars represent the relative percentage error.	93
5.3	a) Image of target mock-up equipped with four IR LEDs, b) image of the pattern acquired with a reduced exposure time, c) relevant features identified in the image.	94
5.4	Experimental setup. High precision motorized linear stages and rotary stage (left), target mock-up equipped with four IR LEDs (right). The reference systems of the experimental setup (green), the camera (yellow) and the target mock-up (blue) are highlighted.	95
5.5	Imposed target trajectory referred to the plane reference frame P . The linear stages were used to impose planar displacements (along x and z -axis) to the target mock-up; y -axis corresponds to the displacement orthogonal to the plane.	96
5.6	Error obtained by the comparison between the real target trajectory and the reconstructed one.	98
5.7	Euler angles measured with the camera (red) and their mean value (black dashed line). The results are obtained by image processing.	98
5.8	CUBE temperature test. Two thermal sensors were used, one connected to the CubeSat structure and another one directly in contact with a coil.	99
5.9	CUBE coil temperature trend during the test considering a possible real-mission profile.	100
5.10	CUBE structure temperature trend during the test considering a possible real-mission profile.	100
5.11	Position of the temperature sensors on the FFT. Arduino UNO with the Adafruit Motor Shield Driver V2 (over the CubeSat docking interface) is used to power the coil while the other one (next to the breadboard) imposes the cycle.	101
5.12	FFT coil temperature trend during the test considering a possible real-mission profile.	101
5.13	FFT structure temperature trend during the test considering a possible real-mission profile.	102
5.14	Voltage drop across the resistance with a PWM duty cycle equal to 100%. The yellow line represents the first channel of the oscilloscope, while the blue line represents the second one. The red line represents the difference between the two measurements and thus the voltage drop (960 mV) across the resistance.	103
5.15	“Plug ‘n’ play” interface and launch plate. The “plug ‘n’ play” interface could be replaced during the long pause after the first 15 parabolas. Different orientations of the matching prisms would have allowed different initial orientations of the CUBE/FFT. The launch plate housed the holding electromagnet used to support the weight of the CUBE/FFT during the hyper-gravity phases.	104
5.16	Holding electromagnet of the release interface. The electromagnet is able to bear a load of 8 kg.	105

6.1	Launch sequence during the 20 s of low-gravity phase. The time sequence is not in scale. The blue rounded cells report the CUBE & FFT operations during the parabola. The free-floating phase starts at 11 s after the injection when the launch velocity is reached and lasts ~ 4 s. The red rounded cells report the main operations executed with the CHAMBER's sensors.	109
6.2	Experimental procedure during each parabolic flight.	110
7.1	Geometrical reference system and the two study cases, $R\text{-bar}$ and $V\text{-bar}$ approaches.	115
7.2	Hohmann transfer ($R\text{-bar}$ approach, blue solid line) and Phasing manoeuvre ($V\text{-bar}$ approach, red dashed line). In both cases, the maximum drift is comparable with the initial distance between target and chaser, making these approaches unsuitable and unsafe for close-range rendezvous manoeuvres.	118
7.3	Glideslope manoeuvre example (left) and reference position and velocity law (right). In this manoeuvre, the chaser approaches the target by means of multiple hopping orbital manoeuvres (red, solid line), with a constant maximum drift from the straight-line approach (dotted blue line).	122
7.4	Glideslope approach, 10 steps, $R\text{-bar}$ (left) and $V\text{-bar}$ (right) directions.	123
7.5	Tethered docking approach: 1) tethered probe deployment, 2) electromagnetic self-alignment, 3) soft-docking 4) tether rewind and hard-docking (courtesy of FELDs experiment).	125
7.6	Working principle of the launch system. After tether release 1), the launch plate is pushed by the spring, driving the probe 2) until its separation 3).	127
7.7	The spring-based launch system developed during FELDs experiment. The release system is positioned laterally.	127
7.8	FELDs releasing system (up), successful (centre, 3 rd drop) and unsuccessful (down, 4 th drop) tether release: the tether snagged into the sliding ring, increasing the friction and preventing the accomplishment of the soft-docking manoeuvre.	129
7.9	The upgraded launch system developed in STAR experiment.	129
7.10	STAR launch system during a drop test. From left to right, the tethered probe before release, the launch phase and the probe after separation from the plate.	130
7.11	Sketch of the controlled tether deployment/retrieval system.	132
7.12	STAR controlled tether deployment/retrieval system tested during the <i>Drop Your Thesis!</i> campaign.	132
7.13	Second drop test, from left to right: deployment, tether fully extended and probe free-floating, retrieval.	133
7.14	Test in micro-gravity conditions of a simplified soft-docking manoeuvre: once the probe reaches the sphere of influence of the target, its motion is clearly perturbed.	134
7.15	Results obtained during three different drop tests. The ferromagnetic probe approaches the electromagnet after entering its sphere of influence, modifying its trajectory.	134

7.16	Tether reference system: the x -axis is along the local vertical, the z -axis gives the direction of motion and the y -axis completes the reference system. The angle ϑ measures the libration angle of the tether in the xz orbital plane.	136
7.17	Equilibrium positions of the dumbbell system: specular positions along the local vertical (left, 1-2) and horizontal (right, 3-4) respectively.	136
7.18	Representation of the electromagnetic dipoles. Each dipole has its own body reference frame (xyz) which can move and rotate with respect to the target reference frame (XYZ) following its centre of mass. The orientation angles are reported in the figure while r represents the distance between the dipoles.	138
7.19	Initial configuration of the system. The dipoles are aligned with the X -axis and thus no torque is transmitted. The attractive force generated by the magnetic fields produces the translation.	141
7.20	Forces between the dipoles. Since the dipoles are aligned with the X -axis, the mutual attractive forces between them is only along that direction. Blue line represents the attractive force of dipole A, while red line represents the attractive force of dipole B.	142
7.21	Position and velocity of the dipoles. Since the dipoles are aligned with the X -axis, the displacements and the velocities are only along that direction. Blue line represents the displacements and velocities of dipole A, while red line represents the same physical quantity of dipole B.	142
7.22	Experimental setup. The magnetic guidance effect was analysed studying the slide displacement due to the electromagnetic attractive force of the electromagnet.	143
7.23	Experimental configuration and reference axes. The rail is inclined by an angle α which allows the evaluation of the contribution to the acceleration profile of the slide due to the gravity force and the residual friction.	144
7.24	Comparison between experimental data collected when the electromagnet is switched off and the mathematical model.	145
7.25	Acceleration profile obtained by experimental data due to the electromagnetic force induced by the electromagnetic field of the electromagnet.	145
7.26	Target and chaser position in the target reference system. The distance d between the spacecraft is of 60.25 m. The spacecraft are in two different orbits: the blue dashed line corresponds to the chaser while the red one is the target orbit, respectively.	146
7.27	Phases of the tether deployment during the orbital motion of the spacecraft. For the R -bar approach, the deployment of the tether has to start at the right time to assure the probe-target encounter: a) initial position of the two spacecraft at 1 s, b) 500 s, c) 1000 s and d) 1458 s after the beginning of the deployment. The blue line represents the trajectory of the probe.	147
7.28	Configuration of the chaser at the beginning of the tether deployment (top) and target and chaser position in the target reference system (bottom) at the end of the soft-docking manoeuvre.	148
7.29	Target and Chaser position in the Target reference system. The Target is at a distance d of 175.4 m ahead of the Chaser. Both spacecraft share the same orbit: the blue stripped line corresponds to the Target orbit while the red one is the Chaser trajectory.	148

7.30	Configuration of the chaser at the beginning of the tether deployment (top) and target and chaser position in the target reference system (bottom) at the end of the soft-docking manoeuvre.	149
7.31	Soft-docking manoeuvre. When the probe reaches the sphere of influence of the electromagnetic interface mounted on the target spacecraft, the generated magnetic field drives it towards the target and realizes an automatic alignment between the two interfaces and the soft-docking is then realized.	150
8.1	PACMAN evolution.	152
8.2	TED development plan, from the initial concept through critical technologies design and verification, in the prospective of an in-space demonstration.	155
8.3	TED-Sat preliminary design.	155
A.1	Block diagram of a generic driver circuit for the CUBE.	159
A.2	Electrical scheme of the custom voltage/current converter.	160
A.3	Results of the simulation. The custom voltage/current converter scheme is powered with a sinusoidal input with an amplitude of 3.3 V and a frequency of 1 kHz.	161
A.4	Scheme of the L298N IC (left) and the complete board (right). This board represents a good alternative as driver circuit, can be used with Arduino UNO and is capable to drive 2 A for each channel.	162
A.5	Arduino UNO Motor Shield. This board has the same characteristics of the L298N in terms of output current and input voltage. In addition, it can monitor the current flowing in the coils.	163
B.1	WBS of PACMAN Experiment.	165
B.2	Technical description of the WBS.	166
B.3	Subdivision of the work among the members of the team and person in charge.	167
B.4	PACMAN interdependences.	168
B.5	PACMAN Gantt Chart.	169
D.1	Bosch profile modelled as a beam with two fixed constrains, the CubeSat lumped mass and the Bosch profile distributed mass.	176
D.2	Bending moment diagram of the Bosch profile, modelled as a beam.	177
D.3	(Left side) The constraints limits all the six degrees of freedom (d.o.f): three translations (1,2,3) and three rotations (4,5,6). (Right side) The weight of the CUBE is applied as a lumped mass.	177
D.4	Resultants of the applied loads q and P (forces acting on the slides).	178
D.5	Resultants of the applied loads q and P (moments acting on the slides).	178

List of Tables

1.1	Summary of recent studies and experiments on magnetic rendezvous and docking.	13
3.1	Emergency landing condition loads (©NoveSpace).	35
4.1	Displacements of a free-floating object obtained from MATLAB [®] model: maximum displacement among the best time windows (column 3); mean displacement among the best time windows (column 4); maximum displacement among all the time windows (column 5); mean displacement among all the time windows (column 6).	45
4.2	Summary of the best launch instants that minimise the maximum CUBE displacement for the <i>X</i> -axis.	50
4.3	Summary of the best launch instants that minimise the maximum CUBE displacement for the <i>Y</i> -axis.	50
4.4	Summary of the best launch instants that minimise the maximum CUBE displacement for the <i>Z</i> -axis.	50
4.5	Functional requirements.	53
4.6	Performance requirements.	54
4.7	Design requirements.	57
4.8	Interface requirements.	57
4.9	Operational requirements.	58
4.10	Human factor requirements.	58
4.11	Peak power consumption of the CUBE components.	79
4.12	Peak power consumption of the FFT components.	87
5.1	Mean values (μ) and standard deviation (σ) of the measured attitude angles.	97
5.2	Duration of the different phases of a parabola during a PCF.	98
7.1	Comparison of continuous thrust manoeuvre and Hohmann transfer velocity budgets at significant instants.	120
7.2	Comparison of continuous thrust and phasing manoeuvre velocity budgets at significant conditions.	121
7.3	Comparison between the results obtained for glideslope manoeuvres and Hohmann transfers with different manoeuvre durations.	123
7.4	Comparison between the results obtained for glideslope and phasing manoeuvres at different manoeuvre durations.	124
7.5	Initial velocity and evaluated friction.	128

Abbreviations

AAREST	A utonomous A ssembly of a R econfigurable S pace T elescope
AMDS	A utonomous M icrosatellite D ocking S ystem
ATV	A utomated T ransfer V ehicle
COTS	C omponents O ff T he S helf
CPOD	C ubeSat P roximity O perations D emonstration
DEOS	D eutsche O rbitaler S ervicing M ission
EMU	E xtravehicular M obility U nit
ESA	E uropean S pace A gency
FELDs	F lexible E lectromagnetic L eash D ocking system
FFT	F ree F loating T arget
IC	I ntegrated C ircuit
ISS	I nternational S pace S tation
MDA	M acDonald D ettwiler and A ssociates
NASA	N ational A eronautics and S pace A dministration
NBL	N eutral B uoyancy L aboratory
NED	N orth E ast D own
OAAN	O n-Orbit A utonomous A ssembly from N anosatellites
PACMAN	P osition and A ttitude C ontrol with M agnetic N avigation
PCB	P rinted C ircuit B oard

PFC	P arabolic F light C ampaign
PWM	P ulse W idth M odulation
RC	R esistor C apacitor
RINGS	R esonant I nductive N ear-field G eneration S ystem
RRM	R obotic R efueling M ission
RSGS	R obotic S ervicing of G eosynchronous S atellites
RVD	R endez V ous and D ocking
SIS	S pace I nfrastructure S ervicing
SPHERES	S ynchronized P osition H old E ngage and R eorient E xperimental S atellite
STAR	S pace T ether A utomatic R etrieval
SWG	S tandard W ire G auge
TED	T ethered E lecttomagnetic D ocking
TRL	T echnology R eadiness L evel

Dedicated to my brother Luca and his girlfriend Alessandra, my parents Franco and Emanuela and all my family. I would not reach this crowning achievement without your continuous support in nourishing my dreams.

Chapter 1

Introduction

Since the beginning of space era, proximity manoeuvres have been performed with the goal of rendezvous and docking between spacecraft: the ability to approach and mate with another vehicle is fundamental for several important on-orbit operations [1], [2] such as refuelling, payload updating, inspections, maintenance, material and crew transfer, modular structure assemblies and in general all those processes requiring the participation of two or more collaborative vehicles. These operations are acquiring growing importance in space related fields and will surely obtain a key role in the near future, allowing the development of longer lifetime missions and ensuring further technological improvements.

As of today, for both large and small satellites, proximity manoeuvres are performed using mainly propulsive units for both position and attitude control. Usually, one vehicle, the chaser, uses actuation capabilities to perform the required tasks while the other one is considered the target. The first rendezvous manoeuvre was performed in 1965, when the Gemini 6A rendezvoused with Gemini 7. The technologies developed in those first years of space exploration from both the U.S. and the Soviet Union were then applied during the Apollo program and the majority of manned missions thereafter. Afterwards, complex and long lasting orbital outposts such as the American Skylab, the Russian MIR and the International Space Station (ISS) were placed in orbit thanks to the rendezvous and assembly of several modules delivered by subsequent launches and manoeuvred to mate. As of today, the propulsive approach is still fundamental in all the operations to ISS and in general to rendezvous and mate with another space vehicle. Concerning on-orbit servicing, Canadian Aerospace firm MacDonald, Dettwiler and Associates (MDA) developed the concept of the Space Infrastructure Servicing (SIS), a spacecraft able to operate as a small scale in-space refuelling depot for communication satellites in geosynchronous orbit [3]. The idea was to dock at the target satellites apogee-kick motor, remove a small part of the target spacecrafts thermal protection,

connect to a fuel-pressure line and deliver the propellant.

ViviSat Mission Extension Vehicle [4] proposed an alternative approach consisting in a connection with the target satellite via the kick motor, without any fuel transfer: the attitude control for the target is supplied by its own thrusters. This concept is considered to be similar to NASA Robotic Refueling Mission (RRM) [5] flown aboard the ISS and tested in January 2013. An extensive series of robotically-actuated propellant transfer experiments on the exposed facility platform of the ISS were completed by the RRM equipment suite and the Canadarm/Dextre robotic arm combination.

By comparison, the Robotic Servicing of Geosynchronous Satellites (RSGS) program (the new name of DARPA Phoenix Project [6]) has an even more complex mission concept: cooperatively harvest and reuse valuable components (like solar arrays, antennas, or other components) from satellites in orbit that have been retired and transport it to another satellite, either a newly constructed spacecraft or one in need of repairs.

In September 2012, the DLR Space Administration [7] announced “DEOS” (German orbital servicing mission), a funded development project to build a two-vehicle set of spacecraft to demonstrate several technologies necessary for on-orbit satellite servicing, including spacecraft refuelling. According to plan, DEOS was expected to be ready for launch in 2018, but the project was cancelled after the definition phase.

Recently, Airbus Defence and Space is developing the Airbus Space Tug [8], a satellite-servicing vehicle capable of accomplishing on-orbit operations such as refuelling, repairing, and monitoring the status of existing spacecraft orbiting Earth. The vehicle should be able to perform autonomous maintenance and logistic operations, as well as cleaning procedures of space debris.

Airbus is already participating to satellite servicing operations through two European Space Agency (ESA) programs, CleanSat [23] (deorbiting technologies) and eDeorbit [24] (ESA satellite removal from a low-Earth orbit), but its entrance in the on-orbit servicing market follows the last significant progresses in this field made by Orbital ATK which developed its new servicing satellite able to extend the life of a healthy one: the Mission Extension Vehicle-1 (MEV-1) [9]. Currently under production and scheduled to launch in 2018, MEV-1 will provide life extension services (acting on the propulsion and attitude control systems) to an Intelsat satellite using a low-risk docking system that can attach to the existing features of the target satellite. The vehicle is able to perform numerous docking and undocking manoeuvres during its life span and thus can serve multiple satellites offering also different service capabilities such as inspection, relocation of the satellite to different orbital slots or to different orbits and inclination pull-down services.

Life-extension and in-orbit services are also the focus of British-Israeli company Effective Space Solutions, which is developing its solution based on the deployment of an operating fleet of small spacecraft equipped with a universal docking system. The details of

the project are still undisclosed [10].

Nowadays, the common missing link among the projects which can make the difference, is an automatic docking system which is able to operate without human assistance and can be utilized efficiently also in unmanned missions or on-orbit servicing. This is one of the main research topic towards which all the space related companies are converging. It is well rendered that an effective, standard and reliable solution is not addressed yet. All the above mentioned systems have higher alignment and attitude control requirements, which represent an onerous obstacle to the development of longer lifetime missions.

1.1 Spacecraft rendezvous and docking manoeuvres

The rendezvous and docking process entails a series of orbital manoeuvres and controlled trajectories, which progressively bring the chaser into contact with the target. The last part of the manoeuvre is used to put the chaser in the right conditions, in terms of position, velocities, attitude and angular rates, required to accomplish the docking process.

A rendezvous and docking mission can be divided into six main phases [25].

1.1.1 Launch

The objective of this phase is the injection of the spacecraft into the selected orbital plane. The possible injection errors due to small deviation from the nominal launch time are corrected during this phase, since the relative velocity is still low and thus the cost in terms of required ΔV is smaller than in the other phases. The adaptability to the launch delay depends on the corrections abilities of the launcher.

At the end of this first phase, the spacecraft is in the correct orbital plane with its steady orbital conditions.

1.1.2 Phasing

The objective of this phase is to reduce the orbital phase angle between the chaser and the target rising and lowering the chaser orbit in order to modify its orbital parameters. During this phase the launch injections errors are corrected and the chaser is placed on the target orbit (or very close to it), ready to start the far range rendezvous manoeuvres. All the phasing procedures are accomplished using the sensors aboard the chaser spacecraft or controlled from the ground segment. During the phasing manoeuvre, spacecraft navigation measurements are referred to a Earth-centred inertial frame (FIGURE 1.1).

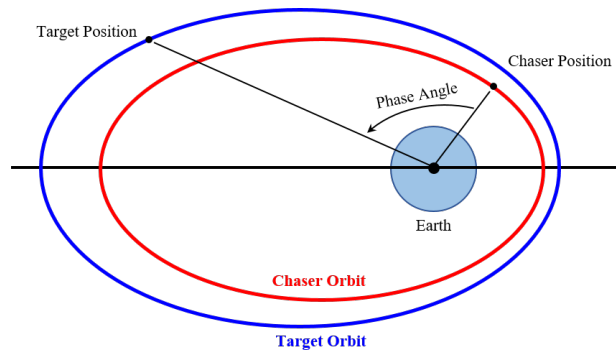


FIGURE 1.1: Earth-centred inertial frame and phase angle definition.

There are no fixed phasing trajectories since the phase angle varies depending on the launch day and the orbital plane the spacecraft has to reach. Different approaching strategies can be performed depending on several factors, the most important ones represented by the position of the docking port and the direction of its axis on the target spacecraft.

1.1.3 Far range rendezvous

Also called “homing”, the goal of this phase is to achieve the conditions (position, velocities and angular rates) essential for the next close range rendezvous phase. The so-called “hold point” on the target orbit is reached during this phase, a particular position in which the chaser can stay indefinitely without consuming propellant. The far range rendezvous manoeuvres are accomplished by using relative navigation sensors (e.g. radars or relative GPS) and the required measurement accuracy varies from a hundred of meters at the beginning to few tens of meters at the end before the start of the close range rendezvous.

During the far range rendezvous and for all the subsequent phases it is more convenient to study the chaser motion in relation to the target one, since the focus is the analyses of the relative trajectory evolution. For this motivation, the target local frame is usually preferred (FIGURE 1.2).

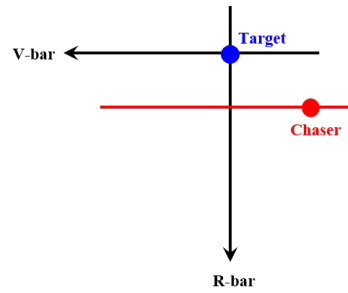


FIGURE 1.2: Target local frame: the coordinate system is centred at the target and it moves with it along its orbit. The direction of motion is defined with a straight line and named as $V - bar$ while the direction toward the centre of the Earth is named $R - bar$. The orbital angular momentum vector H complete the reference system.

1.1.4 Close range rendezvous

The objectives of this phase are the reduction of the distance between chaser and target and the achievement of the conditions (in terms of position, velocities, attitude and angular rates) necessary to perform safely the final approach. Dedicated sensors with ranges from tens of meters to few centimetres are required during the close range rendezvous, with accuracies up to 1% of the range.

Several different final trajectories can be performed in order to accomplish a close range rendezvous manoeuvre, depending on the approaching direction of the chaser: $V - bar$ or $R - bar$.

For the $V - bar$ approaches, the manoeuvre starts after the chaser reaches the “hold point”. From this position, a straight line closing approach can be performed. This manoeuvre aims at maintaining a quasi-rectilinear trajectory to keep the chaser into the right approach corridor to reach the target docking port safely, but since the thrusters used to perform the manoeuvre can be modulated only acting on the burning time, a hopping trajectory is obtained through a series of consecutive ΔV s.

Concerning $R - bar$ approaches, three different manoeuvres can be performed: 1) a fly-around that starts from a position along the $V - bar$ direction and bring the chaser to the $R - bar$; 2) a direct acquisition of the $R - bar$ trajectory arriving from a lower orbit than the target one; 3) the acquisition of a drift trajectory toward the $R - bar$ approach corridor arriving from a slightly lower orbit than the target one.

FIGURE 1.3 shows all these different manoeuvres.

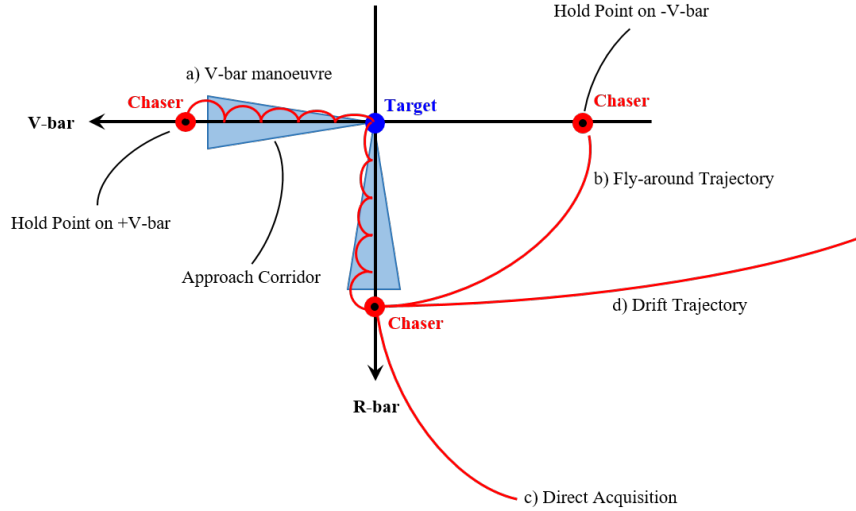


FIGURE 1.3: $V - bar$ (a) and $R - bar$ (b,c,d) close range rendezvous approaches.

1.1.5 Docking

This phase represents the final approach to contact and the goal is to correctly align the chaser/target docking interfaces keeping under control the relative position, velocities, attitude and angular rates. The typical trajectories are closed loop controlled straight (or quasi-straight) line approaches realised by multiple thruster pulses. For the sake of clarity, the term *docking* is used to define all the active operations made by the chaser to mate with the target spacecraft. In particular, the term docking is used when the capture interfaces of the chaser get in contact with those of the target vehicle creating a rigid structural connection between the two spacecraft. According to [25], nine main operations can be identified during a docking manoeuvre involving a manned scenario. These phases are summarized as follows:

1. Reduction of the chaser approach velocity to a constant final value and alignment of the docking interfaces. The constant velocity is achieved to avoid braking thrusts that could negatively affect the target (changing its dynamics or contaminating its external surfaces with particulate), while the alignment between the docking interfaces is performed to guarantee the contact between the spacecraft.
2. Reaching of the range in which physical contact (and thus docking) between the two spacecraft is possible. This range has to be large enough to take into consideration all the possible small relative displacements between chaser and target due to the residual misalignment or to dynamic effects.
3. Attenuation of the impact between the docking interfaces to avoid the bounce-back effect. When the docking interfaces of the spacecraft get in contact during

the docking manoeuvre, they will rebound depending on the nature of the structure material and the impact dynamics (elastic, plastic). A shock absorber has to be applied to reduce the relative velocity between the two vehicles and increase the duration of the connecting phase.

4. Conclusion of the capture phase. At this point of the docking manoeuvre, the two spacecraft are close enough to complete the capture: mechanical latches are actuated and the two spacecraft are joint together. The alignment between the docking interfaces is almost complete, even if the rigid connection (“hard” docking) between the two vehicles is still not concluded.
5. Structural alignment and contact between the docking interfaces. The activation of the latches during the previous phase guarantees that the spacecraft docking interfaces do not detach from each other consequently to the push given by the action of the shock absorber. A retraction mechanism is usually used in this phase to preserve the contact between the docking interfaces and ensure the alignment necessary for the final rigid connection (hard docking).
6. Stiff structural connection under a pre-load. After the alignment, the docking interfaces are pressed together towards each other and the pre-load applied to the surfaces allows a stiff structural connection.
7. Connection of the utilities. When hard docking is achieved, electrical (for both data and power transfer), fluid and gas connections can be performed. In case of manned missions, all the utilities connections are performed after the pressurization of the connected spacecraft and the hatch openings.
8. Pressurization of the volume between the hatches. This phase starts right after the achievement of the rigid connection.
9. Opening of the hatches and post-docking operations initialization.

1.1.6 Departure

The departure phase is the last phase of a RVD manoeuvre and consists in the chaser departure after its separation from the target. The departure manoeuvre take place in conjunction with the re-initialization of the GNC system and the opening of all the connections accomplished during the previous docking phases.

FIGURE 1.4 shows the last five phases of the six usually recognised for space rendezvous and docking. The close range rendezvous is the most demanding from the navigation point of view, due to the strict safety constraints that limit the possible approach strategies and increase the manoeuvring velocity budget [26]. Furthermore, the docking phase

requires dedicated mating mechanisms, which shall be able to realise a soft joining before activating the hard-docking latches.

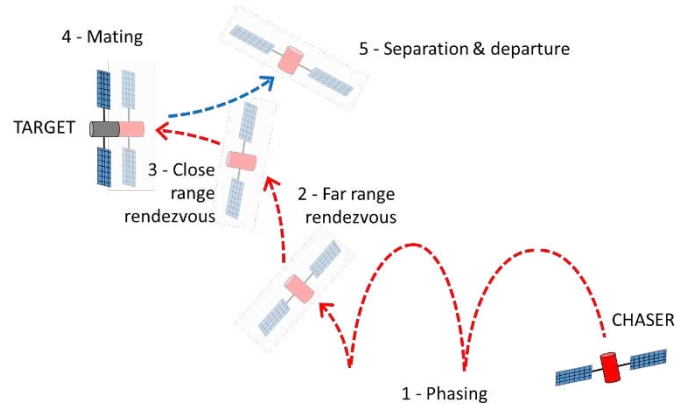


FIGURE 1.4: Standard rendezvous and docking manoeuvre. Usually, the close range rendezvous is the most critical phase due to the strict navigation and safety requirements.

1.2 Docking mechanisms for large spacecraft

The first space rendezvous manoeuvre has been accomplished in December 1965, when NASA launch the Gemini 6A and Gemini 7 spacecraft in the framework of the Gemini Program. Only few months later, in March 1966, Gemini 8 and the Agena Target Vehicle completed the first RVD manoeuvre [27] (FIGURE 1.5).



FIGURE 1.5: Photo of the Agena Target Vehicle taken from the Gemini 8 (courtesy of NASA).

This remarkable achievement marked significantly the following years, allowing scientist to design and develop space assemblies that were merely imaginable at that time.

Important on-orbit operations such as refuelling, payload updating, inspections, maintenance, material and crew transfer, modular structures assemblies and, in general, all those processes requiring the participation of two or more collaborative vehicles became achievable, a wider variety of technological developments and a deeper understanding of the Universe possible.

In 1967 the Soviet Union performed the first fully automated space docking with two unmanned vehicles during the Kosmos 186 and Kosmos 188 missions. The docking mechanism consists in a central probe-drogue docking system with a capturing conical interface mounted on the target and a suspended damping rod on the chaser. At the same time, the U.S. developed a similar probe-drogue system (see FIGURE 1.6, 5 and 6) to allow the Command/Service Module to dock with the Apollo Lunar Module and with the Skylab space station. The docking mechanism has been used in all the Apollo missions.

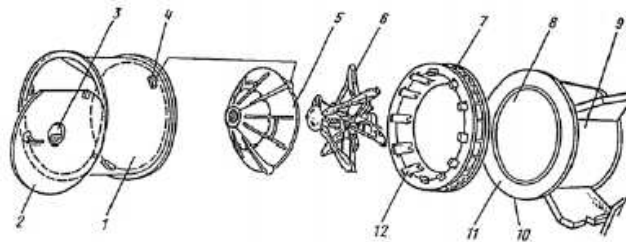


FIGURE 1.6: Apollo probe-drogue docking system (courtesy of NASA).

In 1975 the Apollo-Soyuz Test Project aimed at developing and testing an androgynous docking mechanism. The significant innovation within this project lies mainly in the androgyny characteristic: the docking interfaces are identical on both the spacecraft, in contrast with all the previous docking systems that present a “gender mating”. The advantages of such mechanisms are 1) the system-level redundancy, 2) the possibility of collaboration between any pair of spacecraft and 3) the flexibility in the mission design [11]. The docking interfaces were developed independently, but following common specifications. On the U.S. side, an improved version of the probe-drogue system established for the Apollo Program with reception petals was developed while a similar interface was made by the Soviet side (FIGURE 1.7, left).

In 1994 an improved version of the Soviet docking mechanism, the Androgynous Peripheral Docking System (APDS), developed by the Soviet engineer Vladimir Syromyatnikov [12], was used as the interface for the docking between the Space Shuttle and the ISS (FIGURE 1.7, right).

In 1996 NASA began the development of the Advanced Docking Berthing System which would become the Low Impact Docking System (LIDS) just few years later, in 2004.

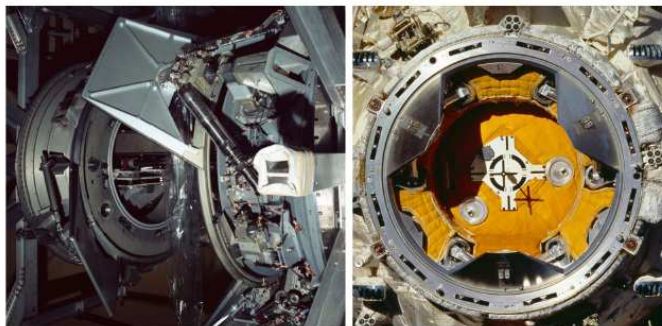


FIGURE 1.7: American and Soviet docking interfaces (left) for the Apollo-Soyuz Test Project and the improved Androgynous Peripheral Docking System (right) (courtesy of NASA).

In 2010, following the guidelines of the International Docking System Standard (IDSS) [11], the LIDS became the international Low Impact Docking System (iLIDS) or simply the NASA Docking System [13] (NDS, FIGURE 1.8).

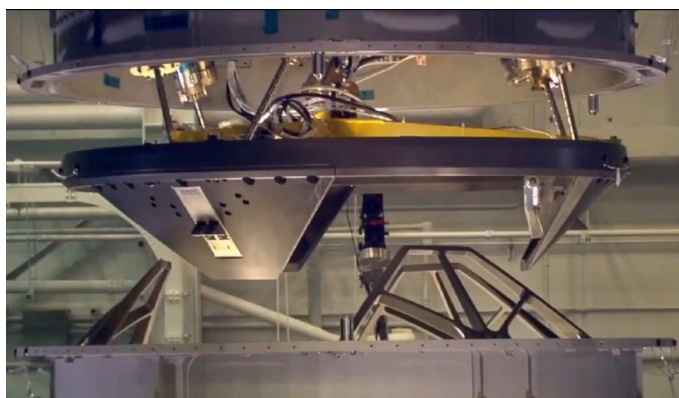


FIGURE 1.8: NASA Docking System (NDS): active androgynous variant (top) and passive interface (bottom) (courtesy of NASA).

Always in the 1996, a hybrid docking mechanism combining both the standard Russian interface developed in 1967 and the APDS has been created, combining the probe-drogue mechanism with the APDS hard-dock collar. This docking system is currently used on the Progress and ATV vehicles.

In 2011 the Chinese Shenzhou spacecraft successfully accomplished a RVD manoeuvre with the chinese Space Station Tiangong-1. The employed docking system was based on the Russian APDS mechanism. The same system will be used to dock also with the future Space Station and cargo vehicles.

In December 2015 QinetiQ Space, funded by ESA, passed the Critical Design Review for the International Berthing and Docking Mechanism [14] (IBDM, the European version of the LIDS) and few months later, in March 2016, successfully tested it. The IBDM is an androgynous low impact docking mechanism that is capable of docking and berthing

large and small spacecraft. The docking mechanism comprises a Soft Capture Mechanism (SCS) which uses 6 motorized legs to facilitate the alignment between the interfaces during capture and a Hard Capture System (HCS) which features mechanical hooks to close the interfaces.

1.3 Docking mechanisms for small satellites

Autonomous rendezvous and docking was hardly addressed in space, with few important exceptions like European ATVs and Russian Progress spacecraft; considering small satellites, no competitive or commercial solution is currently available. Therefore, in the last years there has been an increasing interest in developing different technologies for proximity navigation and rendezvous manoeuvres, addressing the main issues of fuel consumption and strong impact of close range navigation subsystems on satellites mass budget and complexity with innovative solutions and concepts. Above all, one promising solution is represented by the relative magnetic navigation exploited for both close range rendezvous manoeuvre [28] [29] and formation flight [30] [31] [32], where the satellite relative position and attitude can be controlled thanks to magnetic interactions with another vehicle, conserving the system momentum while allowing to save fuel .

The state of the art of small docking interfaces is probably represented by the Synchronized Position Hold, Engage, Reorient, Experimental Satellites (SPHERES) experiment aboard the ISS [33]. The three devices which compose the experiment are capable to connect to each other or to other servicing modules through a common pin-hole architecture [15], in addition to perform precise relative navigation and synchronized maneuvers (FIGURE 1.9).



FIGURE 1.9: (September 4th, 2013) ESA astronaut Luca Parmitano conducting an experiment with a pair of SPHERES (courtesy of NASA).

Another connection system for small-scale spacecraft is represented by AMDS [16]. The docking system within this experiment is composed essentially by an extendable probe

which is captured by a drogue and then retracts, allowing the two vehicles to mate. The Autonomous Rendezvous Control And Docking Experiment (ARCADE) was developed by CISAS “G. Colombo” and consists of a docking system very similar to AMDS and composed by a conical probe which is captured by an electromagnet placed at the end of the drogue. The system is capable to perform both soft and hard docking establishing a rigid connection (FIGURE 1.10).

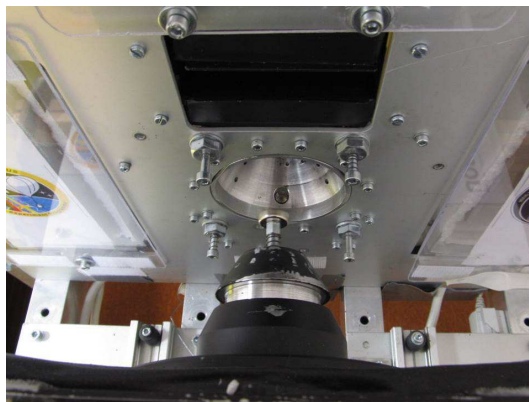


FIGURE 1.10: ARCADE probe-drogue system. The conical probe is captured by an electromagnet placed at the end of the drogue. The rigid connection is realized by pulling the probe towards the drogue and securing it with three latches.

The most important contribution on this concept is the RINGS (Resonant Inductive Near-field Generation System) project in the framework of MIT SPHERES program (FIGURE 1.11). In the on-orbit tests on the ISS, the SPHERES vehicles were equipped with large coils, in order to generate electromagnetic coupling actions for both power transfer and relative navigation [34].

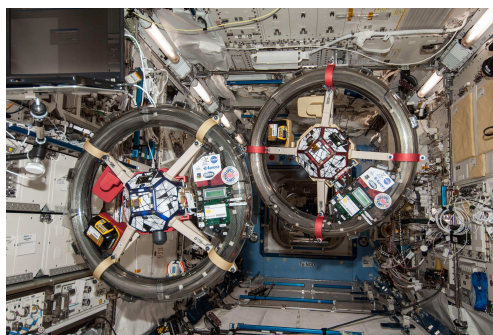


FIGURE 1.11: SPHERES satellites equipped with the RINGS floating in the ISS (courtesy of NASA).

In parallel, in the framework of the Autonomous Assembly of a Reconfigurable Space Telescope (AAReST) program for on-orbit assembly of a space telescope, a simplified technology was designed and tested in ground laboratories by Underwood & Pellegrino [17] on low friction tables. A very similar technology has been developed and tested in

ground laboratory also by Chen [18].

Recently, the Surrey Training Research and Nanosatellite Demonstrator (STRaND) programme is developing and testing in laboratory STRaND-2, a nano-satellite able to perform visual inspection, proximity operations and docking using a series of tuned magnetic coils [19].

Another relevant work was realized in the FELDs experiment (*Drop Your Thesis!* 2014), that tested the self-alignment capabilities of a tethered soft docking system based on a ferromagnetic tethered probe launched towards a target electromagnet: it demonstrated the effect of the magnetic interactions on the probe, that was passively guided to mate with the target [20].

Recently, the CubeSat Proximity Operations Demonstration (CPOD) plans to perform with two identical 3-U modules several on-orbit tests of rendezvous, proximity operations and docking by means of low-cost off the shelf components [21].

Last, the On-Orbit Autonomous Assembly from Nanosatellites (OAAN), a collaboration between NASA's Langley Research Center in Hampton, Virginia, and Cornell University in Ithaca, New York, plans to study autonomous control algorithms for rendezvous and docking manoeuvres, low-power reconfigurable magnetic docking technology, and compact, lightweight and inexpensive precision relative navigation using carrier-phase differential GPS with a three-degree of freedom ground demonstration [22].

TABLE 1.1 shows the relevant investigation on magnetic rendezvous and proximity operations under development.

TABLE 1.1: Summary of recent studies and experiments on magnetic rendezvous and docking.

Name	Institute	Year	Topic
RINGS	MIT	2010-15	Electromagnetic coupling for power transfer and relative navigation
AAReST	CALTECH	2015	Ground test of electromagnetic coupled servicing satellites
STRaND-2	Surrey University	2013	Ground test of proximity operations and docking using a series of tuned magnetic coils
FELDs	UNIPD-CISAS	2014-15	Drop tower test of magnetic guidance
CPOD	Tyvak - NASA	2015-16	CubeSat for rendezvous and docking manoeuvres demonstration
OOAN	Cornell University - NASA	2015-16	CubeSat for rendezvous and docking manoeuvres demonstration

As previously mentioned, reliable and precise navigation sensors are required to perform proximity operations; while for large satellites technologies such as LIDARs [35, 36] and radio systems [25] have been proved, for small satellites the research is focusing on smaller and cheaper infrared and visible optical sensors.

A relevant example is once again represented by SPHERES, that, in the framework of the Universal Docking Port (UDP), design and test a system based on a camera and four markers for close range relative attitude and position determination [37] (FIGURE 1.12).

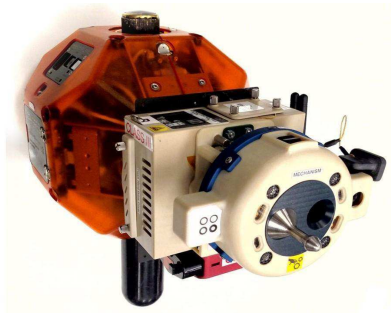


FIGURE 1.12: A SPHERES satellite with the connecting interface, the Universal Docking Port (courtesy of NASA).

The UDP markers are four circles with different circumference thickness, centred on the vertex of a square: a simple image analysis can detect them and calculate the position of their centres. The shape of the quadrangle determined by these points gives enough information to determine the relative position and attitude of the camera with respect to the markers.

In parallel, at the University of Padova, in the framework of the Autonomous Rendezvous Control And Docking Experiment (ARCADE), a 2D proximity sensor based on a modulated infrared emitter and two receivers have been designed and tested [38]; further studies are focusing on an hybrid system merging the IR sensor with a LED and camera system [39].

1.4 Research objectives, thesis structure & work logic

The goal of this research project is to study, with both numerical simulation and laboratory testing, viable strategies for spacecraft RendezVous and Docking (RVD) manoeuvres exploiting electro-magnetic interactions.

The objectives of this research project are:

1. the development of dynamical models for electromagnetic RVD applications and their verification through experiments;
2. the development and experimental verification in relevant environment (low-gravity) of electromagnetic soft docking interfaces.

To fulfil these objectives, the thesis has been divided into two main parts (FIGURE 1.13):

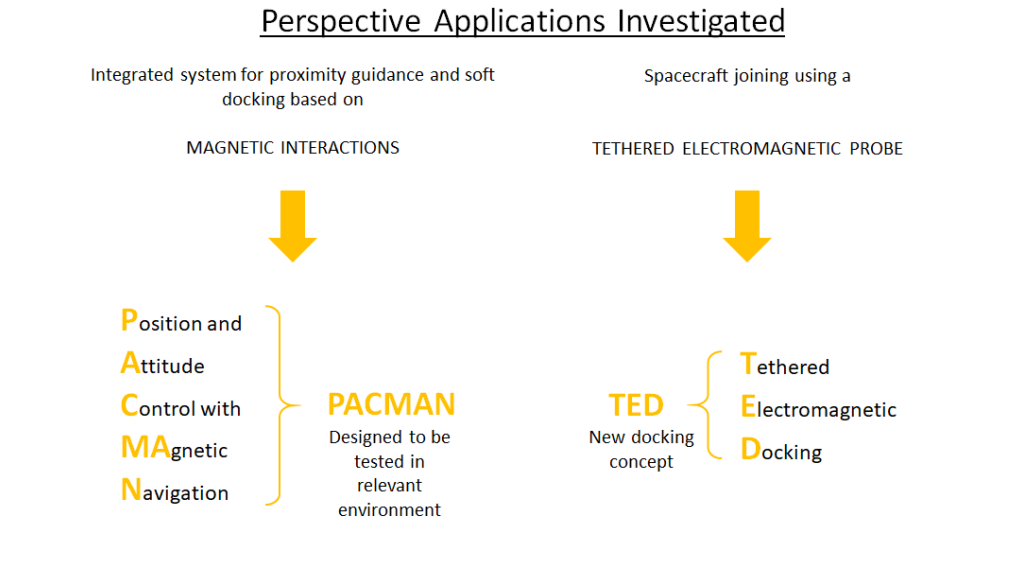


FIGURE 1.13: Investigated perspective applications: PACMAN Experiment & TED.

1. in the first one, PACMAN (Position and Attitude Control with MAGnetic Navigation) experiment is presented. The idea of PACMAN is to actively exploit magnetic interactions for relative position and attitude control during rendezvous and proximity operations between small-scale spacecraft. This is accomplished by launching a miniature spacecraft mock-up (CUBE) and a Free-Floating Target (FFT) that generates a static magnetic field towards each other; a set of actively-controlled magnetic coils aboard the CUBE, assisted by dedicated localization sensors, are used to control its attitude and relative position assuring the accomplishment of the soft-docking manoeuvre. During launch tests, the CUBE and the FFT will be free to float inside a test chamber called CHAMBER. Relative pose between the CUBE and the FFT reference frame will be determined by means of a camera vision system aboard the CUBE and an external reference camera for post processing. The closed-loop system computes the desired control torques from the position/attitude error information collected by a set of sensors and the magnetic field model of the FFT. As this solution is purely based on magnetic forces, there is no need of thrusters reducing mass and overall system complexity.
2. In the second one, TED (Tethered Electromagnetic Docking) is presented. This research presents a novel docking strategy that exploits electro-magnetic interactions. According to this concept, a tethered electromagnetic probe is ejected by the chaser toward a receiving electromagnetic interface mounted on the target spacecraft. The generated magnetic field drives the probe to the target and realizes an automatic alignment between the two interfaces, thus reducing both control

requirements for close approach manoeuvres and fuel consumption necessary for them. After that, hard-docking is accomplished by retracting the tether and bringing the two spacecraft in contact. Controlled rewind could also be exploited to damp the two spacecraft relative motion and stabilize the whole system.

In such context, PACMAN can be “de facto” considered as the electromagnetic probe of TED.

At the end of this introductory Chapter, the work logic and the structure of this work is presented. FIGURE 1.14 shows the Work Breakdown Structure (WBS) of the thesis with the Working Packages (WP).

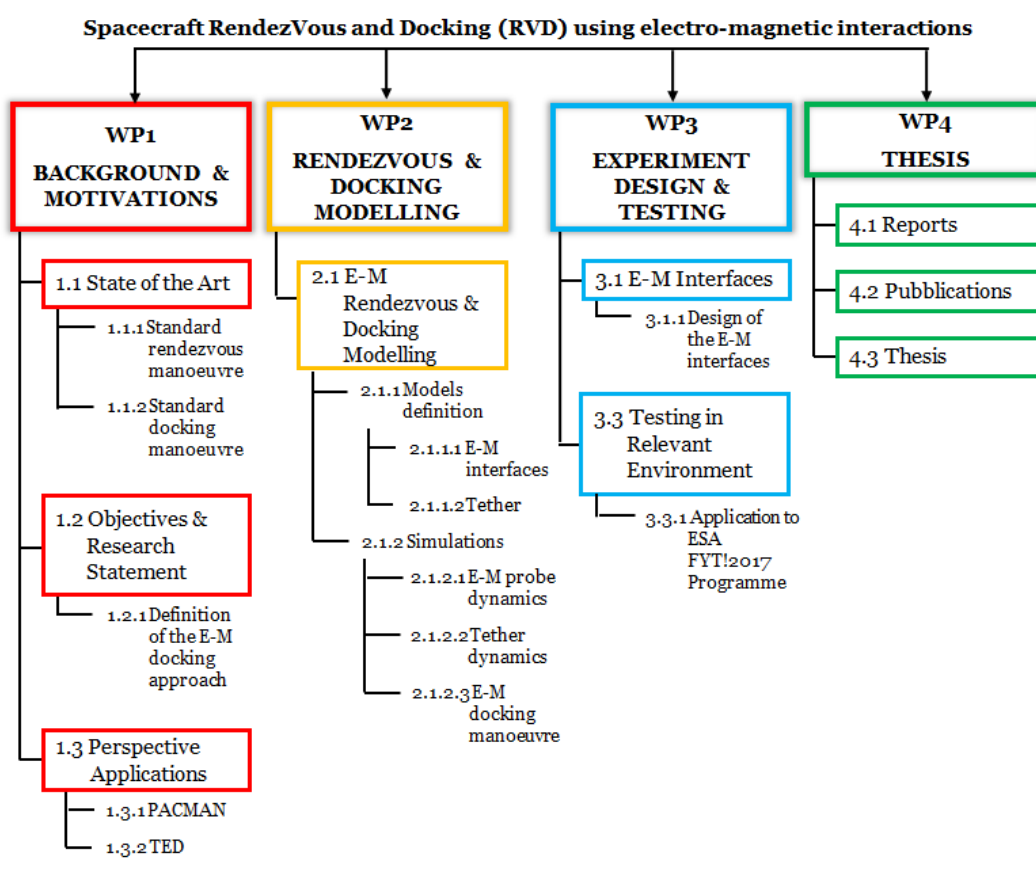


FIGURE 1.14: Work Breakdown Structure.

After a literature review on existing docking systems for both large and small spacecraft and electro-magnetic architectures, the focus concentrate towards a more detailed concept definition and the expected advantages offered by the new ideas (WP1).

First of all, in March 2016, PACMAN Experiment Proposal has been written to participate to ESA *Fly Your Thesis!* programme (WP3). The programme gives master and PhD candidates the opportunity to fly their scientific experiment or technological

research in microgravity conditions using the Airbus A310 Zero-G airplane. Each campaign consists of a series of three flights of 30 parabolas each. These will provide about 20 s of microgravity each (see Chapters 2.2 and 3 for further details). The participation to the programme would have been a remarkable opportunity to develop and test a technological demonstrator in relevant environment.

The preliminary design of the electromagnetic interfaces together with the experimental setup have been carried out during the proposal writing. Numerical simulations were performed taking into consideration the particular boundary conditions (fluctuation of g levels, vibrations of the airplane,) which characterise the parabolic flights. Fortunately, in November 2016, the Selection Board made its final decision and announced that PACMAN team was selected as one of the student teams to fly their experiment in the 68th ESA Parabolic Flight Campaign (PFC), scheduled to take place during the Autumn of 2017 and test the technological demonstrator in low-gravity.

A complete dynamical analysis of the relative CUBE/CHAMBER motions in relation with the disturbances on-board the aircraft (i.e. the g -jitter effects and the intrinsic motion of the aeroplane in terms of heading, roll and pitch) was performed right after PACMAN selection following the feedbacks from ESA Selection Board and using the precious data given by NoveSpace (the company in charge of the flight) concerning previous PFC. The investigations were mandatory in order to understand the range of the relative displacements and the drift of free-floating objects, a well-known problem on parabolic flights. The results obtained were essential to proceed with the experiment design for the best fly configuration.

The fly configuration was definitively approved in January 2017 during ESA Training Week on Gravity Related Experiment. In this occasion, PACMAN design was discussed with ESA and NoveSpace experts following also the useful advices given by students who participate to the previous PFC. A long and intense design phase, started right after the Training Week and lasted several months, brought to the final designs of the CUBE, the FFT and the CHAMBER. In parallel, tests were made at subsystem level in order to verify that the design choices fulfilled the experiment requirements. Once the design have been approved by NoveSpace supervisor, all the mechanical parts were manufactured: the structure and the interfaces of the CUBE, the FFT and the CHAMBER. Part of the on-ground tests performed to verify the reliability of the numerical model used for the study are presented in this thesis, focusing on the guidance, navigation & control subsystem.

In parallel, TED concept has been defined and simulated (WP2). A dynamic model (in MATLAB[®]) was developed to preliminary characterize the mutual interactions (forces/torques) between two magnetic dipoles in a 3D environment and understand the width of the sphere of influence (i.e. the maximum distance at which the authority of the dipoles is enough to neglect the influence of the Earth magnetic field). These studies

were performed since the only necessary condition to have a successful docking manoeuvre is that the tethered probe reaches the sphere of influence of the interface mounted on the target. When the probe reaches this position, the generated magnetic field drives it towards the target and realizes an automatic alignment between the two interfaces. The soft-docking is realized. The electromagnets bodies dynamics were described in terms of spacecraft position and attitude through the implementation of a far-field magnetic model and Eulers differential equations.

The work continued with preliminary simplified simulation of the proposed docking procedure, simulating a real scenario and the mutual interactions between the chaser and the target during the orbital manoeuvre. Tether dynamics was also modelled deriving its equations of motion from the dumbbell model to simulate the probe release from chaser. Both libration along the vertical local direction and the out-of-plane disturbs are considered. Data obtained by simulations confirm that a successful docking manoeuvre could be accomplished deploying the tether when the relative distance between target and chaser is of the order of hundreds of meters, allowing a partial propellant saving, simplifying the close-range rendezvous and docking manoeuvre as well as the proximity operations.

PART 1

PACMAN

(Position and Attitude Control with MAgnetic Navigation)

EXPERIMENT

Chapter 2

PACMAN Experiment & Gravity-related Research Systems

2.1 Introduction to PACMAN experiment

PACMAN (Position and Attitude Control with MAgnetic Navigation) experiment is a technology demonstrator whose main goal is to develop and validate under low-gravity conditions an integrated system for proximity navigation and soft docking based on magnetic interactions, suitable for small-scale spacecraft. This is accomplished by launching a miniature spacecraft mock-up (CUBE) and a Free-Floating Target (FFT) that generates a static magnetic field towards each other; a set of actively-controlled magnetic coils aboard the CUBE, assisted by dedicated localization sensors, are used to control its attitude and relative position assuring the accomplishment of the soft docking manoeuvre (FIGURE 2.1).

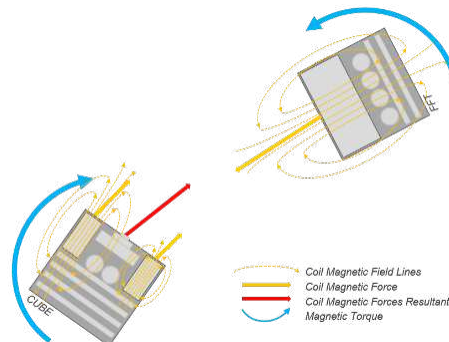


FIGURE 2.1: Electromagnetic soft-docking. The CUBE and the FFT will be launched towards each other. The controller will power separately the coils aboard the CUBE allowing to control its attitude and position.

The relative pose between the CUBE and the FFT reference frame will be determined by means of a camera vision system aboard the CUBE and an external reference camera for post-processing. The closed-loop system (FIGURE 2.2) evaluates the desired control torques from the position/attitude error information collected by a set of sensors and the magnetic field model of the FFT.

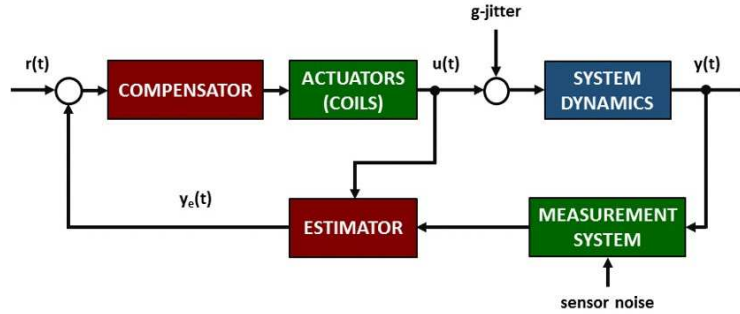


FIGURE 2.2: Sketch of the control algorithm of the closed-loop system.

2.1.1 PACMAN experiment scientific objectives

The realization of PACMAN experiment will allow the validation of the theoretical/numerical models that describe such interactions. Data collected during the experiment testing will allow assessing the system concept feasibility and its limitations; moreover, tests results will provide significant data that will be exploited to improve the proposed technology for future developments.

The main objectives of PACMAN experiment are pointed out in the following list:

1. the development of a system for proximity navigation and soft docking based on magnetic interactions:
 - the investigation of the electromagnetic interaction between two bodies in motion;
 - the definition of the working range for a relative position active control;
 - the implementation of active control algorithms based on electromagnetic interactions;
2. the development of a dedicated low-range navigation system based on markers/-camera system.
3. the validation of the whole PACMAN system in the relevant low-gravity environment:

- the analysis and validation of the magnetic interactions models;
- the verification of PACMAN subsystems in nominal conditions;
- the testing of the attitude and position control algorithms in nominal and off-nominal conditions;
- the definition of PACMAN working range and operative limits.

2.2 Gravity-related research systems

In our life, gravity is a significant force able to shape our world and it conditions many natural phenomena and technological processes: human development, fluid dynamics, combustion, biological and chemical reactions, and material sciences processes represent only few examples. Moreover, since gravity determines all the phenomena occurring on our planet, it influences greatly all human technological developments.

While gravity effects around and within us are practically well known, micro-gravity effects on the aforementioned phenomena and processes are still under investigation and only few studies have been conducted in recent years. This is probably due to the fact that ground-based facilities able to simulate a “micro-gravity” environment (the absence of gravity “0g” is only a theoretical concept since gravitational accelerations always exist) have been developed only in the last century, substantially boosted by the space-race of the 60’s [40] [41].

2.2.1 Ground-based facilities

The existing facilities take advantage of several physical principles to simulate the micro-gravity environment on-ground (see [42] for further information):

1. Neutral buoyancy pools.

Neutral buoyancy is not easily achievable and the viscous friction can have a strong impact on the system dynamics. To accomplish some relevant analysis under such conditions, the mean density of the system of interest has to be less than the one of the fluid in which it is immersed, which is not easy to obtain. Neutral buoyancy is often used to train astronauts for working in the micro-gravity environment of space, as can be seen in FIGURE 2.3.

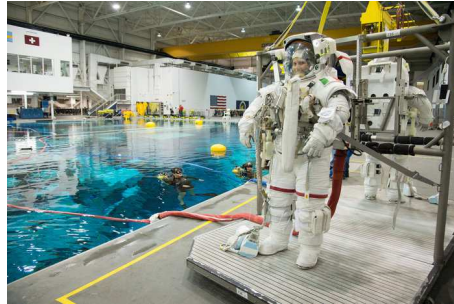


FIGURE 2.3: ESA astronaut Samantha Cristoforetti wearing a training version of her Extravehicular Mobility Unit (EMU) spacesuit in preparation for a spacewalk training session at the Neutral Buoyancy Laboratory (NBL) near NASA's Johnson Space Center (courtesy of NASA).

2. Magnetic levitation facilities.

Magnetic levitation exploits the magnetic intrinsic characteristics of the materials. Every element existing in nature is magnetic to some extent, spreading from the smallest effects known as paramagnetism and diamagnetism to the largest one known as ferromagnetism, which is the most common form of magnetism in our daily lives. Magnetic levitation can be easily used to carry out studies on organic materials, living biological samples or on technological systems.

3. Frictionless tables.

Frictionless tables are testing platforms used to simulate microgravity conditions in 2D in laboratory. They are composed of a flat table over which the system under study (usually a small satellite mock-up) can “float” thanks to particular air pads that create a frictionless air-cushion. These facilities are often used on ground for the development and the verification of GNC and attitude control algorithms, collision avoidance, docking and other proximity manoeuvres as well as testing formation flight strategies.

4. Clinostats.

A clinostat is composed of a disc connected to a motor. The disc is normally held vertically, but can be tilted to simulate different gravity conditions. The motor rotates the disc slowly (at a rate of ~ 1 rpm) and the sample is positioned on the disc, horizontally. The slow rotation of the disc assures a zero net gravitational pull on the sample, since it is averaged in all the directions allowing the study of the effects of micro-gravity on plants, cell cultures and also animal embryos.

5. Sounding rockets.

Sounding rockets (FIGURE 2.4) were originally used in meteorological and upper atmosphere studies, but in the last 50 years this type of platform has been used also to carry out low-gravity experiments. A sounding rocket is composed of

three major parts: (1) the propulsion system (solid fuel), (2) the service systems and (3) the scientific payload. Sounding rockets do not go into orbit, rather they follow a parabolic trajectory which guarantees a low-gravity time window of several minutes.

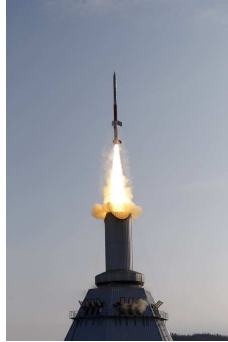


FIGURE 2.4: ESA Maser launched from the Esrange facility near Kiruna, Sweden (©SSC Id 213859).

6. Drop towers.

Drop towers are particular research facilities in which the vacuum is created to remove the effects of drag and friction forces and free-fall conditions can be reached (FIGURE 2.5). Drop towers are very adaptable platforms and they allow studies in different research areas, from biological investigations to technological experiments. The opportunity of performing repeated tests over a period of few days gives scientists the possibility to analyse the outcomes of each launch and modify the test parameters before the following one starts. Drop towers are ideal test platforms for obtaining a large amount of data on physical phenomena with short characteristic times in micro-gravity.



FIGURE 2.5: ZARM drop tower in Bremen (courtesy of ZARM).

7. Parabolic flights.

Parabolic flights (FIGURE 2.6) are particular aircraft flights that execute a series of manoeuvres (parabola) using a specially converted aircraft (FIGURE 2.6). Each

parabola provides up to 22 s of low-gravity ($10^{-2} - 10^{-3} g$) or weightlessness. During this long time window, scientists are able to perform their experiments. A Parabolic Flight Campaign (PFC) consists in three flights, typically performed in three consecutive days. During each flight, around 31 parabolas are completed. The peculiarity of a parabolic flight is that, during each parabola, there are two 20 s phases of hyper-gravity (prior to and after the reduced gravity window) in which $\sim 1.5 - 1.8 g$ can be reached. Similarly to sounding rockets, parabolic flights are sub-orbital carriers that allow experimenters to execute repeated tests in low-gravity conditions.



FIGURE 2.6: ESA Airbus A310 ZERO-G aircraft performing a parabola (©ESA Id 330758).

2.2.2 Relevant environment: why is micro-gravity needed for PACMAN experiment?

Micro-gravity research gives scientists a unique perspective on the study of many natural phenomena allow them to develop numerous technological improvements.

As the proposed technology in PACMAN experiment is conceived for space applications, testing it in a low-gravity environment is of the utmost relevance.

First of all, the order of magnitude of the forces to which a miniature spacecraft is subjected in orbit is smaller than that experienced under laboratory conditions:

- the gravity force during ground testing in laboratory can have a strong influence on the system dynamics because it is orders of magnitude bigger than the expected magnetic interaction forces. This difference between the two physical quantities could represent an obstacle to obtain reasonable and reliable results;
- the friction among the surfaces in contact with each other represents another issue, especially when the electromagnets are far apart. In fact, the attractive forces between two electromagnets decrease drastically with the increasing distance between them, following the trend of the magnetic field magnitude which is proportional to $1/r^3$, with r as the distance. This means that when the electromagnets are far

apart, they are affected by limited attractive forces which can be easily dominated by friction;

- atmospheric disturbances can be limited and should not represent a problem, even if tests performed in monitored atmosphere are more advisable;

All the aforementioned issues can have a strong impact on the measurement of the magnetic interactions, which would not be effective nor measurable under ground conditions.

In addition, a low-gravity environment allows the testing of the proposed technology in a full 3D environment. The experimental ground setup presents some constraints which reduce the movements of the devices (supports, cables, restricted 2D plane, etc.) and can interfere with the magnetic fields, partially neutralising the effectiveness of the measures. Moreover, all the connections to the ground facility alter the main body characteristics (mass, centre of gravity, inertias, etc.) allowing only a partial characterization of the physical effects which would otherwise affect the body in the relevant environment. Thus, the obtained results would not be completely reasonable, allowing only a partial investigation of the topic.

Finally, testing the technology in the relevant environment is the first step to raise the Technology Readiness Level (TRL) in anticipation of a future space demonstration. Data collected during the experiment testings will allow to assess the system feasibility and its limitations; the results will provide significant data that will be exploited to improve the proposed technology for future eventual applications, most of which are expected to be related to on-orbit servicing or de-orbiting operations, contributing to the development of an automatic docking system able to operate without human assistance.

Among all the aforementioned ground-based platforms presented in section 2.2.1, two facilities would be suitable to test PACMAN: drop towers and parabolic flights.

As a matter of fact, neutral buoyancy is not suitable because of the strong impact of the viscous friction on the system dynamics; magnetic levitation would require excessive power consumption and inevitably interfere with the generated magnetic interactions that govern the spacecraft mock-up dynamics. Clinostats are merely not suitable because of the difference in the time-scales of the phenomena studied with this type of platform and the proposed technology experiment. The choice between drop towers and parabolic flights has been done by analysing pro and cons offered by each platform, in particular the provided levels and duration of reduced gravity. FIGURE 2.7 gives an overview of the activities which have already been performed by employing drop towers and parabolic flights [42]. As can be seen from the figure, the A310 ZERO-G is the ideal test platform for the PACMAN experiment. First of all, the level of altered gravity (10^{-2} to 10^{-3} g) allows a much better reproduction of the dynamic phenomena

that occur on orbit and a more accurate analysis of the involved magnetic interactions. Besides, the available volume inside the aircraft is bigger than the available volume aboard a sounding rocket, not to mention the possibility of interactions of the operators with the experiment. ZARM drop tower would have been also an adequate platform guaranteeing even a higher micro-gravity level, but the possibility to execute a higher number of repeated tests in a longer low-gravity time window represented a considerable advantage and made the A310 ZERO-G more suitable. Moreover, the possibility 1) to carry out several series of experiments on consecutive days and 2) of interaction of the operators with their experiment gives the opportunity to analyse the outcome during each flight and modify the test parameters, if necessary.

These represent remarkable advantages for several reasons:

- repeated tests will assure a substantial collection of data to draw statistically valid conclusions, even in the unfortunate case of unsuccessful launches;
- it is possible to test the technology under different or off-nominal initial conditions, in order to assess the technology limits;
- the interaction with the experiment can improve the data collection, allowing the modification of the test parameters in real time. This aspect is very important if an anomaly or malfunction is identified during the low-gravity testing phase, since it assures a partial recovery of the results without wasting an entire parabolic flight outcomes.

For all the above reasons, PACMAN experiment has taken advantage of the ESA Education *Fly Your Thesis!* programme and the Airbus A310 ZERO-G testing platform; therefore, the programme itself, the aircraft characteristics, limits and constraints and parabolic flight manoeuvres are briefly described in Chapter 3.



Activities already performed onboard		
Physiology		
Integrated physiology	✓	✗
Muscle and bone physiology	✓	✗
Neuroscience	✓	✗
Astro/exobiology, Planetary Exploration		
Origin, evolution and distribution of life	✓	✗
Preparation of human planetary exploration	✓	✗
Technological experiment		
Satellite Antenna deployment	✓	✗
Space hardware qualification	✓	✓
Space hardware tests, concept testing	✓	✓
Astronaut training		
Initiation to weightlessness	✓	✗
Test of astronaut procedures	✓	✗
Partial G-level		
Martian gravity simulation	✓	✗
Moon gravity simulation	✓	✗
Direct access of scientists to experiment parameters		
Easy change to hardware during operation	✓	✗
Easy change to hardware during operation	✓	✗
Duration of low-gravity window	up to ~22 s	up to ~10 s

FIGURE 2.7: Comparison among different activities performed during parabolic flights and drop towers.

Chapter 3

ESA Education *Fly Your Thesis!* Programme

3.1 ESA Education *Fly Your Thesis!* programme: parabolic flights

ESA Education *Fly Your Thesis!* programme [43] is a unique opportunity for University students to conduct their experiments in low-gravity conditions through a series of parabolic flights on the Airbus A310 Zero-G, a modified aircraft operated by NoveSpace [44] from Bordeaux, France. The Airbus A310 Zero-G has a total length of 46.4 m, a wingspan of 43.9 m and a maximum mass of 157 t. The space available for testing the experiments is of $20 \times 5 \times 2.3 \text{ m}^3$ (L x W x H), allowing 12 teams to perform their studies.

The programme launches a call for proposals once a year and during this phase the student teams are encouraged to send their proposal. ESA's Education Office makes a first selection of the teams that are then invited to present their proposal to a Review Board. Up to 4 teams are selected after the presentation and given the opportunity to participate in a 2 weeks PFC that takes place in Bordeaux.

3.1.1 Parabolic flight manoeuvre

During a parabolic flight, the aircraft climbs to a high angle, slightly less than 50° for about 20 s, before dramatically reducing its thrust and falling along a parabolic trajectory (see FIGURE 3.1).



FIGURE 3.1: Parabolic flight manoeuvre. Different gravity levels are achieved during the manoeuvre. The low-gravity phase lasts about 22 s and it is reached at the peak of the parabola (©NoveSpace/CNES/DLR/ESA Id 324324).

During the manoeuvre, four main phases can be identified and characterized by different gravity levels as shown in FIGURE 3.2:

1. steady horizontal flight in which the experimenters experience normal gravity (1 g). This represents the beginning of the manoeuvre. The aircraft flies at an approximate altitude of 6000 m with a speed of 810 km/h.
2. pull-up phase in which the aircraft reaches an acceleration between 1.5 and 1.8 times the gravity at sea level (1.5 – 1.8 g); this phase lasts around 20 s and correspond to the ascending phase before the starting of the parabolic trajectory: the aircraft reaches an altitude of 7500 m with an inclination angle of around 47° respect to the horizontal. The air speed is of 650 km/h.
3. low-gravity phase: the engine thrust is reduced to compensate the drag force acting on the aircraft. At this point, the aircraft follows a parabolic trajectory, during which low-gravity is achieved (10^{-2} g, the so-called “0” g). This phase lasts about 22 s. the speed drops to about 390 km/h when the peak of the parabola is achieved at around 8500 m.
4. pull-out phase in which the aircraft reaches again an acceleration between 1.5 and 1.8 g. At the end of this last phase the aircraft is again at an altitude of 6000 m and flies following a steady horizontal path.

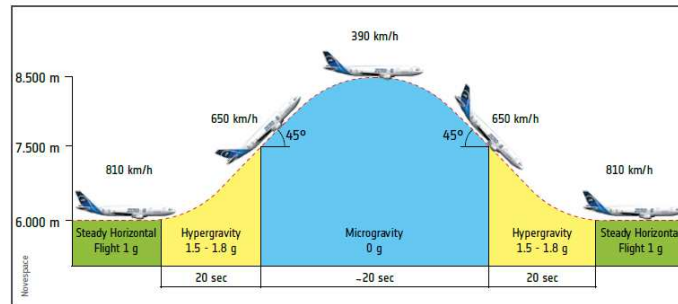


FIGURE 3.2: Phases of the parabolic flight manoeuvre (©ESA Id 330758).

The PFC consists of a series of three flights of 31 parabolas each and it ensures different and unique testing conditions. A 110s period of steady horizontal flight is performed between the end of a parabola and the start of the following one. The parabolas are executed in sets of five and at the end of each set a longer break (five to eight minutes) allows experimenters enough time to carry out modifications to their experimental setup.

3.1.2 Disturbances during a parabolic flight: g-jittering effects and vibrations

During a parabolic flight manoeuvre, there are different external disturbances acting on the aircraft besides gravity. These are the aerodynamic lift, drag and thrust. All these forces prevent a perfect attainment of weightlessness. To balance all these disturbances, pilots accomplish two different actions during the manoeuvre: 1) they try to cancel the lift generated by the wings and 2) they reduce the thrust from the engines to compensate the small drag generated by the aircraft particular configuration (pitch-angle of $\sim 47^\circ$). As a consequence of this manoeuvre, the level of the resulting micro-gravity is not constant, on the contrary it has some fluctuations on the order of ± 0.05 g at a frequency of ~ 1 Hz (see FIGURE 3.3).

Furthermore, as in any type of flight, mechanical vibrations caused by engines and shocks in the plane are also present. These relevant disturbances are due to the unusual manoeuvre and therefore particular attention has to be made during the design of the experiment, since they can greatly influence the performances of the system attached to the aircraft and thus the obtainable data.

Finally, it is important to underline that experiments involving free-floating objects can only exploit a reduced low-gravity time window of ~ 5 s. This is due to safety constraints associated with the release and secure procedures of the free-floating objects that must be performed before and after each micro-gravity phase.

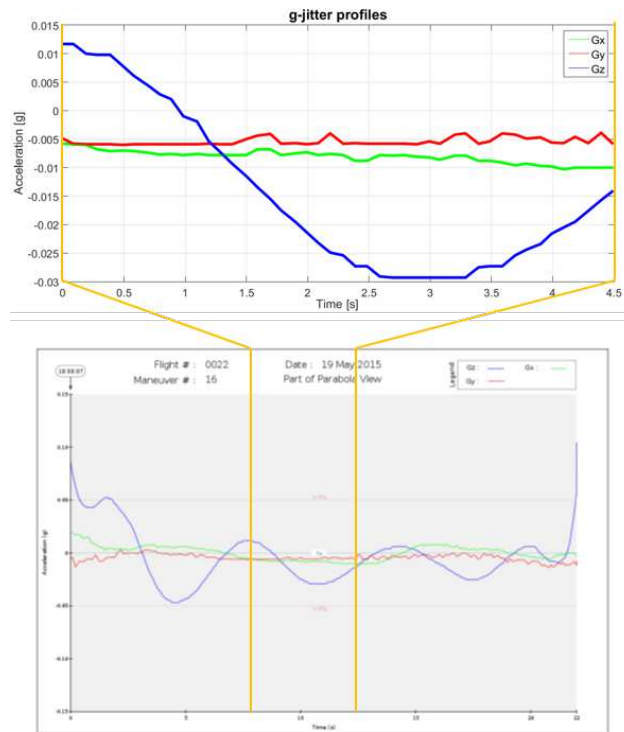


FIGURE 3.3: Extrapolation of the central part of the accelerations profiles of the 16th parabola (parabolic flight #22, 19th May 2015, ©NoveSpace).

3.1.3 The Airbus A310 Zero-G as low-gravity test platform

The Airbus A310 ZERO-G [44] cabin is divided into five sections as shown in FIGURE 3.4.

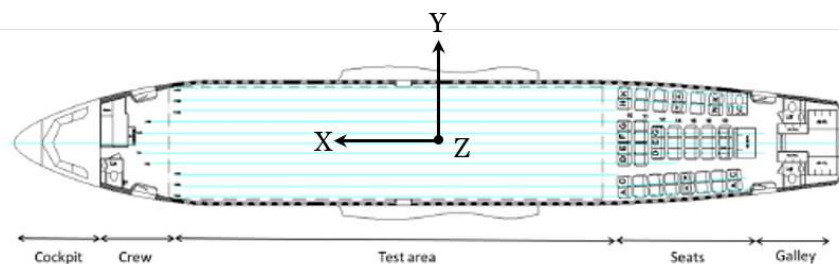


FIGURE 3.4: Top view of the cabin section (©NoveSpace).

The access door used for loading the experiment is located in the crew area. Therefore, the maximum dimensions of an experiment are 1800 mm high and 1060 mm wide.

The experiment dimensions have to be compliant with the testing area dimensions of the A310 ZERO-G shown in FIGURE 3.5.

The experiments are fastened to the floor into tracks used in airliners to attach seats [45]. These tracks are 503 mm apart along the Y-axis, as shown in FIGURE 3.5. The

centre aisle must be kept clear of experiments. Along the X -axis, the seat tracks offer attaching points at 1-inch (25.4 mm) intervals.

Experiment payloads are secured to the floor using specific attachment fittings to the seat tracks. Safety nets are also used to limit the space of the testing area.

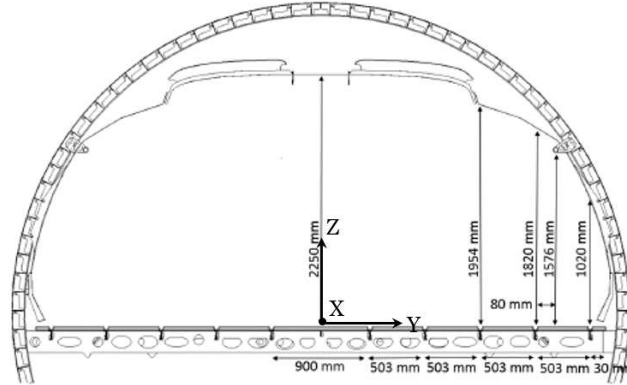


FIGURE 3.5: Cross-section of the Airbus A310 ZERO-G testing area (©NoveSpace).

In order to ease the experiment design process and to be sure that the experiment is able to withstand the particular stressed conditions of a parabolic flight sustaining the emergency landing loads (see TABLE 3.1) with appropriate safety margins, NoveSpace provides experimenters with pre-qualified standard primary structure designs and a step-by-step procedure to choose and customize their own experimental rack [46].

TABLE 3.1: Emergency landing condition loads (©NoveSpace).

Aircraft Axis	Load factor to be considered [g]
+X Forward	9
-X Aft	1.5
$\pm Y$	3
+Z Upward	4.2
-Z Downward	7.3

Chapter 4 will describe PACMAN experiment design evolution: from the proposal written for the *Fly Your Thesis!* programme selection workshop through the dynamic analysis of the CubeSats motion in the Airbus A310 ZERO-G to the magnetic field model and the final experiment design developed following the safety requirements presented above.

Chapter 4

PACMAN Experiment Design Evolution

The final flying configuration of PACMAN is the consequence of a long evolution process, which started with the first sketches for the *Fly Your Thesis!* proposal and finished with a fully operative working technology demonstrator. Here is a summary or synopsis of the main milestones followed during the participation at the *Fly Your Thesis!* programme [43], with special focus on the initial idea presented at the proposal and all the improvements/changes made during the whole campaign in order to compensate the disturbances aboard the aeroplane and obtain a final working configuration.

4.1 PACMAN proposal for the *Fly Your Thesis!* programme

The first idea was to have the experiment composed by two main parts (see FIGURE 4.1): a spacecraft mock-up called CUBE and a test chamber called CHAMBER. During launch tests, the CUBE would have been free to float inside the CHAMBER, a safe environment that limited the CUBE motion avoiding the risk of hurting people, damaging other experiments or the support electronics.

At this early stage of the *Fly Your Thesis!* programme the docking interface (represented by an electromagnet) was supposed to be fixed inside the CHAMBER and only the CUBE was able to fluctuate during the low-gravity phase of the parabolic flight. The CHAMBER would have provided also a number of features to support the test procedures.

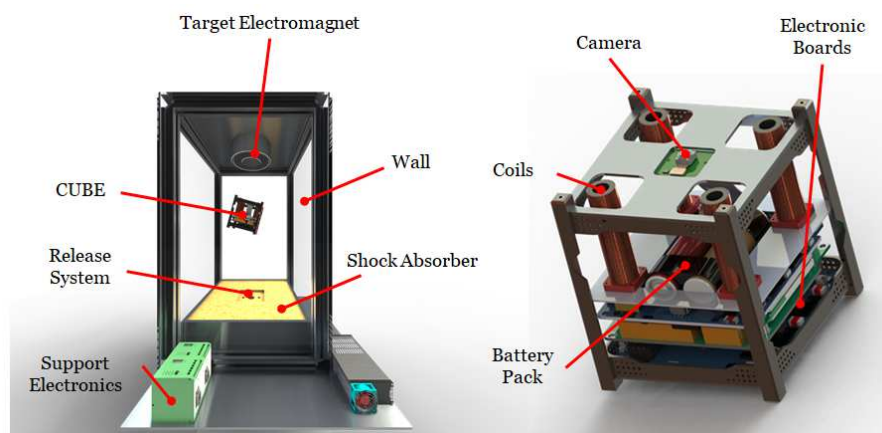


FIGURE 4.1: PACMAN experiment layout and main elements (left), detail of the CUBE (right).

The main components of the CHAMBER were meant to be:

1. Wall of the CHAMBER that would have ensured a confined motion to the CUBE. The CHAMBER wall would have been transparent (e.g. rigid plexiglass plates) to allow the observation of the CUBE. In addition, a net around the CHAMBER would have been implemented to satisfy the safety requirements imposed by NoveSpace. Both systems would have been fixed to the structural profiles with screws. One of the walls would have been removable to ease the access to the CHAMBER for pre-launch activities, quick inspections and post parabolas procedures.
2. Hold & launch system for keeping the CUBE in position and to provide it with a proper initial velocity toward the fixed interface immediately after the low-gravity condition is reached.

The hold system would have been composed of a set of small holding electromagnets, while the launch system would have featured a magnetic or mechanical spring. All this assembly would have been located inside the bottom wall of the CHAMBER. Such wall would have been composed of a rigid plate covered by soft material (e.g. expanded polyurethane); it would have been directly connected to the A310 ZERO-G structure and moulded in order to obtain a small slot at the centre. Part of the slot would have carried a removable dowel of polyurethane containing the holding electromagnets and the launch system. The CUBE would have been placed on top of this assembly. The electromagnets were expected to hold the CUBE in position prior to the low-gravity phase.

For the launch system, two alternative options were being evaluated: one was based on a traditional steel compression spring, while the other was characterised by two small repelling permanent magnets, one on the CUBE bottom face and

the other at the CHAMBER launching interface. The advantages of adopting a mechanical spring system were related to the deep knowledge inherited from both FELDs [20] and STAR [47] Experiments, that had featured this kind of release system; on the contrary, a magnetic launch system would have allowed an easier control of the nominal launch conditions (due to the absence of frictional forces) and a simple fast adjustment of the launch velocity of the CUBE by substituting the small permanent magnet on the CUBE bottom face. This modification could have been done also within a set of parabolas during the same parabolic flight, allowing a wider set of testing conditions.

3. Docking interface composed of an industrial electromagnet powered with constant direct current that would have generated a fixed magnetic field (for each parabola) inside the CHAMBER and would have represented the docking interface located inside the top wall of the CHAMBER. The current flowing into the interface would have been adjustable before each parabola to test different scenarios and would have assured a number of measures as big as possible to draw statistically valid conclusions.

The interface would have been equipped with optical markers required by the CUBE for the relative visual navigation. These markers would have been used as references for the camera aboard the CUBE to collect information about its position. These data would have been used in the feedback loop to control the correct accomplishment of the soft-docking manoeuvre.

A rail inside the top wall of the CHAMBER would have allowed the repositioning of the interface to simulate different off-nominal approaching conditions during the docking manoeuvre.

4. Reference cameras would have been used to determine the absolute position and attitude of the CUBE during the floating phase and for post-processing; an appropriate image analysis algorithm would have recognized passive optical markers located on the external surface of the CUBE. All the cameras would have worked in the IR wavelength, as only the attitude and the position of the CUBE would have been relevant for the experiment. IR emitters would have been considered to facilitate the detection of the CUBE by the reference cameras. The data collected during the floating phase would have been processed by the supporting electronics housed outside the CHAMBER and then, only if necessary, sent to the CUBE via the wireless board to close the feedback loop.
5. Supporting electronics would have been needed to command the hold mechanism represented by the set of small electromagnets 2, the interface electromagnet 3 and to ensure wireless communication with the CUBE for initialization commands, the

basic system status telemetry and eventually the data transfer. A laptop would have processed the following information:

- data about the motion of the CUBE acquired by the external IR reference cameras;
- information regarding the vibrations of the entire structure collected by the set of accelerometers located at the base of the CHAMBER;
- data coming from the set of load cells and accelerometers positioned in proximity of the docking interface (to record information about the impulsive force transmitted by the CUBE during the soft-docking), which would have been stored and used only for post-processing.

The components of the CUBE would have been (see FIGURE 4.1):

1. Structure to hold all the electronic components in place. The structure would have been partially covered to preserve its integrity during the docking phase and prevent experimenter injuries. The design of the structure was completed following all the CubeSat standards.
2. Magnetic coils as actuators of the rendezvous/attitude control system. The set of coils would have been located at the four corners of the CUBE to save space for the electronic boards and to maximize the effectiveness (in terms of torque) to perform the attitude control. The coils would have been composed of a wire wrapped around a structural rod, without any ferromagnetic core.
3. the camera board for the visual relative position/attitude determination. The camera would have been located at the centre of the top face. Passive optical markers (circular or squared patterns) would have covered the docking interface and would have been used by the CUBE as a reference to measure its relative position and attitude. IR emitters would have been considered during the testing phase to ease the detection of the docking interface by the CUBE. The visual navigation system would have been partially based on a previous work [38]. A comparison between the data collected by the CUBE and the video recordings performed by the CHAMBER camera systems would have allowed the analysis and performance assessment of the position/attitude determination and control system.
4. the IMU board powered at the system start-up and during all the floating phase with:

- accelerometers to measure the accelerations of the CUBE and to obtain its position through integration;
 - gyroscopes to measure angular rates and to ensure the correct behaviour of the magnetic coils;
 - magnetometers which would have collected data about the coil magnetic fields.
5. the microcontroller board for control logic, sensor reading and data handling (FIGURE 4.2). The microcontroller board would have collected and processed all the data coming from the sensors aboard the CUBE for the feedback control loop. In particular:
- attitude and position information of the CUBE from the IMU board;
 - data concerning the motion of the CUBE from the on-board IR camera.

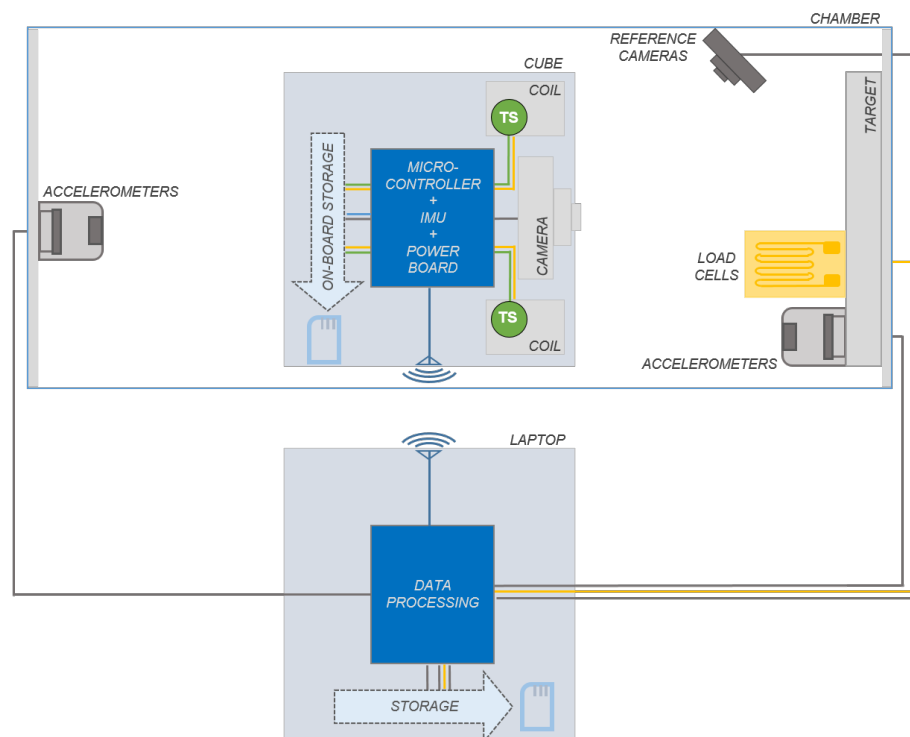


FIGURE 4.2: The microcontroller board would have acquired and processed the data from the IMU, the on-board camera, the temperature sensors and the coils. The laptop would have collected data from the external reference cameras, the load cells, the accelerometers in proximity of the docking interface and those in the bottom wall of the CHAMBER. If necessary, useful telemetry data would have been processed and sent to the CUBE via the wireless board for the close-control loop.

Other important information like the temperature of the coils to monitor the system status and the coil power consumption and their magnetic fields would have

been analysed, stored and kept under control during the whole operative phase.

If the processing phase would have become particularly demanding from the computational point of view, part (or all) the data collected by the sensors aboard the CUBE would have been sent to the laptop, processed and then sent back to the CUBE via the wireless board.

6. Two battery packs to provide power to the electronic boards and to the magnetic actuators. The battery packs would have occupied a large part of the available room inside the CUBE. Spare packs would have been used to power the CUBE in case of complete power drain.
7. A driver circuit to supply the proper voltage to the magnetic coils.
8. A wireless board to allow communication between the laptop and the CUBE before testing and/or during it, if necessary.
9. A memory board to save the data flow from sensors and commands during micro-gravity tests.
10. Hold & launch system interface composed of four small iron plates and the launch system counterpart. The latter would have been a permanent magnet located at the centre of the base of the CUBE or a mechanical interface for the steel spring. The small iron plates would have been at the ends of the four structure pins of the CUBE. The iron plates would have matched precisely the four electromagnets placed in the small dowel at the bottom of the CHAMBER: the magnetic field of the electromagnets would have interacted with the plates generating an electromagnetic force which would have held the CUBE in the right position during pre-test operations. During the low-gravity phase, the electromagnets would have been switched off and the elastic force (of the spring) or the repelling force (on the permanent magnets) of the launch system would have pushed the CUBE towards the docking interface at a given initial velocity.

4.2 Dynamic analysis of the CUBE motion during a parabola

The first configuration of PACMAN experiment presented in Section 4.1 was quite different from the one introduced at the beginning of Chapter 2. This is due to the fact that a complete dynamical analysis of the relative CUBE/CHAMBER motions in relation with the disturbances aboard the aircraft (i.e. the g-jitter effects and the intrinsic motion of the aircraft in terms of heading, roll and pitch, see Section 3.1.2) was not performed at the early stage of the *Fly Your Thesis!* proposal.

These analyses were performed right after PACMAN selection for the 68th PFC, on the basis of the feedbacks from the ESA Selection Board and using the valuable data given by NoveSpace concerning previous PFCs. The investigations were mandatory to understand the range of the relative displacements between the CUBE and the CHAMBER and the obtained results were essential to proceed with the experiment design for the best flight configuration. The focus of these analyses was the drift of free-floating objects, a well-known problem of parabolic flights.

In order to simplify the exposition of the dynamic analysis results, the aircraft reference system is shown in FIGURE 4.3, where the X -axis is defined as that towards the cockpit, the Y -axis is oriented in the direction of the wings and the Z -axis is perpendicular to the aircraft floor. It is worth noting that the aircraft reference system is a North East Down (NED) reference system, commonly used in aviation. Down is chosen as opposed to Up to comply with the right-hand rule (the positive Z -axis is up).



FIGURE 4.3: NED reference system of the Airbus A310 ZERO-G (©NoveSpace).

PACMAN preliminary design (the one presented in the proposal) had considered a vertical CHAMBER, with the longest side along the Z -axis of the aircraft; the CUBE would have been launched towards the docking interface, as shown in FIGURE 4.1, along the Z -axis.

The difficulties with this first solution were mainly due to the docking interface that cannot be kept fixed. During the free-floating phase, in fact, the CUBE would have moved along the initial release direction with its initial velocity. The docking interface, instead, fixed to the CHAMBER (and thus to the aircraft), would have followed the aircraft motion. The g-jitter effects combined with the aircraft motion would have been responsible of these two different motions and should have been considered as external disturbances (see Section 3.1.2). In fact, they would not have facilitated the accomplishment of the soft-docking manoeuvre, but rather they would have prevented it.

The first solutions proposed was 1) to compensate disturbances aboard the aircraft by creating a movable docking interface and 2) to lay the CHAMBER horizontally, with the longest side along the Y -axis (instead of vertically, along the Z -axis) of the aircraft (see FIGURE 4.4). The second modification was due to the presence of less disturbances along the Y -axis of the aircraft (along the wingspan).

These two different solutions would have improved greatly the results obtainable from the tests without significantly altering the design of the experiment.

The main drawback was due to the fact that the controlled motion of the docking interface would have had to be very accurate and quick enough to compensate the disturbances and to guarantee the correct accomplishment of the soft-docking manoeuvre in the tight time window (5 s at maximum). This first solution seemed not to be effective, since it would have further complicated the experiment design without adding a relevant benefit. An accurate and complete analysis of these disturbances is presented in Section 4.2.1 and shows that the displacements of the docking interface would have been relevant ($\sim 0.5 - 1$ m in 3.5 s in the best case scenario).

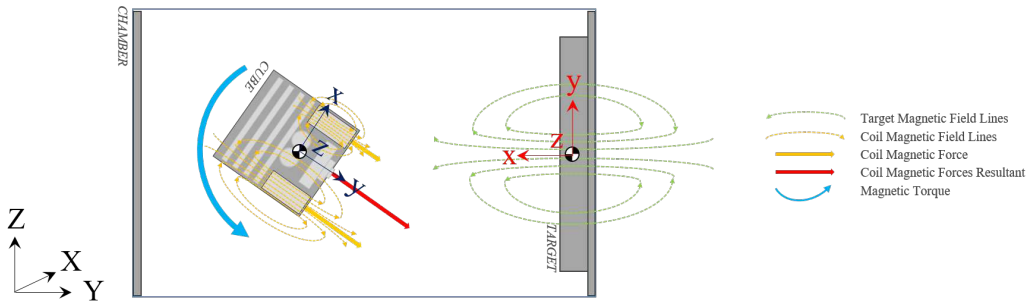


FIGURE 4.4: Reference systems: CUBE reference system ' xyz ', docking interface reference system ' xyz ', Airbus A310 ZERO-G reference system ' XYZ '. The CHAMBER lays horizontally along the aircraft wingspan.

4.2.1 Identification of the ideal launch window

An analytical dynamic model has been implemented in MATLAB[®] to understand if an ideal launch window during the low-gravity phase exists, i.e. a time window that has statistically the lowest possible disturbances. This MATLAB[®] model loads all the acceleration profiles provided by NoveSpace concerning previous PFCs and identifies all the best time windows in which the combination of the disturbances gives the lowest total disturbance using the mean value theorem for integrals.

The results obtained from MATLAB[®] model are shown in FIGURE 4.5. Each graph contains the best launch time window for each parabola of the set. The time window

length is set to 3.5 s, long enough to accomplish the soft-docking manoeuvre, but sufficiently short to have a limited drift.

FIGURE 4.5 (a), (b), (c) show the combined pitch/g-jitter effect, while FIGURE 4.5 (d), (e), (f) show the combined roll/g-jitter effect. The effect of the yaw motion is not considered here because the CHAMBER is supposed to lay horizontally, with the longest side along the Y -axis of the aircraft and, thus, the docking interface could move only in the XZ plane.

The pitch/g-jitter combination seems to be predictable and suggests that the best launch time window can be at about 4 s or at about 16 s after the beginning of the low-gravity phase. This is due to the motion of the aircraft that is almost the same for each parabola. On the contrary, the roll/g-jitter combination seems to be quite unpredictable, especially for the roll/ g_z and roll/ g_y combination. In particular, for the last-mentioned combination, the best launch time window seems to be around 12–13 s from the beginning of the low-gravity phase. Unfortunately, the information obtainable from these analyses were not satisfying, since an ideal launch window suitable for any parabolas was not pointed out, even if some important considerations could be made: 1) there is not a preferable launch time window that assures the accomplishment of a soft-docking manoeuvre easily, 2) the success of the manoeuvre depends considerably on the launch instant and 3) the disturbances change markedly from parabola to parabola (they are random).

TABLE 4.1 summarizes all the relevant data obtained from the previous analyses.

TABLE 4.1: Displacements of a free-floating object obtained from MATLAB[®] model: maximum displacement among the best time windows (column 3); mean displacement among the best time windows (column 4); maximum displacement among all the time windows (column 5); mean displacement among all the time windows (column 6).

Rotation	g-jitter	Max best cases [m]	Mean best cases [m]	Max all cases [m]	Mean of max all cases [m]
Pitch	g_z	± 1.52	± 0.25	± 3.93	± 2.17
	g_x	± 0.40	± 0.10	± 1.46	± 0.75
	g_y	± 0.45	± 0.10	± 0.79	± 0.48
Roll	g_z	± 0.72	± 0.21	± 3.93	± 2.17
	g_x	± 0.59	± 0.13	± 1.46	± 0.75
	g_y	± 0.30	± 0.10	± 0.80	± 0.48

Ideally, if the best launch time window was exploited in each parabola, the mean displacement of a free-floating object would be on the order of $\sim 0.1 - 0.2$ m (column 4). However, it is important to highlight that, even in these best cases, the maximum displacement could reach also ~ 1.5 m (column 3). Columns 5 and 6 in TABLE 4.1 shows that, if the free-floating object was launched randomly, the displacement in the time window (3.5 s) would be huge (~ 0.5 m is the minimum).

The results collected from the simulations and recapped in TABLE 4.1 were extremely important.

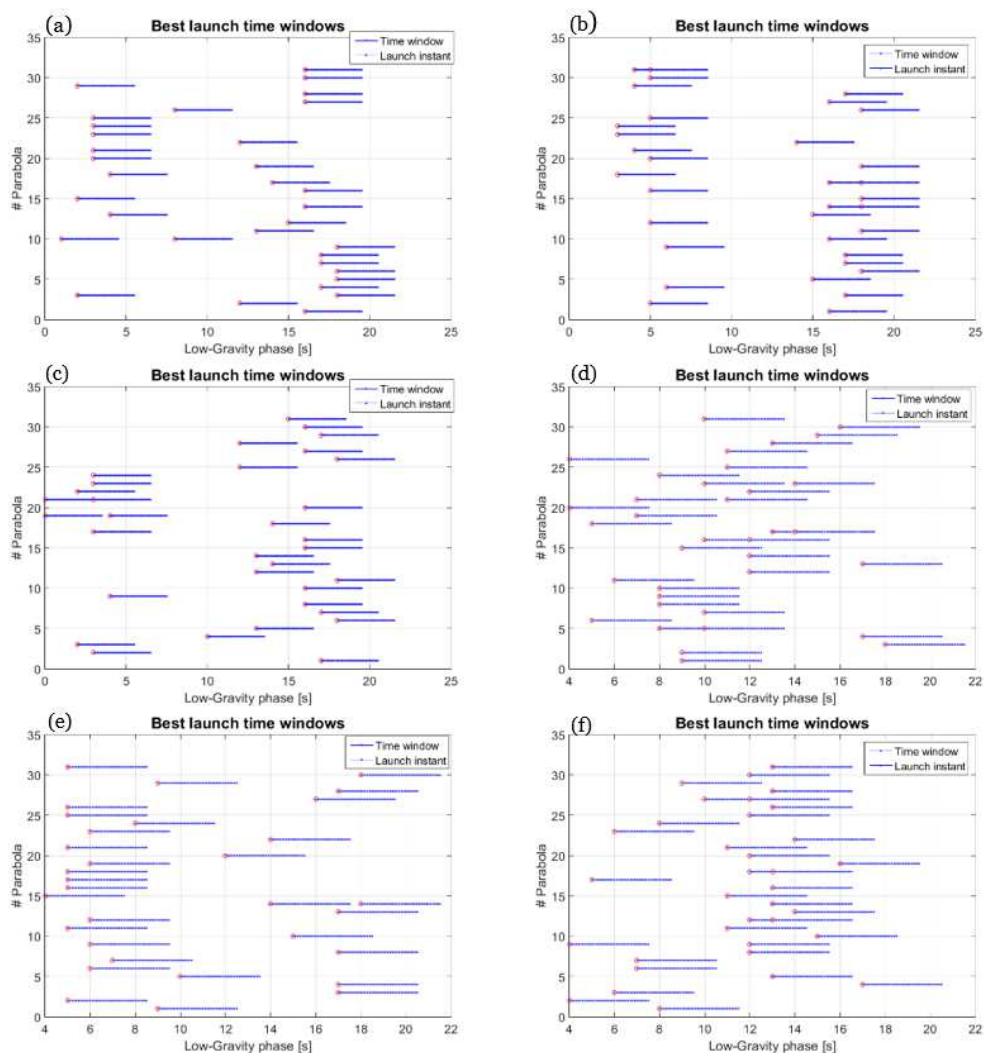


FIGURE 4.5: Best launch time windows for each parabola. Combined effect of the g-jitter along z (a), along x (b) and along y (c) with the aircraft pitch. Combined effect of the g-jitter along z (d), along x (e) and along y (f) with the aircraft roll.

In fact, they contain significant information regarding the displacements the docking interface should have performed, if the first experiment design of PACMAN experiment (the one proposed during the *Fly Your Thesis!* Selection Workshop and described in Section 4.1) had been developed. The docking interface should be able to move with high accuracy and quickly enough to compensate the drift of the CUBE and guarantee the correct accomplishment of the soft-docking manoeuvre in the tight time window. The movement should be controlled by a microcontroller that has to analyse the disturbances, process the information in real time and use them to move the docking interface in the XZ plane. This first solution seemed not to be effective since it would further complicate the experiment design without adding a relevant benefit.

Therefore, the first experiment design of PACMAN experiment was not the best flight configuration to successfully accomplish the predetermined objectives and thus a new

design concerning two free-floating objects, the CUBE and the FFT, was proposed (see FIGURE 2.1). This new solution, instead, seems to be more effective since the two free-floating objects are not subjected to disturbances (they are not fixed to the aircraft and thus disturbances do not have to be compensated) and can move autonomously during the low-gravity phase. Moreover, the experiment would acquire more relevance compared to a real space scenario.

4.2.2 Analysis of the CUBE motion inside the Airbus A310 ZERO-G

Concurrently with the analysis for the identification of the ideal launch window, an accurate model that describes the CUBE motion inside the aircraft has been developed in Simulink to correctly estimate the range of the CUBE displacements.

Three different reference systems have been implemented in the model to perform the dynamic analysis, as shown in FIGURE 4.6:

- the CUBE reference system ‘xyz’ is a clockwise frame centred in the CUBE centre of mass;
- the aircraft reference system ‘XYZ’ is a NED reference system and is centred in the aircraft centre of mass (see FIGURE 4.3);
- the Inertial reference system coincides ‘ $X_I Y_I Z_I$ ’ with the aircraft NED reference frame at the CUBE launch instant and has the same orientation. This reference system is fixed in space and all the data obtained by the dynamic analysis are referred to this reference frame.

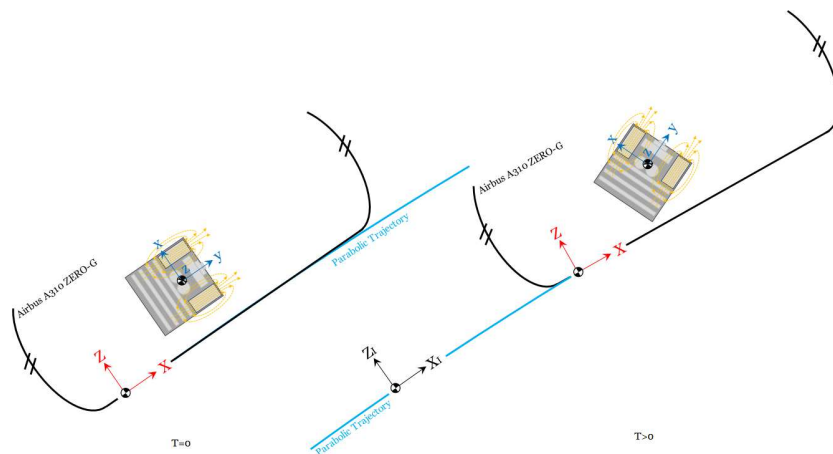


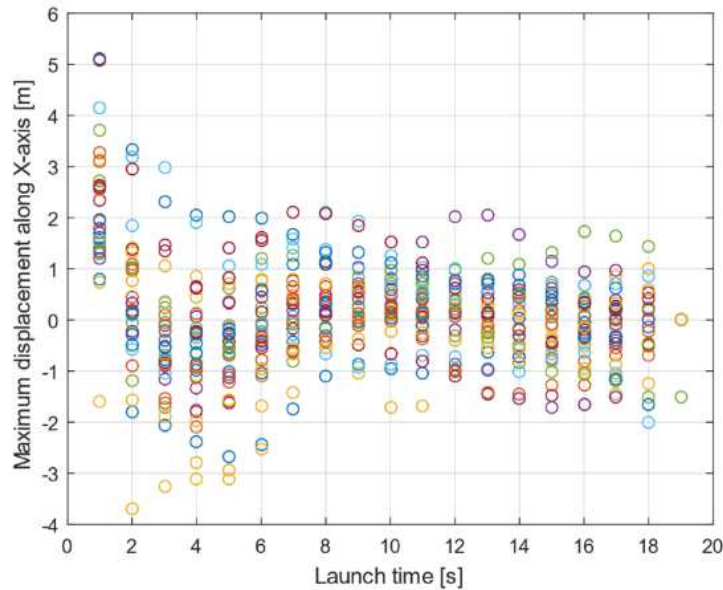
FIGURE 4.6: Reference systems used in the simulations. The three reference frames at the moment of launch ($T = 0$, left) and the same reference frames during the low-gravity phase ($T > 0$, right).

The dynamic analysis has been split into two different phases.

First of all, the parabolic motion of the Airbus A310 ZERO-G has been reconstructed through the acceleration profiles provided by NoveSpace. Unfortunately, the available data were referred only to the #22nd Parabolic Flight that took place the 19th of May (2015) and thus only marginal statistical information could be drawn from the analyses. However, they were sufficient for limiting the selection of the exploitable launch instants. Secondly, the CUBE free-floating motion has been simulated through the propagation of its equation of motion. The velocities obtained by the reconstruction of the aircraft motion have been used as initial conditions for the propagation of the CUBE motion. The initial hypothetical position of the CUBE inside the aircraft was set to $[-5; 1; 0]$ m with respect to the aircraft centre of mass. This disadvantageous position was chosen since it represented the worst possible position for PACMAN experiment inside the Airbus A310 ZERO-G.

To obtain statistically relevant results, each parabola has been analysed. 19 soft-docking manoeuvres were simulated during each parabola, considering each second after the injection into microgravity as the starting instant (i.e. $t_{start} = t_{injection} + k, k \in N$).

FIGURE 4.7 shows the results obtained by these analyses and focuses on the maximum CUBE displacements along each axis individually.



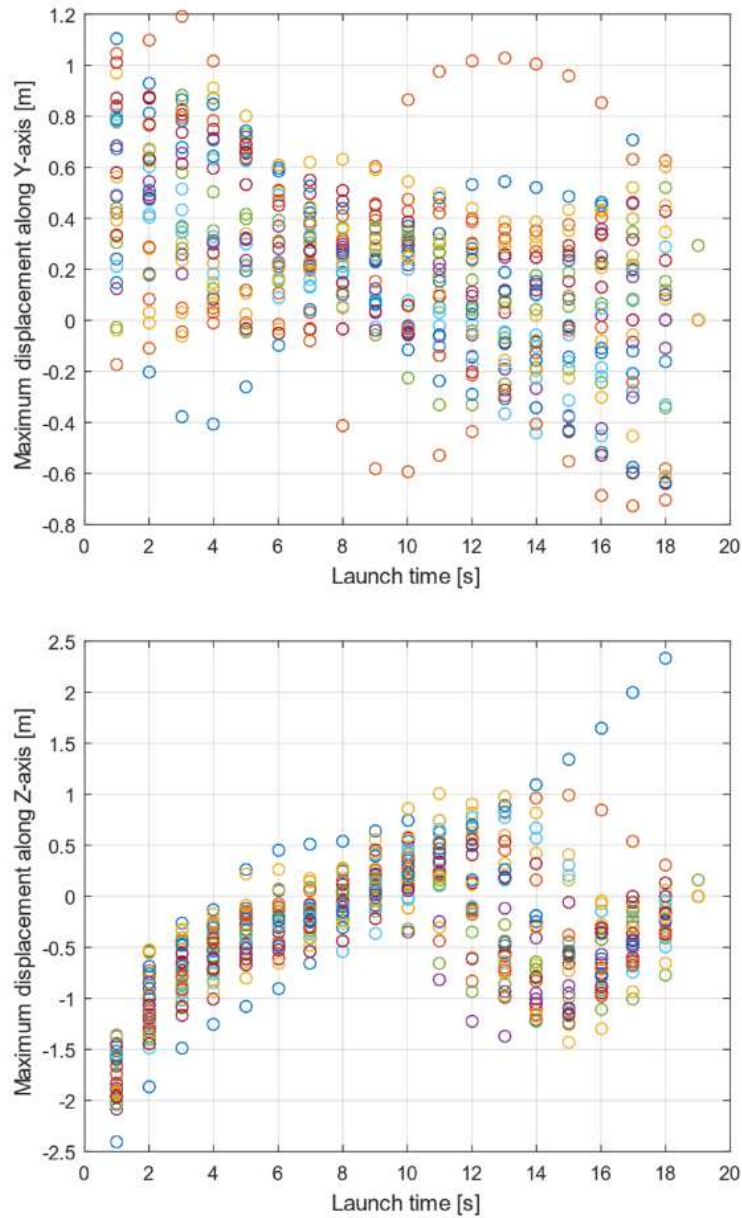


FIGURE 4.7: The graphs represent the maximum displacements of the CUBE inside the Airbus A310 ZERO-G. The axis of the abscissae represents the launch instant, the ordinates axis the maximum displacement for each parabola. The duration of the free-floating phase was set to 4.5 s.

The launch instants that statistically minimise the maximum displacements are determined as a result for a search problem. The best launch instants are summarized in TABLES 4.2, 4.3 and 4.4.

TABLE 4.2: Summary of the best launch instants that minimise the maximum CUBE displacement for the X -axis.

Launch instant [s]	X max [m]	X min [m]	X mean [m]	$2\sigma_X$ [m]
7	0.08	-0.41	-0.18	0.48
8	0.18	-0.25	-0.035	0.45
11	0.66	-0.14	0.24	0.80

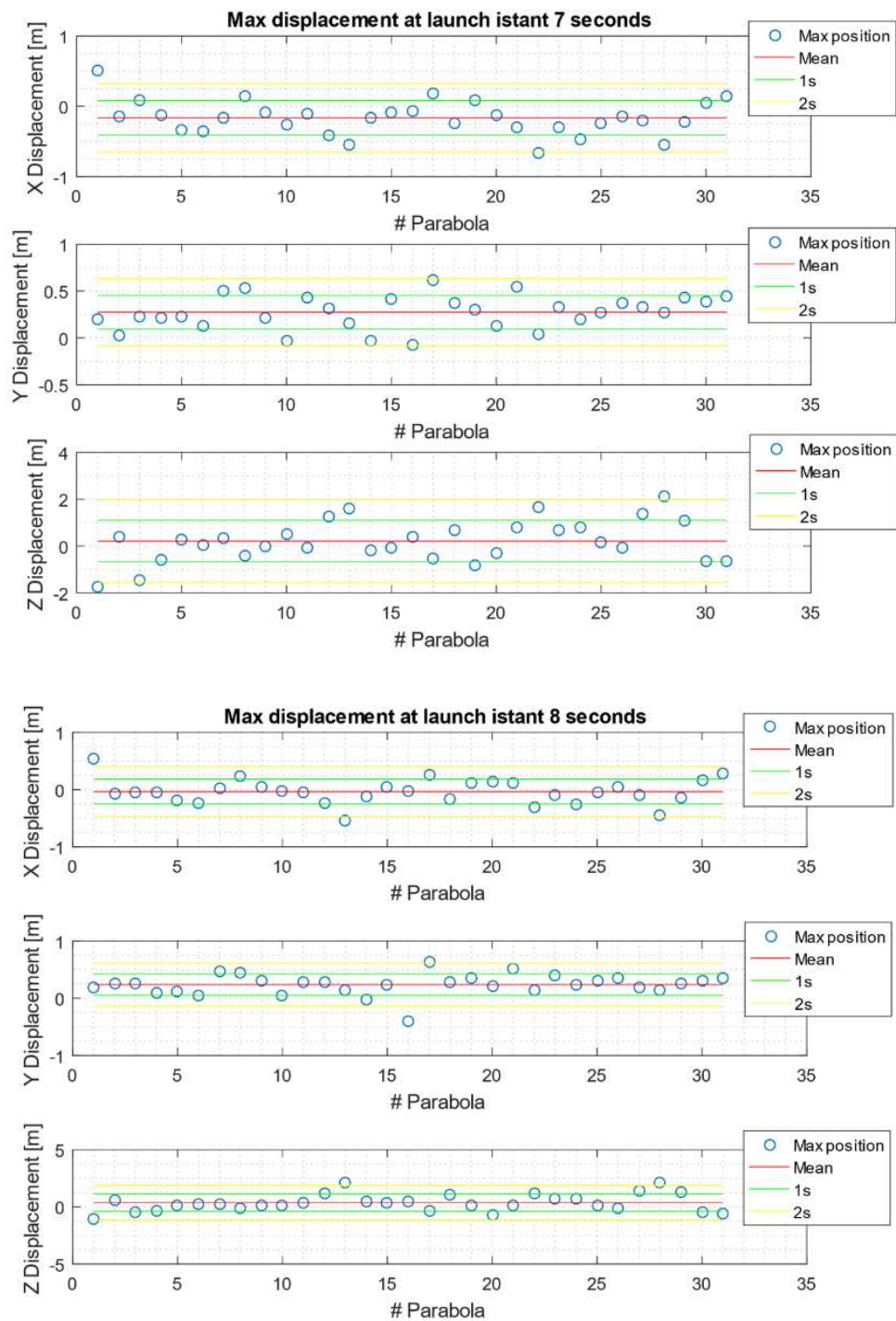
TABLE 4.3: Summary of the best launch instants that minimise the maximum CUBE displacement for the Y -axis.

Launch instant [s]	Y max [m]	Y min [m]	Y mean [m]	$2\sigma_Y$ [m]
7	0.45	0.1	0.28	0.35
8	0.43	0.05	0.25	0.38
11	0.42	-0.15	0.14	0.57

TABLE 4.4: Summary of the best launch instants that minimise the maximum CUBE displacement for the Z -axis.

Launch instant [s]	Z max [m]	Z min [m]	Z mean [m]	$2\sigma_Z$ [m]
7	1.1	-0.67	0.22	1.80
8	1.11	-0.4	0.33	1.52
11	0.87	-0.48	0.21	1.38

FIGURE 4.8 shows the maximum displacements (grouped by launch instant) and the mean and standard deviation calculated to obtain a confidence interval to determine the displacement bounds. The obtained results were fundamental to improve the final design of the experiment and to determine the best launch instant to start the soft-docking manoeuvre.



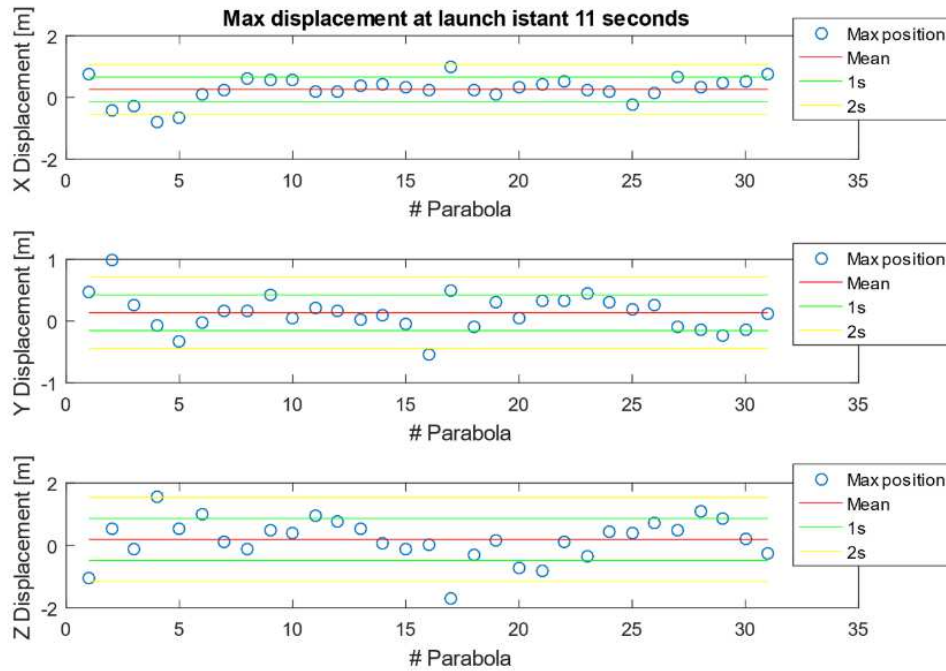


FIGURE 4.8: The graphs represent the maximum displacements of the CUBE inside the Airbus A310 ZERO-G along each axis at the best launch instants: 7, 8 and 11 s. The axis of the abscissae represents the considered parabola, the ordinate axis the maximum displacement for each parabola. The mean value and the standard deviation 's' are plotted as reference.

4.3 PACMAN experiment requirements

Before starting PACMAN final design, a complete list of requirements was drawn up to be able to effectively test in low-gravity the proposed innovative technologies and to achieve the predetermined scientific objectives.

Particular attention was paid to fulfill all the safety constraints recommended by Novespace [44]. The testing environment of a parabolic flight is quite different from the rest of the gravity-related facilities since it includes the presence of the experimenters during the tests. This peculiarity led to a series of limitations that must be observed and considered as requirements to be fulfilled during the experiment design process. The requirements were divided into six different types [48] and verified [49] by satisfying the technical specifications included in the European Cooperation for Space Standardization (ECSS) book. The following verification methods were adopted:

- physical Test (T) of a subsystem or of the whole experiment;
- Analysis (A) with simulations or by similarity with a subsystem that did already successfully fly;

- Review of design (R) using schematics, engineering models, drawings, etc. to show that the experiment will perform as expected;
- visual Inspection (I).

4.3.1 Functional requirements

Functional requirements define the necessary functionalities of the experiment in order to achieve the scientific objectives. They should only be functions directly linked to the fulfilment of the objectives and should not give information about the quality of the measurements or the sensors used. TABLE 4.5 shows the functional requirements of PACMAN experiment referred to the scientific objectives presented in Section 2.1.1.

TABLE 4.5: Functional requirements.

ID	Requirement text	Verification
F.1	The CUBE shall be able to perform autonomous soft-docking manoeuvre exploiting magnetic interactions	A, T
F.2	The CUBE shall be able to perform proximity guidance manoeuvre exploiting magnetic interactions	A, T
F.3	The low-range sensor system (on-board camera and IMU) shall be able to determine the pose of the CUBE with respect to the FFT	T, I
F.4	The acceleration of the airplane shall be measured	A, T
F.5	The angular velocities of the airplane shall be measured	A, T
F.6	The hold & launch system shall be able to launch the CUBE and FFT towards each other	R, T
F.7	The pose of the CUBE and the FFT during the low-gravity phase shall be measured with the External Reference Cameras	R, T
F.8	The acceleration of the CUBE shall be measured	R, T
F.9	The angular velocity of the CUBE shall be measured	R, T
F.10	The acceleration of the FFT shall be measured	R, T
F.11	The hold & launch systems shall be able to hold the CUBE and FFT during the hyper-gravity phase	R, T

4.3.2 Performance requirements

Performance requirements define the quality of the experiment quantifying at what level the functional requirements of the experiment have to be met in terms of accuracy, frequency and range of the sensors. TABLE ?? recap all the performance requirements of PACMAN experiment.

TABLE 4.6: Performance requirements.

ID	Requirement text	Verification	Motivation
P.1	The magnetic actuators on board the CUBE shall be able to perform a torque of $5 * 10^{-4}$ Nm	A, T	Maximum allowable authority of the magnetic actuators obtained from dynamical simulations
P.2	The on-board camera shall record IR images with a frequency of at least 10 Hz	R, T	A lower acquisition frequency would decrease the performances of the navigation system and thus compromise the proximity operations
P.3	The maximum allowable initial misalignment of the CUBE along the <i>X</i> and <i>Y</i> axis either respect to the FFT shall be of $\pm 15^\circ$	A, R, T	Maximum initial misalignment recoverable by the CubeSats during the free-floating phase (data obtained from dynamical simulations)
P.4	The hold & launch systems shall launch the CUBE and the FFT with an initial velocity of 0.02 m/s	R, A, T	Minimum initial velocity allowable to complete the soft-docking manoeuvre in the 5 s free-floating window
P.5	The hold & launch systems shall launch the CUBE and the FFT with a nominal angular velocity equal to $0^\circ/s$	R, A, T	A null nominal angular velocity is needed to assess the effective performance of the CubeSats and to correctly investigate the influence of the electromagnetic fields action
P.6	The hold & launch systems shall launch the CUBE and the FFT with a maximum angular velocity equal to $3^\circ/s$	R, A, T	Maximum angular velocity recoverable by the CubeSats during the free-floating phase
P.7	The impact velocity between the CUBE and the FFT shall be lower than 0.07 m/s	R, T	A higher impact velocity would produce a bounce-back effect compromising the soft-docking manoeuvre
P.8	The estimation of the angular error of the CUBE shall be lower than 2°	R, A, T	A higher angular error estimation would compromise the final CubeSats alignment during the soft-docking manoeuvre
P.9	The CUBE shall be able to estimate its attitude at a distance lower than 0.4 m with respect to the FFT	R, A, T	0.4 m represents the maximum distance between the two CubeSats before the release
P.10	The soft-docking manoeuvre shall be performed in less than 5 s	T, I, A	After 5 s of free-floating, the CubeSats will hit the floor or the roof of the aircraft and thus this represent the maximum time available to perform the soft-docking manoeuvre
P.11	The power supply given by the batteries shall be granted for 15 parabolas	R, T	If the power supply of the CubeSats is not enough for an entire flight, data retrieved from 15 parabolas (45 in total, considering the 3 flights) are still sufficient to draw valuable conclusions. However, 2 spare CubeSats (1 CUBE and 1 FFT) are available to cover the entire flight
P.12	The control frequency of the CUBE should be at least 10 Hz	R, T	A lower frequency would decrease the performances of the navigation system and thus compromise the proximity operations
P.13	The magnetic actuators on board the CUBE may decrease its velocity during the docking approach	A, T	Decreasing the CubeSats approaching velocity would reduce the possibility of bounce-back effects

P.14	The difference between the release time of the CUBE and the FFT shall be lower than 0.1 s	R, T	A higher difference between the release time of the CubeSats would produce different initial launching conditions due to the disturbances aboard the aircraft and would compromise the proximity operations during the low-gravity phase (data obtained from dynamical simulations)
P.15	The angular velocity of the CUBE shall be measured with an accuracy of ± 25 mdps in each axis	R	The final proximity operations depend on the inertial measurements propagation, since the Raspberry Pi NoIR Camera V2 module is no more effective when the CubeSats are very close to each other (the 5 LEDs are outside the camera field of view). Therefore, the measurements of the angular velocity has to be accurate enough to guarantee the navigation
P.16	The acceleration of the CUBE shall be measured with an accuracy of ± 4 mg in each axis	R	The final proximity operations depend on the inertial measurements propagation, since the Raspberry Pi NoIR Camera V2 module is no more effective when the CubeSats are very close to each other (the 5 LEDs are outside the camera field of view). Therefore, the measurements of the acceleration has to be accurate enough to guarantee the navigation
P.17	The angular velocity of the CUBE shall be measured with a frequency of 50 Hz in each axis	R	A lower acquisition frequency would decrease the performances of the navigation system and thus compromise the proximity operations (data obtained from dynamical simulations)
P.18	The acceleration of the CUBE shall be measured with a frequency of 50 Hz in each axis	R	A lower acquisition frequency would decrease the performances of the navigation system and thus compromise the proximity operations (data obtained from dynamical simulations)
P.19	The angular velocity of the CUBE shall be measured in a range between $\pm 90^\circ/s$ in each axis	R	The range has been established considering the worst case scenario in which the CUBE accidentally hits the hold & launch system and starting to rotate
P.20	The acceleration of the CUBE shall be measured within a range between ± 2 g in each axis	R	The range has been established considering the different phases during the parabolic flight manoeuvre (1 g - 2 g - 0 g - 2 g - 1 g) to avoid the saturation of the accelerometer
P.21	The angular velocity of the aircraft shall be measured with an accuracy of $\pm 1^\circ/s$ in each axis	R	These additional data are collected just for post-processing (if needed, they are unnecessary to achieve the main objectives of PACMAN experiment) or for a comparison with the data collected by NoveSpace
P.22	The acceleration of the aircraft shall be measured with an accuracy of ± 4 mg in each axis	R	These additional data are collected just for post-processing (if needed, they are unnecessary to achieve the main objectives of PACMAN experiment) or for a comparison with the data collected by NoveSpace
P.23	The angular velocity of the aircraft shall be measured with a frequency of at least 100 Hz in each axis	R	These additional data are collected just for post-processing (if needed, they are unnecessary to achieve the main objectives of PACMAN experiment) or for a comparison with the data collected by NoveSpace
P.24	The acceleration of the aircraft shall be measured with a frequency of at least 100 Hz in each axis	R	These additional data are collected just for post-processing (if needed, they are unnecessary to achieve the main objectives of PACMAN experiment) or for a comparison with the data collected by NoveSpace
P.25	The angular velocity of the aircraft shall be measured in a range between $\pm 90^\circ$ in each axis	R	These additional data are collected just for post-processing (if needed, they are unnecessary to achieve the main objectives of PACMAN experiment) or for a comparison with the data collected by NoveSpace

P.26	The acceleration of the aircraft shall be measured within a range between $\pm 4g$ in each axis	R	These additional data are collected just for post-processing (if needed, they are unnecessary to achieve the main objectives of PACMAN experiment) or for a comparison with the data collected by NoveSpace
P.27	The angular velocity of the FFT shall be measured with an accuracy of ± 100 mdps in each axis	R	Since the FFT is an uncooperative module, these data are collected only to have redundant measurements (together with the information obtained from the stereo-camera) to correctly retrace the CubeSat trajectory in post-processing (they are unnecessary to achieve the main objectives of PACMAN experiment)
P.28	The acceleration of the FFT shall be measured with an accuracy of ± 20 mg in each axis	R	Since the FFT is an uncooperative module, these data are collected only to have redundant measurements (together with the information obtained from the stereo-camera) to correctly retrace the CubeSat trajectory in post-processing (they are unnecessary to achieve the main objectives of PACMAN experiment)
P.29	The angular velocity of the FFT shall be measured with a frequency of 50 Hz in each axis	R	Since the FFT is an uncooperative module, these data are collected only to have redundant measurements (together with the information obtained from the stereo-camera) to correctly retrace the CubeSat trajectory in post-processing (they are unnecessary to achieve the main objectives of PACMAN experiment)
P.30	The acceleration of the FFT shall be measured with a frequency of 50 Hz in each axis	R	Since the FFT is an uncooperative module, these data are collected only to have redundant measurements (together with the information obtained from the stereo-camera) to correctly retrace the CubeSat trajectory in post-processing (they are unnecessary to achieve the main objectives of PACMAN experiment)
P.31	The angular velocity of the FFT shall be measured in a range between $\pm 90^\circ/s$ in each axis	R	Since the FFT is an uncooperative module, these data are collected only to have redundant measurements (together with the information obtained from the stereo-camera) to correctly retrace the CubeSat trajectory in post-processing (they are unnecessary to achieve the main objectives of PACMAN experiment)
P.32	The acceleration of the FFT shall be measured within a range between $\pm 4g$ in each axis	R	Since the FFT is an uncooperative module, these data are collected only to have redundant measurements (together with the information obtained from the stereo-camera) to correctly retrace the CubeSat trajectory in post-processing (they are unnecessary to achieve the main objectives of PACMAN experiment)

4.3.3 Design requirements

Design requirements (see TABLE 4.7) define the design aspects the experiment needs to fulfil to achieve the experiment objectives. While functional and performance requirements originate from the experiment team, design requirements come from other sources like flight environment, safety restrictions, physical limitations, etc.

TABLE 4.7: Design requirements.

ID	Requirement text	Verification
D.1	The CUBE mass shall be less than 10 kg	R, T
D.2	The space available for the test shall be at least equal to 1.5x1.5 m	R, A
D.3	The CUBE and FFT shall be covered with shock protections	I, R
D.4	The magnetic field intensity of both the CUBE and the FFT shall be less than 40 mT	R, T
D.5	The experiment shall be designed to withstand the loads in case of emergency landing	A, T
D.6	The structural design shall provide an ultimate safety factor equal to 1.5	R, T
D.7	The temperature of the coils shall be lower than 60°C	R, T
D.8	The FFT mass shall be less than 10 kg	R, T
D.9	The CUBE and the FFT shall be built as two distinct modules having the same size of a 1U CubeSat	R, A, T
D.10	The hold & launch systems shall withstand the 2 g loads during the pull-up manoeuvre	R, T
D.11	The battery packs may be replaceable	R, T
D.12	The movements of the CUBE and the FFT shall be limited by a net	R, I
D.13	The laptop shall be fixed to a plate by means of Velcro	R, I
D.14	External cameras shall be placed in such a way that the CUBE and the FFT are always within their field of view	R, T
D.15	The laptop shall be powered through NoveSpace power block	A, I
D.16	The CUBE and the FFT shall be launched automatically using a timer	R, T

4.3.4 Interface requirements

Interface requirements (see TABLE 4.8) are requirements related to the interfaces between the experiment and the aircraft as well as between different subsystems of the experiment.

TABLE 4.8: Interface requirements.

ID	Requirement text	Verification
I.1	The hold & launch systems shall be mountable on the aircraft seat tracks as specified in the ITF document	A, T
I.2	The hold & launch systems shall be able to keep the CUBE and the FFT in position before the low-gravity phase	A, T
I.3	The laptop shall be powered by NoveSpace power block	I
I.4	The laptop shall be able to communicate via wireless with the CUBE and the FFT to check the nominal status	I

4.3.5 Operational requirements

Operational requirements (see TABLE 4.9) are requirements that the experiment has to meet to be handled and operated safely and reliably. 'Operations' refer not only to

operations during the flight but also to the handling of the experiment prior to and after flight.

TABLE 4.9: Operational requirements.

ID	Requirement text	Verification
O.1	The launch of the CUBE and FFT shall be synchronous	A, T
O.2	The experimenter shall be able to recover the CUBE and the FFT inside the netted area and to set again the hold & launch systems during the steady phase	T, I
O.3	The battery packs shall be fully charged	T
O.4	The CUBE and the FFT should autonomously switch from operative to idle mode after the accomplishment of soft-docking manoeuvre	R, T
O.5	Changing one battery pack shall not take longer than 60 s	R, T
O.6	The launch instant shall be at around 11 s (during the low-gravity phase - second part of each parabola)	A, T

4.3.6 Human factor requirements

Human factor requirements (see TABLE 4.10) are requirements related to a product or a process adapted to human capabilities considering basic human characteristics such as decision making, coordination, body dimensions, perceptions and judgement, etc.

TABLE 4.10: Human factor requirements.

ID	Requirement text	Verification
H.1	The battery pack replacement shall be unambiguous	R, T
H.2	The experiment shall display information on a GUI or with no more than two windows on the screen at the same time	R
H.3	The experiment shall be able to start and conclude the procedure during the low-gravity phase autonomously	R
H.4	The experimenter shall be able to set new profiles on the linear guides during the short or long pauses	T
H.5	The experimenter shall be able to stop the experiment acting on a single switch in case of emergency	T
H.6	The experimenter shall be able to recover the two CubeSats during the steady flight	T
H.7	The experimenter shall be able to vary the inclination of the release interface during the short or long pauses	T
H.8	The experimenters shall be able to register the results (successful/unsuccessful) of the soft-docking manoeuvre	T
H.9	The experimenter shall be able to connect the two CubeSats to the hold & launch interfaces during the steady flight	T

4.4 Magnetic field model for PACMAN experiment

This section presents the magnetic field model implemented during the research to validate PACMAN experiment. Since the electromagnetic interaction between the CUBE and the FFT is due to the electromagnets aboard the CubeSats, the study focuses on the interaction between two electromagnets.

The most intuitive interactions between two electromagnets are probably represented by the mutual attractive and repelling force obtained when the coil plane normal vectors are co-axial. However, magnets are also able to produce 'shear' forces (when the coil plane normal vectors are orthogonal) and skew movements (when the coil plane normal vectors are orthogonal).

The composition of all these interactions can be used to obtain any relative complex manoeuvre between the two magnets. Moreover, along with forces, magnets can produce torques that have to be taken into account to control the rotation of the single magnet and conserve the angular momentum of the system [50].

In order to calculate the forces and torques between two electromagnets, a step back has to be done to the calculation of the mutual forces generated between two current loops. The forces produced by two current loops are always equal and opposite and are given by the formula 4.1, which is valid at any distance between the two coils:

$$\mathbf{F}_{AB} = \frac{\mu_0}{4\pi} I_A I_B \oint \oint \frac{d\mathbf{l}_B \times (d\mathbf{l}_A \times \mathbf{r})}{|\mathbf{r}|^3} \quad (4.1)$$

where μ_0 is the vacuum permeability, I_A and I_B are the currents flowing into the loops, $d\mathbf{l}_A$ and $d\mathbf{l}_B$ are the infinitesimal lengths of conductors A and B respectively and \mathbf{r} is the distance between the two loops.

As can be seen from equation 4.1, analytical expressions of the mutual forces can be obtained only when two circular loops have their plane normal vectors aligned. For all the other situations, a double numerical integration must be carried out.

FIGURE 4.9 shows two arbitrary current loops. A very accurate Near-Field model derived from the Lorentz force equation [51] was used to characterize PACMAN experiment and its control loop. This model can be used for calculating the magnetic force between inclined circular loops placed in any desired position.

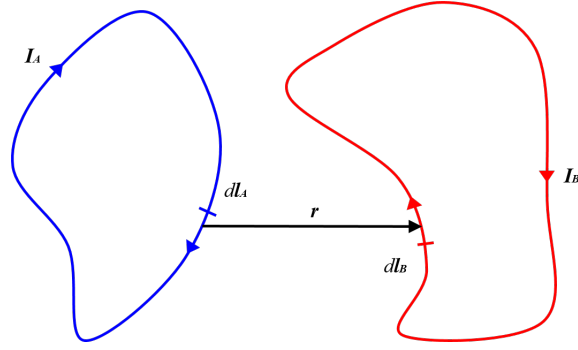


FIGURE 4.9: Two arbitrary current loops. The magnetic field produced by the current flowing in the blue coil interacts with the magnetic field produced in the red one. The interaction generates an electromagnetic force which acts on both coils in opposite directions.

4.4.1 Near-Field model based on Lorentz approach

The model presented in this section is a new general formula for calculating the magnetic force between inclined circular loops placed in any desired position. The complete description of the model can be found in [51]. FIGURE 4.10 shows two circular coils. The large one is the primary coil (blue) and is centred in the plane XOY with the Z -axis as normal vector of the plane. The XYZ reference system coincides with the origin of the primary coil, which has the radius R_P . The current I_P flows into the primary coil. The second smaller coil is the secondary coil (red) and is placed in a different arbitrary plane, inclined with respect to the primary one. The radius of the secondary coil is R_S and the current is defined by I_S . As it was for the previous one, for this coil as well the $X'Y'Z'$ reference system coincides with its origin. In this way, it is possible to define the positions of the coils in a 3D space, allowing for the calculation of all the necessary parameters needed to obtain the mutual magnetic forces acting on them.

The formula was derived from the Lorentz force equation in which the magnetic force between two line elements is given by

$$d\mathbf{F} = I_s d\mathbf{l}_S \times \mathbf{B}_P(\mathbf{l}_S) \quad (4.2)$$

where $d\mathbf{F}$ is the force acting on the line element $d\mathbf{l}_S$ of the secondary coil due to the external magnetic field \mathbf{B}_P produced by the primary one.

Integrating equation 4.2 along the whole loop, it is possible to obtain the force on the secondary coil due to the primary one as

$$\mathbf{F} = I_S \oint d\mathbf{l}_S \times \mathbf{B}_P(\mathbf{l}_S) \quad (4.3)$$

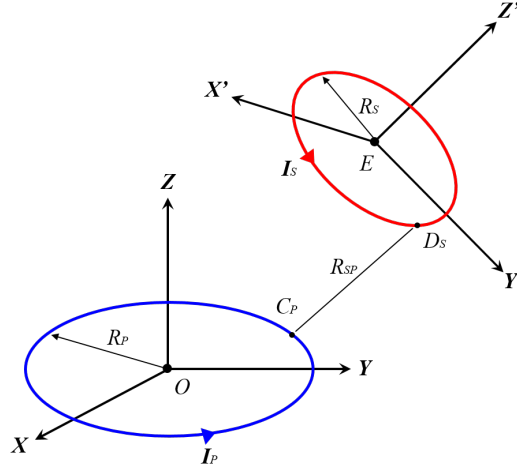


FIGURE 4.10: Two arbitrary circular coils. The magnetic field produced by the primary coil interacts with the one generated by the secondary coil. The result is an electromagnetic force acting on both the coils.

The magnetic field $\mathbf{B}_P(\mathbf{l}_S)$ produced by the primary coil can be calculated in any arbitrary point D_S on the secondary by

$$\mathbf{B}_P(\mathbf{l}_S) = \frac{\mu_0 I_P}{4\pi} \oint_{l_P} \frac{d\mathbf{l}_P \times \mathbf{r}_{SP}}{r_{SP}^3} \quad (4.4)$$

where r_{SP} is the distance between two arbitrary points $C_P(x_P, y_P, z_P)$ on the primary coil and D_S on the secondary one, respectively.

Resolving the integral in equation 4.4, it is possible to obtain the final form of the three components of the magnetic field in an arbitrary point $D_S(x_S, y_S, z_S)$ in the secondary coil produced by the primary one (see [51] for further information)

$$\begin{aligned} B_x(x_S, y_S, z_S) &= -\frac{\mu_0 I_P z_S x_S k}{8\pi \sqrt{R_P} (x_S^2 + y_S^2)^{\frac{5}{4}}} L_0 \\ B_y(x_S, y_S, z_S) &= -\frac{\mu_0 I_P z_S y_S k}{8\pi \sqrt{R_P} (x_S^2 + y_S^2)^{\frac{5}{4}}} L_0 \\ B_z(x_S, y_S, z_S) &= \frac{\mu_0 I_P k}{8\pi \sqrt{R_P} (x_S^2 + y_S^2)^{\frac{3}{4}}} L_0 \end{aligned} \quad (4.5)$$

where

$$\begin{aligned}
L_0 &= 2K(k) - \frac{2-k^2}{1-k^2}E(k) \\
S_0 &= 2\sqrt{x_S^2 + y_S^2}K(k) - \frac{2\sqrt{x_S^2 + y_S^2} - (R_P + \sqrt{x_S^2 + y_S^2})k^2}{1-k^2}E(k)
\end{aligned} \tag{4.6}$$

$K(k)$ represents the complete elliptic integral of the first kind, while $E(k)$ represents the complete elliptic integral of the second kind expressed in terms of the modulus k (see [52] for further details).

Applying equations 4.6 to equation 4.3, it is possible to obtain, after some transformations, the final form of the magnetic force components:

$$\begin{aligned}
F_x &= \frac{\mu_0 I_P I_S R_S}{8\pi\sqrt{R_P}} \int_0^{2\pi} I_x d\phi \\
F_y &= \frac{\mu_0 I_P I_S R_S}{8\pi\sqrt{R_P}} \int_0^{2\pi} I_y d\phi \\
F_z &= \frac{\mu_0 I_P I_S R_S}{8\pi\sqrt{R_P}} \int_0^{2\pi} I_z d\phi
\end{aligned} \tag{4.7}$$

where

$$\begin{aligned}
I_x &= \frac{k}{(x_S^2 + y_S^2)^{\frac{5}{4}}} \left[z_S y_S l_{S_z} L_0 + \sqrt{(x_S^2 + y_S^2)} l_{S_y} S_0 \right] \\
I_y &= \frac{k}{(x_S^2 + y_S^2)^{\frac{5}{4}}} \left[z_S x_S l_{S_z} L_0 + \sqrt{(x_S^2 + y_S^2)} l_{S_x} S_0 \right] \\
I_z &= \frac{k}{(x_S^2 + y_S^2)^{\frac{5}{4}}} z_S \left[x_S l_{S_y} - y_S l_{S_x} \right] L_0 \\
k^2 &= \frac{4R_P \sqrt{(x_S^2 + y_S^2)}}{\left(R_P + \sqrt{(x_S^2 + y_S^2)} \right)^2 + z_S^2}
\end{aligned} \tag{4.8}$$

with (x_S, y_S, z_S) the parametric coordinates of an arbitrary point of the secondary coil referred to its centre and $(l_{S_x}, l_{S_y}, l_{S_z})$ the differential elements of the secondary coil.

4.4.2 PACMAN simulation

An accurate model that describes the CUBE-FFT interaction was developed in Matlab[®]-Simulink in order to correctly simulate the CUBE and the FFT dynamics aboard the aircraft (FIGURE 4.11).

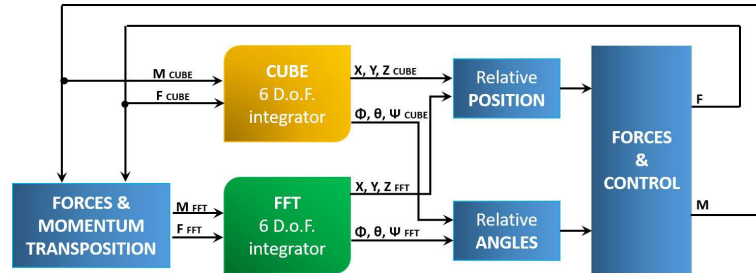


FIGURE 4.11: Block diagram of the Simulink model implemented.

The model uses a Simulink block to integrate the six-degrees-of-freedom equations of motion. This block requires the total force and torque acting on the object for each time step and the mass characterization of the system as inputs.

The distance vectors between the CUBE coils and the FFT coil can be obtained from the knowledge of the CUBE and the FFT position in the inertial reference frame. These vectors are used to evaluate the magnetic forces and thus the torque on the CUBE and the FFT.

Simulations were made to optimize the set of parameters for the coils geometry (diameter and height) and magneto-motive force (number of turns and current). The parameters have been selected considering both the total power consumption and the space available in the CubeSats. The analyses were carried out considering the initial nominal configuration (position, release velocities and inclinations) of the two CubeSats, adjusting the parameters to determine the best configuration able to ensure a successful attitude control and accomplish the soft-docking manoeuvre with the lowest energy consumption.

The set of parameters selected are:

- Diameter CUBE coils = 36 mm
- Diameter FFT coil = 100 mm
- Magneto-Motive Force CUBE coils = 100 A – turns (for each coil)
- Magneto-Motive Force FFT coils = 450 A – turns

FIGURE 4.12 shows the axial force acting on the CUBE without initial rotation and angular velocity. As it can be seen, the attractive force is highly non-linear and its trend

follows the magnetic field equation that is proportional to $\frac{1}{r^3}$ where r is the distance from the magnetic source. FIGURE 4.13, instead, shows the relative misalignment and torque acting on the CUBE with an initial rotation of 15° around the x -axis, which represents the maximum initial misalignment recoverable by the CubeSats during the free-floating phase. The CUBE is able to re-align itself with the FFT in ~ 3.5 s, covering a distance of 20 cm. The initial misalignment is recovered, bringing the docking interfaces mounted aboard the CUBE and the FFT parallel to each other (the misalignment change from 15° to 0° in FIGURE 4.13).

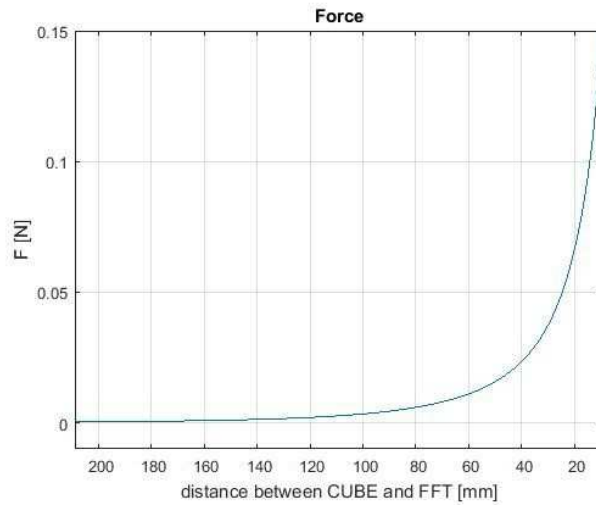


FIGURE 4.12: Axial force acting on the CUBE with no initial rotation/angular velocity.

The control algorithm implemented (see Section 4.5.2.2 for further information) in the simulation acts on the current of the coils, controlling them to deliver the right torque to the CUBE (FIGURE 4.14). The effective current variation allows the accomplishment of the soft-docking manoeuvre. No initial angular velocity has been considered in the simulation since the use of the linear guide together with the holding electromagnet to launch the CubeSats should ensure a nominal null angular velocity at the release. However, dynamical analyses showed that the maximum initial angular velocity recoverable by the CUBE and the FFT during the free-floating phase is equal to $3^\circ/\text{s}$. A higher initial angular velocity would compromise the docking manoeuvre.

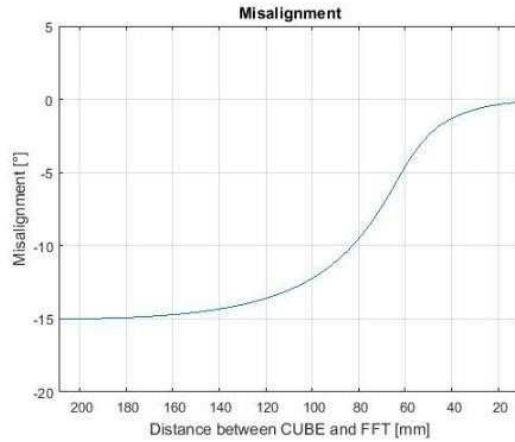


FIGURE 4.13: Relative misalignment of 15° around the x -axis between the CUBE and the FFT.

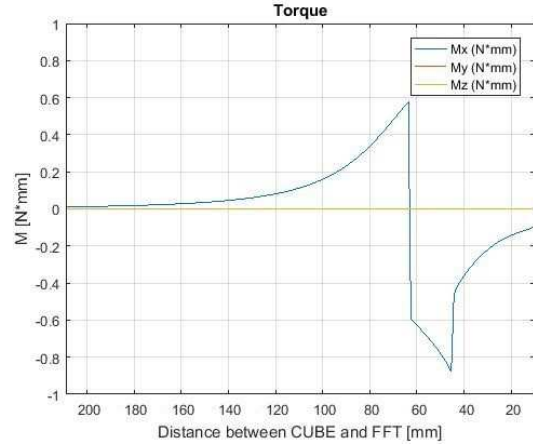


FIGURE 4.14: Torque acting on the CUBE with initial rotation of 15° around the x -axis.

4.5 PACMAN Experiment final design

As previously mentioned in Section 4.2.1, the first design of PACMAN experiment was not the best flight configuration to successfully accomplish the soft-docking manoeuvre during a parabolic flight. Therefore, a new design concerning two free-floating objects, the CUBE and the FFT, was proposed. This new solution seems to be more effective, since the two CubeSats are not subjected to the disturbances aboard the aircraft and can move autonomously during the low-gravity phase.

Considering the new configuration, PACMAN is composed of four main systems: a spacecraft mock-up CUBE, a Free-Floating Target FFT and a test chamber called CHAMBER. During the launch tests, the CUBE and the FFT are free to float inside the CHAMBER. The fourth system is represented by the Supporting Electronics, consisting in the CHAMBER sensors, data acquisition boards and the monitoring computer.

PACMAN final configuration is the result of the design of these four systems.

4.5.1 System 1: CHAMBER

The CHAMBER is a safe environment for the CUBE and the FFT to float as it avoids the risk of hurting other people, damaging the experiments or the Supporting Electronics. It provides also a number of features to support the test procedures. FIGURE 4.15 presents all the CHAMBER sensors: the external reference stereo-camera “DUO MC” to record the motion of the CUBE and the FFT and the IMU “Phidget Spatial Basic” to collect data about the structural vibrations of the aircraft.

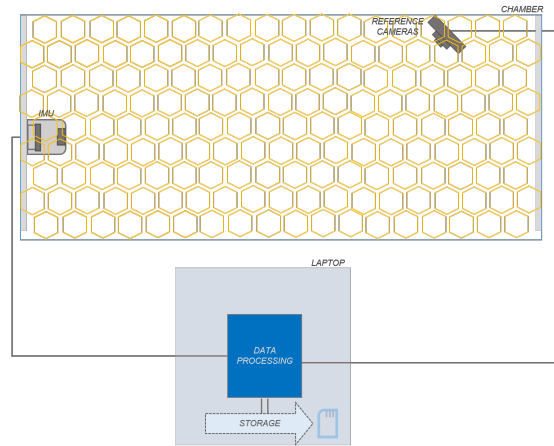


FIGURE 4.15: CHAMBER sensors. The data collected by these chamber sensors will be processed by the Supporting Electronics outside the CHAMBER (laptop).

All the devices and sensors connected to the CHAMBER are powered by the NoveSpace electrical power block using the aircraft power panel which includes the necessary safety devices and interfaces the experiment with the aircraft electrical distribution panels. The power is then correctly distributed among all the subsystems of the CHAMBER by the Supporting Electronics. FIGURE 4.16 shows the electrical block diagram of the experiment.

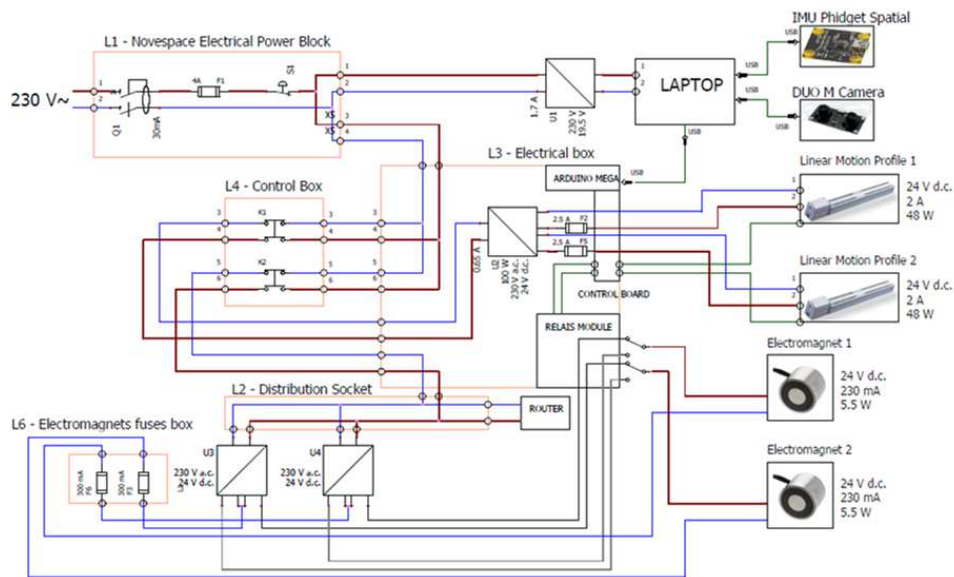


FIGURE 4.16: Electrical block diagram of PACMAN experiment text.

The laptop is connected to the power block through its power supply, with the IMU and the stereo-camera.

The hold & launch systems power line is divided into three parts:

- motor section, connected to the power block through the dedicated 48 V power supply unit with built-in output overcurrent protection.
- logic section, connected to the power block through the dedicated 24 V power supply unit with built-in output overcurrent protection.
- electromagnets section, connected through a dedicated AC/DC converter to the power block. As the nominal voltage is 24 V, the logic section power supply unit is used as the AC/DC converter for the holding electromagnets as well.

4.5.1.1 Structure of the CHAMBER

The structure of the CHAMBER is composed of a net used to limit the motion of both the CUBE and the FFT during the low-gravity phase. The space available for the experiment is about 2 x 2 m along $X - Y$ directions (see FIGURE 4.3). The CHAMBER contains the two launch systems, facing each other, employed to launch the CUBE and the FFT towards each other. FIGURE 4.17 shows the CHAMBER with the two hold & launch systems and the CubeSats.

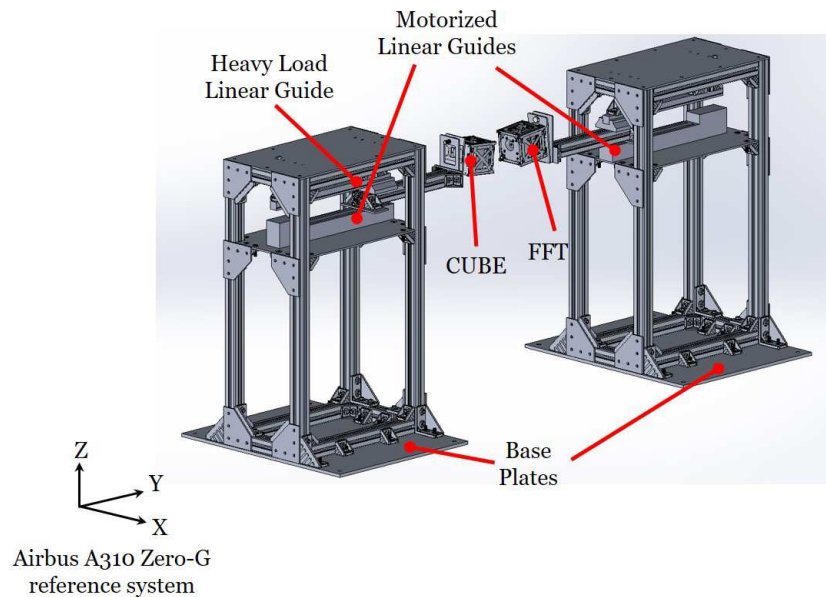


FIGURE 4.17: CHAMBER structure. The CUBE and the FFT will be launched towards each other. The CHAMBER will be surrounded by a net (not showed in the figure).

The CHAMBER is composed by two racks entirely made of Rexroth Bosch items in order to fulfil NoveSpace structural requirements. The launch systems are fixed at two identical rectangular baseplate (695 x 563 x 10 mm in aluminium 6082 alloy): one for the CUBE and one for the FFT hold & launch systems respectively. The baseplates are

used to bolt the experiment to the aircraft rails. The distance between the two base plates is equal to the length of two rails (1006 mm) and they are positioned along the Y-axis of the aircraft, as shown in FIGURE 4.18.

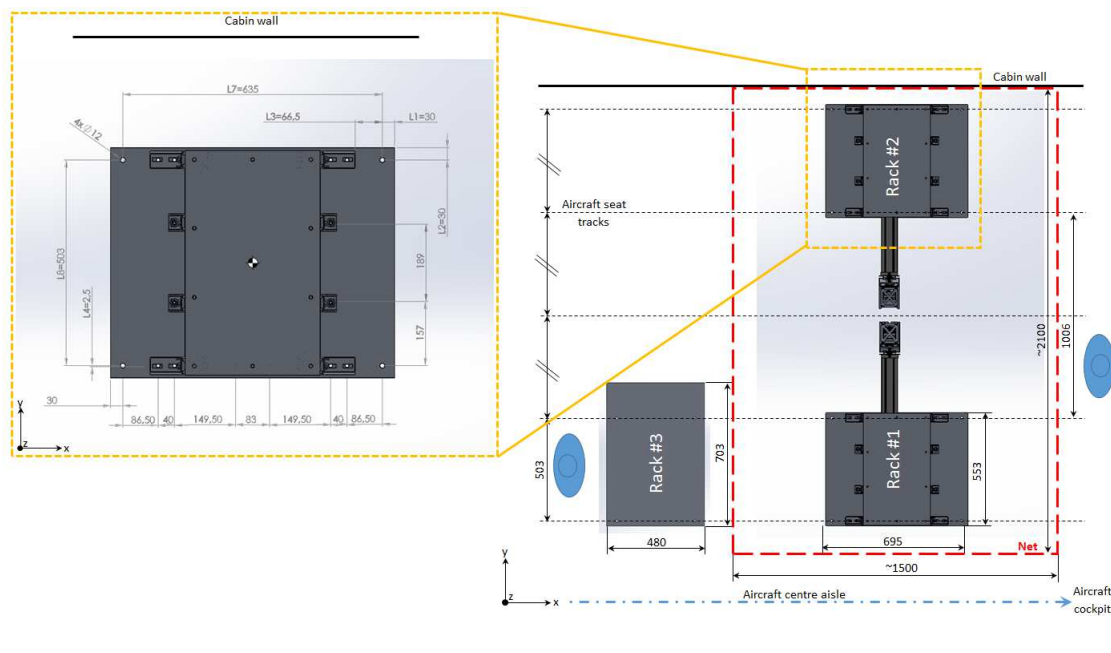


FIGURE 4.18: Top view of cabin layout with the main dimensions (right) and zoom of the baseplate with the distances of the fixing holes highlighted (left). All the measures are in [mm].

On top of each baseplate, four uprights (910 mm along the Z-axis) and twelve horizontal profiles (six of 240 mm along the X-axis and six of 460 mm along the Y-axis), fixed together by brackets, have been used to form the structure of the rack. A 5 mm thick intermediary shelf, with the angles cut to accommodate the profiles, is added to support the linear guide that weights approximately 6 kg. The connection among all the profiles of the structure is guaranteed by the following connecting elements:

- the four uprights and the four bottom horizontal profiles are connected by two 45 x 90 mm and four 45 x 45 mm brackets at each bottom corner;
- other two 45 x 45 mm and one 45 x 90 mm brackets are used to connect the four uprights with the intermediary shelf and the four horizontal profiles;
- finally, two 45 x 45 mm and one 45 x 90 mm brackets are used to connect the four uprights with the last four horizontal profiles.

Gussets are used to reinforce the structure. FIGURE 4.19 shows the rack configuration.

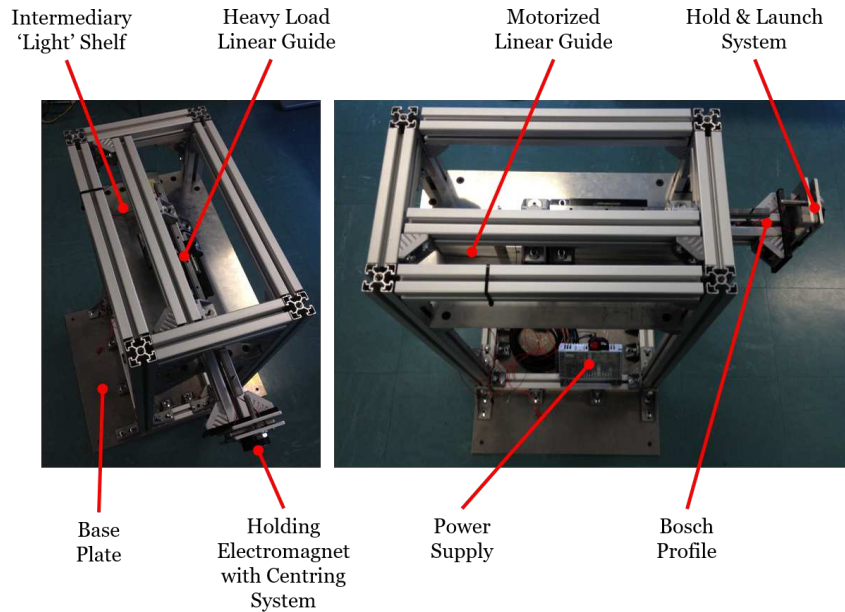


FIGURE 4.19: Photo of the rack structure and its main elements.

4.5.1.2 Hold & launch subsystems

The hold & launch subsystems are used to keep the CUBE and the FFT in position and to provide them with a proper initial velocity immediately after the low-gravity phase is reached.

The hold systems are composed of one small holding electromagnet, while the launch systems features two linear guides, one controlled by a servo-motor and one not motorized. All these assemblies are located inside the racks. The electromagnet is used to hold the CUBE and the FFT in position prior to the low-gravity phases (until the launch). The same system is used during the hyper-gravity phase, allowing an easy and fast repositioning of the CubeSats during the horizontal steady phase before the next parabola. The maximum estimated time to complete the repositioning operation is of 90s. An iron interface mounted at the bottom of the CUBE and the FFT matches the launch plate connected to the Bosch profile, allowing also the regulation of the initial orientation of the two objects. This is useful to test the system in different conditions. The release interface can be oriented during the short (5 min) or long (8 min) pauses among the parabolas. FIGURE 4.20 shows the design and final assembly of the hold systems. The initial orientation of the CubeSats can be varied simply by screwing and unscrewing the orienting screw during a pause to obtain different initial launching conditions. A special control knob is mounted on top of the screw to ease the operation.

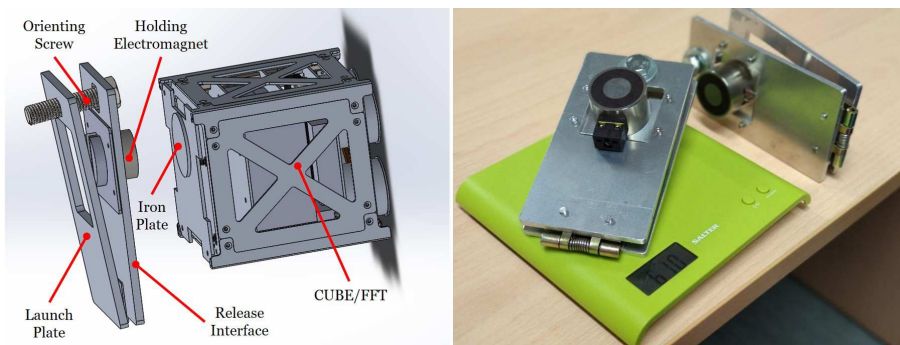


FIGURE 4.20: Hold system design (left) and final assembly (right). The launch plate is directly connected to the Bosch profile on the linear guide, while the release interface can be oriented simply by screwing and unscrewing the orienting screw.

The launch systems are based on a motorized linear guide (FIGURE 4.21) that provides the right initial speed of 2 cm/s to both the CUBE and the FFT and a second linear guide (not motorized) used to decrease the moment and the load acting on the motorized one, as explained in Appendix D.

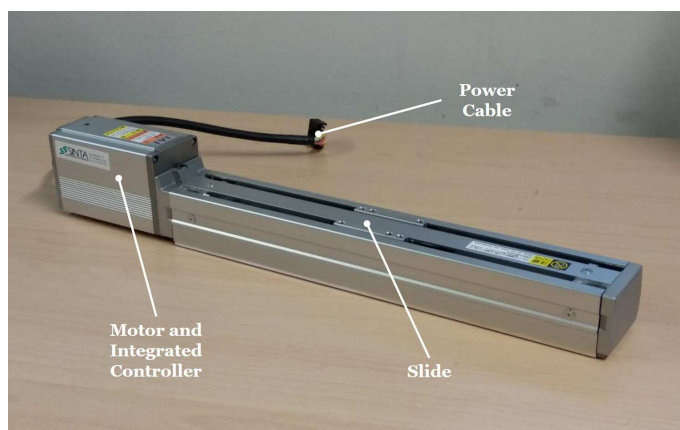


FIGURE 4.21: Linear guide used to launch the CUBE and the FFT during the low-gravity phase.

The speed of the motorized linear guide during the launch phase is tuned via software to transfer the right initial velocity in around 5 – 6 s. It should start at around 4 s after the beginning of the low-gravity phase to be able to release the CubeSats at 10 – 11 s. The initial distance between the two CubeSats (before the launch) is of about 502 mm (top face to top face). At the release (when the CUBE and the FFT detach from the launch plate) the distance should be in a range between 120 and 200 mm depending on the initial velocity. During the retract phase the speed of the linear guide should be of about 4 cm/s. The advantages of adopting a linear guide are:

- its accuracy: the initial velocity is guaranteed also in the presence of external disturbances (this would not have been granted in case of a mechanical spring);
- its regulation: the initial speed can be changed via software, allowing different testing conditions during the parabolic flights;
- its “retrieval” capability: once reached the right speed, the CUBE and the FFT are released and the linear guide can “retract” reducing the chances of collisions between the free-floating objects and the structure.

4.5.1.3 Vision subsystem

A DUO MC stereo-camera is used as the external reference camera to acquire images of the CUBE and the FFT during the floating phase of the experiment. Since the reference camera is not aimed at obtaining information to be used in the control loop of the CUBE, the acquired images will be exploited in post-processing to retrieve the pose of the CUBE with respect to the FFT. The dynamic state obtained through the processing of the external camera is treated as a reference to validate navigation data provided by the sensors aboard the CUBE. An appropriate image analysis algorithm is employed to reconstruct the movement of the CUBE and the FFT. Data collected by the reference camera will be processed and stored by the supporting electronics housed outside the CHAMBER.

The reference camera is powered via the laptop USB port. A monocular system is sufficient to estimate the pose of an object if its geometry is known with respect to an arbitrary reference frame, as it is in PACMAN experiment. Even though a single camera is sufficient to estimate the pose of the free floaters, a stereo-camera can boost the performances of the algorithms thanks to redundant measurements. Moreover, it provides the capability to recover information about the view depth by means of triangulation. The stereo-camera is a DUO MC (FIGURE 4.22): it seems to be the optimal solution since its weight is lower than 6.5 g and it is a very compact system with a wide field of view (170°). The stereo-camera features global shutter and the optical sensors are hardware-synchronized. The positioning of the camera is crucial to satisfy the aforementioned requirements. Given its negligible weight, it is stucked to the ceiling of the aircraft with velcro dual lock.



FIGURE 4.22: DUO MC stereo-camera used as the external reference camera to acquire images of the CUBE and the FFT during the floating phase.

4.5.2 System 2: CUBE

The CUBE represents the real core of PACMAN experiment. It is equipped with an integrated system for proximity navigation and soft-docking based on a set of actively-controlled magnetic actuators that are used to interact with the static magnetic field produced by the FFT. Through this magnetic interaction, the CUBE controls its attitude and relative position with respect to the FFT.

The structure of the CUBE is made of aluminium alloy 7075 and it has the function of keeping all the electronic components in place (FIGURE 4.23).

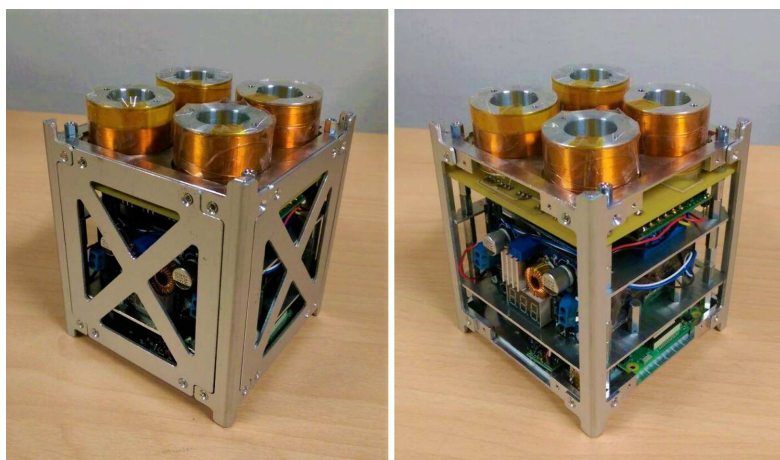


FIGURE 4.23: Photo of the complete CUBE in aluminium (left) and electronic boards stacking (right).

4.5.2.1 Navigation subsystem

The navigation subsystem consists of the magnetic actuators, the camera board and the IMU board.

1. Magnetic actuators

The magnetic coils are used as actuators of the rendezvous/attitude control system (FIGURE 4.24). The set of coils are located at the four corners of the CUBE, to save space for the electronic boards and to maximize the effectiveness (in terms of torque) to perform the attitude control. The coils are composed of a wire wrapped on a structural rod made in aluminium, without a ferromagnetic core since its contribution to the electromagnetic field strength is negligible outside the coil and thus it does not significantly improve the performance of the attitude control. Moreover, the weight of the CUBE without the cores is considerably reduced. Electrical insulation is obtained using enamelled wire, with polymer coatings and a special tape is used to protect the windings.

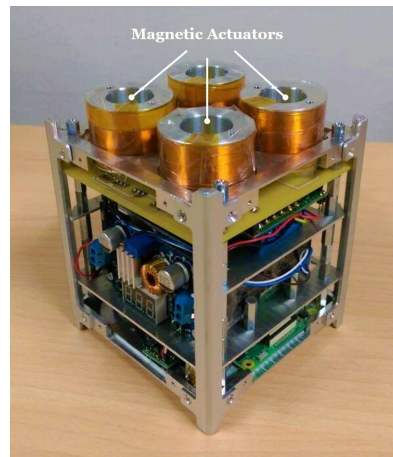


FIGURE 4.24: The CUBE magnetic actuators. The coils are the actuators of the rendezvous/attitude control system.

Dedicated TMP36GZ thermal sensors (FIGURE 4.25) are mounted on the CUBE to monitor the coil status and, if necessary, the software switches off automatically the power circuits to prevent any unexpected additional heating.

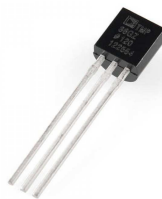


FIGURE 4.25: TMP36GZ thermal sensor used to monitor the coil temperature.

Each coil has 317 turns and is powered with a current of 330 mA. The cross section of the wire is of 0.0429 mm^2 (34 SWG). The internal diameter of the coil is equal

to 36 mm. Each coil has a resistance of $16.6\ \Omega$ and an inductance of 820 mH.

2. Camera board

The camera aboard the CUBE is used for visual relative pose (position/attitude) determination. The camera is the Raspberry Pi NoIR Camera V2 module and is located at the centre of the face of the CUBE with its optical axis oriented along the direction of motion (Y -axes of the aircraft), as shown in 4.26.

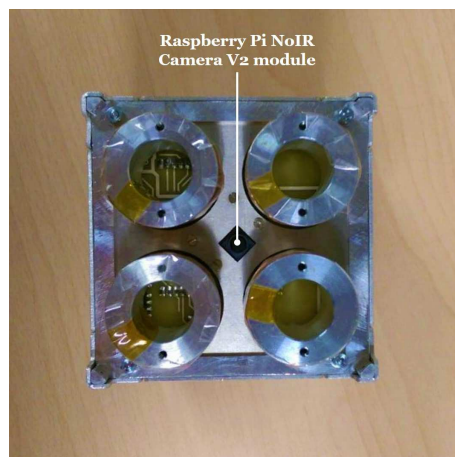


FIGURE 4.26: Raspberry Pi NoIR Camera V2 module. The camera aboard the CUBE is used for visual relative pose (position/attitude) determination.

The computational power available is provided by a Raspberry Pi 3 model B, which is interfaced to the Raspberry Pi NoIR Camera V2 module. The camera is optically calibrated (i.e. intrinsic parameters and optical distortions are known) by means of the calibration method described in [53]. The board is responsible for the image acquisition, the image analysis and the following pose estimation step (see Section 5.2 for further information about the calibration and tests).

3. IMU board

The IMU board (FIGURE 4.27) mounted aboard the CUBE is powered at system start-up and acquires data during all the floating phases with:

- accelerometers to measure the accelerations of the CUBE and to obtain its position through integration;
- gyroscopes to measure angular rates and to ensure the correct behaviour of the magnetic coils;
- magnetometers which collects data about the magnetic fields of the magnetic actuators.

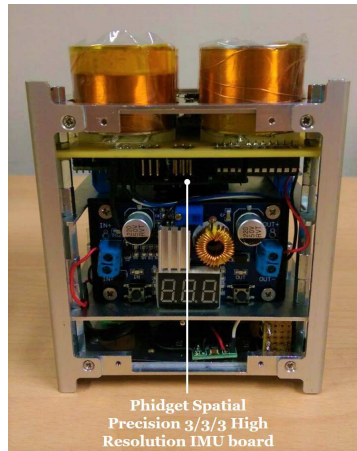


FIGURE 4.27: IMU board. The IMU board is powered at system start-up and acquires data for the whole duration of the floating phase.

The IMU board is the ‘Phidget Spatial Precision 3/3/3 High Resolution’. This board was selected for its really high resolution at nominal conditions:

- Accelerometer
 - Range of ± 2 g
 - Resolution of $76.3 \mu\text{g}$
- Gyroscope
 - Max speed of $\pm 400^\circ/\text{s}$ on x and y -axis and $\pm 300^\circ/\text{s}$ on z -axis
 - Resolution of $0.02^\circ/\text{s}$ on x and y -axis and $0.013^\circ/\text{s}$ on z -axis
- Compass
 - Max Magnetic Field measurable of 5.5 G
 - Resolution of 3 mG

Moreover, it has backup devices with reduced performances that are still able to collect relevant data during the testing phase in case of malfunctions. The complete features of this board are reported in FIGURE 4.28.



Precision Accelerometer	
Acceleration Measurement Max	± 2 g
Acceleration Measurement Resolution	76.3 μ g
Acceleration Bandwidth	497 Hz
Accelerometer White Noise σ	280 μ g
Accelerometer Minimum Drift σ	40.6 μ g
Accelerometer Optimal Averaging Period	396 s

Backup Accelerometer	
Acceleration Measurement Max	± 8 g
Acceleration Measurement Resolution	976.7 μ g
Accelerometer White Noise σ	2.8 mg

Precision Gyroscope	
Gyroscope Speed Max (X-Axis, Y-Axis)	± 400°/s
Gyroscope Speed Max (Z-Axis)	± 300°/s
Gyroscope Resolution (X-Axis, Y-Axis)	0.02°/s
Gyroscope Resolution (Z-Axis)	0.0137°/s
Gyroscope White Noise σ	0.095°/s
Gyroscope Minimum Drift σ	0.0042°/s
Gyroscope Optimal Averaging Period	7743 s

Backup Gyroscope	
Gyroscope Speed Max	± 2000°/s
Gyroscope Resolution	0.07°/s
Gyroscope White Noise σ	0.99°/s

Compass	
Magnetic Field Max	5.5 G
Compass Resolution	3 mG
Compass White Noise σ	1.1 mG
Compass Minimum Drift σ	78 μ G
Compass Optimal Averaging Period	1443 s

Board	
API Object Name	Spabal
Current Consumption Max	55 mA
Sampling Speed Min	1 s/sample
Sampling Speed Max	4 ms/sample
Sampling Speed Min (Webservice)	1 s/sample
Sampling Speed Max (Webservice)	12 ms/sample
Analog to Digital Converter Resolution	16 bit
USB Voltage Min	4.4 V DC
USB Voltage Max	5.3 V DC
USB Speed	Full Speed
Operating Temperature Min	-40 °C
Operating Temperature Max	85 °C

FIGURE 4.28: Phidget Spatial Precision 3/3/3 High Resolution IMU board.

4.5.2.2 Data handling & communication subsystem

The data handling & communication subsystem consists of the microcontroller, wireless and memory boards (FIGURE 4.29).

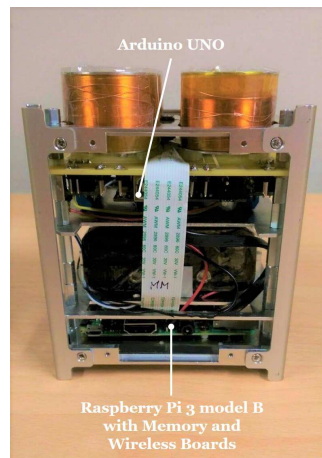


FIGURE 4.29: Data Handling & Communication Subsystem. Raspberry Pi 3 model B is used to manage the video data obtained from the Raspberry Pi NoIR Camera V2 module and process the attitude and position information coming from the IMU board. Arduino UNO uses these pieces of information for the feedback control loop to correctly power the magnetic actuators.

1. Microcontroller board

The microcontroller board is used for control logic, sensor reading and data handling. The selection of the microcontroller board was based on a hardware trade-off among different boards. As a result, two different microcontroller boards are used to collect data and control the CUBE.

Raspberry Pi 3 model B, with its quad core @ 1.2 GHz, is used to (1) manage video

data obtained from the Raspberry Pi NoIR Camera V2 module and process them in real time and (2) collect, store and process the attitude and position information of the CUBE coming from the IMU board.

Arduino UNO (referred as the ‘controller board’ from now on) processes all the data coming from Raspberry Pi 3 model B for the feedback control loop. Other important information like the temperature of the coils to monitor the system status and the coil power consumption and their magnetic fields will be analysed, stored and kept under control during the whole operative phase. The controller board merges the data coming from the sensors aboard the CUBE with the data coming from the camera and run the control algorithm. Data relative to the pose of the CUBE collected from Raspberry Pi 3 model B are sent to the controller board through the serial transmission.

Simulations in Simulink were carried out to test the effective performances of the control algorithm, which is a PID with an anti-windup scheme that allows a faster response to the feedback (FIGURE 4.30).

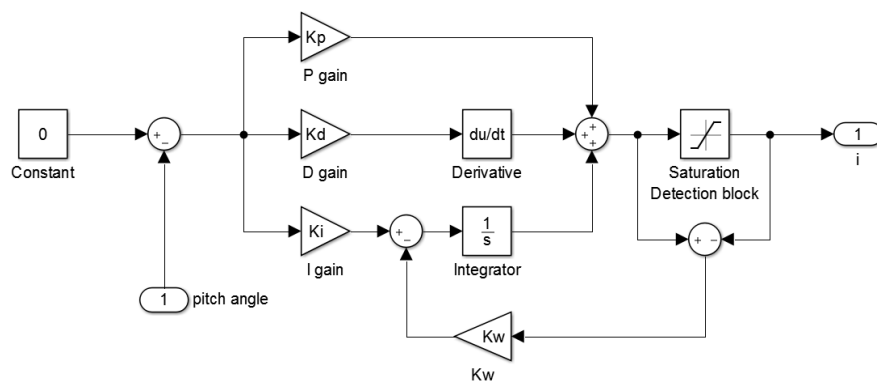


FIGURE 4.30: PID control algorithm. The scheme presents an anti-windup that allows a faster response to the feedback loop. Several constant parameters were tested during the simulations. As a result, the P gain selected is bigger than the D and I gains.

Several constant parameters were tested during the simulations. The results show that a bigger proportional gain than the derivative and the integral gains seems to be the best solution.

Two different PID controls command the pitch and roll angle of the CUBE, powering in pairs the magnetic actuators and summing the resulting control signal on each coil (FIGURE 4.31). This solution allows to control two degrees of freedom with the current configuration. The algorithm was tested during the simulations and it is able to reduce to approximately zero the misalignment of the free-floating CubeSats in ~ 3.5 s.

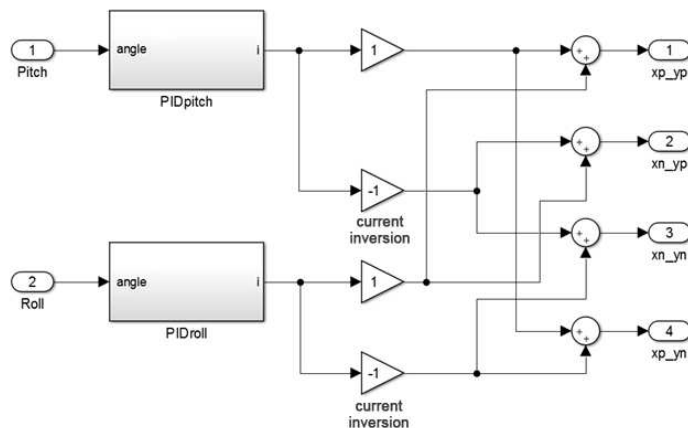


FIGURE 4.31: PID control algorithm and current inversion. Two different PID controls command the pitch and roll angle of the CUBE, powering in pairs the coils and summing the resulting control signal on each coil.

2. Wireless board

Raspberry PI 3 model B has an integrated Wi-Fi antenna that is used for wireless communication between the supporting electronics and the CUBE before testing and during it. Simple check signals will be transmitted from the CUBE to the laptop to check the status of all the components.

3. Memory board

A micro SD card, connected to Raspberry Pi 3 model B, is used to save the data flow from sensors and commands during microgravity tests. The same stream of information are stored in another usb memory used as backup.

4.5.2.3 Power subsystem

The power subsystem consists of the battery pack, the driver circuit and two different buck converters (FIGURE 4.32).

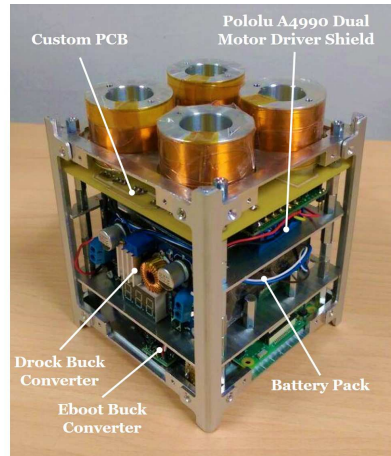


FIGURE 4.32: Power subsystem. Battery pack and buck converters highlighted inside the CUBE with the custom Printed Circuit Board (PCB) and the two Pololu A4990 dual motor drivers.

1. Battery pack

The battery pack is used to provide power to the electronic boards and to the magnetic actuators. The battery pack occupies a large part of the room available inside the CUBE and is composed of 10 cells of Duracell NiMH DX1500H. These batteries were chosen since they can supply the CUBE for the whole duration of the flight and are compliant with the safety requirements of NoveSpace. The complete power consumption of the CUBE is recapped in TABLE 4.11.

TABLE 4.11: Peak power consumption of the CUBE components.

Component	Peak Power Consumption
Arduino UNO	0.65 W
Coil (x4)	1.63 (6.52) W
Pololu A4990 Dual Motor Driver Shield	Negligible
Raspberry PI 3 Model B	1.75 W
Phidget Spatial Precision IMU	0.3 W
Raspberry Pi NoIR Camera V2	0.5 W
Proximity Sensor TCRT1000	Negligible
Temperature Sensor TMP36GZ (x2)	Negligible
Micro SD Card	~ 0.11 W
Usb Memory Card	~ 0.5 W
Drock Buck Converter	Negligible
Eboot Boost Buck Converter	Negligible

Laboratory tests show that up to ~ 20 W (peak power consumption) could be drained from the batteries.

2. Driver circuit

The driver circuit is used to supply the proper current to the magnetic actuators. After laboratory tests, the custom circuit developed for the CUBE and all the previous solutions were discarded in favour of the Pololu A4990 Dual Motor Driver Shield board, since they did not satisfy the performance requirements of PACMAN experiment. However, all the previous solutions can be found in Appendix A. The selected driver circuit can be connected easily to Arduino UNO (FIGURE 4.33).

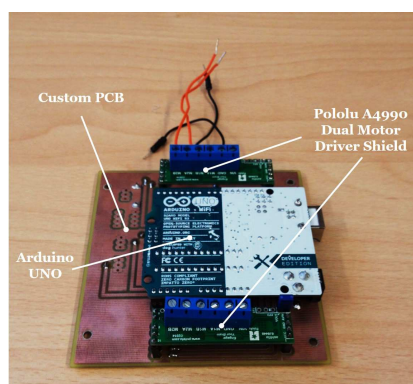


FIGURE 4.33: Driver circuit. Pololu A4990 Dual Motor Driver Shield boards connected to the microcontroller Arduino UNO.

The board is equipped with the IC A4990 which is based on a H-Bridge electric circuit and it operates in the 6 – 32 V range. Each H-Bridge can deliver 0.65 A continuously to the coil and the current on the load can be inverted applying a voltage in opposite direction. These circuits are often used in robotics allowing DC motors to run forwards or backwards. Moreover, the A4990 features a protective control circuit based on a sense resistor that limits the maximum current to 0.9 A (FIGURE 4.34). The sense resistor is used to monitor the current flowing in a circuit by translating the amount of current into a voltage that can be easily monitored and measured, eliminating the risk of short circuits and over current conditions.

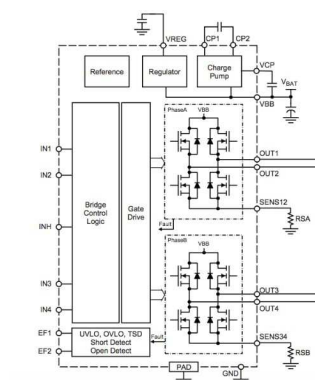


FIGURE 4.34: Schematic of the A4990 Dual Motor Driver Shield board.

The board has two pins for the debug operation (EF1 and EF2), which allows the user to get useful information in case of malfunctions. In addition, the blue jumper located in the corner of the board can be used to supply Arduino UNO (without exceeding the upper limit of Arduino UNO voltage converter that is equal to 12 V). Arduino UNO uses two pins to drive each coil: the first pin carries the Pulse Width Modulation (PWM) signal, while the second one gives information about the direction of the current flowing in the coil (FIGURE 4.35).

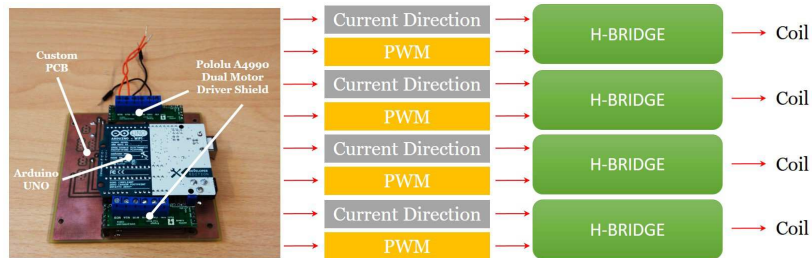


FIGURE 4.35: Block diagram of the driver circuit.

Each board can drive two coils and thus two boards are used in the CUBE. They are assembled on a custom PCB board to be connected on Arduino UNO and save space and wirings. Laboratory tests show that the board can be driven with its own library receiving a PWM signal at ~ 32 kHz. The high frequency was selected to have a limited current ripple when powering the coils and thus supplying the drivers with a current as stable as possible. Two different buck converters are used in the CUBE, since the devices used have different power supplies. The purpose of the Drock buck converter is to lower the voltage from 11.6 V to 7 V, in order to correctly power the Pololu A4990 Dual Motor Driver Shield boards and Arduino UNO. The Eboot buck converter, instead, is used to power the Raspberry Pi 3 model B with a different voltage of 5.1 V. FIGURE 4.36 shows the schematic and the block diagram of the electrical connection of the whole CUBE.

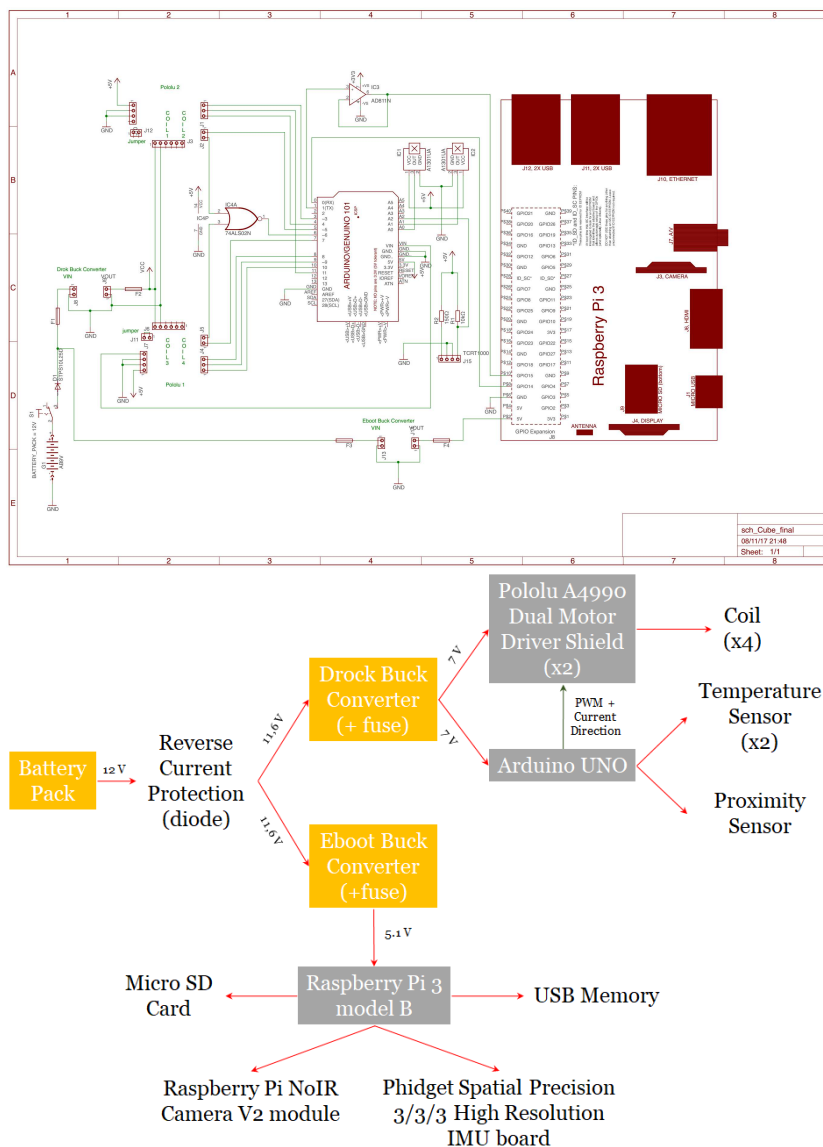


FIGURE 4.36: Schematic (top) and block diagram (bottom) of the electrical connection of the CUBE. The battery pack supplies both the Drock buck and the Eboot buck converters. The Drock buck converter lower the voltage to 7 V to supply the Pololu A4990 Dual Motor Driver Shield boards and Arduino UNO while the Eboot buck converter gives 5.1 V in input to the Raspberry Pi model B. The power supply to all the other devices is directly managed by the microcontrollers boards.

4.5.2.4 Hold & launch system interface

The hold & launch system interface is composed of an iron plate modelled precisely to hold the CUBE during the hyper-gravity phase and to release it easily during the low-gravity phase. The electromagnet mounted on the hold & launch plate of the hold & launch system matches precisely, thanks to a centring system, the small iron plate mounted at the bottom of the CUBE (FIGURE 4.37).

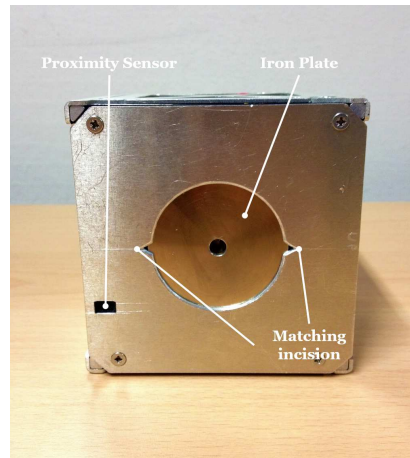


FIGURE 4.37: Hold & launch system interface. The small iron plate at the centre of the bottom face of the CUBE matches connect precisely to the holding electromagnet. The small incisions are used to align correctly the CubeSat after the recovery. The proximity sensor is used to trigger the data acquisition

The magnetic field of the electromagnet interacts with the plate generating an electromagnetic force which holds the CUBE in position during the pre-test operations. During the low-gravity phase, after the linear guide reaches the right initial velocity, the electromagnet is switched off and the CUBE continues its motion towards the FFT. The proximity sensor mounted at the bottom of the CUBE triggers the data acquisition.

4.5.3 System 3: FFT

The FFT represents the other crucial module of PACMAN experiment. It is equipped with an active single magnetic actuator (the docking interface of the FFT) that produces a static magnetic field that can interact with the set of actively-controlled magnetic actuators of the CUBE. Through this magnetic interaction, the CUBE controls its attitude and relative position with respect to the FFT and performs the soft-docking manoeuvre. The structure and the hold & launch interface of the FFT are the same used for the CUBE. The structure is made of aluminium alloy 7075 and it has the function of keeping all the electronic components in place (see FIGURE 4.23 in the previous section). FIGURE 4.38 shows a photo of the FFT.

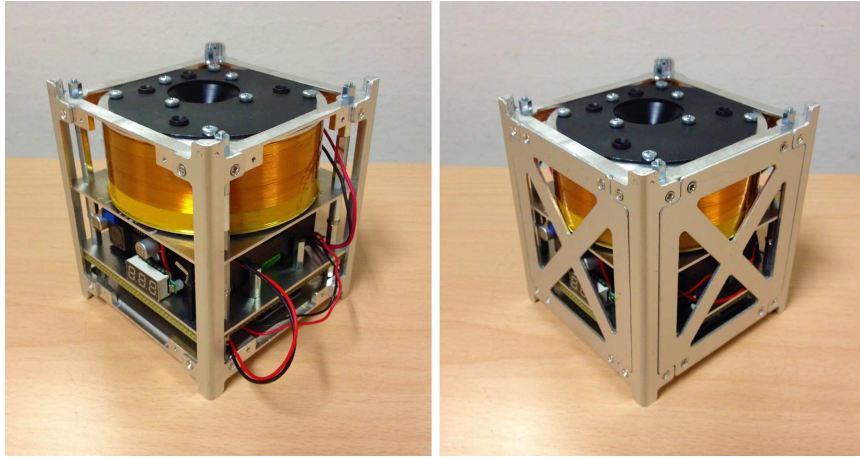


FIGURE 4.38: Photo of the FFT. The mechanical structure of the CubeSat is the same used for the CUBE. An Arduino UNO is used as microcontroller to power the coil properly through the driver circuit.

4.5.3.1 Docking interface

The docking interface is composed of a wire wrapped on a structural rod made in aluminium, without a ferromagnetic core. Electrical insulation is obtained using enamelled wire, with polymer coatings and a special tape is used to protect the windings. A dedicated thermal sensor (see FIGURE 4.25) is mounted on the FFT to monitor the coil status and, if necessary, the software switch off automatically the power circuits to prevent any unexpected additional heating. The docking interface has 375 turns and is powered with a current of 1.2 A. The cross section of the wire is of 0.164 mm^2 (26 SWG). The internal diameter of the coil is of 91 mm (FIGURE 4.39).

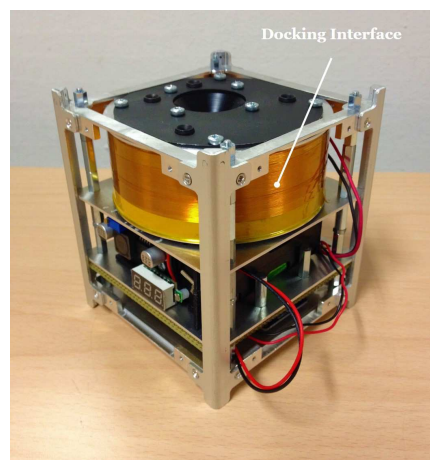


FIGURE 4.39: Docking interface. The coil of the target is wrapped around the aluminium structural rod and powered by the driver circuit.

The docking interface of the FFT is equipped with five OSRAM SFH 487 P (FIGURE 4.40) IR LED: they are characterized by a peak emission at 880 nm and a wide angle of view (half angle: 65°). The LEDs are mounted on suitable holders to ensure the correct positioning and to ease their detection by the Raspberry Pi NoIR Camera V2 module aboard the CUBE.



FIGURE 4.40: OSRAM SFH 487 P LED.

Four LEDs are positioned on the surface of the docking interface (i.e. they are located on the same geometrical plane) while one is placed in a different plane, 1 cm inside the coil. This particular position of the five LEDs facilitates their detection by the Raspberry Pi NoIR Camera V2 module aboard the CUBE and increases the accuracy of the CUBE angular estimation (see FIGURE 4.41 and Section 5.2 for more details).

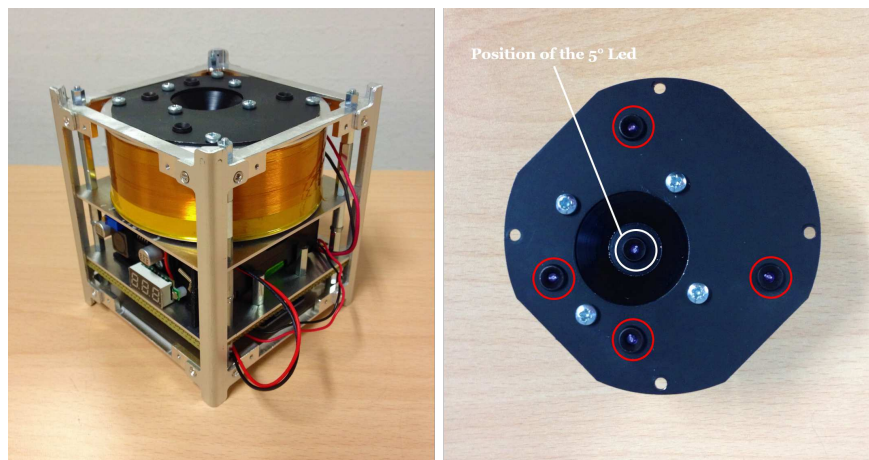


FIGURE 4.41: Position of the five LEDs on the docking interface. Four LEDs are positioned on the surface (red circle) while the fifth one is on a different plane.

4.5.3.2 Microcontroller board

Arduino UNO is used as the microcontroller board to power correctly the docking interface (FIGURE 4.42) through the Boost buck converter. The microcontroller board selection was based on a hardware trade-off among different boards. Arduino UNO represented the best compromise between performances and power consumption.

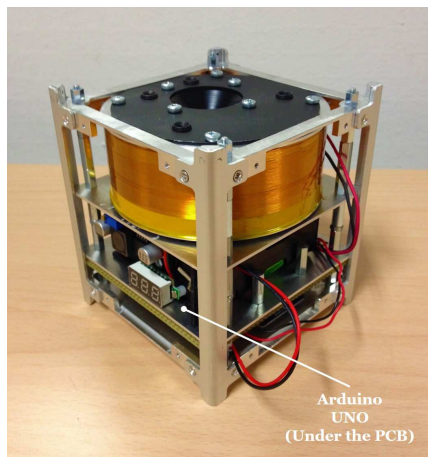


FIGURE 4.42: Microcontroller board. Arduino UNO is used as the microcontroller board of the FFT to power correctly both the docking interface (through the Boost buck converter) and the IMU. A micro SD card is used to store all the data.

The microcontroller board drives the current in the docking interface and monitors its temperature to keep the system status under control during the whole operative phase. The “SparkFun 9 Degrees of Freedom - Sensor Stick” IMU board is mounted aboard the FFT to obtain further information about the entire systems dynamics (FIGURE 4.43). All the data collected are stored into a micro SD card connected to the microcontroller board and are used in post-processing to better analyse the soft-docking manoeuvre.

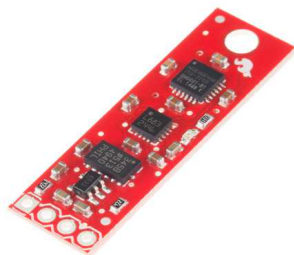


FIGURE 4.43: SparkFun 9 Degrees of Freedom - Sensor Stick IMU board powered at system start-up.

4.5.3.3 Power subsystem

The power subsystem consists of the battery pack and two buck converters (FIGURE 4.44).

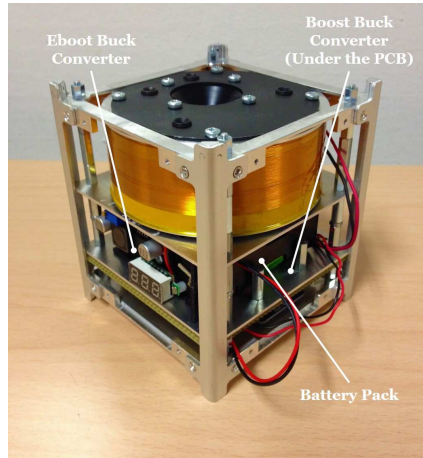


FIGURE 4.44: The power subsystem of the FFT is composed of two different buck converters and the battery pack.

1. Battery pack

The battery pack provides power to the whole FFT. The battery pack is made with 10 cells of Duracell NiMH DX1500H batteries and is the same used in the CUBE.

The complete power consumption of the FFT is recapped in TABLE 4.12.

TABLE 4.12: Peak power consumption of the FFT components.

Component	Peak Power Consumption
Arduino UNO	0.65 W
Coil	14.4 W
Boost Buck Converter	Negligible
Eboot Buck Converter	Negligible
Proximity Sensor	Negligible
IMU SparkFun 9 Degrees of Freedom - Sensor Stick	0.025 W
Temperature Sensor (x2)	Negligible
OSRAM SFH 487 P LEDs (x5)	0.03 (0.15) W
Micro SD Card	~ 0.65 W

2. Buck converters

Two different buck converters are used in the FFT, to power separately Arduino UNO and the coil. The Eboot buck converter is used to power Arduino UNO with 5.1 V. The power supply to the temperature sensors, the proximity sensor, the micro SD card and the IMU is directly managed by the microcontroller board.

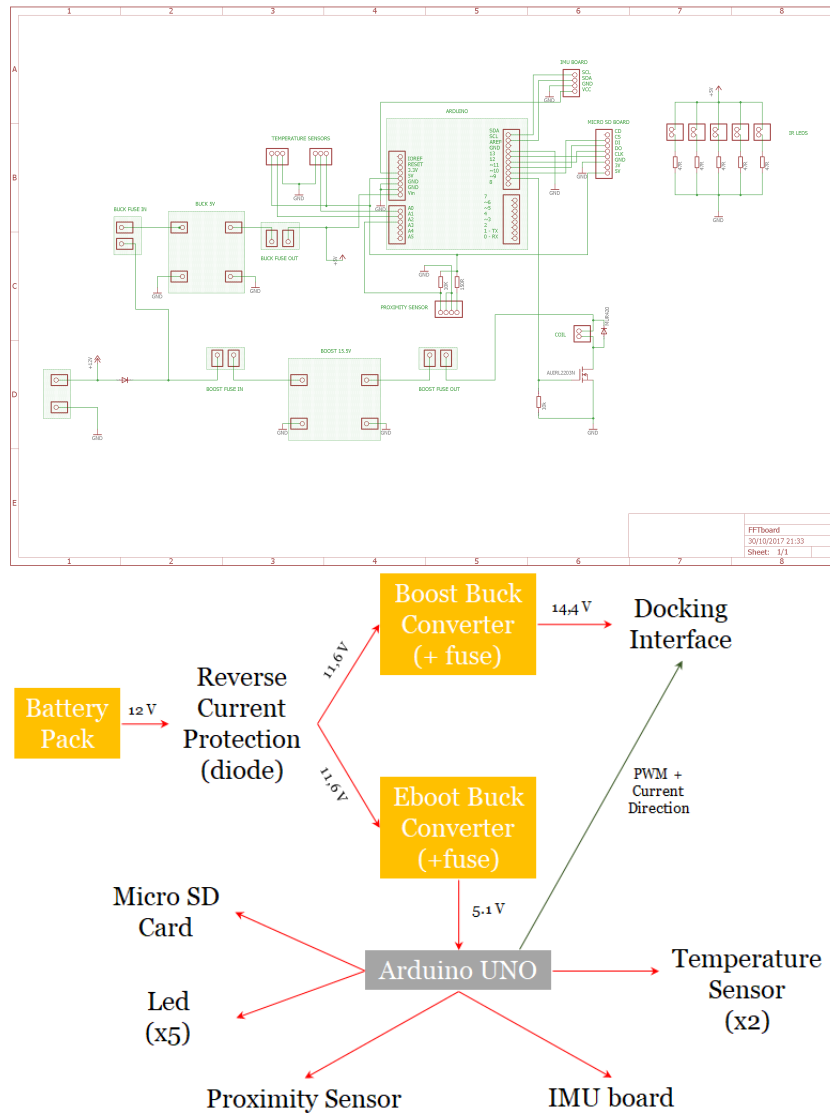


FIGURE 4.45: Block diagram of the electrical connection of the FFT. The battery pack supplies both the Eboot buck and the Boost buck converters. The Eboot buck converter lower the voltage to 5 V to supply Arduino UNO and the LEDs while the Boost buck converter gives 14.4 V in input to the docking interface.

The Eboot buck converter is also responsible of powering the five LEDs on the docking interface. The purpose of the Boost buck converter, instead, is to higher the voltage coming from the battery pack to power the coil at 14.4 V. FIGURE 4.45 shows the schematic and the complete block diagram of the electrical connection of the FFT.

4.5.4 Supporting electronics

Supporting electronics is needed to command the linear guides and the hold & launch interfaces and to ensure wireless communication with the CUBE and FFT for initialization commands and basic system status telemetry. The laptop is used to process the data about the motion of the CUBE acquired by the external stereo-camera DUO MC and the information regarding the vibrations of the entire structure collected by the IMU attached to the CHAMBER.

Chapter 5

Ground Tests

This chapter aims at presenting the ground tests performed in the laboratory during PACMAN design phase. These tests were of utmost importance since the obtained results were used as a baseline to understand the limits of the proposed technology and the feasibility of the experiment. Moreover, the results of the studies were essential to verify the outcomes obtained from the implemented dynamic model and to proceed correctly with the experiment design to develop the best flight configuration.

5.1 Validation of PACMAN dynamic model: coil test

The whole PACMAN experiment was based on the results obtained from a dynamic model implemented in Matlab-Simulink environment. In the model, the mass characterization of the system, the initial velocities, positions and orientations of the CUBE and the FFT and the geometrical and electrical characterization of the coils were used as inputs. The mutual magnetic interactions between the free-floating objects were then calculated as outputs and used to determine the system dynamics. The forces, torques, velocities, positions and attitude of both the CUBE and the FFT were evaluated, as well as the coil current. The information collected from the simulations, along with the provided data about the g-jittering and the aircraft motion, was used to drive the experiment design towards the best flight configuration.

5.1.1 Methodology

The tests aim at presenting the coil tests performed in the laboratory. Since the dynamic model of the whole PACMAN experiment was based on the near-field magnetic model

(see Section 4.4 for more details), these tests were mandatory to understand its accuracy. The main issue connected to the experiment setup was due to the low magnetic field intensity produced by the coils and thus the small forces exerted in their mutual interaction.

After the evaluation of several different experimental setups, the final adopted solution involved a very precise balance (with an accuracy equal to 0.0001 g) normally used to weight special glues.

A calibration process was performed before each measurement, following these steps:

- 1) level the balance using the levelling feet, so that the air bubble is centred within the circle of the level indicator;
- 2) warm up the balance for at least 30 minutes after turning it on;
- 3) wait for the automatic self-test of the balance electronic circuitry;
- 4) reset the weight display;
- 5) calibrate the balance with the built-in weight;
- 6) perform the measurement.

5.1.2 Experimental setup

Figure 5.1 shows the used experimental setup. Two coils have been used for these tests: one was positioned over the balance while the other was hung up right over the first one, fixed to a structure made with Bosch profiles. The coils were built with a special device to obtain a precise and uniform number of windings (90). A weight variation was measured each time the coils were powered (with a current of 1.5 A) as a consequence of the mutual repellent force between the two coils. The measurements were then compared with the data obtained from the model developed in Matlab[®].

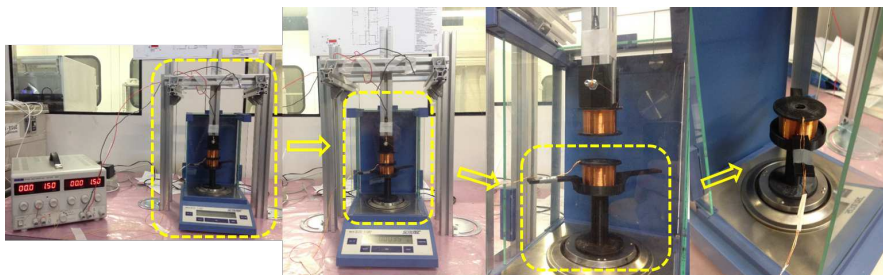


FIGURE 5.1: Experimental setup. The repellent force between the two coils is measured as a weight variation.

5.1.3 Experimental results

FIGURE 5.2 shows a comparison between the experimental results obtained in laboratory conditions and the data obtained from the model implemented in Matlab[®].

The distance (in mm) between the two coils is represented on the X -axis. The force (in mN) due to the mutual interaction of the electromagnetic fields of the coils is shown on the Y -axis (left); the error (in %) between the results obtained from the measures and those from the model is also shown on the Y -axis (right).

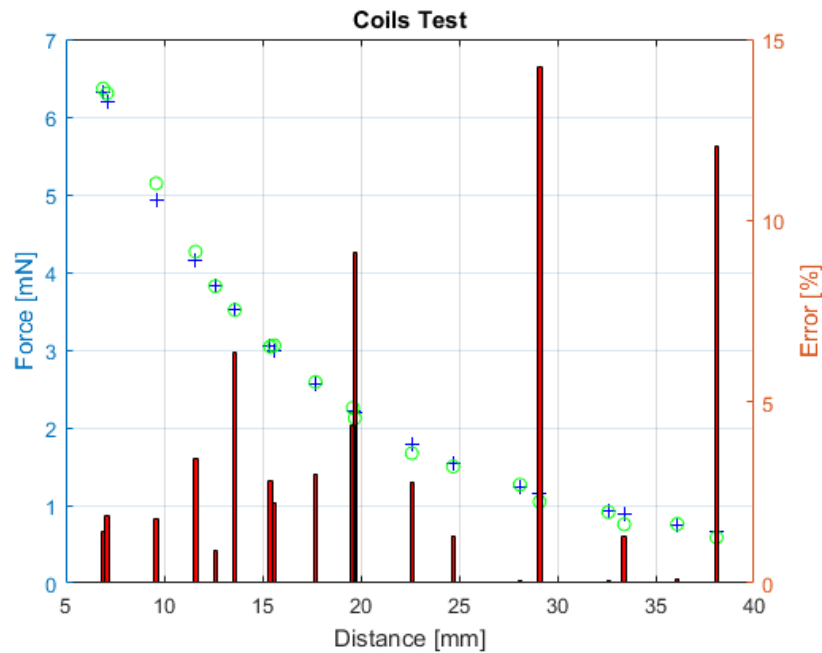


FIGURE 5.2: Comparison between the experimental results obtained in laboratory conditions and the data obtained from the model. The green circles represent the measured force (in mN), while the blue cross represent the force obtained from the model (in mN) as a function of the distances (in mm) between the two coils. The red bars represent the relative percentage error.

As it can be seen from the graph, there was a good correlation between the experimental results obtained in the laboratory (green circles) and the data obtained from the model (blue crosses). The maximum error recorded was of 14.22 % and was probably due to a slightly misalignment between the coils. The validation of the model was essential to be confident of the experimental design with the two free-floating modules.

5.2 CUBE camera test

The vision subsystem aboard the CUBE is responsible, together with the IMU board, for the relative navigation of the CUBE.

This test aims at assessing the real performances of the camera aboard the CUBE and to understand the resolution of the device. To achieve this objective an experimental setup was used to impose translational and rotational displacements to the target mock-up with an uncertainty at least one order of magnitude lower than the one associated to the vision system.

5.2.1 Methodology

The available computational power is provided by a Raspberry Pi 3 Model B board, which was interfaced to the Raspberry Pi NoIR Camera V2 module. The camera was optically calibrated (i.e. intrinsic parameters and optical distortions were known) by means of the calibration method described in [53]. The board was responsible for the image acquisition, the image analysis and the following pose estimation steps. Since the image processing time increases as the number of features in the image plane increases, the following strategy was adopted to boost the performances of the vision subsystem (i.e. reducing the processing time): (a) the exposure time of the sensor was reduced, (b) the FFT was equipped with IR LEDs and (c) through a thresholding operation the image was converted into a binary image. By properly tuning the threshold level, the LEDs on the target could be easily identified as the only features visible in the binary image (FIGURE 5.3).

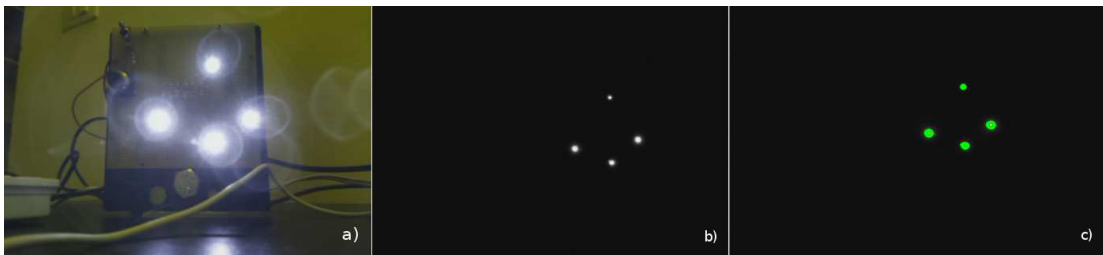


FIGURE 5.3: a) Image of target mock-up equipped with four IR LEDs, b) image of the pattern acquired with a reduced exposure time, c) relevant features identified in the image.

The first step of the measurement procedure was to identify the projections ${}^C\mathbf{x}_i$ in camera frame C of each 3D feature point ${}^T\mathbf{X}_i$ located on the observed target surface. The 3D point coordinates were initially known with respect to the target fixed reference frame T . Once the 2D and the 3D points were correctly associated, the relative position

and orientation between the camera and the target could be retrieved by solving the perspective-three-point (P3P) problem. The pose estimation was performed by means of the solver proposed by Kneip et al. [54], which provides a closed-form solution to the problem. The P3P solver uses as input three 3D points ${}^T\mathbf{X}_i$ and their corresponding 2D projections ${}^C\mathbf{x}_i$, ($i = 1 \dots 3$). The method provides as output four rotation matrices ${}^T_C\mathbf{R}_j$ that transform coordinates from the target frame T to the camera frame C , and four position vectors ${}^C\mathbf{t}_{T,j}$, ($j = 1 \dots 4$) of the target frame expressed in the camera frame. By means of the four calculated rotations ${}^T_C\mathbf{R}_j$ and translations ${}^C\mathbf{t}_{T,j}$, the fourth point was back-projected to the image plane:

$${}^C\mathbf{X}_{4,j} = [{}^CX_{4,j}, {}^CY_{4,j}, {}^CZ_{4,j}]^T = {}^T_C\mathbf{R}_j^T \mathbf{X}_4 + {}^C\mathbf{t}_{T,j} \quad (5.1)$$

$${}^C\bar{\mathbf{x}}_{4,j} = \left[\frac{{}^CX_{4,j}}{{}^CZ_{4,j}}, \frac{{}^CY_{4,j}}{{}^CZ_{4,j}}, 1 \right]^T. \quad (5.2)$$

The correct rotation matrix ${}^T_C\mathbf{R}$ and translation ${}^C\mathbf{t}_T$ were selected among the four pairs such that the projected fourth point ${}^C\bar{\mathbf{x}}_{4,j}$ was the closest in the image plane to the measured fourth point ${}^C\mathbf{x}_4$.

5.2.2 Experimental setup

To assess the measurement performances of the vision subsystem, the target mock-up was mounted on two high precision motorized linear stages and a rotary stage as shown in FIGURE 5.4.

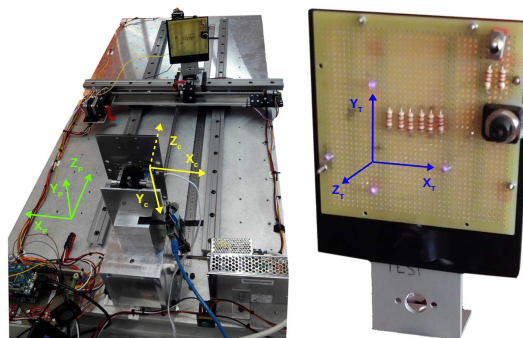


FIGURE 5.4: Experimental setup. High precision motorized linear stages and rotary stage (left), target mock-up equipped with four IR LEDs (right). The reference systems of the experimental setup (green), the camera (yellow) and the target mock-up (blue) are highlighted.

The linear stages were driven by stepper motors with a resolution of 0.005 mm/step and they allowed imposing planar displacements to the target mock-up, while the rotary stage was equipped with a graduated scale, allowing rotations around the normal to the operative plane.

The imposed displacement profile is shown in FIGURE 5.5, where the translations were referred to the plane fixed reference frame P .

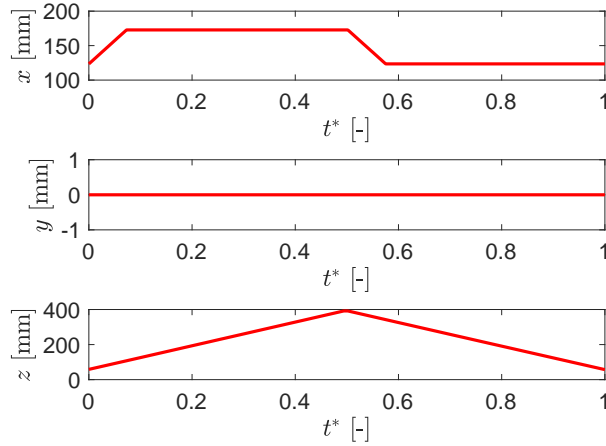


FIGURE 5.5: Imposed target trajectory referred to the plane reference frame P . The linear stages were used to impose planar displacements (along x and z -axis) to the target mock-up; y -axis corresponds to the displacement orthogonal to the plane.

From an operational point of view, the imposed displacements were defined at software level, while the target attitude was imposed before the manoeuvre began and it was kept fixed for all the test duration.

The camera, which was kept in a fixed position, acquired images at a resolution of 1280x960 pixels with a field of view of 62.2 x 48.8°. The pose of the target could be measured by means of the vision subsystem and then compared to the imposed motion. Two main aspects must be considered to compare the two sets of measurements:

- 1) since the acquisition systems were not synchronized, the translation profile was referred to a dimensionless time t^* , expressed as a fraction of the whole manoeuvre time (i.e.: $t^* = t/t_f$, $0 \leq t^* \leq 1$);
- 2) the measured displacements provided by the camera and the motorized stages were referred respectively to the camera C and the plane P reference frames: thus, to refer all the displacements to the C frame, the rotation matrix ${}^C_P R$ that transforms vectors from P to C was estimated in post-processing as the result of the following optimization problem:

$${}^C_P R = \underset{\mathbf{R}}{\operatorname{argmin}} \left(\sum_k \left\| {}^C \mathbf{t}_{meas,k} - \mathbf{R}^P \mathbf{t}_{imposed,k} \right\| \right). \quad (5.3)$$

5.2.3 Experimental results

FIGURE 5.6 shows the error computed by the comparison between the imposed target trajectory and the reconstructed one obtained from the image analysis algorithm. The maximum error is limited to a range of about ± 3.5 mm, ± 1 mm and ± 5 mm along the x , y and z -axis respectively.

FIGURE 5.7 shows the attitude, in terms of Euler angles, measured by means of the camera (in red), and the mean value of the angles (black dashed lines). The estimation of yaw (ψ) angle is more accurate than the measured roll (ϕ) and pitch (θ) angles, that present a noisy behaviour. TABLE 5.1 summarizes the mean values of the attitude angles and their standard deviation for the considered manoeuvre.

TABLE 5.1: Mean values (μ) and standard deviation (σ) of the measured attitude angles.

	μ [deg]	σ [deg]
Roll (ϕ)	2.79	4.61
Pitch (θ)	0.04	2.69
Yaw (ψ)	-1.26	0.29

As it can be seen in FIGURE 5.6 and FIGURE 5.7, the measurements show some anomalous peaks that are probably due to small vibrations of the linear stages during the movement of the target mock-up.

Overall, the proposed measurement algorithm proved to be capable of performing real-time pose estimation. The obtained results highlight that further improvements are required to boost the metrologic performances of the system: in particular, by exploiting a larger number of IR LEDs, the P3P algorithm can be embedded in a RANSAC scheme [55] allowing the refinement of the pose estimation by rejecting outliers and false matchings. This last solution has been implemented in the final configuration of the FFT, in which there are five LEDs: four are placed on the surface of the docking interface while the fifth one is placed on a lower level. This latter position of the fifth LED should improve the metrologic performances of the system reducing the errors in the estimations of both the position and the attitude (See FIGURE 4.41 in Chapter 4.5.3).

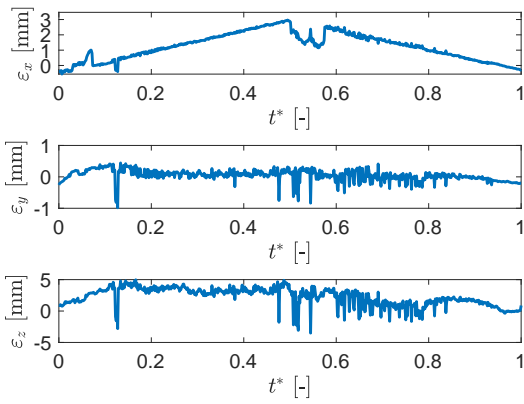


FIGURE 5.6: Error obtained by the comparison between the real target trajectory and the reconstructed one.

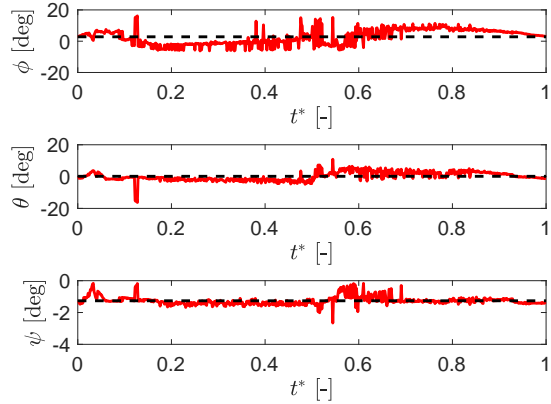


FIGURE 5.7: Euler angles measured with the camera (red) and their mean value (black dashed line). The results are obtained by image processing.

5.3 Temperature tests

Temperature tests were performed to estimate the temperature variation during the low-gravity phase for both the CUBE and the FFT. The tests were carried out to verify the compliance with NoveSpace safety requirement [56] that states "during normal operations, experimenters shall not be exposed to ... continuous skin contact with surfaces above 49 °C or below 4 °C." Therefore, particular attention was made in monitoring the coils temperature to control that the overall temperature of the CubeSats was kept under the limits.

The temperature test aims at (1) evaluating the temperature variation on the CubeSats coils during the simulated operative profile and at (2) verifying that the temperature of the structures do not exceed the maximum allowable temperature of 49 °C.

The coils temperature has been monitored assuming a real operative profile during the parabolic flight. During each parabola of the PFC, the operative phases are divided as showed in Table 5.2.

TABLE 5.2: Duration of the different phases of a parabola during a PCF.

Phase	Duration [s]
Hyper-gravity	20
Transition	3 – 5
Low-gravity	20
Transition	3 – 5
Hyper-gravity	20
Normal gravity	110

The coil of the FFT and the coils in the CUBE were switched on only for the duration of the low-gravity phase (20 s, maximum duration of the operative phase, worst case) and were switched off during all the other phases (the CubeSats were in IDLE mode, with the coils unpowered). Therefore, to simulate the operative phase during each parabola, a cycle of 20 s of activity and 150 s of inactivity was considered. This cycle was repeated for 30 parabolas without taking into consideration the pauses.

Thermal sensors were positioned directly in contact with the CubeSats structure and the coils to evaluate both the external and the inner module temperatures. The thermal sensors used during the test (TMP36GZ, the same selected to be used in the CUBE and FFT during the PFC) were positioned in two significant positions to analyse the temperature distribution on the CubeSats

5.3.1 Testing conditions and experimental setup for the CUBE

FIGURE 5.8 shows the experimental setup used for the CUBE. The external Arduino UNO was used to impose the cycle and it was directly connected to the laptop to acquire the temperature values in real time.

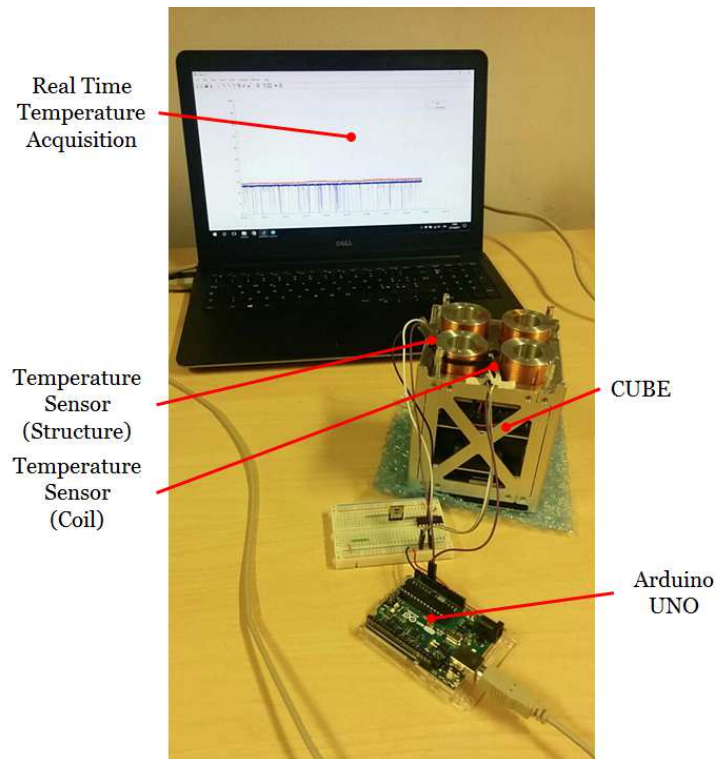


FIGURE 5.8: CUBE temperature test. Two thermal sensors were used, one connected to the CubeSat structure and another one directly in contact with a coil.

FIGURES 5.9 and 5.10 present the results of the test: the temperature of the CUBE coil does not exceed 32.5°C and the overall temperature of the module does not exceed 29.5°C (the room temperature was $\sim 25.5^{\circ}\text{C}$).

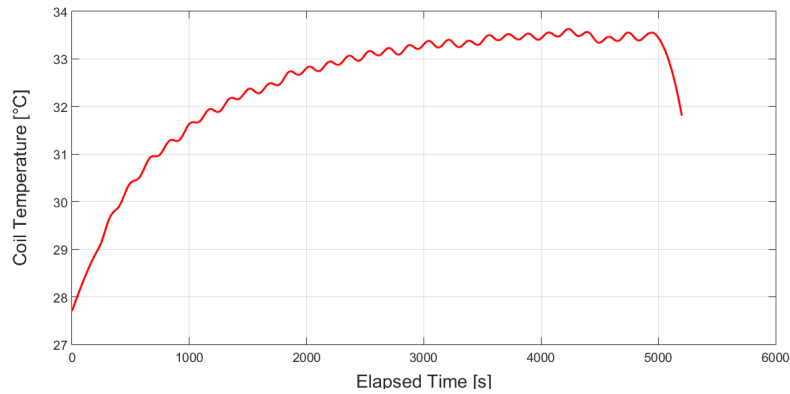


FIGURE 5.9: CUBE coil temperature trend during the test considering a possible real-mission profile.

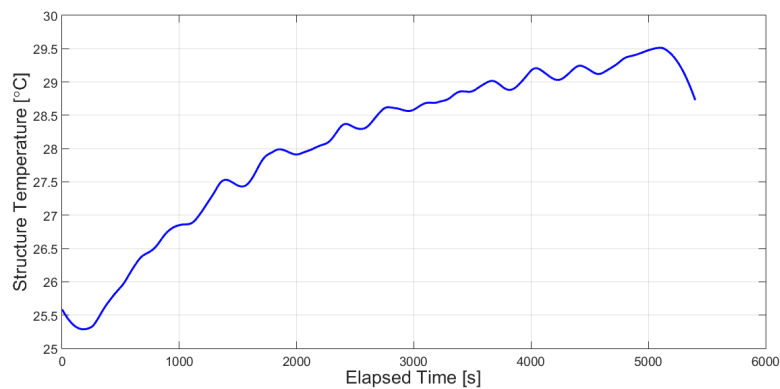


FIGURE 5.10: CUBE structure temperature trend during the test considering a possible real-mission profile.

5.3.2 Testing conditions and experimental setup for the FFT

FIGURE 5.11 shows the experimental setup used for the FFT, that is the same used for the CUBE.

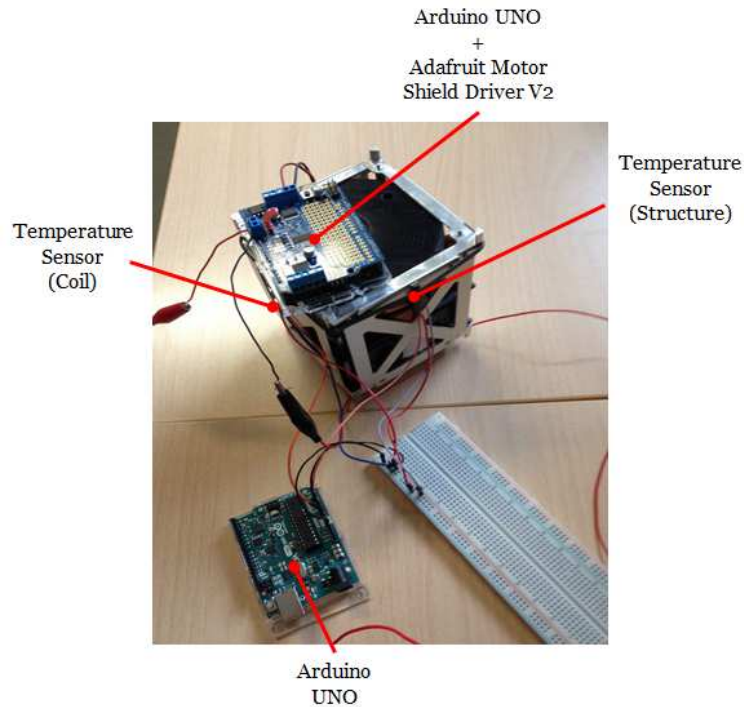


FIGURE 5.11: Position of the temperature sensors on the FFT. Arduino UNO with the Adafruit Motor Shield Driver V2 (over the CubeSat docking interface) is used to power the coil while the other one (next to the breadboard) imposes the cycle.

FIGURES 5.12 and 5.13 present the results of the test: the temperature of the FFT coil does not exceed 34°C and the overall temperature of the module does not exceed 27°C (the room temperature was $\sim 24^{\circ}\text{C}$).

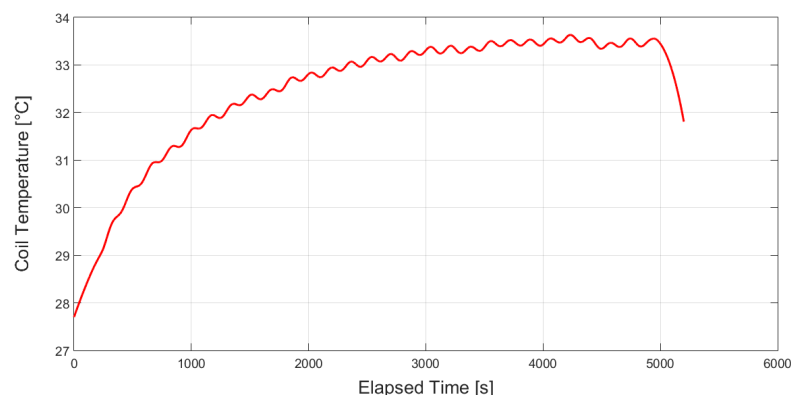


FIGURE 5.12: FFT coil temperature trend during the test considering a possible real-mission profile.

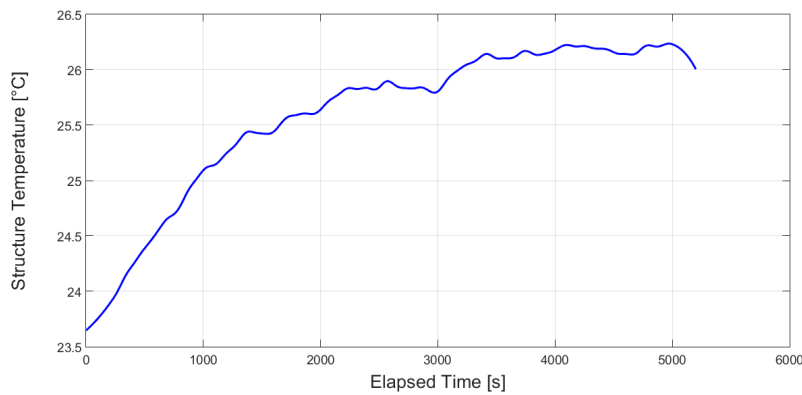


FIGURE 5.13: FFT structure temperature trend during the test considering a possible real-mission profile.

The experiment shows that, even if the CubeSats coils are powered for the complete low-gravity phase (worst case), the temperatures of both the modules and the coils would not exceed the allowable limit of 49 °C.

5.4 CUBE driver circuit test

The driver circuit is used to supply the proper current to the magnetic coils of the CUBE. This test aims at assessing the performance of the selected driver, the Pololu A4990 Dual Motor Driver Shield board, connected to the microcontroller Arduino UNO.

5.4.1 Experimental setup

The experimental setup used to carry out the tests was composed of:

- a CUBE's coil (resistive component of $15\ \Omega$ and an inductive component of 2.6 mH) and a resistance ($3,3\ \Omega$) in series. The resistance was used only to evaluate the voltage drop across it through the use of two probes. Thanks to the voltage measurements, it was possible to obtain the current trend: in fact, the current had the same trend of the voltage and its magnitude could be obtained just by dividing the voltage values by the resistance. The small value of the resistance was chosen not to modify excessively the time constant of the load and alter the results;
- a stabilized power supply with an input voltage of 7 V connected to the driver circuit. Arduino UNO was powered by the driver circuit through the blue jumper and no other power sources were used (see Section 4.5.2.3);

- two probes used to evaluate the voltage drop across the resistance. The three extremities of the probe were connected to a) one channel of the oscilloscope, b) the ground of the circuit and c) one extremity of the load;
- an oscilloscope used to monitor the voltage trend and record the measurements;

5.4.2 Experimental results

FIGURE 5.14 shows the voltage drop across the resistance with a PWM duty cycle equal to 100%. The yellow line represents the first channel of the oscilloscope, while the blue line represents the second one. The red line represents the difference between the two measurements and thus the voltage drop (960 mV) across the resistance. The current has the same trend of the voltage and its magnitude (~ 300 mA) can be obtained just by dividing the voltage values by the resistance.

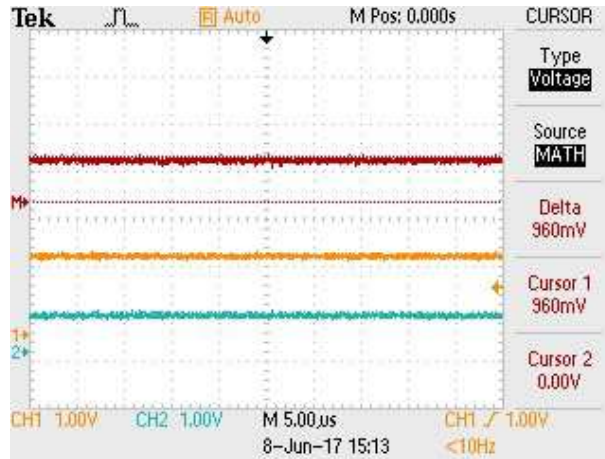


FIGURE 5.14: Voltage drop across the resistance with a PWM duty cycle equal to 100%. The yellow line represents the first channel of the oscilloscope, while the blue line represents the second one. The red line represents the difference between the two measurements and thus the voltage drop (960 mV) across the resistance.

As expected, when the duty cycle of the PWM is at 100%, the H-bridge delivers to the coil 300 mA, which is the maximum current flowing into the coil, in compliance with the coil design. The value of the current is stable since the observed ripple is negligible. Other tests were carried out to verify the performances of the driver with different duty cycles. The results prove that the Pololu A4990 Dual Motor Driver Shield board was the right choice for PACMAN experiment, since it fulfilled the requirements.

5.5 Static load test for the hold system

The hold system is composed of one small holding electromagnet that is used to hold the CUBE and the FFT in position prior to the low-gravity phases (until the launches). The same system is used to hold the CubeSats during the hyper-gravity phase, allowing an easy and fast repositioning of the modules during the horizontal steady phase before the following parabola.

The hold system was subjected to various modification during the design phase of PAC-MAN experiment. Here, the two main solutions that were developed and tested are presented. The second one was employed as the final configuration of the hold system.

5.5.1 “Plug ‘n’ play” interface

The “plug ‘n’ play” release interface was composed of an interface mounted at the bottom of the CUBE and the FFT designed to match precisely the launch plate connected directly to the linear guide. The interface was a small plate that could be replaced during the short (5 min) or long (8 min) pauses among the parabolas. FIGURE 5.15 shows how the plate connects to the CUBE or the FFT and match the launch plate connected to the linear guide of the hold & launch system.

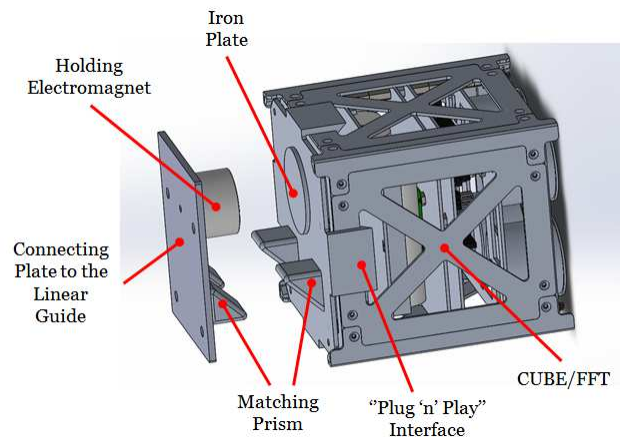


FIGURE 5.15: “Plug ‘n’ play” interface and launch plate. The “plug ‘n’ play” interface could be replaced during the long pause after the first 15 parabolas. Different orientations of the matching prisms would have allowed different initial orientations of the CUBE/FFT. The launch plate housed the holding electromagnet used to support the weight of the CUBE/FFT during the hyper-gravity phases.

The initial orientation of the CubeSats could be varied simply substituting the “plug ‘n’ play” interface during a pause. Different interfaces would be built with several inclinations of the matching prisms and the iron plate to obtain different initial launching conditions. The interface could be connected to the CubeSats without using any tools.

Static load tests were made to estimate whether the “plug ‘n’ play” interface was able to sustain 8 kg, that was 4 times the weight expected for the CubeSats. The electromagnet was able to bear a load of 8.8 kg. The prisms on the “plug ‘n’ play” interface were used to lower the action of the shear forces on the electromagnet. The gripping surfaces of the matching prisms would have assured a partial absorption of the load on the electromagnet during the hyper-gravity phase. The initial right position of the CubeSats was guaranteed by both the matching prisms (that were in contact with each other) and the holding electromagnet (that would be precisely centred with the iron plate on the “plug ‘n’ play” interface).

5.5.2 Orienting release interface

The release interface selected for the final configuration of PACMAN experiment is described in Chapter 4.5.1.2.

Static load tests (FIGURE 5.16) were made to estimate whether the release interface with the holding electromagnet was able to sustain 8 kg. The electromagnet, stronger than the previous one, was able to bear a load of 8 kg without any additional support.

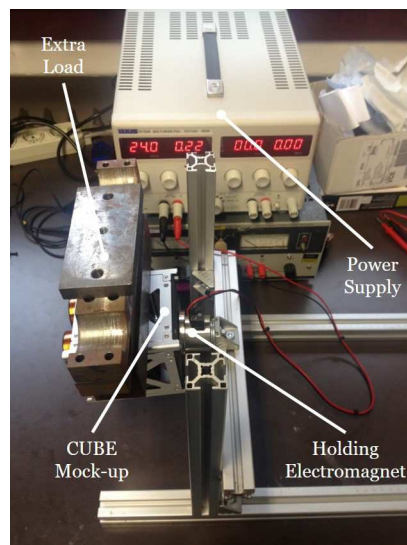


FIGURE 5.16: Holding electromagnet of the release interface. The electromagnet is able to bear a load of 8 kg.

Chapter 6

PACMAN Parabolic Flight Procedures

This Chapter briefly presents the procedures foreseen during each parabola of the parabolic flight campaign. The detailed list of the procedures can be found in Appendix E.

The initial conditions during the launch of both the CUBE and the FFT vary considerably due to the relevant disturbances on board the aircraft and the randomness of the parabolas. For these reasons, it is possible to state that there is not a real “nominal” condition to perform the tests: each parabola has different unexpected disturbances that influence the motion of the two free-floating objects.

Considering these disturbances, it is possible to assume that each test during each parabola is unique and therefore only minor modification to the hold & launch systems will be done during each flight, since the randomness of the disturbances represent itself a change about the initial launch conditions.

Taking into account this essential characteristic of the parabolic flights, two main parameters can be changed in order to obtain even more interesting results: the initial velocity and the orientation of both the CUBE and the FFT. The initial velocity of the two free-floating objects can be varied via software by adjusting the initial velocity of the linear guide while the orientation can be modified acting on the release interface used to connect the CUBE and the FFT to the hold & launch systems. Both these solutions do not include a modification of the CHAMBER structure, that is kept fixed for all the three parabolic flights. The adverse conditions of each parabola is exploited in order to understand the technology limits and the extension of the sphere of influence of the magnetic fields (i.e. the maximum distance between the CUBE and the FFT at which the effectiveness of the magnetic fields is sufficient to perform the docking manoeuvre).

6.1 Procedures during the parabolas

The whole proposed flight experimental procedure is reported in FIGURE 6.2 with the operations planned during each parabolas.

Five main phases can be identified during each parabola, with the first one performed only at the beginning of the flight:

- A) INITIALIZATION. It occurs at the beginning of the flight (only once per flight). The whole PACMAN experiment is initialized: the laptop, CUBE and FFT are powered on and set to idle mode. The microcontrollers are initialized and the camera aboard the CUBE checked. The external stereo-camera is switched on, the alignment of the hold & launch systems checked.
- B) INJECTION. As soon as the low-gravity phase is reached, a timer switches the CUBE and the FFT to the operative mode in order to start the autonomous operations. No operations nor measurements will be performed during the hyper-gravity phases.
- C) AUTONOMOUS OPERATIONS (See FIGURE 6.1). This represent the core of the experiment. The CUBE and the FFT are launched one towards the other at a velocity of few cm/s. The expected launch time is around 11 s (during the low-gravity phase - second part of each parabola) and performed using a timer. The linear guide reaches the correct release velocity exactly in that moment. Once the CUBE and the FFT are released, the linear guides retract restoring their initial position, to be ready for the next parabola. The camera aboard the CUBE is used to measure the relative pose between the CUBE and the FFT; the measurements from the IMU are used to gather information regarding the initial conditions and accelerations. The microcontroller board merges the information coming from both these sensors and uses them to drive the power to the magnetic actuators. The soft-docking manoeuvre is performed in ~ 4 s during the low-gravity phase and it represents the free-floating phase. The IMU connected to the rack together with the external stereo-camera are used to record the disturbances of the aircraft and the CUBE motion for post processing, respectively.

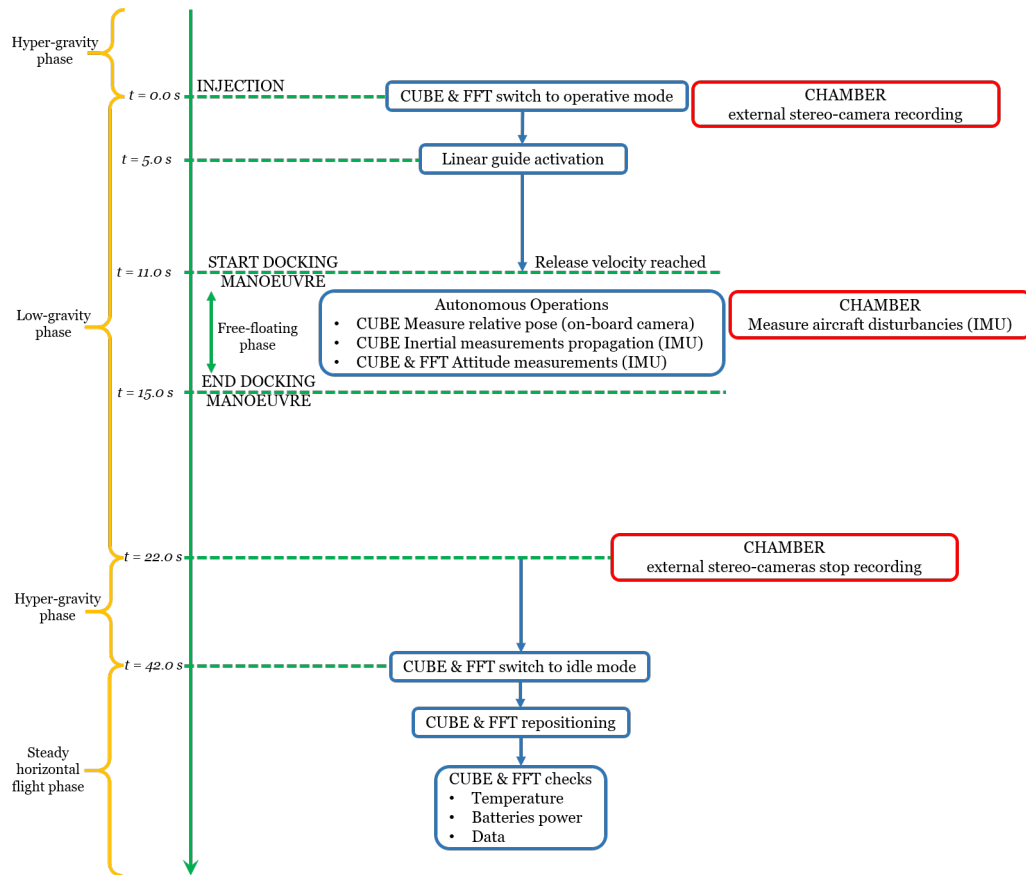


FIGURE 6.1: Launch sequence during the 20s of low-gravity phase. The time sequence is not in scale. The blue rounded cells report the CUBE & FFT operations during the parabola. The free-floating phase starts at 11s after the injection when the launch velocity is reached and lasts ~ 4 s. The red rounded cells report the main operations executed with the CHAMBER's sensors.

- D) END DOCKING MANOEUVRE. The CUBE and the FFT status is checked after the accomplishment of the soft-docking manoeuvre: coils temperature, batteries power and measurement/data stored.
- E) STEADY FLIGHT. This represents the last phase before the next parabola. CUBE and FFT are on the foam in the netted area. An experimenter recovers the two modules or brings them from outside. Both the CUBE and the FFT are then positioned again on the release interface connected to the hold & launch systems. The iron plate on the bottom face of both the CUBE and the FFT matches the holding electromagnet connected to the release interface. The magnetic force produced by the holding electromagnet is enough to keep the two modules in position, locked. The CubeSats status is checked. PACMAN is ready for the next parabola. During the long (8 min) or short (5 min) pauses the inclination of the release interface connected to the hold & launch systems can be changed in order to vary the initial orientation of both the CUBE and the FFT.

X30 PARABOLAS

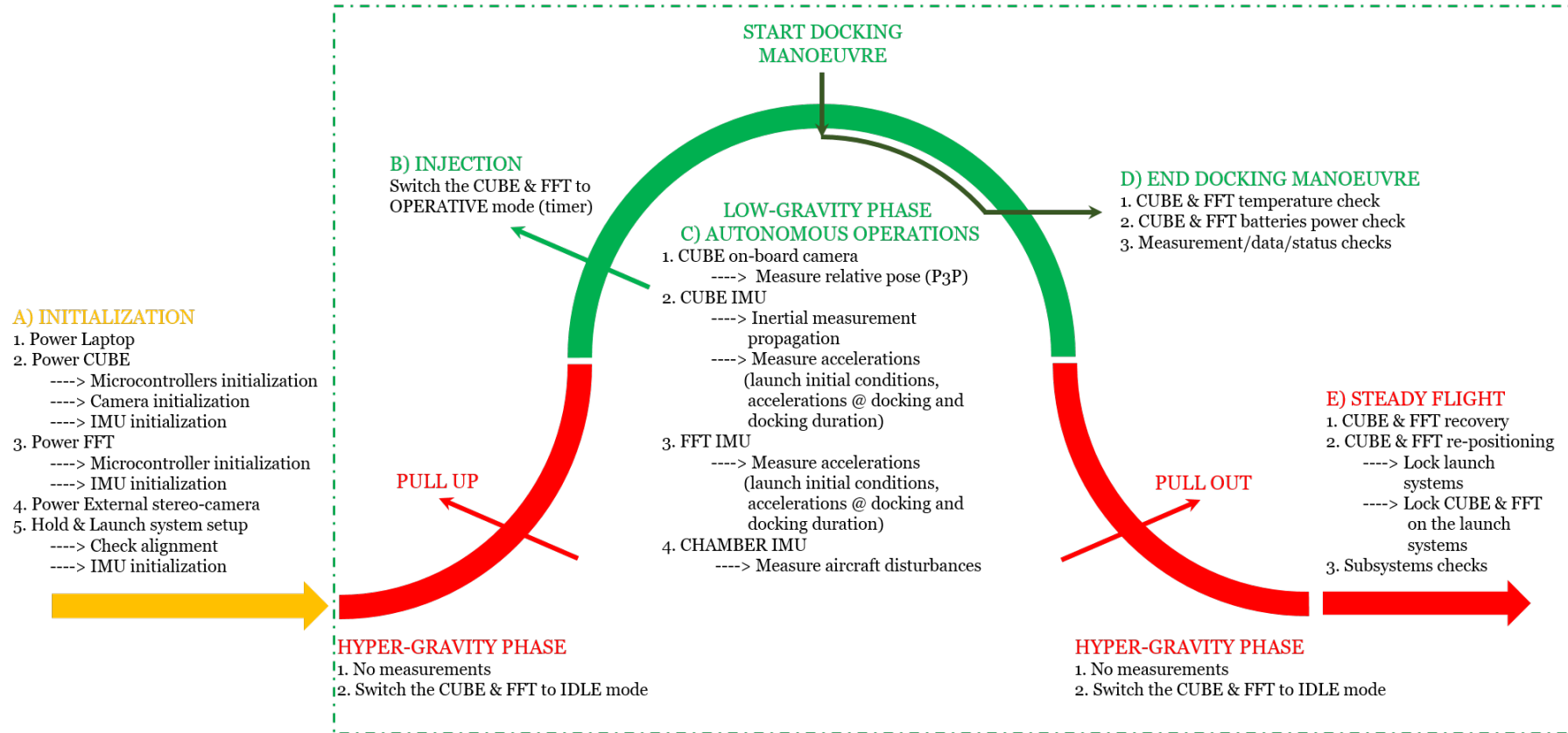


FIGURE 6.2: Experimental procedure during each parabolic flight.

PART 2

TED

(Tethered Electromagnetic Docking)

Chapter 7

TED: Tethered Electromagnetic Docking

Automatic systems to make viable the connection of two or more satellites in space are recently gaining importance for several future applications, most of which related to on-orbit servicing. Currently, spacecraft joinings can be performed with autonomous chaser satellites that accurately fly around targets up to docking, or with the aid of robotic arms that place the two spacecraft in contact with each other. In the first case (docking), the chaser must be capable of very high Guidance, Navigation and Control (GNC) accuracy to reach its target within specific relative position and velocity requirements. Very precise sensors are required to monitor the satellite relative motion during this phase, while a high propellant consumption is necessary due to the multiple correction manoeuvres. In the second case (berthing), a dedicated platform is needed to host the robot and significant complexity is related to the robotic arm configuration and control, to safely manage unexpected situations and transmitted loads.

Currently, the mating procedure between a chaser and a target vehicle can be accomplished as following: while during the phasing and far-range rendezvous phases the chaser reaches the target orbit and reduces the relative distance to few hundreds of meters, in the final approach phase (close-range rendezvous) it reaches the target with well defined position and velocity conditions to achieve docking or berthing. Usually, very precise sensors (with an accuracy of about 1% of the range or better [25]) are used to monitor the satellites relative motion during this phase, as the approach should be operated within strict safety boundaries. This leads to remarkable propellant consumption, due to the multiple correction manoeuvres the chaser should perform to satisfy such constraint.

As of today, mating procedures have been extensively proven for large autonomous and manned spacecraft, but automatic docking for small satellites has not been effectively demonstrated yet, apart from the on-orbit tests on the ISS during the MIT SPHERES

program. The research in this field is focusing on the enabling technologies (from miniaturized docking mechanisms [57, 58] to navigation sensors [39] and strategies [59]) and only subsystem tests have been performed in the relevant environment, due to the complexity and the number of constraints of such operations.

In such context, this chapter presents a novel docking concept, where a tethered electromagnetic probe is ejected by the chaser toward a receiving electromagnetic interface mounted on the target spacecraft, comparing it to traditional docking approaches and proposing it as an alternative solution. The generated magnetic field drives the probe to the target and realizes an automatic alignment between the two interfaces, thus reducing control requirements for close approach manoeuvres as well as fuel consumption. After that, the “hard” docking is accomplished by retracting the tether and bringing the two spacecraft in contact. Controlled rewind should be also exploited to damp the two spacecraft relative motion and stabilize the whole system. This approach would allow also to perform the docking manoeuvre with a non-cooperative target spacecraft [60].

A preliminary simplified simulation of the tethered docking procedure, reproducing a real scenario and the mutual interactions between the chaser and the target during the manoeuvre, is presented as an alternative solution to traditional docking approaches. The two docking interfaces of the spacecraft are modelled as magnetic dipoles, which are subjected to mutual interactions in a 3D environment, and the two body dynamics are described in terms of spacecraft position and attitude.

The results underlines the possible advantages of performing the new close-range rendezvous and docking procedure.

7.1 Reference system and model

Referring to FIGURE 7.1, the study has been conducted considering a local reference system fixed on the target satellite, having the x -axis in the direction of the target velocity $V - bar$, the z -axis pointing to the centre of the Earth $R - bar$, and the y -axis in the direction of the orbital angular momentum vector H to complete the coordinates system.

The following simplifying hypotheses were assumed in the proposed model:

- the target and the chaser are on the same orbital plane xz , and the relative motion is limited to this plane;
- the satellite attitude does not influence the thrusters performance and the guidance strategy;
- the target orbit and the initial chaser orbit are circular;

- the distance between the target and the chaser is negligible with respect to the orbit radius;
- the target is placed in the origin of the xyz reference system.
- the chaser initial position is in the orbit radius direction (R -bar approach) or in the velocity vector direction (V -bar approach).

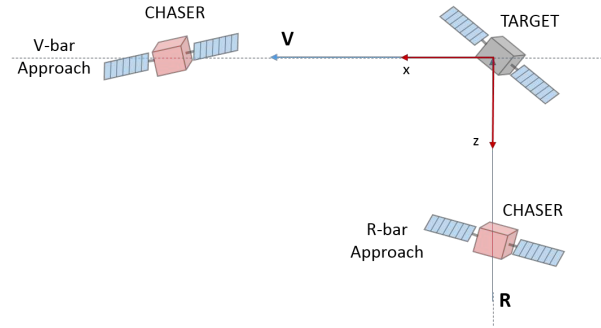


FIGURE 7.1: Geometrical reference system and the two study cases, R -bar and V -bar approaches.

Under these considerations, it is possible to use the Hill equations [61] to calculate the relative motion of the chaser with respect to the target

$$\begin{cases} \ddot{x} - 2\omega\dot{z} = a_x \\ \ddot{y} + 2\omega^2\dot{y} = a_y \\ \ddot{z} + 2\omega\dot{x} - 3\omega^2z = a_z \end{cases} \quad (7.1)$$

with \mathbf{a} the acceleration vector imposed to the chaser and ω the angular frequency of the circular target orbit. It is important to notice that, under the aforementioned hypotheses, the out-of-plane motion and the xz in-plane motion are independent, simplifying therefore the study.

From the system of differential equations 7.1, the time-variant solution known as Clohessy-Wiltshire (CW) equations 7.2 was derived [61] and expressed in vector notation as

$$\begin{cases} \mathbf{r}(t) = [\Phi_{rr}]\mathbf{r}_0 + [\Phi_{rv}]\mathbf{v}_0 \\ \mathbf{v}(t) = [\Phi_{vr}]\mathbf{r}_0 + [\Phi_{vv}]\mathbf{v}_0 \end{cases} \quad (7.2)$$

where $\mathbf{r}(t)$ and $\mathbf{v}(t)$ are the position and the velocity of the chaser respectively, and \mathbf{r}_0 and \mathbf{v}_0 the initial conditions (i.e. after an impulsive manoeuvre $\Delta\mathbf{V}_0$: $\mathbf{v}_0 = \mathbf{v}_0^- + \Delta\mathbf{V}_0$). $[\Phi_{rr}]$, $[\Phi_{rv}]$, $[\Phi_{vr}]$, $[\Phi_{vv}]$ are time dependent non-linear matrices, that are functions of

the orbital frequency ω . Their formulation can be found in Appendix C.

For the *V – bar* approach the chaser relative position and velocity required before any impulsive manoeuvre are reported in equation 7.3.

$$\begin{cases} \mathbf{r}_0 &= (x_0 \ 0 \ 0) \\ \mathbf{v}_{0-} &= (0 \ 0 \ 0) \end{cases} \quad (7.3)$$

Similarly, for the *R – bar* approach, the relative position is reported in equation 7.4

$$\mathbf{r}_0 = (0 \ 0 \ z_0) \quad (7.4)$$

Since the chaser is on a lower orbit (considering $z_0 > 0$, see FIGURE 7.1), its velocity calculation (higher than the target one) is more complicated. The complete procedure to calculate v_{0-} is reported in Appendix C. The final result is given by

$$\mathbf{v}_{0-} = \left(\frac{3}{2} \omega z_0 \ 0 \ 0 \right) \quad (7.5)$$

7.2 Rendezvous manoeuvres description

The close-range rendezvous phase is usually performed using path planning algorithms; by far, the most known one is the glideslope [62–64] algorithm, which is similar to an hybrid between a path-planning and a velocity-control algorithm.

In order to understand the glideslope working principle and constraints, an introduction of simpler transfer manoeuvre is reported in the following sections: a description of the Hohmann transfers (for *R – bar* approaches) and phasing manoeuvres (*V – bar* rendezvous) is followed by a brief description of continuous thrust manoeuvres. Finally, the glideslope algorithm is presented.

The constraints on the close-range rendezvous process are due to safety concerns and reliable range of measurements; as previously mentioned, an approach on the line-of-sight is required (i.e. the navigation path should lie in an approach corridor), avoiding dangerous trajectories in proximity of the target. Furthermore, it is important to consider also the limitations of the approach velocities due to safety concerns, which can affect the proximity manoeuvres.

7.2.1 Hohmann transfer as reference for the *R-bar* approach

The Hohmann transfer is the simplest in-plane two-impulses orbital manoeuvre between two spacecraft in circular or elliptical orbits. The resulting transfer orbit after the application of a Hohmann transfer has the shape of a semi-ellipse, with the apsides on the original (chaser) and final (target) orbits. To a first approximation, the velocity budget required for the two impulses [25] is given by

$$\Delta V_{1,H} = \Delta V_{2,H} = \frac{1}{4} \omega z_0 \rightarrow \Delta V_H = \frac{1}{2} \omega z_0 \quad (7.6)$$

The transfer time is equal to half of the Hohmann transfer orbit period computed as

$$t_H = \frac{1}{2} T_H = \frac{\pi}{\omega} \quad (7.7)$$

It is worth to point out that the use of the impulse $\Delta V_{1,H}$ to inject the chaser into the transfer orbit affects also the motion on the *V-bar* direction: the drift Δx_H of the spacecraft can be calculated with the CW equations as

$$\Delta x_H = \frac{3}{4} \omega z_0 \quad (7.8)$$

Therefore, the presence of the drift Δx_H forces to execute the manoeuvre from an initial position $\mathbf{r}'_0 = \begin{pmatrix} -\frac{3}{4}\omega z_0 & 0 & z_0 \end{pmatrix}$ different from the needed $\mathbf{r}_0 = \begin{pmatrix} 0 & 0 & z_0 \end{pmatrix}$ to reach the target, as visible in FIGURE 7.2 (blue solid line). Therefore, the manoeuvre does not lie exactly in the *R-bar*, making the navigation measurements more complicated. Furthermore, the chaser reaches the target with a relevant approach velocity V_{t_H} , as calculated with the CW equation 7.9

$$V_{t_H} = \frac{1}{4} \omega z_0 = \Delta V_{2,H} \quad (7.9)$$

For these reasons, the Hohmann transfer is usually not employed in close-range rendezvous manoeuvres. However, due to its simple formulation, the value of Hohmann velocity budget $\Delta V_H = \frac{1}{2} \omega z_0$ is used in this composition as a reference for all the further calculations in the *R-bar* approach.

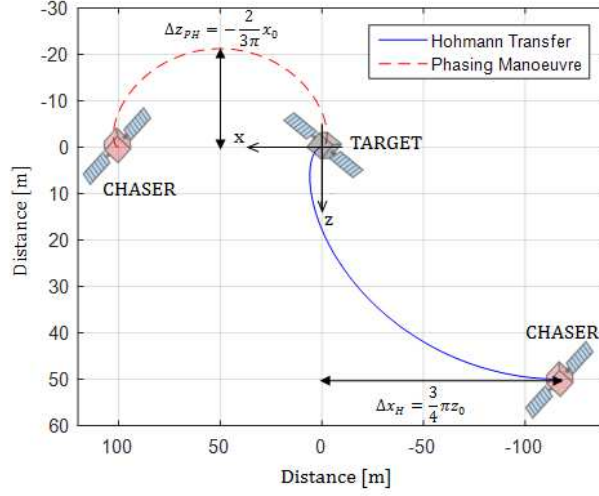


FIGURE 7.2: Hohmann transfer ($R - bar$ approach, blue solid line) and Phasing manoeuvre ($V - bar$ approach, red dashed line). In both cases, the maximum drift is comparable with the initial distance between target and chaser, making these approaches unsuitable and unsafe for close-range rendezvous manoeuvres.

7.2.2 Phasing manoeuvre as reference for the $V - bar$ approach

If the chaser precedes the target in the same orbit at a distance x_0 , the phasing manoeuvre is employed instead of a Hohmann transfer. In this case, a first impulse inserts the chaser into an elliptical orbit, having the semi-major axis greater than the target one and thus with a longer orbital period. On the contrary, if the chaser follows the target spacecraft, the first impulse is used to inject it into an elliptical-orbit that has the semi-major axis minor respect to the target, with a shorter orbital period. After one orbit, the chaser reaches the target and is inserted by a second impulse in its orbit. The velocity budget, the period of the phasing manoeuvre and the drift in the $R - bar$ direction are given by equations 7.10, 7.11 and 7.12, respectively

$$|\Delta V_{1,PH}| = |\Delta V_{1,PH}| = \frac{\omega}{6\pi} x_0 \rightarrow \Delta V_{PH} = \frac{\omega}{3\pi} x_0 \quad (7.10)$$

$$t_{PH} = \frac{2\pi}{\omega} \quad (7.11)$$

$$\Delta z_{PH} = -\frac{2}{3\pi} x_0 \quad (7.12)$$

Similarly to the previous case, the phasing manoeuvre limitations are related to 1) the high approach velocity of the chaser towards the target, and 2) the drift Δz_{PH} from the $V - bar$ approach during the transfer (FIGURE 7.2). Nevertheless, for reasons

of simplicity, the value of the phasing manoeuvre velocity budget ΔV_{PH} is used as a reference for all the further calculations for the $V - bar$ approaches.

7.2.3 Continuous thrust manoeuvres

Even though simple, Hohmann transfer and phasing manoeuvres are affected by drifts [25] as described in Sections 7.2.1 and 7.2.2. To overcome this issue, straight-line approaches can be realized using continuous thrust manoeuvres. Unfortunately, these are hard to be realized by spacecraft actuators, that usually are not able to perform variable thrusts and therefore need to be pulsed. Furthermore, the straight-line procedure requires an actuation at the end of the manoeuvre to reduce the approach velocity of the chaser towards the target.

For these reasons, continuous thrust manoeuvres operations are employed only by large vehicles in the last few meters of the close-range rendezvous manoeuvre. As the velocity is already reduced, the required thrust is smaller and it is easier to execute the manoeuvre using the on-board pulsed control. Nevertheless, for the sake of completeness, the calculation of the required velocity budget for this manoeuvre is presented here for both the $R - bar$ and the $V - bar$ approaches.

7.2.3.1 $R - bar$ approach

The required velocity budget $\Delta V_{CTM,R}$ for an $R - bar$ approach with constant speed on the line-of-sight is composed of four contributions, as visible in equation 7.13: the initial \mathbf{V}_{in} and final \mathbf{V}_{fin} impulses, the drift control on the $V - bar$ direction ΔV_x and the constant velocity control on the $R - bar$ direction ΔV_z .

$$\Delta V_{CTM,R} = |\mathbf{V}_{in}| + |\mathbf{V}_{fin}| + |\Delta V_x| + |\Delta V_z| \quad (7.13)$$

The constant approach velocity $V = V_{in} = -V_{fin}$ can be defined as a function of the manoeuvre duration and the distance from the target, as shown in equation 7.14

$$V = \frac{z_0}{t_{CTM}} \quad (7.14)$$

Fehse [25] presents a mathematical solution for the calculation of the contribution ΔV_x and ΔV_z . The equations are

$$\Delta V_x = \int_0^{t_{CTM}} -2\omega V dt = -2\omega V t_{CTM} \quad (7.15)$$

$$\Delta V_z = \int_0^{t_{CTM}} -3\omega^2 (Vt + z_0) dt = -\frac{3}{2}\omega^2 V t_{CTM}^2 \quad (7.16)$$

Considering Equations 7.15 and 7.16, the total velocity budget can be re-written as

$$\Delta V_{CTM,R} = v \left(2 + 2\omega t_{CTM} + \frac{3}{2}\omega^2 t_{CTM}^2 \right) \quad (7.17)$$

or, referring to the initial distance z_0 , as shown in equation 7.18

$$\Delta V_{CTM,R} = z_0 \left(\frac{2}{t_{CTM}} + 2\omega + \omega^2 t_{CTM} \right) \quad (7.18)$$

The value of $\Delta V_{CTM,R}$ can be evaluated and compared to the ΔV budget of a standard Hohmann transfer from the same distance z_0 , provided that the manoeuvre duration t_{CTM} is known.

TABLE 7.1 reports the significant cases of minimization of $\Delta V_{CTM,R}$ and of $t_{CTM} = t_H$.

TABLE 7.1: Comparison of continuous thrust manoeuvre and Hohmann transfer velocity budgets at significant instants.

Case	Velocity budget	Manoeuvre duration
Minimization of $\Delta V_{CTM,R}$	$\Delta V_{CTM,R} = 10.9 \cdot \Delta V_H$	$t_{CTM} = 0.37 \cdot t_H$
Manoeuvre duration for the Hohmann transfer	$\Delta V_{CTM,R} = 14.7 \cdot \Delta V_H$	$t_{CTM} = t_H$

7.2.3.2 *V-bar* approach

Like the previous case, for the *V – bar* approach the required velocity budget $\Delta V_{CTM,V}$ is composed of several contributions: the initial and final impulses and the drift control on the *R – bar* direction. Defining the constant approach velocity as shown in equation 7.19

$$V = \frac{x_0}{t_{CTM}} \quad (7.19)$$

it is possible to calculate the total velocity budget, as

$$\Delta V_{CTM,V} = V (2 + 2\omega t_{CTM}) \quad (7.20)$$

$$\Delta V_{CTM,V} = x_0 \left(\frac{2}{t_{CTM}} + 2\omega \right) \quad (7.21)$$

The value of $\Delta V_{CTM,V}$ is evaluated and compared to the ΔV budget of a phasing manoeuvre performed from the same distance x_0 . It is important to underline that in this case is not possible to find a minimum value for the velocity budget but only an asymptotic value, being equations 7.20 and 7.21 a monotone decreasing function.

TABLE 2 reports the values of $\Delta V_{CTM,V}$ calculated for several manoeuvre durations.

TABLE 7.2: Comparison of continuous thrust and phasing manoeuvre velocity budgets at significant conditions.

Velocity budget	Manoeuvre duration
$\Delta V_{CTM,V} = 27.85 \Delta V_{PH}$	$t_{CTM} = \frac{1}{3} t_{PH}$
$\Delta V_{CTM,V} = 24.85 \Delta V_{PH}$	$t_{CTM} = \frac{1}{2} t_{PH}$
$\Delta V_{CTM,V} = 21.85 \Delta V_{PH}$	$t_{CTM} = t_{PH}$
$\Delta V_{CTM,V} = 20.359 \Delta V_{PH}$	$t_{CTM} = 2 t_{PH}$
$\Delta V_{CTM,V} = 19.45 \Delta V_{PH}$	$t_{CTM} = 5 t_{PH}$
$\Delta V_{CTM,V} = 6 \pi \Delta V_{PH} = 18.85 \Delta V_{PH}$	$t_{CTM} \rightarrow \infty$

7.2.4 Glideslope algorithms

The aforementioned strategies do not satisfy the main constraints of a close-range rendezvous manoeuvre, that are 1) the necessity to reach the target with a low velocity for safety concerns, 2) the necessity to use impulsive trajectory modifications due to the spacecraft actuator, and 3) the need of a line-of-sight approach. To overcome these limitations, the glideslope algorithm is often applied.

The glideslope manoeuvre, as visible in FIGURE 7.3 (left), consists in a sort of hybrid between a path-planning algorithm (as it uses multiple steps to reach the target while monitoring the maximum drift from the straight-line approach) and a velocity control (as the chaser approach velocity decreases with the distance from the target).

The first formulation of a glideslope approach was presented in polar coordinates by Pearson [63] and was determined for a spacecraft with a reduced number of manoeuvring thrusters; further generalizations [62] and optimizations [64] were then accomplished.

A simplified version based on constant time steps is employed here to determine the total velocity budget with respect to the aforementioned strategies. In this simplified case, the glideslope reference trajectory is expressed as a linear function of both r and v , as visible in FIGURE 7.3 (right) and reported in equation 7.22, with the a coefficient

expressed in equation 7.23 and representing the angular coefficient of the approaching profile.

$$v(t) = a r(t) + v_{FIN} \quad (7.22)$$

$$a = (v_0 - v_{FIN})/r_0 < 0 \quad (7.23)$$

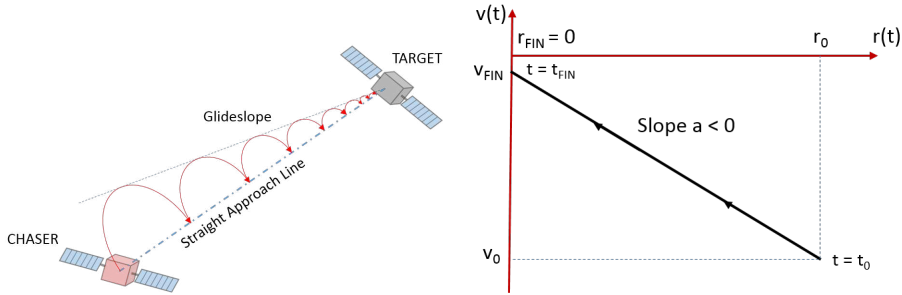


FIGURE 7.3: Glideslope manoeuvre example (left) and reference position and velocity law (right). In this manoeuvre, the chaser approaches the target by means of multiple hopping orbital manoeuvres (red, solid line), with a constant maximum drift from the straight-line approach (dotted blue line).

This formulation allows the determination of the desired approach law as

$$r(t) = r_0 e^{at} + \frac{v_{FIN}}{a} (e^{at} - 1) \quad (7.24)$$

The glideslope algorithm consists in a discretisation of equation 7.24 in way-points. The calculation of way-points depends on the chosen optimization (maximum allowable drift, fuel optimization, safety velocity ranges, etc.). In this simplified case, constant time steps have been employed. Once the way-points are calculated, the total impulse of the manoeuvre can be evaluated as the sum of all the way-points impulses obtained with the CW equations

$$\Delta V_{GL} = \sum_i \Delta V_i = \sum_i (|V_i^+| + |V_{i+1}^-|) \quad (7.25)$$

$$V_i^+ = [\Phi_{rv}]^{-1} \cdot (r_{i+1} - [\Phi_{rr}] \cdot r_i) \quad (7.26)$$

$$V_{i+1}^- = [\Phi_{vr}] \cdot r_i + [\Phi_{vv}] \cdot v_i \quad (7.27)$$

All the following results have been determined for a reference orbit at an altitude of 600 km and a distance between target and chaser equal to 200 m.

7.2.4.1 *R-bar* approach

FIGURE 7.4 (left) reports an example of glideslope trajectory in the *R – bar* approach for a 10 steps manoeuvre. The maximum lateral drift is less than 4.5 m.

TABLE 7.3 shows a comparison between the glideslope manoeuvre and the Hohmann transfer in terms of velocity budget. The reference orbit is 600 km high and the initial distance between the chaser and the target is 200 m. It is worth to underline that the ΔV budget is directly proportional to the number of impulses and inversely proportional to the manoeuvre duration. Furthermore, if more than 10 impulses are performed, the drift is lower than 1.5° in all the considered cases, and the approach becomes close to the straight-line one. Plausible values for the manoeuvre time and the number of impulses ($T = 0.37 T_H$, $N = 10$) foresee a velocity budget of about 3.7 m/s for the close-range rendezvous manoeuvre. These results demonstrate the advantages of this algorithm with respect to the Hohmann transfer.

TABLE 7.3: Comparison between the results obtained for glideslope manoeuvres and Hohmann transfers with different manoeuvre durations.

Number of pulses	$T = T_H$		$T = T_{CTM,R} = 0.37 T_H$	
	Velocity Budget	Max. Drift	Velocity Budget	Max. Drift
1	$\Delta V_G = 1.00 \Delta V_H$	$\delta = 26.57^\circ$	$\Delta V_G = 3.74 \Delta V_H$	$\delta = 12.41^\circ$
5	$\Delta V_G = 6.68 \Delta V_H$	$\delta = 4.00^\circ$	$\Delta V_G = 17.35 \Delta V_H$	$\delta = 1.95^\circ$
10	$\Delta V_G = 12.93 \Delta V_H$	$\delta = 1.23^\circ$	$\Delta V_G = 34.49 \Delta V_H$	$\delta = 0.60^\circ$
50	$\Delta V_G = 63.70 \Delta V_H$	$\delta = 0.06^\circ$	$\Delta V_G = 172.07 \Delta V_H$	$\delta = 0.03^\circ$
100	$\Delta V_G = 127.35 \Delta V_H$	$\delta = 0.01^\circ$	$\Delta V_G = 344.13 \Delta V_H$	$\delta = 0.01^\circ$

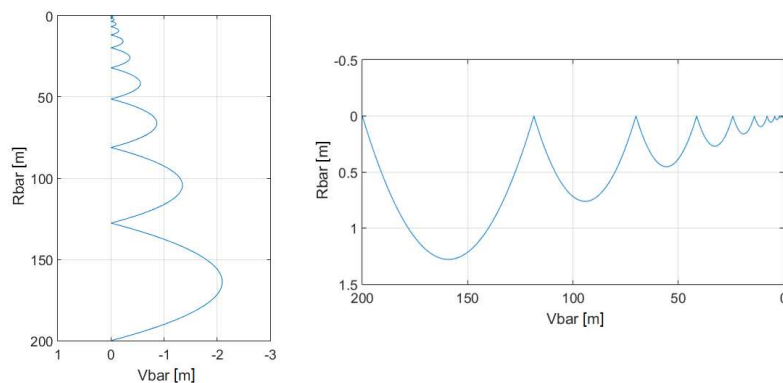


FIGURE 7.4: Glideslope approach, 10 steps, *R – bar* (left) and *V – bar* (right) directions.

7.2.4.2 *V-bar* approach

Similarly, FIGURE 7.4 (right) shows a 10-step simulation of a glideslope trajectory for the *V – bar* approach. Also in this case, the maximum lateral drift is less than 4.5 m and, from the comparison with a phasing manoeuvre, it is possible to state that the velocity budget increases with the number of impulses and decreases as the manoeuvre duration increases.

The best case in terms of manoeuvre duration and number of pulses ($T = T_{PH}$, $N = 5$) foresees a ΔV budget of 1.14 m/s, but more realistic values ($T = 0.1 T_{PH}$, $N = 10$) are around 6.91 m/s as shown in TABLE 7.4.

TABLE 7.4: Comparison between the results obtained for glideslope and phasing manoeuvres at different manoeuvre durations.

Number of impulses	$T = 0.1 \cdot T_{PH}$	
	Velocity Budget	Max. Drift
5	$\Delta V_G = 150.98 \Delta V_{PH}$	$\delta = 0.45^\circ$
10	$\Delta V_G = 300.50 \Delta V_{PH}$	$\delta = 1.73^\circ$
Number of impulses	$T = 0.5 T_{PH}$	
	Velocity Budget	Max. Drift
5	$\Delta V_G = 36.33 \Delta V_{PH}$	$\delta = 6.40^\circ$
10	$\Delta V_G = 62.65 \Delta V_{PH}$	$\delta = 1.40^\circ$
Number of impulses	$T = T_{PH}$	
	Velocity Budget	Max. Drift
5	$\Delta V_G = 49.60 \Delta V_{PH}$	$\delta = 16.22^\circ$
10	$\Delta V_G = 59.11 \Delta V_{PH}$	$\delta = 2.64^\circ$

7.3 ΔV budget and propellant consumption

The velocity budgets obtained in the last section (about 3.7 m/s for the *R – bar* and 6.91 m/s for the *V – bar* approaches in a 600 km orbit) give an idea of the propulsion capabilities the chaser should perform to complete the close-range rendezvous.

Manoeuvres based on algorithms like the glideslope require high accuracy and precise ΔV modifications that only attitude control thrusters could perform and can not be demanded to the chaser main propulsion system. For this reason, some calculations were performed to evaluate the influence of a close-range rendezvous on the satellites thrusters propellant budget. A fast review on small size and small satellites chemical and cold-gas thrusters [65, 66] indicates a total impulse in the range of about $10^2 - 10^3$ Ns with an equivalent ΔV of about 1 – 10 m/s (considering a spacecraft of 100 kg, a ΔV of about 10 – 100 m/s for a 10 kg satellite). This result is consistent with the calculated

ΔV budget.

Furthermore, there could be particular mission architectures that may require repeated close-range rendezvous and docking manoeuvres (formation flight, inspection missions, space tugging, etc.). A possible solution to save part of the propellant is to use tethered docking procedures to perform the proximity operations up to mating. The next section will explain in detail the concept and its benefits, introducing a preliminary simplified simulation of TED.

7.4 TED manoeuvre

The novel docking approach proposed for close-range rendezvous manoeuvre consists in the exploitation of electro-magnetic interactions occurring between two electromagnets. A low stiffness joint between the vehicles is provided thanks to the use of a small electromagnetic tethered probe that is ejected by the chaser toward a receiving electromagnetic interface mounted on the target spacecraft. The generated magnetic field drives the probe to the target and realizes an automatic alignment between the two interfaces, thus reducing proximity navigation and guidance requirements for close approach manoeuvres as well as the consequent fuel consumption. After that, hard docking is accomplished by retracting the tether and bringing the two spacecraft in contact. FIGURE 7.5 resumes all the main characteristic steps followed during the manoeuvre.

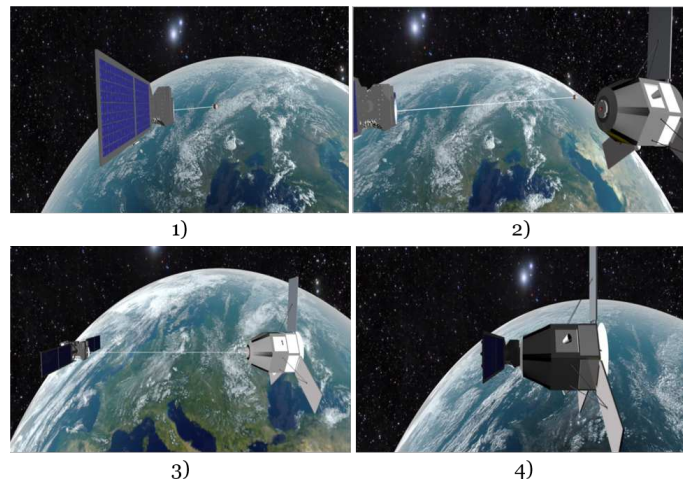


FIGURE 7.5: Tethered docking approach: 1) tethered probe deployment, 2) electromagnetic self-alignment, 3) soft-docking 4) tether rewind and hard-docking (courtesy of FELDs experiment).

When the spacecraft are at the right distance, the tethered electromagnetic probe is ejected from the chaser towards the target (FIGURE 7.5 - 1). The soft-docking phase (FIGURE 7.5 - 2,3) is accomplished when the probe reaches the sphere of influence (i.e.

the maximum distance at which the authority of the dipoles is enough to neglect the influence of the Earth's magnetic field) of the electromagnetic interface mounted on the target. FIGURE 7.5 - 4) shows the conclusion of the retrieval phase, which allows the accomplishment of the hard-docking and the conclusion of the manoeuvre.

The benefits of performing a tethered docking manoeuvre with respect to standard docking procedure are not limited to the partial fuel saving (the chaser would not perform the complete close-range rendezvous manoeuvre and thus the propellant needed to conclude it is saved). The implementation of a small probe for realizing the preliminary connection would assure a negligible impulsive force transmitted to the target system. Moreover, this concept would increase the docking manoeuvre reliability allowing the tether retrieval in case of unsuccessful deployment. These are very important results in terms of resource savings: TED approach would allow the development of longer-lifetime missions and could ease on-orbit operations of refuelling, payload updating, inspection and maintenance. These operations are acquiring growing importance in space-related fields and will surely play a key role in the near future.

7.4.1 Technological developments for TED

It is worth to point out that, to successfully accomplish a tethered electromagnetic docking manoeuvre, the development of new effective and reliable technologies is mandatory: (1) a launch mechanism and (2) a controlled tether deployment and retrieval system are of utmost importance to deploy (at the beginning of the manoeuvre) and retrieve (at the end of the manoeuvre, to accomplish the hard-docking or to recover an unsuccessful launch) the probe correctly. Moreover, the (3) probe must be carefully designed to make the magnetic field action as effective as possible and hopefully extend its effect, easing the relative attitude and position control and guaranteeing the soft-joining.

These technologies and their state of the art are now discussed in detail.

7.4.1.1 Launch mechanism

The launch system goal is to release the tethered probe towards the target with a desired initial velocity. In-space tethered deployments have been performed mainly using two technologies: propelled probes (e.g. TSS-1 [67]) or spring-based systems (e.g. SEDS-1 [68], SEDS-2 [69], YES2 [70]).

Considering TED operations, a spring-based system was developed for its interesting features: 1) it is easily adjustable to give a specific speed to the probe, 2) it is easily rechargeable through its re-compression and, finally, 3) it can be used for a large number of launch attempts without deteriorating or consuming propellant.

The launch system working principle is reported in FIGURE 7.6: it is composed of a spring-based release system, a launch plate and three vertical linear guides. The release system has the function of releasing the probe with the right initial velocity. The launch plate, together with the tethered probe, keeps the spring compressed till the launch instant. When the tether is released, the spring pushes the launch plate which glides on the three vertical linear guides driving the probe till the separation.

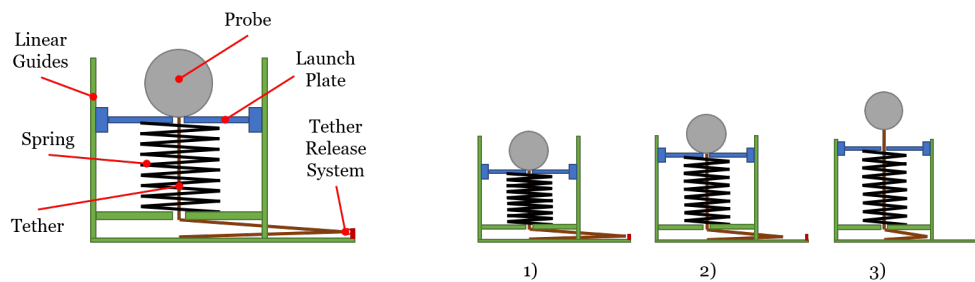


FIGURE 7.6: Working principle of the launch system. After tether release 1), the launch plate is pushed by the spring, driving the probe 2) until its separation 3).

The first prototype of this concept used a single-shot actuator for the release system, instead of a reusable mechanism. This solution was initially selected during the design phase for its simplicity, thus focusing the investigation on other elements of the deployer, i.e. the spring-plate-probe dynamics and the effect of tether friction during launch. The launch mechanism was tested with the Flexible Electromagnetic Leash Docking system (FELDs) experiment [71] (FIGURE 7.7) in the framework of ESA Education Office *Drop Your Thesis!* 2014 programme at ZARM drop tower in Bremen (see Section 2.2.1).

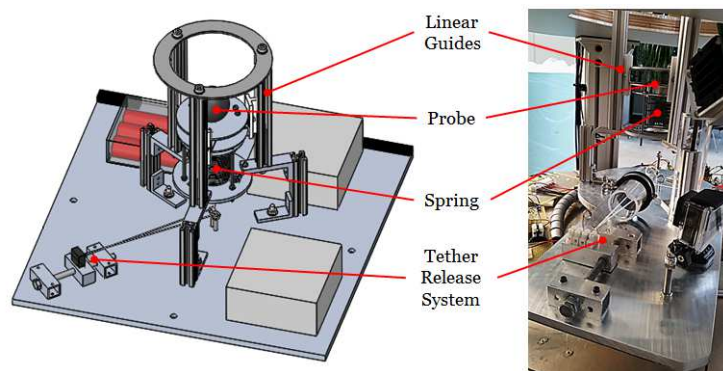


FIGURE 7.7: The spring-based launch system developed during FELDs experiment. The release system is positioned laterally.

FELDs was a technology demonstrator whose main objective was to develop and test in a micro-gravity environment an electromagnetic tethered soft-docking technology able to guarantee a mechanical connection between two spacecraft through the use of a flexible tether. The soft-docking manoeuvre was performed launching a spherical ferromagnetic

probe towards an electromagnetic target: the static magnetic field produced by the target attracted the probe assuring the soft-connection.

The innovation behind FELDs lied in the self-adjusting feature of the system: the flexible connection obtained by the use of a tether did not require a precise positioning of the chaser with respect to the target spacecraft, relaxing the requirements of the attitude control system. This represented a significant advantage compared to existing mechanical docking systems, which have strict alignment requirements and significant fuel consumption during proximity manoeuvres.

FELDs experiment was tested at ZARM drop tower in a test campaign of five launches: three were completely successful and allowed the estimation of the tether friction along the launch mechanism during the release phase of the probe. The frictional forces measured were always under 0.01 N in all the tests, as recapped in TABLE 7.5.

TABLE 7.5: Initial velocity and evaluated friction.

# Drop Test	Initial velocity [cm/s]	Friction [N]
1	23.5	0.009
2	13.0	0.005
3	14.3	0.002
4	11.5	0.006*
5	11.1	0.005*

*estimation before tether snag

The last two drops failed due to malfunctions during the release phase of the probe: the tether snagged in the sliding ring of the release mechanism, slowing the probe that was unable to reach the docking interface and complete the soft-docking manoeuvre. FIGURE 7.8 shows the releasing system before the drop and during the 3rd and 4th drops for comparison.

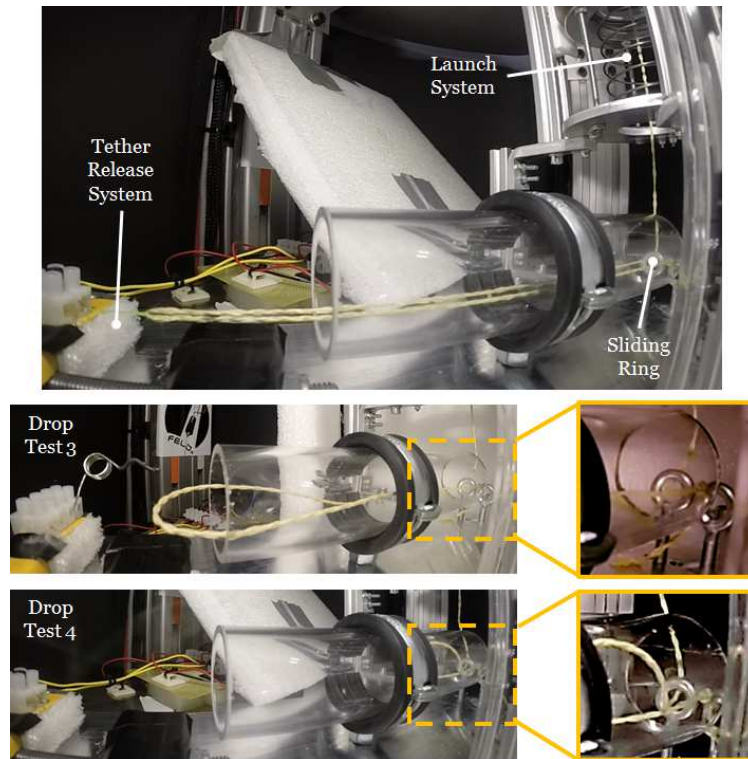


FIGURE 7.8: FIELDS releasing system (up), successful (centre, 3rd drop) and unsuccessful (down, 4th drop) tether release: the tether snagged into the sliding ring, increasing the friction and preventing the accomplishment of the soft-docking manoeuvre.

An updated mechanism featuring an electromagnetic release system (FIGURE 7.9) was developed in the Space Tether Automatic Retrieval (STAR) experiment [72] in the framework of ESA Education Office *Drop Your Thesis!* 2016.

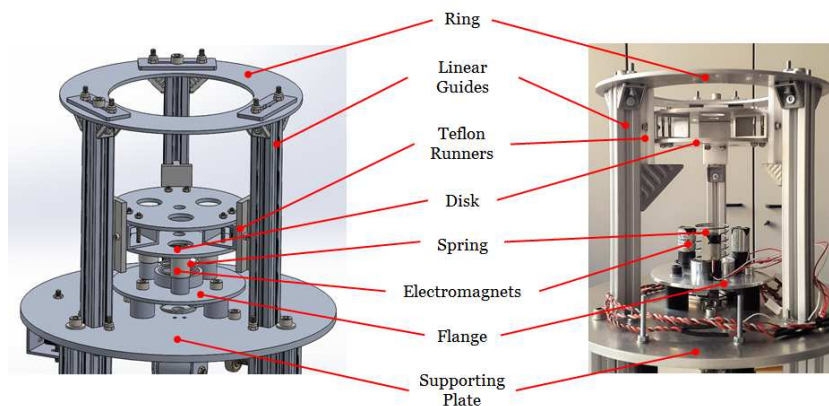


FIGURE 7.9: The upgraded launch system developed in STAR experiment.

STAR main objective was to develop and validate in a micro-gravity environment the technology used to build a new concept for a space tether deployer with retrieval capability. STAR deployer features a closed-loop feedback with a braking system to control the deployment, whilst the retrieval of a tethered tip mass was performed with an open-loop

control. The idea on which this project was based was to adapt the well-established fixed-spool fishing reel technology to obtain a highly autonomous system suitable for space use. STAR experiment was complementary to FELD's experiment and it partially exploited its experience and results, focusing however on the deployment/retrieval system rather than on the electromagnetic docking system.

The advantages of the new launch mechanism were: 1) the launch repeatability, 2) the prevention of snagging failures by winding the tether on a spool aligned with the launch direction and 3) the ability to perform a smoother tether release replacing the mechanical release system with an electromagnetic one. The launch system worked nominally for the whole drop test campaign, releasing the tethered probe with the expected initial velocity (Figure 7.10).

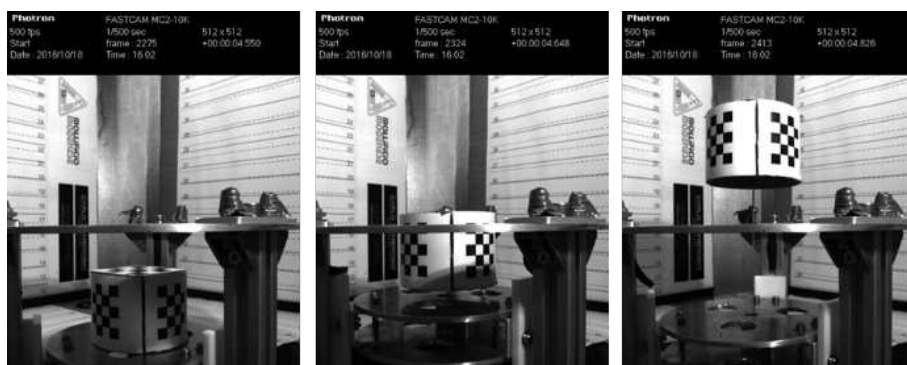


FIGURE 7.10: STAR launch system during a drop test. From left to right, the tethered probe before release, the launch phase and the probe after separation from the plate.

7.4.1.2 Controlled tether deployment and retrieval

The ability to perform a controlled deployment and retrieval of the tethered probe is fundamental for TED development.

Over the past years, an impressive number of contributions and deep insights have been made to widen the understanding of tether dynamics in space [73] to investigate their possible perspective applications: from debris mitigation and de-orbiting [74] through tethered formation flight applications [75], to electrodynamic tethers used to transform orbital energy in electric power [76, 77] and Tethered Satellite Systems (TSS) [78–80]. However, the deployment of a space tether has always been a critical issue in the past space tether missions: a successful release requires a refined mechanical design of both deployment mechanisms and brakes, as well as robust and adaptive control strategies. In this context, NASA-ASI TSS-1 tether deployment failed due to an obstruction in the tether levelling system of the deployer [67], and the tether was eventually retrieved. This is, at the time of writing, the sole known mission where a partially successful tether retrieval was performed. The deployment hardware was, in that case, massive (about

5500 kg without the end-mass) and complex. Considering only tether deployments, a compact and reliable mechanism was designed for YES2 [70]), that behaved successfully; other missions worth mentioning are SEDS-I [68] and SEDSII [69], for which a dedicated, simple and lightweight hardware and a robust control strategy were designed. Both of these missions were fully successful in deploying a 20 km tether with a swinging manoeuvre. At present, both Space Agencies and aerospace industries are interested in tether-related technologies to enable various mission concepts.

In this context, due to the lack of available technologies for both tether deployment and retrieval, a novel mechanism has been developed and tested for TED [81] application, with the following characteristics:

1. Low inertia and friction reel.

Tether deployment starts with the launch of the probe performed by the spring-based launch system described in Section 7.4.1.1 (FIGURE 7.9). The reel system should not pose any inertial and frictional resistance to the flying probe during tether unwinding to avoid sudden jerks to the tether, which would imply an immediate failure of the deployment.

2. Tether retrieval capability.

The deployment system must be able to perform also the tether retrieval after the accomplishment of the soft-docking manoeuvre. This means that the launch mechanism has to be active, not passive like the deployers of SEDS missions [68]-[69].

3. Deployment/retrieval control.

During the deployment, the trajectory of the probe must be controlled to reach the target and achieve the soft-docking. In addition, during the tether retrieval, the reel system must be able to rewind reliably the tether without jamming the mechanism. Therefore, a feedback control is needed for the reel system. This involves the use of sensors (e.g., for the position, the velocity, the tension of the tether) and of a brake system as actuator.

FIGURE 7.11 shows a sketch of the developed mechanism. The deployment is initiated by means of the spring-based launch device described in Section 7.4.1.1. The deployer has an active brake mechanism used to control the tether tension during the deployment. A peculiar locking mechanism, the bail, is used to engage the tether after the complete controlled deployment. An electric motor is then powered to retrieve the tip mass. Before the deployment, the tether is wound up around a fixed spool aligned with the launch direction. Once the launch procedure is initiated, the tether is free to flow out from the spool with minimal inertia (without trailing rotating parts). The only resistance to the

tether exit motion is due to its negligible inertia. The tip mass is released along the desired direction acting on the tether tension controlled by the brake mechanism.

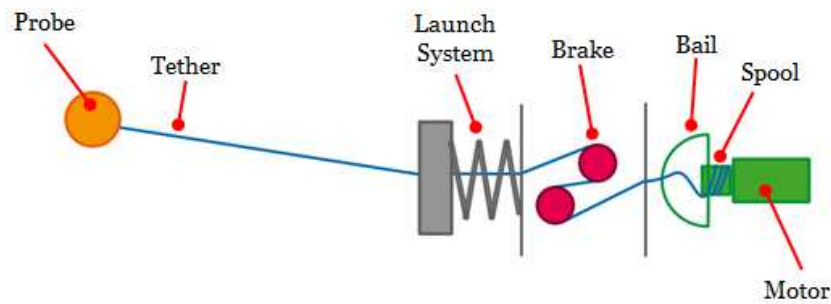


FIGURE 7.11: Sketch of the controlled tether deployment/retrieval system.

FIGURE 7.12 shows the final configuration of the tether reel system, successfully tested by STAR experiment.

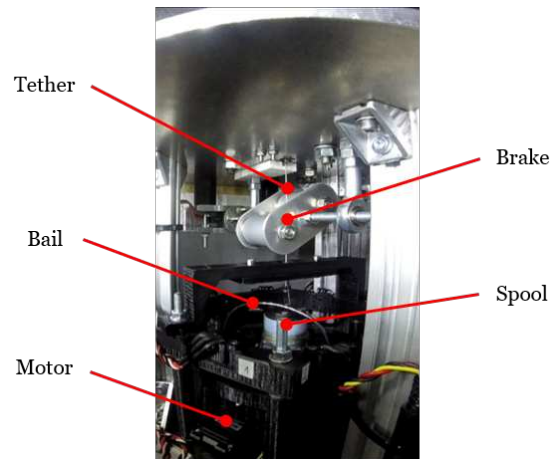


FIGURE 7.12: STAR controlled tether deployment/retrieval system tested during the *Drop Your Thesis!* campaign.

FIGURE 7.13 shows three sequences of the second drop test: the system was able to completely deploy the probe and retrieve it correctly, proving the good performances of the device even if further improvements are necessary to be able to test it in a real space mission.

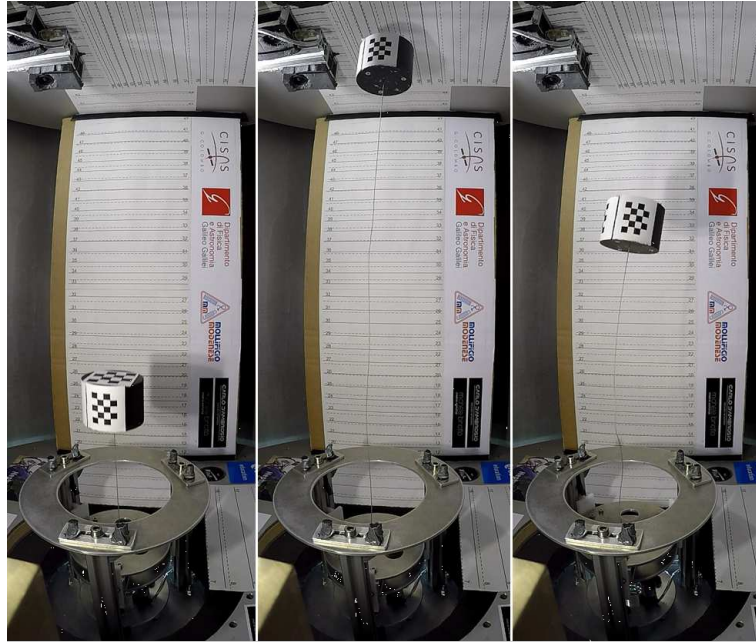


FIGURE 7.13: Second drop test, from left to right: deployment, tether fully extended and probe free-floating, retrieval.

7.4.1.3 Passive probe design

The objectives of the tether launch and deploy systems are to place the probe in proximity of the target, i.e. into the sphere of influence of the electromagnetic field generated by the target and/or the probe itself. Proximity operations exploiting electromagnetic interactions are therefore expected to complete the close-range rendezvous and soft-docking manoeuvre.

The probe shape has to be developed to guarantee the adaptability with the target interface. This component must be carefully designed since it must make effective the magnetic field action and possibly extend its effect. Moreover, it must have a reduced mass in order to transmit a negligible impulsive force on the target system. A high impulsive force on the target could not only damage the receiving interface but also certainly disturb its attitude.

A simplified scenario was investigated in micro-gravity conditions by FIELDS experiment using a ferromagnetic tethered probe launched towards a fixed electromagnetic target. The performed tests allow to 1) study the self-guidance effect due to the electromagnetic interaction between the ferromagnetic probe and the target and 2) analyse the momentum and energy transfer due to the probe impact on the target (FIGURE 7.14).

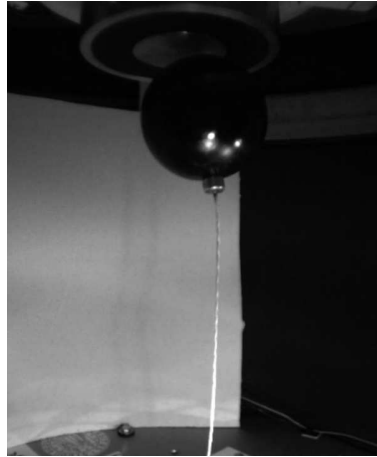


FIGURE 7.14: Test in micro-gravity conditions of a simplified soft-docking manoeuvre: once the probe reaches the sphere of influence of the target, its motion is clearly perturbed.

FIGURE 7.15 shows the vertical trajectory followed by the probe during the three successful drop tests. The action of the electromagnetic field produced by the target on the ferromagnetic probe is clearly visible in the last 5 – 10 cm, where the probe trajectory is modified. The extent of the sphere of influence of the target is correlated with the probe size and the generated electromagnetic field. These are the main design drivers that can be adjusted to create different and more effective configurations, as described in [71]. In fact, scaling the operational conditions to real in-space missions, the dimension of the sphere of influence can vary from about 20 cm for CubeSat-sized spacecraft, up to ~ 1 m for 100 kg-class satellites.

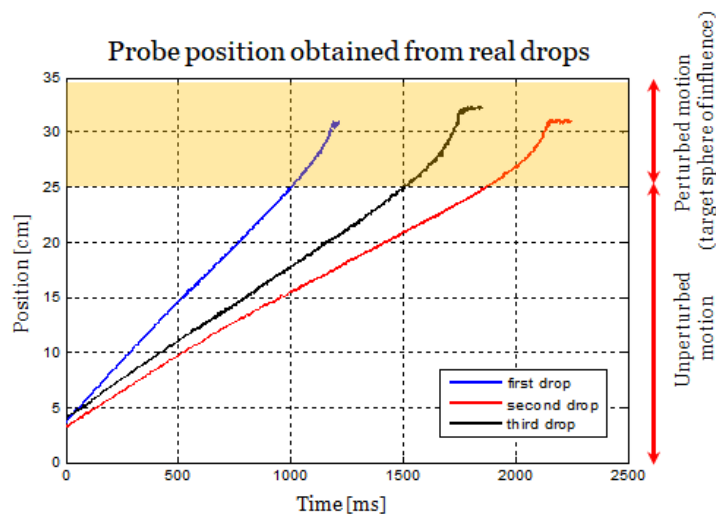


FIGURE 7.15: Results obtained during three different drop tests. The ferromagnetic probe approaches the electromagnet after entering its sphere of influence, modifying its trajectory.

7.4.2 Tether model for TED application

The tether, with the electromagnetic probe and the deployment/retrieval system, establishes the connection between the chaser and the target spacecraft during the soft-docking manoeuvre. This link guarantees milder requirements in terms of GNC accuracy than the standard docking procedures, since it limits the close-range rendezvous manoeuvres normally necessary to complete the docking phase. Hard-docking is then accomplished through tether retrieval after the actuation of mechanical latches that secure a rigid connection between the target spacecraft and the probe.

The tether is modelled as a varying length dumbbell as illustrated in [47, 82]. Its attitude can be described by three variables: the length l , the in-plane libration angle ϑ and the out-of-plane libration angle ϕ . Since the tether is short, it is considered as a rigid body. The constitutive material of the tether is Dyneema, a high-strength fibre that is produced from polyethylene. The diameter is in the order of 0.5 – 1 mm to reproduce the behaviour of real space tethers.

It is not the purpose of this thesis to investigate the tether motion and its dynamics in space in detail, since an in-depth study could provide data for another complete dissertation. The tether motion out of the orbital plane (libration angle ϕ) is neglected, given that it does not influence the tether deployment. Moreover, the tether retrieval manoeuvre has not been simulated, since the presented results are obtained from preliminary studies and the focus was limited to the close-range rendezvous and soft-docking approach.

The free tether motion is described by the following equations:

$$\ddot{l} = \frac{\rho \dot{l}^2}{2(m + \rho l)} + l \frac{2m + \rho l}{2(m + \rho l)} \left[(w + \dot{\vartheta})^2 + 3w^2 \cos^2 \vartheta \right] - \frac{T}{m + \rho l} \quad (7.28)$$

$$\ddot{\vartheta} = -3 \frac{2m + \rho l}{3m + \rho l} (w + \dot{\vartheta}) \frac{\dot{l}}{l} - 3w^2 \sin \vartheta \cos \vartheta \quad (7.29)$$

where m is the tip mass, ρ the tether linear density, w the orbital mean motion and T the tether tension. The angle ϑ is measured from the local vertical axis x . FIGURE 7.16 shows the tether reference frame, with the x -axis along the local vertical, the z -axis gives the direction of motion and the y -axis completes the reference system.

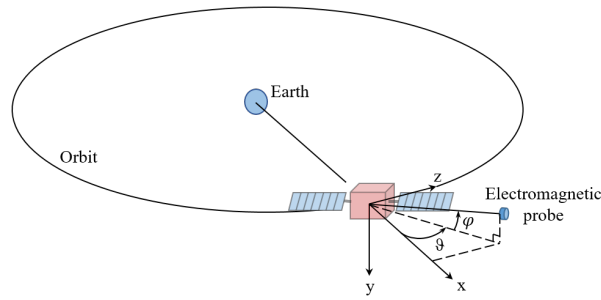


FIGURE 7.16: Tether reference system: the x -axis is along the local vertical, the z -axis gives the direction of motion and the y -axis completes the reference system. The angle ϑ measures the libration angle of the tether in the xz orbital plane.

7.4.2.1 Tether deployment

Tether deployment has been extensively studied in the last decades in the most varied areas of interest: debris mitigation and de-orbiting [74], electrodynamic tethers [77], thrust-aided librating deployments [82] and spinning deployments [83], to mention just a few of them. Even if a tether can be deployed in any direction, there are four preferential directions: two specular deployments when the tether is aligned along the local vertical and other two specular deployments when the system is aligned along the local horizontal, as shown in FIGURE 7.17. The tether deployment along these directions guarantees to reach four equilibrium positions, due to the intrinsic properties of Equations 7.28 and 7.29.

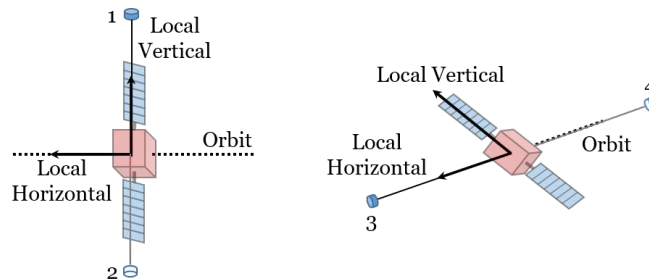


FIGURE 7.17: Equilibrium positions of the dumbbell system: specular positions along the local vertical (left, 1-2) and horizontal (right, 3-4) respectively.

Among the four equilibrium positions, only those two along the local vertical are stabilized by the effect of the gravity gradient and thus a tether deployment along this direction (*R-bar* approach) could benefit from this natural stabilization. This represents an important advantage for the chaser-tether system dynamics and should be taken into consideration.

The main drawback of this kind of deployment is related to the fact that it is not convenient for performing a docking manoeuvre, since the two spacecraft (chaser and target) would be in two different orbits with different relative velocities.

This means that also the electromagnetic probe ejected from the chaser has a relevant velocity and could transmit a significant impulsive force to the target, changing its attitude. Moreover, since the appropriate relative position between the spacecraft occurs once per orbit (considering circular orbits), the docking manoeuvre could be performed only with this frequency. Therefore, tether deployment has to be carefully planned in advance to guarantee the probe-target rendezvous. An accurate timing in the tether deployment is needed for the accomplishment of a successful docking manoeuvre.

On the contrary, a tether deployed along the local horizontal (*V-bar* approach) is not as stable as the previous one but it has not the aforementioned disadvantages. Moreover, the reliability of the approach is higher, given that, in case of an unsuccessful deployment, the tether can be retrieved and deployed again without waiting an entire orbital period.

The two approaches will be compared in Section 7.4.4. For both approaches, all the orbital parameters are calculated in the Earth-Centred Inertial reference system. The initial conditions for the resolution of the orbital differential equations are given by the classical orbital parameters. The attitude and motion of the spacecraft are therefore calculated.

7.4.2.2 Tether retrieval

Differently from tether deployment strategies, that have been largely investigated in the past, tether retrieval manoeuvres have been very poorly studied except for some works about analytical solutions [79, 84] and optimizations [85].

As previously mentioned, the tether retrieval manoeuvre has not been investigated since it does not represent the focus of the thesis: the presented results are only preliminary studies about the close-range rendezvous manoeuvre (the tether deployment) and the soft-docking. The orbital attitude of the chaser-tether-target system after the accomplishment of the soft-docking manoeuvre and the tether retrieval phase have not been taken into consideration in the work.

Before the retrieval manoeuvre initiation, assuming that the probe has a small mass with respect to the target (in a way that the probe soft-docking to the target does not perturb the latter spacecraft dynamics), the system is essentially a fixed-length dumbbell, unrolled along the local horizontal of the reference frame. As mentioned, this is an unstable equilibrium position and can be maintained for a short time: hypothetically, for the time necessary to gain control of the target spacecraft if it is a non-cooperating object (de-tumbling, etc.). During this phase, the attitude of the entire system may be controlled by the thruster system of one of the two vehicles (or, if possible, of both). After this, the system attitude should reach a configuration in which the tether is aligned

with the local vertical: as mentioned, this attitude is stable and may be maintained indefinitely, allowing the two vehicles to perform the tether retrieval and the hard-docking. Furthermore, the tether retrieval itself should be performed along the local vertical for stability reasons: by keeping the length rate of the tether small during the retrieval, the gravity gradient keeps the system libration angle ϑ close to the local vertical. If the retrieval is not performed along the local vertical, the system starts to spin around the y -axis of the orbital frame.

7.4.3 Magnetic field model for TED application

Both the coils contained in the probe and in the interface mounted aboard the target spacecraft can be considered as current loops. The simplest model of a current loop is the magnetic dipole [50] which is the approximated model considered in this composition and follows the magnetic dipole moment equation

$$\boldsymbol{\mu} = N i A \mathbf{n} \quad (7.30)$$

where N is the number of turns, i the current, A the area of the loop and \mathbf{n} the normal to the loop. FIGURE 7.18 shows the dipole reference frame of two magnetic dipoles whose centres lie on the X -axis. The angles ϕ_A , ϕ_B and ψ_A , ψ_B represent the rotation of the dipoles about the X -axes and Z -axes, respectively.

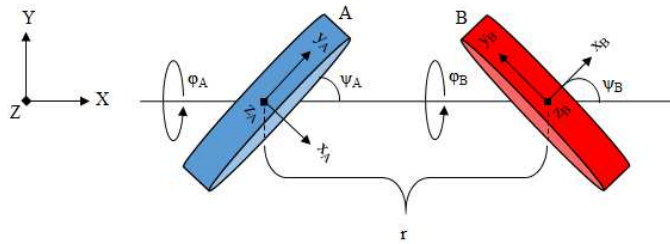


FIGURE 7.18: Representation of the electromagnetic dipoles. Each dipole has its own body reference frame (xyz) which can move and rotate with respect to the target reference frame (XYZ) following its centre of mass. The orientation angles are reported in the figure while r represents the distance between the dipoles.

The external magnetic field produced by a magnetic dipole moment is given by equation 7.31

$$\mathbf{B}(\mathbf{r}) = \frac{\mu_0}{4\pi} \left(\frac{3\mathbf{r}(\boldsymbol{\mu} \cdot \mathbf{r})}{r^5} - \frac{\boldsymbol{\mu}}{r^3} \right) \quad (7.31)$$

where μ_o is the vacuum permeability, \mathbf{r} is the vector distance outside the source region where the magnetic field is evaluated and r its modulus. The expression to evaluate the force \mathbf{F}_A acting on dipole A due to the magnetic field produced by dipole B is:

$$\mathbf{F}_A = \frac{2\mu_o}{4\pi} \left\{ -\frac{(\mu_A \cdot \mu_B)}{r^5} \mathbf{r} - \frac{(\mu_A \cdot \mathbf{r})}{r^5} \mu_B - \frac{(\mu_B \cdot \mathbf{r})}{r^5} \mu_A + 5 \frac{(\mu_A \cdot \mathbf{r})(\mu_B \cdot \mathbf{r})}{r^7} \mathbf{r} \right\} \quad (7.32)$$

where μ_A and μ_B are the magnetic moment of the dipoles, \mathbf{r} is the distance vector between them and r its modulus. The torque \mathbf{T}_A acting on dipole A due to the magnetic field produced by dipole B is given by

$$\mathbf{T}_A = \mu_A \times \frac{\mu_o}{4\pi} \left[3 \frac{\mathbf{r}(\mu_B \cdot \mathbf{r})}{r^5} - \frac{\mu_B}{r^3} \right] \quad (7.33)$$

Now recalling Equations 7.32 and 7.33 and referring them to FIGURE 7.18 it is possible to obtain the forces and torques acting on dipole A due to dipole B as follows

$$\begin{aligned} F_{A,x} &= \frac{3\mu_o\mu_A\mu_B}{4\pi d^4} (2 \cos \psi_A \cos \psi_B - \cos(\phi_B - \phi_A) \sin \psi_A \sin \psi_B) \\ F_{A,y} &= -\frac{3\mu_o\mu_A\mu_B}{4\pi d^4} (\cos \psi_A \sin \psi_B \cos \phi_B + \sin \psi_A \cos \psi_B \cos \phi_A) \\ F_{A,z} &= -\frac{3\mu_o\mu_A\mu_B}{4\pi d^4} (\cos \psi_A \sin \psi_B \sin \phi_B + \sin \psi_A \cos \psi_B \sin \phi_A) \\ T_{A,x} &= -\frac{\mu_o\mu_A\mu_B}{4\pi d^3} (\sin \psi_A \sin \psi_B \sin(\phi_B - \phi_A)) \\ T_{A,y} &= \frac{\mu_o\mu_A\mu_B}{4\pi d^3} (\cos \psi_A \sin \psi_B \sin \phi_B + 2 \sin \psi_A \cos \psi_B \sin \phi_A) \\ T_{A,z} &= -\frac{\mu_o\mu_A\mu_B}{4\pi d^3} (\cos \psi_A \sin \psi_B \cos \phi_B + 2 \sin \psi_A \cos \psi_B \cos \phi_A) \end{aligned} \quad (7.34)$$

Similarly, it is possible to easily calculate \mathbf{F}_B and \mathbf{T}_B , which are the force and torque acting on dipole B due to the magnetic field produced by dipole A.

7.4.3.1 Dipoles equations of dynamics

The mutual interactions between the two dipoles can be studied using the Eulers equations of dynamics. These equations describe the two dipoles in terms of translations and rotations and are obtained substituting the expressions of the force and torque into the first and second cardinal equations projected in the body reference frame. The final system of equations is given by 7.35

$$\left\{ \begin{array}{l} I_x \dot{\omega}_x + \omega_y \omega_z (I_z - I_y) = \mathbf{T}_{\mathbf{A},\mathbf{x}} \\ I_y \dot{\omega}_y + \omega_z \omega_x (I_x - I_z) = \mathbf{T}_{\mathbf{A},\mathbf{y}} \\ I_z \dot{\omega}_z + \omega_x \omega_y (I_y - I_x) = \mathbf{T}_{\mathbf{A},\mathbf{z}} \\ \left\{ \begin{array}{l} \dot{\phi} \\ \dot{\theta} \\ \dot{\psi} \end{array} \right\} = [R_{rel}]^{-1} \omega_{\mathbf{abs}}^{(\mathbf{B})} \end{array} \right. \quad (7.35)$$

where ω_x , ω_y and ω_z are the components of the absolute angular velocities of dipole A expressed in the body reference frame, $\dot{\omega}_x$, $\dot{\omega}_y$ and $\dot{\omega}_z$ the corresponding angular accelerations and $\mathbf{T}_{\mathbf{A},\mathbf{x}}$, $\mathbf{T}_{\mathbf{A},\mathbf{y}}$ and $\mathbf{T}_{\mathbf{A},\mathbf{z}}$ the components of the torque vector due to the magnetic field produced by dipole B. I_x , I_y and I_z are the diagonal entries of the inertial matrix. The matrix $[R_{rel}]$ is obtained by the sequence of rotation 3-2-1 around $z - y - x$ -axis, respectively, and it is equal to

$$[R_{rel}] = \begin{bmatrix} 1 & 0 & -\sin \theta \\ 0 & \cos \phi & \sin \phi \cos \theta \\ 0 & -\sin \phi & \cos \phi \cos \theta \end{bmatrix} \quad (7.36)$$

while $\omega_{\mathbf{abs}}^{(\mathbf{B})}$ is the absolute angular velocity vector in the body reference frame. $\dot{\phi}$, $\dot{\theta}$ and $\dot{\psi}$ are the derivative of the Eulers angles. Equations 7.32, 7.33 and 7.35 are used to study the dipole dynamics in terms of rotations and translations.

7.4.3.2 Dipole dynamic simulations

Simulations were carried out to study the dipole dynamics. The optimization process started considering the main parameters of a dipole that are expressed in equation 7.30. A systematic procedure was adopted varying the number of turns, the current and the diameter of the coils for both the dipoles. Other physical properties, such as the diameter of the wire, the length, the mass and the power consumption were obtained from these initial values. Once the dipoles were characterized, dynamic simulations were performed to understand if the selected parameters (and thus the dipoles) were suitable for TED application. A routine was implemented in a MATLAB[®] code to find the maximum distance at which the authority of the dipoles could be considered sufficient for a docking approach, comparing the magnetic field produced by the dipoles with the Earth one at the selected altitude.

In order to maximize the effect of the magnetic guidance and limit the transmitted force during the soft-docking phase, the dipoles have different characteristics. The electromagnet aboard the target spacecraft is bigger than that of the probe with a diameter of 100 mm, 700 turns and a mass of 1.2 kg. The current is of 1.2 A with a power consumption of 5 W; the electromagnet into the probe, instead, is smaller with a diameter of 50 mm, 300 turns and a mass of 0.24 kg. The current is again of 1.2 A with a power consumption of 1 W.

The two different configurations allows a reduced power consumption, especially for the tethered probe. However, it is worth noting that the activation of the dipoles covers only a limited amount of time during the entire manoeuvre, which corresponds to the final phase before the soft-docking.

FIGURE 7.19 shows the initial configuration of the system considered, with the electromagnets aligned with the X -axis. In this configuration no torque is transmitted and the attractive force between the two dipoles generated by the magnetic fields acts along the X -axis, producing a straight translation motion.

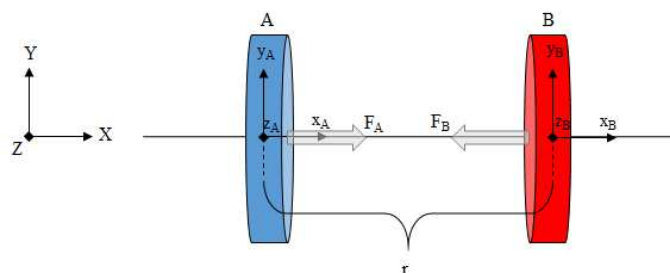


FIGURE 7.19: Initial configuration of the system. The dipoles are aligned with the X -axis and thus no torque is transmitted. The attractive force generated by the magnetic fields produces the translation.

FIGURE 7.20 confirms that the transmitted force between the two interfaces is contained, assuring an affordable attitude variation.

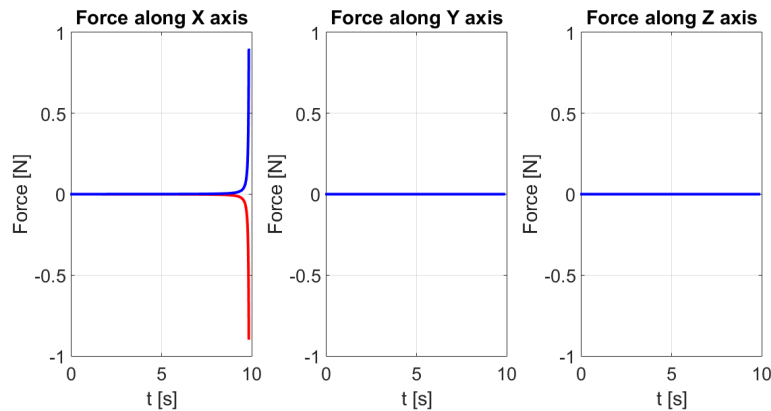


FIGURE 7.20: Forces between the dipoles. Since the dipoles are aligned with the X -axis, the mutual attractive forces between them is only along that direction. Blue line represents the attractive force of dipole A, while red line represents the attractive force of dipole B.

It is worth noting that the forces increase drastically as the distance between the two dipoles decreases. This is due to the fact that the magnetic field magnitude is proportional to $1/r^3$ and thus the peak in these figures is reached immediately before dipoles connect. This trend is followed also by the displacement and the velocities of the dipoles centre of mass, which are plotted in FIGURE 7.21.

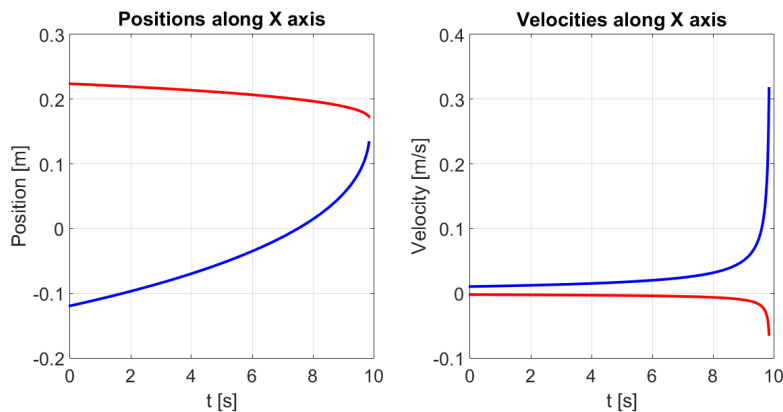


FIGURE 7.21: Position and velocity of the dipoles. Since the dipoles are aligned with the X -axis, the displacements and the velocities are only along that direction. Blue line represents the displacements and velocities of dipole A, while red line represents the same physical quantity of dipole B.

7.4.3.3 Laboratory test

Preliminary experimental results about the peculiar magnetic guidance capability were carried out in the laboratory. The setup used to perform the tests is shown in FIGURE 7.22 and is composed of:

- a 2 m long air-cushion low-friction rail which ensures a near-frictionless motion of the slide;
- a slide equipped with two square markers used to track its position using a high-definition camera;
- a small iron plate on the slide used as interface to interact with the electromagnetic field produced by the electromagnet;
- an electromagnet positioned at one end of the rail used to produce the attractive electromagnetic force on the slide due to the electromagnetic field.

Only the last section of the rail (0.2 m) close to the electromagnet were used for the tests because the effectiveness of the electromagnetic field decreases quickly with the distance.

The displacement of the slide were recorded using an external high-definition camera. The obtained data were processed in real time using an identification algorithm (which analyses the slide position comparing the displacement of the markers during two consecutive time steps) implemented through a Matlab[®] code. The video analysis allowed the evaluation of the acceleration profile of the slide due to the attractive force produced by the electromagnetic field of the electromagnet.

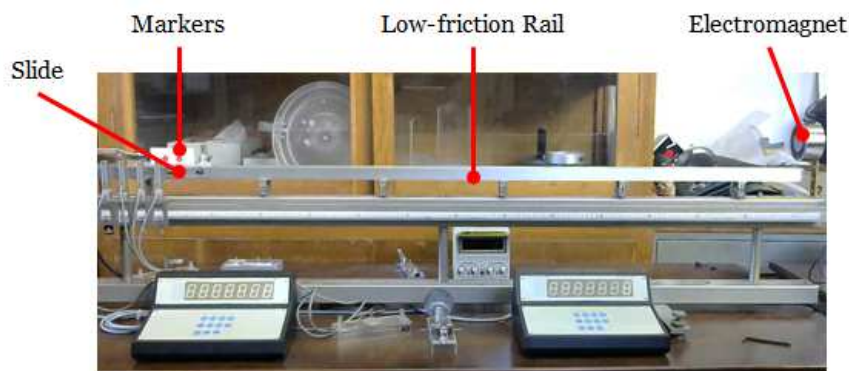


FIGURE 7.22: Experimental setup. The magnetic guidance effect was analysed studying the slide displacement due to the electromagnetic attractive force of the electromagnet.

7.4.3.4 Experimental results

The experimental configuration, reported in FIGURE 7.23, allowed the evaluation of the acceleration profile of the slide and study the magnetic guidance effect and its extent.

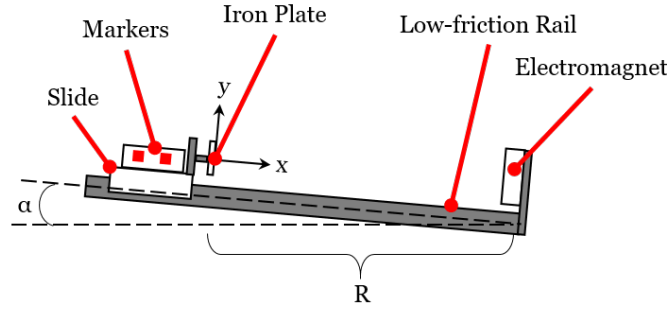


FIGURE 7.23: Experimental configuration and reference axes. The rail is inclined by an angle α which allows the evaluation of the contribution to the acceleration profile of the slide due to the gravity force and the residual friction.

Considering the rail with a constant inclination and the slide subjected to a dynamic friction (i.e. independent from the slide velocity), the slide movement is the result of three different contributions: 1) the acceleration due to the gravity force, 2) the deceleration due to the small residual friction between the slide and the rail and, finally, 3) the acceleration due to the electromagnetic force when the electromagnet is switched on.

From the data obtained on the slide motion when the electromagnet is switched off, it is therefore possible to determine the non-electromagnetic contributions to the acceleration profile. These can be considered constant since they always affects the measurements collected during the tests. Their entire contribution is given by equation 7.37

$$a_0 = g(\sin \alpha - \mu_d \cos \alpha) = cost \quad (7.37)$$

in which g is the acceleration due to the gravity force, μ_d is the dynamic friction coefficient and α the inclination of the rail. FIGURE 7.24 shows the acceleration profile of the slide subjected only to the non-electromagnetic contributions compared with the mathematical model for constant acceleration. It is worth noting the good agreement between the measures and the implemented model.

Knowing the constant acceleration contribution a_0 , it is possible to obtain the acceleration acting on the slide due to the electromagnetic attractive force produced by the electromagnet. These analyses were carried out under the hypothesis that the magnetic field is not time-variant (i.e. the slide motion does not influence the quasi-static magnetic field). Under this hypothesis, the acceleration due to the electromagnetic force was calculated.

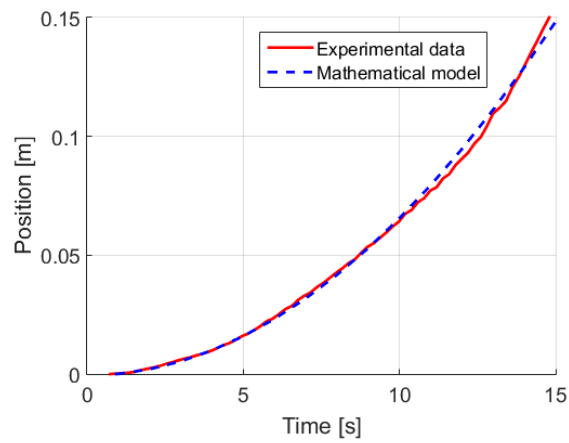


FIGURE 7.24: Comparison between experimental data collected when the electromagnet is switched off and the mathematical model.

FIGURE 7.25 shows a comparison among the results collected during the testing phase with the switched-on electromagnet, the experimental data collected without the electromagnet contribution and the mathematical model. As expected, the contribution due to the electromagnetic interaction between the iron plate and the electromagnetic field is visible and significant.

Here again, it is possible to underline the good agreement between the experimental results and the implemented model, which is validated accordingly.

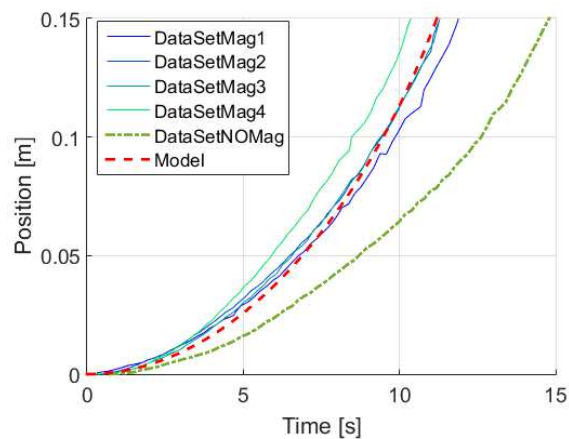


FIGURE 7.25: Acceleration profile obtained by experimental data due to the electromagnetic force induced by the electromagnetic field of the electromagnet.

7.4.4 Real in-space manoeuvre

Tether deployments can be performed along any direction, but there are two preferential stable directions: along the local horizontal ($V\text{-bar}$ approach) or along the local vertical ($R\text{-bar}$ approach). The $V\text{-bar}$ approach is not as stable, as the $R\text{-bar}$ but it presents some remarkable advantages as previously explained in Section 7.4.2.1.

The two different approaches are compared, paying particular attention towards the $V\text{-bar}$ approach. For both approaches, all the orbital parameters are calculated in the Earth-Centred Inertial reference system. The initial conditions for the resolution of the orbital differential equations are given by the classical orbital parameters: the angular momentum h , the inclination of the orbit i , the right ascension Ω , the eccentricity of the orbit e , the argument of periapsis w and the true anomaly Θ . The attitude and motion of the spacecraft are therefore calculated. The close-range rendezvous and soft-docking manoeuvres were studied through a complete simulation.

7.4.4.1 $R\text{-bar}$ approach

In the $R\text{-Bar}$ approach, the two spacecraft are in two different circular orbits around Earth, at an altitude of 600 km and of 600.06025 km (i.e. the two orbit differs by 60.25 m) for the chaser and the target, respectively. FIGURE 7.26 shows the initial configuration of the two spacecraft and the relative position between the target and the chaser in their orbits. As explained in Section 7.4.2.1, the tether deployment has to start before reaching the rendezvous position to assure the probe-target encounter and guarantee the accomplishment of the soft-docking manoeuvre. The two spacecraft are separated by a distance of 142.33 m when the deployment starts.

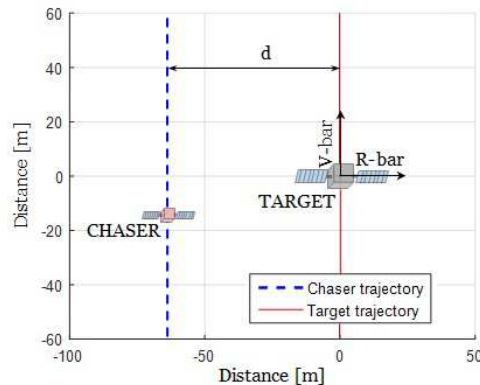


FIGURE 7.26: Target and chaser position in the target reference system. The distance d between the spacecraft is of 60.25 m. The spacecraft are in two different orbits: the blue dashed line corresponds to the chaser while the red one is the target orbit, respectively.

During the orbital motion, the tethered probe is deployed from the chaser at an initial velocity of 0.075 m/s along the local vertical.

The main issues for this kind of manoeuvre are due to the fact that the two spacecraft are not in the same orbit and thus the tether deployment can be performed only once per orbit.

FIGURE 7.27 shows all the phases of the tether deployment during the orbital motion of the spacecraft.

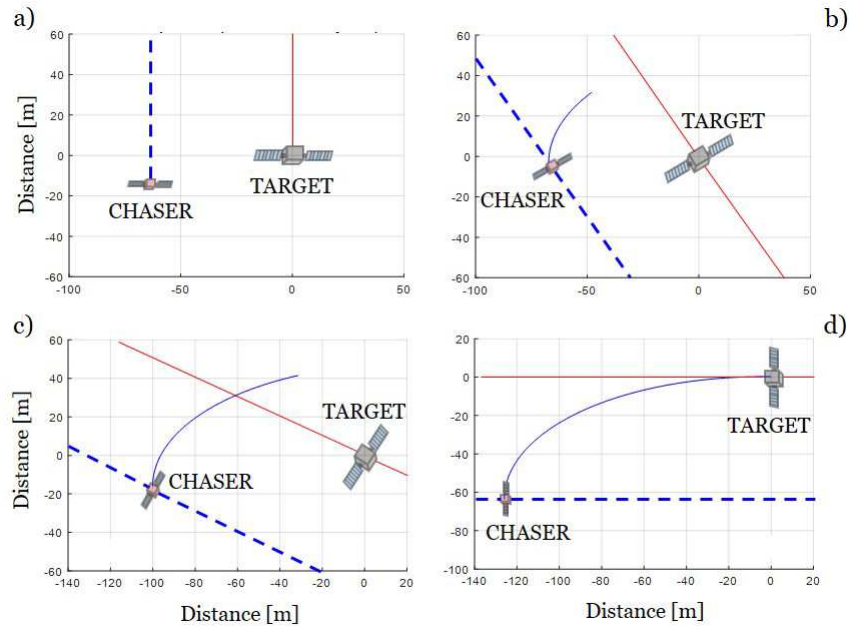


FIGURE 7.27: Phases of the tether deployment during the orbital motion of the spacecraft. For the $R - bar$ approach, the deployment of the tether has to start at the right time to assure the probe-target encounter: a) initial position of the two spacecraft at 1 s, b) 500 s, c) 1000 s and d) 1458 s after the beginning of the deployment. The blue line represents the trajectory of the probe.

The deployment of the tether has to start (FIGURE 7.27 a) before reaching the rendezvous position to assure the probe-target encounter. The tether has to be completely deployed exactly in the moment when the target is in the right position in its orbit (FIGURE 7.27 d) and thus has to be carefully planned in advance. A failure in the encounter between the probe and the target spacecraft means a failure in the docking manoeuvre. If such a scenario occurs, the docking manoeuvre is compromised and can not be accomplished before a new orbital period (the appropriate relative position between the spacecraft occurs once per orbit).

The deployment last 1458 s and the final tether length is about 146.44 m. FIGURE 7.28 shows the deployment configuration and the relative position between target and chaser at the end of the soft-docking manoeuvre, when the tether is completely deployed.

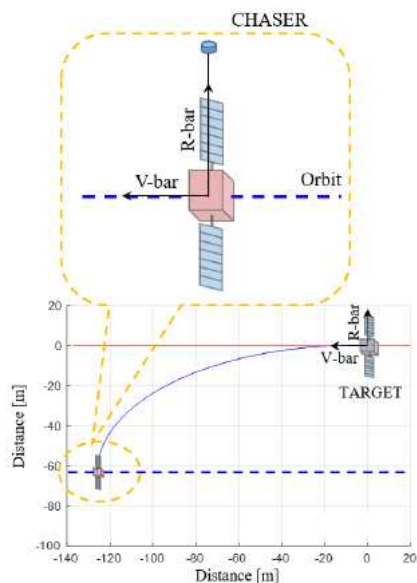


FIGURE 7.28: Configuration of the chaser at the beginning of the tether deployment (top) and target and chaser position in the target reference system (bottom) at the end of the soft-docking manoeuvre.

7.4.4.2 *V-bar* approach

In this configuration, the two spacecraft are in the same circular orbit around the Earth, at an altitude of 600 km. The target is 175.4 m ahead of the chaser. FIGURE 7.29 shows the relative position between target and chaser at the beginning of the docking manoeuvre. During the orbital motion, the tethered probe is deployed from the chaser at an initial velocity of 0.075 m/s along the local horizontal towards the target.

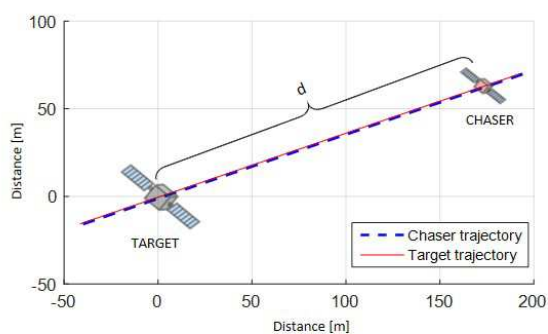


FIGURE 7.29: Target and Chaser position in the Target reference system. The Target is at a distance d of 175.4 m ahead of the Chaser. Both spacecraft share the same orbit: the blue striped line corresponds to the Target orbit while the red one is the Chaser trajectory.

The tether deployment last 1786 s and the final tether length is about 176 m. FIGURE 7.30 shows the deployment configuration and the complete soft-docking manoeuvre.

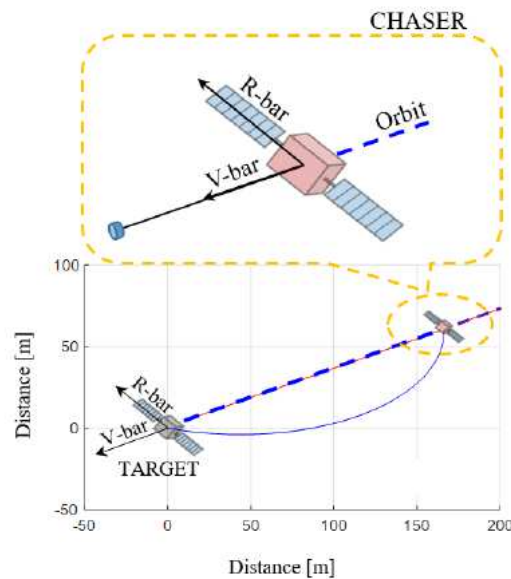


FIGURE 7.30: Configuration of the chaser at the beginning of the tether deployment (top) and target and chaser position in the target reference system (bottom) at the end of the soft-docking manoeuvre.

A successfully soft-docking manoeuvre can be achieved if the tethered probe reaches a particular position close enough to the electromagnetic interface aboard the target spacecraft. When the probe reaches this position, the interaction between the generated magnetic fields drives it towards the target and realizes an automatic alignment between the two interfaces. This particular position can be any position belonging to a spherical region centred in the target interface and called “sphere of influence”. It can also be defined as the maximum distance at which the interaction between the magnetic fields of the dipoles is enough to neglect the influence of Earth’s magnetic field. The soft-docking is then realized, as shown in FIGURE 7.31, which depicts the position of the dipoles at the end of the tether deployment.

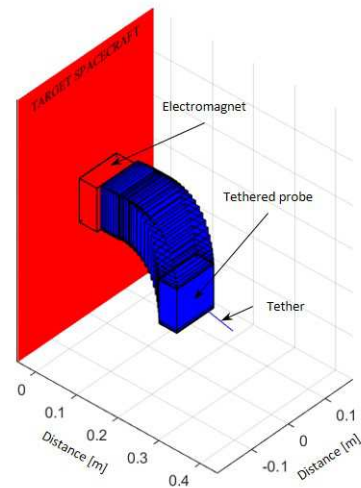


FIGURE 7.31: Soft-docking manoeuvre. When the probe reaches the sphere of influence of the electromagnetic interface mounted on the target spacecraft, the generated magnetic field drives it towards the target and realizes an automatic alignment between the two interfaces and the soft-docking is then realized.

In the simulation, the sphere of influence obtained has a radius of 33 cm. It is worth noting that the extension of the sphere of influence strongly depends on the dipole characteristics.

Chapter 8

Conclusions & Future Works

The work presented in the dissertation is briefly summarised here, with the preliminary outcomes obtained through numerical analysis and simulations and the results collected in laboratory.

PACMAN experiment and the activities connected to the ESA Education *Fly Your Thesis!* 2017 programme are recapped, focusing mainly on the CUBE which represents the core of the experiment. The final objective is to reach a TRL of 5-6 for the technologies developed in the framework of PACMAN experiment, collecting important data during the PFC in December.

In parallel, TED concept is also proposed as alternative to standard close-range rendezvous and docking procedures.

The connection between the two prospective applications investigated is presented at the end of the chapter, in which the future development of the project is depicted and integrated in the roadmap pursued in the last years.

8.1 Results and discussion

The main topic of this thesis was the study of viable strategies for spacecraft RVD manoeuvres exploiting electro-magnetic interactions. This argument has been widely investigated, introducing two connected and prospective applications.

The first one, PACMAN experiment, concerns a 1 U CubeSat (CUBE) equipped with a set of actively-controlled magnetic coils and a dedicated localization sensors system based on a camera board. The idea of PACMAN is to actively exploit magnetic interactions for relative position and attitude control during rendezvous and proximity operations between small-scale spacecraft. This could be realized studying the behaviour (in terms of motion and attitude) of the CUBE while is interacting with a target spacecraft (FFT,

1 U CubeSat) equipped with an electromagnet that generates a static magnetic field. The mutual interaction between the generated magnetic fields is used to control the CUBE attitude and relative position, assuring the accomplishment of the soft-docking manoeuvre.

The design of the whole PACMAN experiment has been a long process (FIGURE 8.1), started with the first concept and sketches, when the CUBE was still an idea (FIGURE 8.1 a)), passing through several prototypes (FIGURE 8.1 b)) and mock-ups (FIGURE 8.1 c)-d)) during the design phase and finishing with a working system to be tested in low-gravity (FIGURE 8.1 e)).

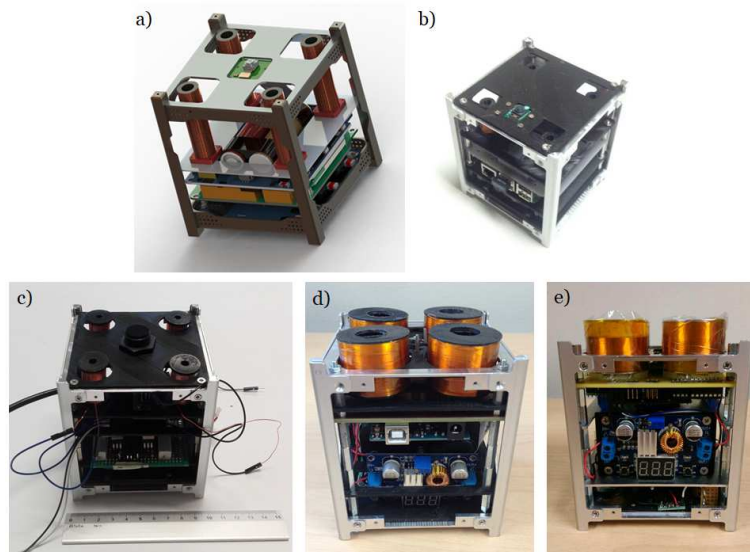


FIGURE 8.1: PACMAN evolution.

The final configuration of the experiment setup (CHAMBER and FFT) used on the Airbus A310 Zero-G was subjected to several modifications, mainly due to the different motion of a free-floating objects with respect to the aircraft. During the free-floating phase, in fact, a floating object moves along the initial release direction with its initial velocity. All the fixed parts connected to the aircraft, instead, follow the latter one motion. For this reason, the initial idea of having a free-floating CUBE launched towards a fixed target was discarded in favour of the new one with two free-floating CubeSats. Numerous dynamic analysis have been performed to identify the ideal launch window for releasing the CubeSats. Ideally, if the best launch time window is exploited in each parabola, the mean displacement of a free-floating object would be on the order of $\sim 0.1 - 0.2$ m but even in this best cases the maximum displacement could reach also ~ 1.5 m.

Since each parabola has different unexpected disturbances that influence randomly the motion of the two free-floating objects, several other analysis about the CUBE motion inside the aircraft have been carried out to estimate the range of its displacements. The

simulations show that the launch instants that statistically minimise the maximum displacements (determined as a result of a search problem) are around 7, 8 and 11 s after the injection. Therefore, the launch instant selected to perform the tests in low-gravity is around 11 s, since it minimizes the displacements of the free-floating objects along the Z (~ 0.21 m) and Y -axis (~ 0.675 m) of the aircraft, that are the directions with the lowest operative volume available. Moreover, launching in that instant, the CubeSats should move towards the roof of the Airbus A310 Zero-G, giving them more floating autonomy before hitting the nets that confine the free-floating area.

To correctly simulate the CUBE and the FFT dynamics aboard the aircraft, an accurate model that describes their interaction was developed in Matlab[®]-Simulink. The results show that the axial force acting on the CUBE when it encounters the FFT is of about 0.15 N (without considering any initial rotation and angular velocity). Moreover, the CUBE is able to re-align itself with the FFT in ~ 3.5 s, covering a distance of 20 cm. It is worth to underline that the free-floating window of just 3.5 s has been used in the simulations since the experiments involving free-floating objects can only exploit a reduced low-gravity time window of ~ 5 s. This is due to safety constraints associated with the release and secure procedures of the sample that must be performed before and after each micro-gravity phase. Furthermore, after ~ 5 s, free-floating objects usually hit the roof, the floor or the nets of the free-floating area.

Together with the IMU board, the vision subsystem aboard the CUBE is responsible for the relative navigation of the CubeSat. Laboratory tests have been performed to assess the real performances and the resolution of the Raspberry Pi NoIR Camera V2 module. The maximum error obtained by the comparison between the imposed target trajectory and the reconstructed one obtained from the image analysis is limited to a range of about 3.5 mm, ± 1 mm and ± 5 mm along the x , y and z -axis respectively. The angular estimation of yaw (ψ) angle is more accurate in comparison with the measured roll (ϕ) and pitch (θ) angles, that present a noisy behaviour. The mean values (μ) and standard deviation (σ) of the measured attitude angles are, respectively: $\mu_\psi = -1.26$ - $\sigma_\psi = 0.29$, $\mu_\phi = 2.79$, $\sigma_\phi = 4.61$ and $\mu_\theta = 0.04$, $\sigma_\theta = 2.69$. It is worth to point out that, for the final configuration, an improved algorithm able to refine the pose estimation by rejecting outliers and false matchings is adopted.

The second prospective application studied in this thesis is the Tethered Electromagnetic Docking concept. The dissertation presents an alternative and innovative approach for accomplishing close-range rendezvous and soft-docking manoeuvres. According to this new strategy, a tethered electromagnetic probe is ejected by the chaser toward a receiving electromagnetic interface mounted on the target spacecraft. The interaction between the generated magnetic field drives the probe to the target and realizes an automatic alignment between the two interfaces, thus reducing control requirements for close approach manoeuvres and saving part of the propellant necessary for them. After that,

“hard” docking is accomplished by retracting the tether and bringing the two spacecraft in contact.

The investigation was conducted considering two different scenarios: in the first one the chaser is moving on a lower orbit with respect to the target spacecraft, approaching it from the orbit radius direction ($R - bar$ approach) while in the second case, the two spacecraft share the same orbit, with the chaser following the target spacecraft ($V - bar$ approach).

Considering a glideslope manoeuvre, for both the two selected scenarios, the velocity budget required to complete the close-range rendezvous manoeuvre is of about 3.5 m/s. Even if other close-range rendezvous manoeuvres that requires lower velocity budget are possible, their application is avoided since they entail large drifts and high approach velocities to the target.

TED is therefore proposed as an effective alternative solution to these strategies, since it presents some advantages, like a reduced propellant consumption among all. This would be especially important for particular mission architectures involving multiple docking manoeuvres like formation flight missions, inspection manoeuvres or space tugging. The proposed TED procedure is therefore investigated for both the considered scenarios.

The $R - bar$ approach benefits of the tether deployment stabilization along the local vertical due to the gravity gradient but the docking manoeuvre performed in this configuration is quite complicate as shown by the simulations and it does not assure an effective saving in terms of fuel consumption. On the contrary, a tether deployment along the local horizontal is not as stable as the deployment along the $R - bar$, but it is easier and guarantees the repeatability of the manoeuvre phases with acceptable timings, in case of an unsuccessful deployment. The tether can be rewound and deployed again without waiting an entire orbital period. In this case, the simulations show that a soft docking approach can be performed in less than 30 min, considering the two spacecraft on a 600 km altitude orbit and at a mutual distance of 175.4 m. Further more in-depth studies are necessary in order to improve the results presented, considering also the tether retrieval manoeuvre, even if promising outcomes can already be underlined by these preliminary simulations.

8.2 PACMAN & TED correlation and future works

As described in the Introduction 1 of this dissertation, there is a tight correlation between PACMAN experiment and TED manoeuvre. Even if these two prospective applications can be thought as independent, PACMAN can be “de facto” considered as the electromagnetic probe of TED. This has not to be thought as a coincidence, rather it is a milestone belonging to a wider project that foresees an in-space demonstration in

the near future. FIGURE 8.2 shows the roadmap followed in the last years to develop and verify in relevant environment some critical technologies for future TED application in-space.

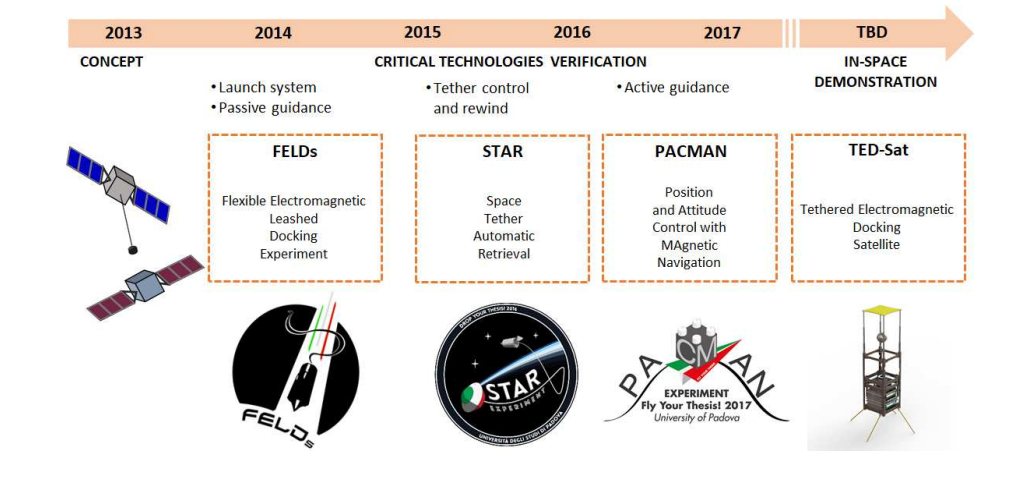


FIGURE 8.2: TED development plan, from the initial concept through critical technologies design and verification, in the prospective of an in-space demonstration.

In 2014 the investigations about tether deployment and the passive magnetic guidance effects have been conducted with FELDs experiment, launching in micro-gravity a tethered ferromagnetic probe towards a fixed electromagnet. Two years later, in 2016, an innovative mechanism for controlled tether deployment and retrieval was developed and tested with STAR experiment. Both these project have been validated during a drop test campaign at the ZARM drop tower in Bremen, in the framework of ESA Education *Drop Your Thesis!* programme. PACMAN experiment represents the next step in this roadmap and aims to examine in depth the active electromagnetic guidance used for attitude control and soft-docking and test new technologies during a PFC before the end of 2017.

The final milestone of the roadmap is an in-orbit demonstration with TED-Sat (FIGURE 8.3) to further raise the TRL of all the technologies developed.

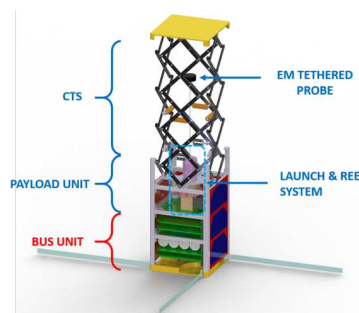


FIGURE 8.3: TED-Sat preliminary design.

The main objectives of the mission are:

- test the technologies developed for the controlled tether deployment and retrieval in space;
- study the self-alignment and guiding effect exploiting the electromagnetic interactions in space;
- evaluate the dynamics of the whole TED-Sat during the probe-target impact phase.

A preliminary design of the spacecraft has already been done. TED-Sat will consist in a 2 U CubeSat: one unit will be used for the bus electronics (made of COTS components) while the other one will contain the payload that is composed of (1) a deployable face (CubeSat Target Surface - CTS) acting as a target, (2) the Launch and Reel System (LRS), and (3) an electro-magnetic tethered probe. However, several improvements have to be done before testing these existing technologies in space. STAR mechanism should be miniaturized to fit in a CubeSat, which is not as straightforward as it could seem. The work needed to adapt the mechanism could be very challenging and the process could last at least a year including a testing campaign to validate the new proposed device. Most of the efforts should focus on the hardware with a new design phase for the launch system, the brake, the bail and the spool, while the control algorithm could be improved easily via software. Moreover, a re-work and probably a re-design of PACMAN CUBE should be necessary. The module should be re-adapted for TED-Sat entailing a substantial structural re-adjustment and hardware replacement. In this perspective, the data retrieved from PACMAN PFC would be very useful and essential since they would be used as design drivers to improve the technologies already developed. Anyway, the results obtainable from this in-space demonstration would be extremely interesting, thanks to the scalability of the outcomes: under both mechanical and dynamical points of view, the deployment of a short tether (few centimetres) entails exactly the same issues as the deployment of a longer tether (meters) and thus a CubeSat-size mission would not affect the meaningfulness of a TED technology demonstration.

8.3 Conclusions

As recapped in this conclusive chapter, the research activities performed during the PhD of the author allows the implementation of a dynamical model for electromagnetic RVD applications and the development of electromagnetic soft-docking interfaces and their verification in relevant environment, fulfilling the initial scientific objectives.

The experience acquired during the design and development of PACMAN has been of utmost importance to focus on the next steps to follow. Keeping in mind the final milestone of the roadmap presented in the previous section, a long research work is still

necessary to achieve the goal of an in-space demonstration of TED-Sat, starting from the analysis of the data that will be obtained from PACMAN experiment.

Presently, rendezvous strategies, proximity procedures and docking manoeuvres between spacecraft are of utmost importance for the development of longer lifetime missions. On-orbit servicing operations represent the future for both commercial and scientific missions, and thus new, effective, standard and reliable solutions are needed to ensure further technological developments.

Appendix A

CUBE Driver Circuit Evolution

A.1 Introduction

The final driver circuits selected for both the CUBE and the FFT are the consequence of a long evolution process.

The selection of the CUBE driver circuit has been the most difficult and critical one due to the particular application of the driver and the different devices that have to be powered (the coils, Arduino UNO, Raspberry Pi 3 model B, the IMU board, the temperature sensors, etc.) with completely different requirements in terms of power supply. It started with a first custom board, passes through a long trade-off of various driver circuits and finished with the final selection, the Pololu A4990 Dual Motor Driver. The selection of the FFT driver circuit, instead, has been simpler since the management of the devices to be powered was less complicated.

A.2 Custom driver circuit

Figure A.1 shows the generic block diagram of the CUBE driver circuit.

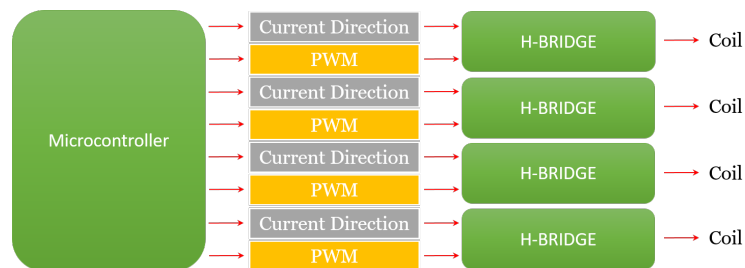


FIGURE A.1: Block diagram of a generic driver circuit for the CUBE.

The first solution for the driver circuit was a custom driver circuit composed of the following elements:

- Microcontroller.

Arduino UNO was used as microcontroller board to collect, store and process all the data coming from the sensors aboard the CUBE for the feedback control loop.

- Driver circuit signal.

The circuit was driven using a PWM signal with an amplitude of 3.3 V and a frequency of 1 kHz.

- Filter.

A low pass filter was implemented in order to transform the PWM signal (that is a digital signal) in an analogue one. In this way it was possible to obtain a linear driver and thus, given a defined input signal, the output would be proportional. The simplest filter that could be used in the circuit was a passive filter that could be obtained using a Resistor Capacitor (RC) circuit. The advantage of adopting such configuration was due to the very small current ripple ($\sim 100 \mu\text{A}$); on the contrary, the main drawback was the reduction in the response velocity of the circuit due to the small raising time.

- Voltage/Current converter.

The voltage/current converter would be based on a classic non-inverting scheme (Figure A.2) with the OPA548 of Texas Instrument used as operation amplifier.

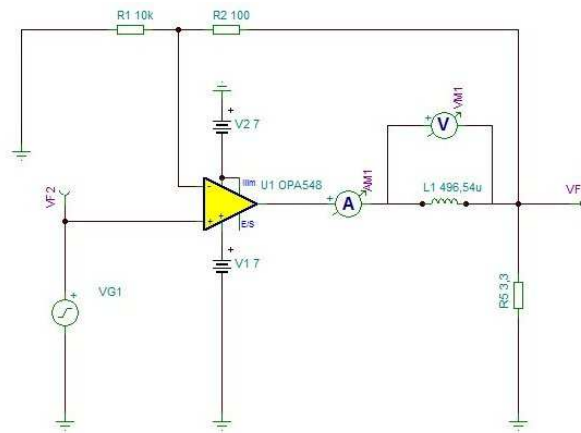


FIGURE A.2: Electrical scheme of the custom voltage/current converter.

A detailed description of the circuit is presented:

- The OPA548 (the yellow triangle in Figure A.2) is an operation amplifier fully compensated until the crossing frequency is reached. After this point, the Bode diagram of the magnitude has a constant decrease of 20 dB/dec and thus it does not need any compensation (with this configuration the theoretical phase margin is of 90 deg).
- $R_1 = 10\text{ k}\Omega$ and $R_2 = 100\ \Omega$ (the two resistances at the top of the scheme) are used in order to obtain a gain of the circuit equal to $G = 1 + \frac{R_2}{R_1} = 1$. This decision was made in order to have the same input voltage at node VF1 and minimize the power consumption.
- $R_5 = 3.3\ \Omega$ has been selected to obtain a current of 1 A at the output of the circuit, since the maximum amplitude of the input signal is equal to 3.3 V. It is worth noting that the output current of OPA548 is split at node VF1 but the amount of current that would pass through the $R_{1,2}$ branch is negligible.
- L_1 represents the coil. The resistive part of the load has not been considered since its contribution is negligible.
- The circuit can be fully powered at 7 V (dual) that can be provided by 2 COTS battery in series.

Figure A.3 shows the good results of the simulation. A sinusoidal input with an amplitude of 3.3 V and a frequency of 1 kHz has been used. The yellow line is the input signal, the red is the voltage across the coil and the green is the current flowing in the coil. As can be seen, the yellow line and the red one are very similar and out of phase of a quarter of period. The maximum current in the coil is very close to 1 A without any spikes (marker a).

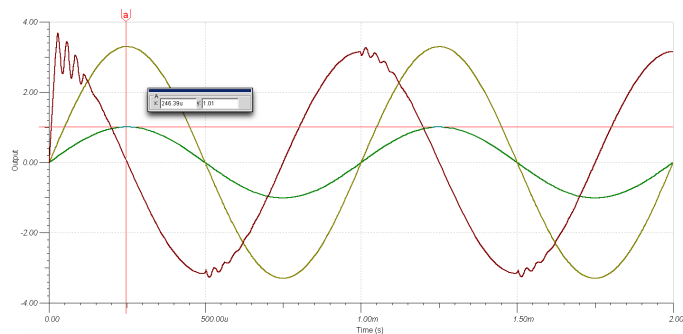


FIGURE A.3: Results of the simulation. The custom voltage/current converter scheme is powered with a sinusoidal input with an amplitude of 3.3 V and a frequency of 1 kHz.

A.3 Alternatives to the custom driver circuit

Two different options are now presented as alternative of the custom circuit developed.

1. L298N Integrated Circuit

The first one is an Arduino UNO board based on L298N IC with two output channel. This IC is an H-Bridge capable to drive 2 A for each channel and has been designed properly for applications concerning solenoids.

Figure A.4 shows the block diagram of this circuit and the complete board.

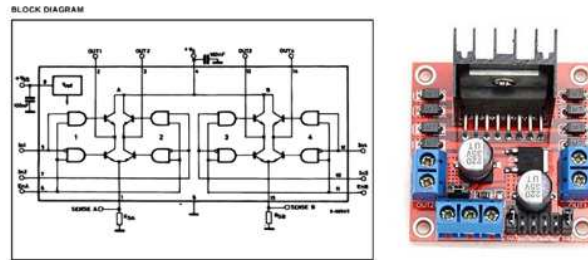


FIGURE A.4: Scheme of the L298N IC (left) and the complete board (right). This board represents a good alternative as driver circuit, can be used with Arduino UNO and is capable to drive 2 A for each channel.

The main features of the board are: 1) it drives the current in the coil with a PWM signal, 2) it is able to reverse the direction of the current in the coil and 3) it has reduced dimensions (43 mm x 43 mm) and thus it is easy to integrate in a CubeSat. The main drawback is connected to the fact that it is not possible to have any sensing of the current flowing in the coils and thus the control of the system is less efficient.

2. Arduino UNO Motor Shield

The second alternative is the Arduino UNO Adafruit Motor Shield Driver V2 (Figure A.5) that has the same characteristics of the previous one in terms of output current and input voltage. Moreover, it is possible to monitor precisely the current flowing in the coils. The main drawback are the dimensions that are bigger than the previous one.



FIGURE A.5: Arduino UNO Motor Shield. This board has the same characteristics of the L298N in terms of output current and input voltage. In addition, it can monitor the current flowing in the coils.

All the solutions presented were discarded in favour of the Pololu A4990 Dual Motor Driver Shield, since it presents the right features for PACMAN application with limited dimensions, as described in Chapter 4.5.2.3.

Appendix B

PACMAN project management

During the development of PACMAN experiment, the work was equally divided among all team members in order to achieve the best outcome for the project. A Work Breakdown Structure (WBS) was created in order to identify the different Working Packages (WP). Finally, a project timeline was drawn from the WBS in order to control the experiment development.

B.1 Work Breakdown Packages

The WBS is shown in FIGURE B.1.

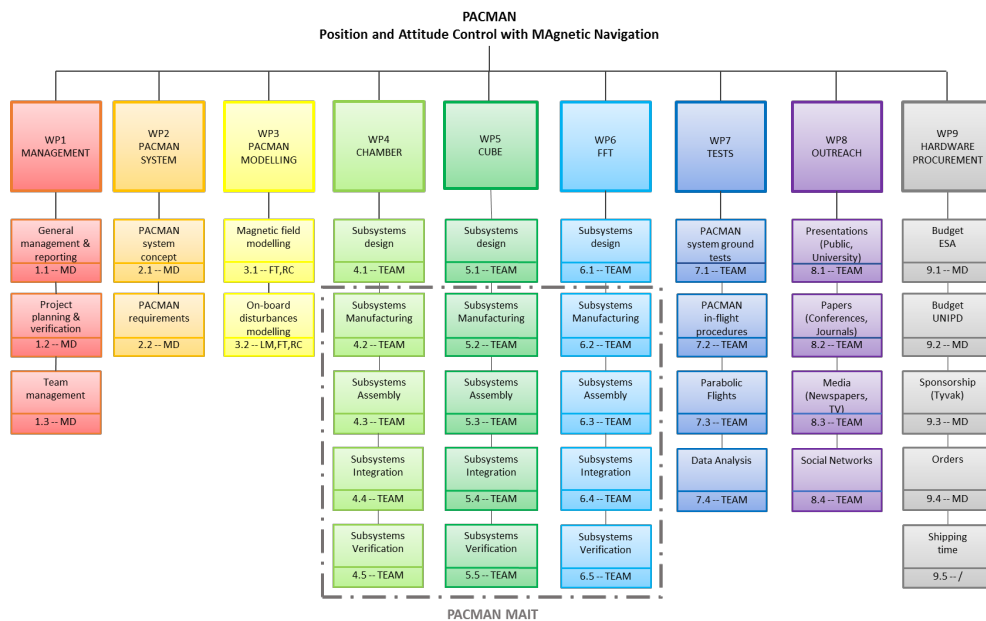


FIGURE B.1: WBS of PACMAN Experiment.

The WPs are described in FIGURE B.2. Each WP had a responsible with a background linked with his field of studies (see FIGURE B.3).

WP	TECHNICAL DESCRIPTION
1000	MANAGEMENT
1100	General management of the project; writing of the documents (Proposals, Reports, Experiment Safety Data Packages).
1200	Project planning with the WBS and the Gantt Chart; definition of the milestones and the critical phases.
1300	team management; sub-division of the team; tasks assignment.
2000	PACMAN SYSTEM
2100	Definition of the concept; definition of the objectives and motivations; evaluation of the innovative aspects and the perspective applications
2200	State of the Art of existing systems; definition of the pros and cons of the innovative concept; definition of the requirements.
3000	PACMAN MODELLING
3100	Magnetic field modelling: from preliminary Far Field model to accurate Near Field model; extensive numeric simulations.
3200	Detailed study about the environment that has to face the systems; particular attention towards the microgravity aspect; coils characterization; systems dynamics simulations; extensive numeric simulations.
4000	CHAMBER
4100	CHAMBER subsystems design; selection of the IMU, accelerometers and cameras based on system dynamics simulations; particular attention towards the Hold & Launch systems design; electronic design; electric block diagram of the sensors connections; study of the cameras position in the CHAMBER.
4200	Hold & Launch systems manufacturing; electronic boards manufacturing; sensors procurement.
4300	Components testing; assembly of the CHAMBER subsystems.
4400	Integration of the CHAMBER.
4500	Verification of the CHAMBER subsystems after integration;
5000	CUBE
5100	CUBE subsystems design; optimization of the volume available; selection of the IMU and the on-board camera based on system dynamics simulations and requirements; electronic design; electric block diagram of the sensors connections;
5200	CUBE manufacturing; electronic boards manufacturing; sensors procurement.
5300	Components testing; assembly of the CUBE subsystems.
5400	Integration of the CUBE.
5500	Verification of the CHAMBER subsystems after integration.
6000	FFT
6100	FFT subsystems design; optimization of the volume available; coil characterization; electronic design; electric block diagram for the power circuit.
6200	FFT manufacturing; electronic boards manufacturing.
6300	Components testing; assembly of the FFT subsystems.
6400	Integration of the FFT.
6500	Verification of the FFT subsystems after integration.
7000	TESTS
7100	PACMAN experiment ground tests on 2D low-friction table; Hold & Launch systems tests on 2D low-friction table; CHAMBER cameras tests.
7200	Parabolic flights procedures.
7300	Tests in relevant environment (parabolic flights).
7400	Data analysis of the results retrieved during the parabolic flights.
8000	OUTREACH
8100	Presentations to general public; presentations at high schools and universities.
8200	Papers at International Conferences during the development of the project (subsystem level); papers in Journals and International Conferences about the whole PACMAN Experiment after the results of the flight campaign.
8300	Local newspapers, local TV/radio.
8400	Social networks (Facebook, Twitter, Youtube).
9000	HARDWARE PROCUREMENT
9100	ESA Budget for requesting sponsorship and related documents
9200	UNIPD Budget for requesting funds and related documents
9300	Contacts with Tyvak International for Intrepid Board
9400	Hardware orders: electronic boards and components, microcontrollers, cameras, IMUs, laboratory materials, profiles, plates, CubeSat frames, ...
9500	Hardware orders made considering shipping time/delays

FIGURE B.2: Technical description of the WBS.

WP	Description	Detailed description	Responsible	Supporting Team members	External Support
WP1 Management	General management & reporting		Matteo D.	Mattia M.	Davide P.
	Project planning & verification		Matteo D.	Mattia M.	
	Team management		Matteo D.	Mattia M.	
WP2 PACMAN System	PACMAN system concept		Matteo D.	Mattia M.	
	PACMAN requirements		Matteo D.	Mattia M.	
WP3 PACMAN Modelling	Magnetic field modelling		Riccardo C.	Filippo T. Matteo V.	Luca M.
	On-board disturbances modelling		Filippo T.	Riccardo C. Mattia M.	
WP4 Chamber	Subsystems design & MAIT	Structure	Filippo T.	Matteo D.	Davide P.
		Hold & Launch	Filippo T.	Matteo D.	Davide P. Luca M.
		Sensors	Mattia M.	Matteo V. Fabrizio V.	
		Power	Fabrizio V.	Riccardo C.	
WP5 CUBE	Subsystems design & MAIT	Structure	Matteo D.	Filippo T.	Davide P.
		Hold & Launch	Matteo D.	Filippo T.	Davide P. Luca M.
		GNC	Mattia M.	Matteo V. Fabrizio V. Riccardo C.	
		OBDH & TC	Matteo V.	Mattia M. Fabrizio V.	
		Power	Fabrizio V.	Riccardo C.	
WP6 FFT	Subsystems design & MAIT	Structure	Matteo D.	Filippo T.	Davide P.
		Hold & Launch	Matteo D.	Filippo T.	Davide P. Luca M.
		OBDH & TC	Matteo V.	Mattia M.	
		Power	Riccardo C.	Fabrizio V.	
WP7 Tests	On-ground tests		Mattia M.	All	All
	Parabolic Flights		Matteo D.	All	
	Data Analysis		Matteo D.	Filippo T. Mattia M. Matteo V.	Luca M.
WP8 Outreach	Presentations, papers, social networks		Matteo D.	Matteo V.	
WP9 Hardware Procurement	Budgets, sponsorships and orders		Matteo D.	Mattia M.	

FIGURE B.3: Subdivision of the work among the members of the team and person in charge.

FIGURE B.4 shows the interdependencies among PACMAN systems.

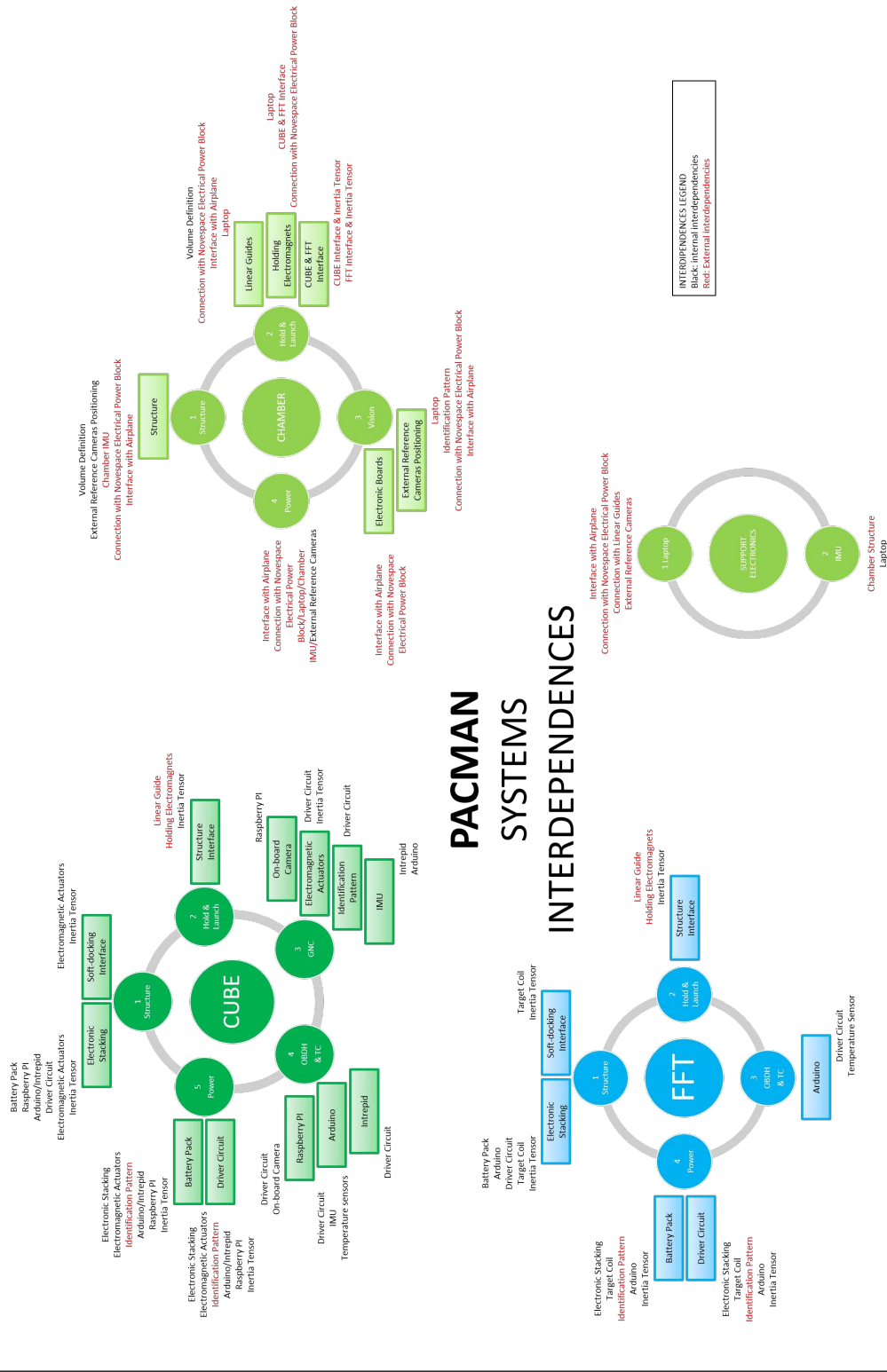


FIGURE B.4: PACMAN interdependencies.

B.2 Project timeline

FIGURE B.5 shows the development plan of PACMAN Experiment. The timeline derives from the WBS.

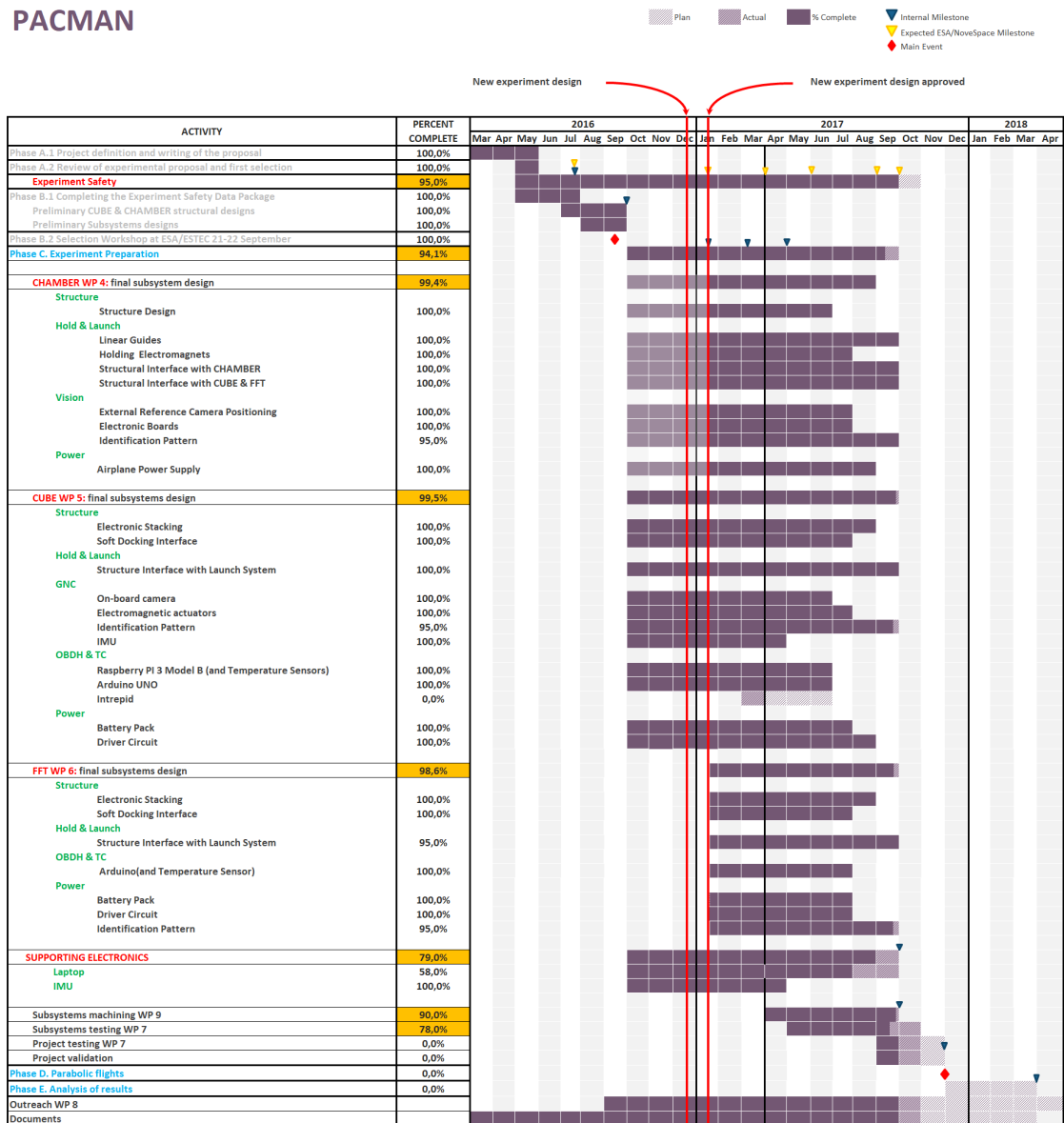


FIGURE B.5: PACMAN Gantt Chart.

As can be seen from the Gantt Chart, the development of the experiment had some delays and not followed perfectly the schedule. The reason for the delays were due to the change in the experiment design occurred in December 2016 that contributed to several improvements but had also the following implications:

1. the CHAMBER design changed and a new design started after the Training Week in Redu. The delays connected to this system were due to the fact that it has been subjected to a complete modification and unfortunately part of the work done could not be used for the new design;
2. the CUBE system was quite on schedule, since it was subjected only to minor modifications from the proposal. The main subsystems affected by the delays were the ones connected to the CHAMBER (due to its new design) and the FFT (due to the fact that it represented a new system introduced after the Training Week) systems;
3. the FFT system design was presented during the Training Week and started right after it. Thus, the design of this new system was delayed compared with the CUBEs one.

The whole PACMAN design phase required much more time than expected at the beginning of the project.

Appendix C

Clohessy-Wiltshire Formulation

C.1 CW matrices formulation

$$[\Phi_{rr}(t)] = \begin{bmatrix} 1 & 0 & 6 \cdot (\omega t - \sin(\omega t)) \\ 0 & \cos(\omega t) & 0 \\ 0 & 0 & 4 - 3 \cdot \cos(\omega t) \end{bmatrix} \quad (\text{C.1})$$

$$[\Phi_{rv}(t)] = \begin{bmatrix} \frac{4}{\omega} \sin(\omega t) - 3t & 0 & \frac{2}{\omega} (1 - \cos(\omega t)) \\ 0 & \frac{\sin(\omega t)}{\omega} & 0 \\ \frac{2}{\omega} (\cos(\omega t) - 1) & 0 & \frac{\sin(\omega t)}{\omega} \end{bmatrix} \quad (\text{C.2})$$

$$[\Phi_{vr}(t)] = \begin{bmatrix} 0 & 0 & 6\omega \cdot (1 - \cos(\omega t)) \\ 0 & -\omega \cdot \sin(\omega t) & 0 \\ 0 & 0 & 3\omega \cdot \sin(\omega t) \end{bmatrix} \quad (\text{C.3})$$

$$[\Phi_{vv}(t)] = \begin{bmatrix} 4\cos(\omega t) - 3 & 0 & 2\sin(\omega t) \\ 0 & \cos(\omega t) & 0 \\ -2\sin(\omega t) & 0 & \cos(\omega t) \end{bmatrix} \quad (\text{C.4})$$

C.2 Initial velocity calculation for the R-bar approach

In the reference frame fixed on the target satellite, in free-floating conditions, the chaser relative velocity \mathbf{v}_{0-} can be calculated from the target velocity \mathbf{V}_C , the chaser velocity \mathbf{V}_T and the distance between target and chaser \mathbf{r}_0 as follows

$$\mathbf{v}_{0-} = \mathbf{v}_{\text{rel}} = \mathbf{V}_C - \mathbf{V}_T - \omega \times \mathbf{r}_0 \quad (\text{C.5})$$

where the satellites velocities for circular orbits can be written as

$$\mathbf{V} = \omega \times \mathbf{R}_{\text{orb}} \quad (\text{C.6})$$

In the simplified case of $\mathbf{r}_0 = \begin{pmatrix} 0 & 0 & z_0 \end{pmatrix}$, the problem can be reduced since the orbital angular frequency can be written as $\mathbf{w}_{\text{orb},i} = \begin{pmatrix} w_{\text{orb},i} & 0 & 0 \end{pmatrix}$. The chaser velocity is therefore in the form $\mathbf{v}_{0-} = \begin{pmatrix} v_{0-} & 0 & 0 \end{pmatrix}$, with

$$v_{0-} = \omega_C R_C - \omega R - \omega z_0 = \omega_C (R - z_0) - \omega R - \omega z_0 \quad (\text{C.7})$$

The chaser orbital angular frequency ω_C can be written in function of the orbit radius $R_C = R - z_0$ and the standard gravity parameter μ as reported in equation C.8

$$\omega_C = \frac{\sqrt{\mu}}{R_C^{\frac{3}{2}}} = \frac{\sqrt{\mu}}{(R - z_0)^{\frac{3}{2}}} \quad (\text{C.8})$$

Considering that $z_0 \ll R$, it is possible to reduce the formulation of ω_C to

$$\omega_C = \frac{\sqrt{\mu}}{(R - z_0)^{\frac{3}{2}}} = \sqrt{\mu} \left(R^{-\frac{3}{2}} - \frac{3}{2} R^{-\frac{5}{2}} z_0 + o(z_0^2) \right) \quad (\text{C.9})$$

$$\omega_C \approx \sqrt{\frac{\mu}{R^3}} - \frac{3}{2} \sqrt{\frac{\mu}{R^3}} \frac{z_0}{R} \approx \omega \left(1 - \frac{3}{2} \frac{z_0}{R} \right) \quad (\text{C.10})$$

Substituting this result in equation C.7 and rejecting the negligible factors, it is possible to obtain

$$v_{0-} = \omega \left(1 - \frac{3}{2} \frac{z_0}{R} \right) (R - z_0) - \omega R - \omega z_0 = \frac{3}{2} \omega z_0 \quad (\text{C.11})$$

Therefore, the chaser relative velocity expressed in the target reference frame can be written as

$$\mathbf{v}_{0-} = \begin{pmatrix} \frac{3}{2}\omega z_0 & 0 & 0 \end{pmatrix} \quad (\text{C.12})$$

Appendix D

Validation of PACMAN launch system

PACMAN launch system is composed of several parts:

- a motorized linear guide (ERC2-SA6C) with its slide. This linear guide is used to move the CUBE and the FFT during the low-gravity phase, providing them with the right initial velocity;
- a NSK second linear guide (not motorized) with its slide. This linear guide composed by a rail and a slide is used to lower the moment and the load acting on the ERC2-SA6C motorized linear guide, as explained afterwards;
- a 45 x 45 mm Bosch profile used to mount the release interface with the holding electromagnet. The function of the Bosch profile is to move the CUBE and the FFT outside the rack and to put them closer before the release during the low-gravity phase. The holding electromagnet is positioned on the release interface and is used to keep the CUBE and the FFT in position prior to the low-gravity phase.

The ERC2-SA6C motorized linear guide is bolted on the intermediary shelf of the rack and positioned at one extremity of the rack. On top of the motorized slide of the ERC2-SA6C, a 45 x 45 mm Bosch profile (400 mm) is mounted. At the free extremity of the profile, the CUBE or the FFT is mounted through two brackets to the release interface with the holding electromagnet.

Under the top plate of the rack, the NSK linear guide is mounted. This linear guide is composed by a rail and a slide and is not motorized. The slide mounted on this second

linear guide is also bolted to the 45 x 45 mm Bosch profile which hold the CUBE or the FFT. The function of this second linear guide is to lower the moment and the load acting on the ERC2-SA6C motorized linear guide.

When powered, the ERC2-SA6C motorized linear guide pushes ahead its slide and thus the CUBE or the FFT connected to the Bosch profile. At the release instant, the holding electromagnet connected to the release interface is switched off and the CUBE or the FFT is free to float. Then the ERC2-SA6C motorized linear guide retracts the 45 x 45 mm Bosch profile to increase the operational volume for the two floating CubeSats.

The configuration has been validated using PATRAN software. Since the 45 x 45 mm Bosch profile is bolted with both the ERC2-SA6C motorized linear guide and the NSK linear guide, the schematic representation of the structure when is completely extended is given in FIGURE D.1

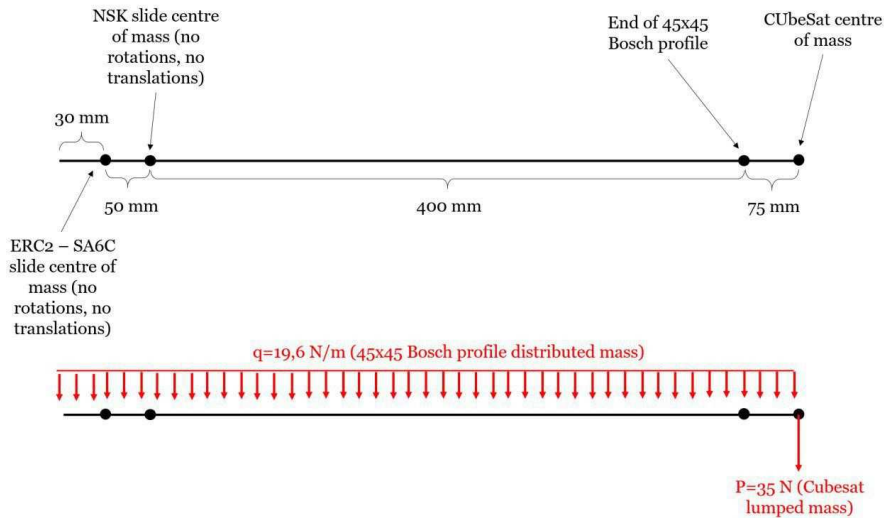


FIGURE D.1: Bosch profile modelled as a beam with two fixed constrains, the CubeSat lumped mass and the Bosch profile distributed mass.

where q represents the distributed load along the 45 x 45 mm Bosch profile (i.e. its weight) and P represents the weight of the CUBE or the FFT at its extremity. The distributed load q (19.6 N/m) has been obtained by considering the linear weight of the 45 x 45 mm Bosch profile (2 g/mm). The weight of the CUBE, the holding electromagnet and the release interface have been obtained from the datasheet/CAD assemblies (2.3 kg in total). The total weight applied at the extremity of the 45 x 45 mm Bosch profile has been obtained considering a safety factor k of 1.5. Therefore, the total applied weight used in the analysis is of 3.5 kg (i.e. $P = 35 \text{ N}$). This force has been applied in the CUBE centre of mass.

FIGURE D.2 shows the bending moment trend along the length of the Bosch profile.

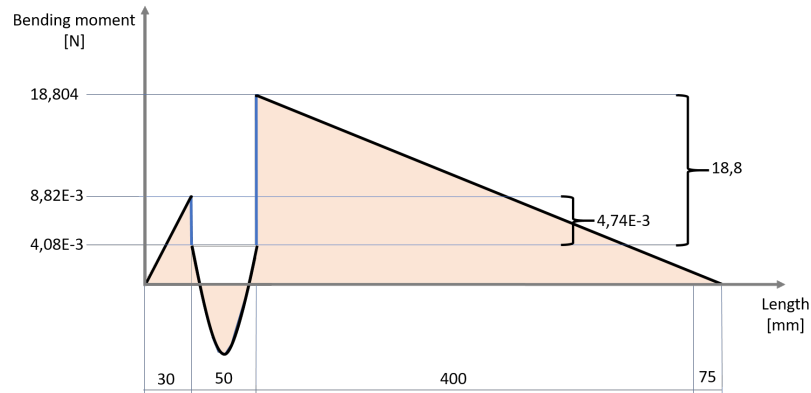


FIGURE D.2: Bending moment diagram of the Bosch profile, modelled as a beam.

The particular configuration with the two linear guides and their slides positioned at different distances along the 45 x 45 mm Bosch profile allow to lower markedly the moment and the load acting on the ERC2-SA6C slide stressing more the NSK linear guide.

FIGURE D.3 shows the constraints obtained from the schematic representation (on the left). The constraints limit all the six degrees of freedom (d.o.f): three translations (1,2,3) and three rotations (4,5,6). The weight of the CUBE P is shown on the right and is equal to 35 N). The distributed load q is applied along all the profile in the simulations but is not showed just for clarity.

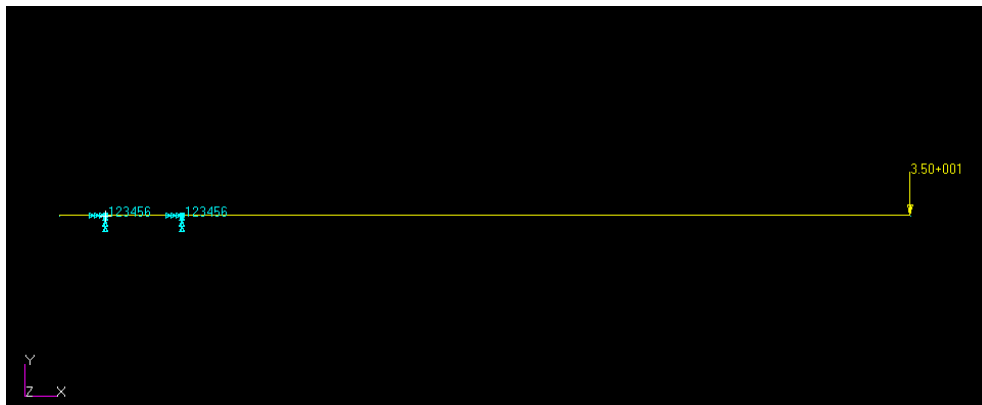


FIGURE D.3: (Left side) The constraints limits all the six degrees of freedom (d.o.f): three translations (1,2,3) and three rotations (4,5,6). (Right side) The weight of the CUBE is applied as a lumped mass.

FIGURE D.4 shows the loads (1.8 N on ERC2-SA6C slide and 44.8 N on the NSK slide) while FIGURE D.5 shows the moments ($4.74 \cdot 10^{-3}$ Nm on ERC2-SA6C slide and 18.88 Nm on the NSK slide) obtained after the analysis.

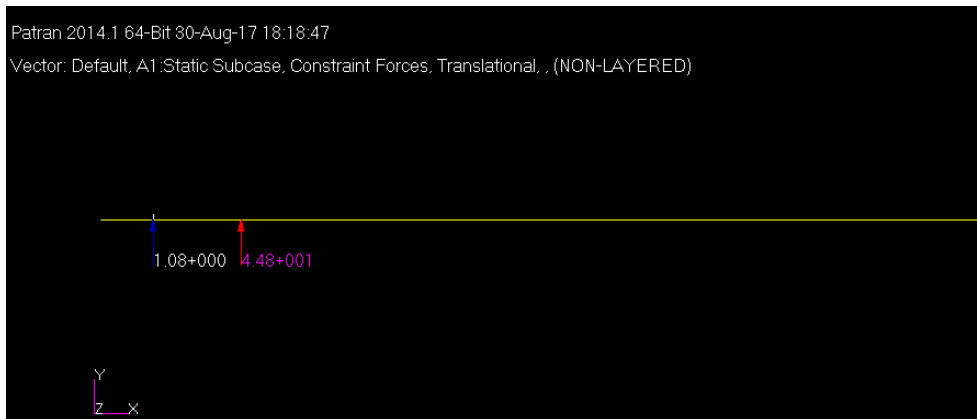


FIGURE D.4: Resultants of the applied loads q and P (forces acting on the slides).

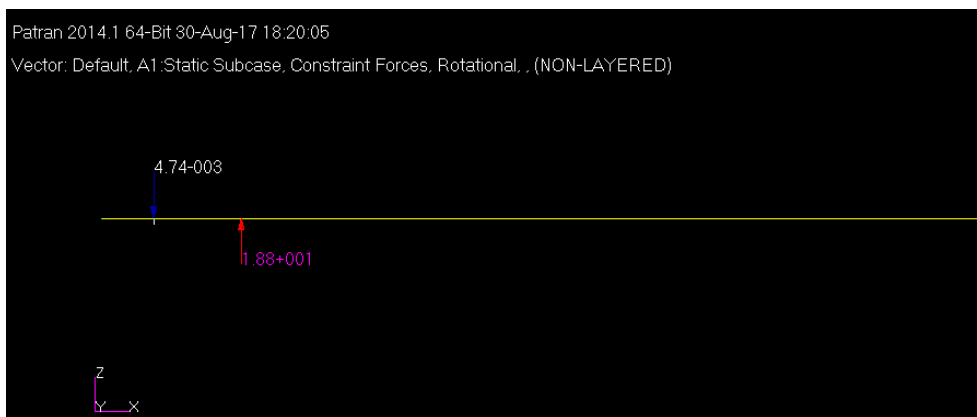


FIGURE D.5: Resultants of the applied loads q and P (moments acting on the slides).

It is worth to underline that the higher loads and moments are almost completely absorbed by the NSK slide. The results show that the configuration designed for the launch system is effective since it does not stress the motorized linear guide that is able to withstand easily the weight of the CubeSats also during the hyper-gravity phases.

Appendix E

Procedures for ground and in-flight operations

All the activities that have to be performed on ground before the flight are recapped below.

E.1 Preparation before each flight

1. Check of the CHAMBER
 - Structure
 - Connection among the profiles (brackets, screws, nuts,) and the plates
 - Hold & launch systems
 - Alignment
 - Power connection of the holding electromagnet
 - Structural connection of the holding electromagnet with the launch plate
 - Power connection of the linear guide
 - Power connection between the linear guide and the aircraft power block
 - Communication with the laptop
 - Structural connection of the linear guide with the launch plate
 - Structural connection of the linear guide with the base plate
 - IMU status
 - Power connection with laptop
 - Structural connection with the base plate

- External reference stereocamera status
 - Power connection with laptop
 - Communication with laptop
 - Structural connection with the roof of the airplane
- Sensors reading tests
 - IMU
 - Hold & launch systems controllers
 - External reference stereocamera
- Communication tests
 - IMU communication with laptop
 - External reference cameras communication with laptop
 - Laptop communication with hold & launch systems controllers
 - Wi-fi communication with CUBE & FFT
- Software routines tests
 - Hold & launch systems release procedure

2. Check of the CUBE

- Magnetic coils status
 - Power connections with the driver circuit
 - Structural connections with the temperature sensors
 - Structural connections with the interface
- Arduino UNO status
 - Power connection with the driver circuit
 - Power connection of the micro SD card
 - Power connection of the temperature sensors
 - Power connection with battery pack
 - Structural connection with the interface
- IMU status
 - Power connection with Raspberry Pi 3 Model B
 - Structural connection with the interface
- Raspberry Pi NoIR Camera V2 module status
 - Power connection with Raspberry Pi 3 Model B
 - Structural connection with the interface
- Raspberry PI 3 Model B status

- Power connection with the IMU
- Power connection with Raspberry Pi NoIR Camera V2 module
- Power connection with battery pack
- Power connection of the micro SD card
- Structural connection with the interface
- Battery pack status
 - Power connection with Raspberry Pi 3 Model B
 - Power connection with Arduino UNO
 - Power connection to the driver circuit
 - Power connection with the Drock Buck converter
 - Structural connection with the interface
- Emergency stop button status
 - Emergency circuit power interruption
 - Structural connection with the interface
- Sensors reading tests
 - IMU
 - Temperature sensors
 - Raspberry Pi NoIR Camera V2 module
 - Proximity sensor
- Communication tests
 - Communication among electronic boards
 - Wi-Fi Communication with laptop
- Software routines tests
 - Control algorithms tests
 - Data handling tests
- Micro SD memory tests
 - Data storage tests

3. Check of the FFT

- Magnetic coil status
 - Power connection with the driver circuit
 - Structural connection with the temperature sensor
 - Structural connections with the interface
- Arduino UNO status

- Power connection with the IMU
- Power connection with the driver circuit
- Power connection of the micro SD card
- Power connection of the temperature sensor
- Power connection with battery pack
- Structural connections with the interface
- IMU status
 - Power connection with Arduino UNO
 - Structural connections with the interface
- Battery pack status
 - Power connection with Arduino UNO
 - Power connection to the driver circuit
 - Power connection with the regulator/protector
 - Structural connections with the interface
- LEDs status
 - Power connection with Arduino UNO
 - Structural connections with the interface
- Emergency stop button status
 - Emergency circuit power interruption
 - Structural connection with the interface
- Sensors reading tests
 - IMU
 - Temperature sensor
 - LEDs
 - Proximity sensor
- Software routines tests
 - Data handling tests
- Micro SD memory tests
 - Data storage tests

E.2 Procedures during the flight before first parabola

1. Steady horizontal flight

- CUBE removal from trolley
- FFT removal from trolley
- Positioning of the CUBE on the hold & launch system
- Positioning of the FFT on the hold & launch system
- Check status of the systems from the laptop
 - Wi-Fi communication with FFT
 - Wi-Fi communication with CUBE
 - Communication with the hold & launch systems controllers
 - Communication with the IMU in the CHAMBER
 - Communication with the external reference cameras

E.3 Procedures during the pauses between parabolas

1. Steady horizontal flight
 - Change launch interface
 - Tune liner guide velocity

E.4 Preparation after each flight

1. Operations
 - Change battery pack
 - Replace failed components
 - Check integrity of the structure
 - CHAMBER
 - CUBE
 - FFT
 - Transfer data from micro SD to laptop and external memories
 - Follow “Preparation before each flight” instructions E.1

Bibliography

- [1] Alex Ellery, Joerg Kreisel, and Bernd Sommer. The case for robotic on-orbit servicing of spacecraft: Spacecraft reliability is a myth. *Acta Astronautica*, 63(5): 632–648, 2008.
- [2] Angel Flores-Abad, Ou Ma, Khanh Pham, and Steve Ulrich. A review of space robotics technologies for on-orbit servicing. *Progress in Aerospace Sciences*, 68: 1–26, 2014.
- [3] URL <http://mdacorporation.com/isg/robotics-automation/space-based-robotics-solutions/robotics-and-on-orbit-servicing1>.
- [4] URL <http://www.vivisat.com/1>.
- [5] URL https://www.nasa.gov/mission_pages/station/research/experiments/778.html.
- [6] URL <https://www.darpa.mil/program/phoenix1>.
- [7] URL http://space.skyrocket.de/doc_sdat/deos.htm.
- [8] URL <http://spacenews.com/airbus-to-challenge-ssl-orbital-atk-with-new-space-tug-htm>.
- [9] URL <https://www.orbitalatk.com/news-room/feature-stories/MEV/default.aspx>.
- [10] URL <https://www.effective-space.com/>.
- [11] Cryan Scott P. Kelly, Sean M. *International Docking Standard (IDSS) Interface Definition Document (IDD)*, volume NASA report HQ-E-DAA-TN39050. 2016.
- [12] V. S. Syromyatnikov. Docking system of androgynous and peripheral type. *The 7th Aerospace Mechanism Symposium*, page 27, 1972.
- [13] D. Schwaab. *NASA Docking System (NDS) Users Guide*.

- [14] W. H. Warr. R. J. McLaughlin. The common berthing mechanism (cbm) for international space station. *31st International Conference On Environmental Systems*, page 27, 2001. URL http://spacecraft.ssl.umd.edu/design_lib/ICES01-2435.ISS_CBM.pdf.
- [15] David Miller, A Saenz-Otero, J Wertz, A Chen, G Berkowski, C Brodel, S Carlson, D Carpenter, S Chen, S Cheng, et al. Spheres: a testbed for long duration satellite formation flying in micro-gravity conditions. In *Proceedings of the AAS/AIAA Space Flight Mechanics Meeting, Clearwater, FL, Paper No. AAS 00-110*, 2000.
- [16] P Tchoryk Jr, Anthony B Hays, and Jane C Pavlich. A docking solution for on-orbit satellite servicing: part of the responsive space equation. *AIAA-LA Section/SSTC*, 2001:1–3, 2003.
- [17] Underwood C. et al. Using cubesat/micro-satellite technology to demonstrate the autonomous assembly of a reconfigurable space telescope (aarest). *Acta Astronautica*, 114:112–122, 2015.
- [18] Wenwen Chen, Zhongcheng Mu, Wei Wang, Guowen Sun, and Hongyu Chen. The multiple coils to perform autonomous rendezvous & docking of cubesat/micro-satellite. In *Control And Decision Conference (CCDC), 2017 29th Chinese*, pages 3178–3183. IEEE, 2017.
- [19] C. P. Bridges, B. Taylor, N. Horri, C. I. Underwood, S. Kenyon, J. Barrera-Ars, L. Pryce, and R. Bird. Strand-2: Visual inspection, proximity operations amp; nanosatellite docking. In *2013 IEEE Aerospace Conference*, pages 1–8, March 2013. doi: 10.1109/AERO.2013.6497348.
- [20] Petrillo D et al. Flexible electromagnetic leash docking system (felds) experiment from design to microgravity testing. *Acta Astronautica*, October 66th IAC, Jerusalem, 2015.
- [21] John Bowen, Marco Villa, and Austin Williams. Cubesat based rendezvous, proximity operations, and docking in the cpod mission. 2015.
- [22] . URL http://www.nasa.gov/sites/default/files/atoms/files/oaan_fact_sheet-26oct2015.
- [23] URL http://www.esa.int/Our_Activities/Space_Engineering_Technology/Clean_Space/CleanSat_new_satellite_technologies_for_cleaner_low_orbits.
- [24] URL http://www.esa.int/Our_Activities/Space_Engineering_Technology/Clean_Space/e.Deorbit.

- [25] Wigbert Fehse. *Automated rendezvous and docking of spacecraft*, volume 16. Cambridge university press, 2003.
- [26] Duzzi M, Olivieri L, and Francesconi A. Tether-aided spacecraft docking procedure.
- [27] J. M. Grimwood B. C. Hacker. *On the Shoulders of Titans: A History of Project Gemini*, volume NASA report SP-4203. 1977.
- [28] Laura L Jones, William R Wilson, and Mason A Peck. Design parameters and validation for a non-contacting flux-pinned docking interface. In *AIAA SPACE 2010 Conference & Exhibition, Anaheim, CA, Paper No. AIAA*, volume 8918, 2010.
- [29] Yuan-wen Zhang, Le-ping Yang, Yan-wei Zhu, Huan Huang, and Wei-wei Cai. Non-linear 6-dof control of spacecraft docking with inter-satellite electromagnetic force. *Acta Astronautica*, 77:97–108, 2012.
- [30] Raymond J Sedwick and Samuel A Schweighart. Electromagnetic formation flight. *Advances in the Astronautical Sciences*, 113:71–83, 2003.
- [31] Umair Ahsun and David W Miller. Dynamics and control of electromagnetic satellite formations. In *American Control Conference, 2006*, pages 6–pp. IEEE, 2006.
- [32] Robert C Youngquist, Mark A Nurge, and Stanley O Starr. Alternating magnetic field forces for satellite formation flying. *Acta astronautica*, 84:197–205, 2013.
- [33] URL <http://www.nasa.gov/spheres/satellites.html>.
- [34] Porter AK et al. Demonstration of electromagnetic formation flight and wireless power transfer. *Journal of Spacecraft and Rockets*, 2014.
- [35] Woffinden D. and Geller D. Navigating the road to autonomous orbital rendezvous. *Journal of Spacecraft and Rockets*, 4(44):898–909, July 2007.
- [36] Rainey K. Final flight of european space vehicle to space station goes out with a big bang. 2014.
- [37] . URL <http://ssl.mit.edu/spheres/spheresLibrary/projectDocumentation.html>.
- [38] Sansone F., Branz F., Francesconi A., Barbetta M., and Pelizzo M.G. 2d close range navigation sensor for miniature cooperative spacecraft. *IEEE Transactions on Aerospace& Electronic Systems*, 50:160–169, 2014.
- [39] Sansone F., Branz F., Olivieri L., and Francesconi A. Proximity relative navigation sensors for small-scale spacecraft and drones. pages 160–169, 66th IAC, Jerusalem, 12-16 October 2015.

- [40] Sonja Brungs, Marcel Egli, Simon L Wuest, Peter CM Christianen, Jack JWA van Loon, Thu Jennifer Ngo Anh, and Ruth Hemmersbach. Facilities for simulation of microgravity in the esa ground-based facility programme. *Microgravity science and technology*, 28(3):191–203, 2016.
- [41] Raul Herranz, Ralf Anken, Johannes Boonstra, Markus Braun, Peter CM Christianen, Maarten de Geest, Jens Hauslage, Reinhard Hilbig, Richard JA Hill, Michael Lebert, et al. Ground-based facilities for simulation of microgravity: organism-specific recommendations for their use, and recommended terminology. *Astrobiology*, 13(1):1–17, 2013.
- [42] URL http://www.esa.int/Our_Activities/Human_Spaceflight/Research/European_user_guide_to_low_gravity_platforms1.
- [43] URL http://www.esa.int/Education/Fly_Your_Thesis/Fly_Your_Thesis!_programme.
- [44] URL <http://www.novespace.fr/en,home.html>.
- [45] B. Verthier. *NOVSPACE A310 ZERO-G Interface Document*. 2016.
- [46] B. Verthier. *NOVSPACE STANDARD PRIMARY STRUCTURE CATALOG*. 2015.
- [47] 1st Symposium on Space Educational Activities, editor. *Modeling a new concept of tether deployer with retrievable capability for space applications*.
- [48] . URL <http://everyspec.com/ESA/download.php?spec=ECSS-E-ST-10-06C.048163.pdf>.
- [49] . URL <http://everyspec.com/ESA/download.php?spec=ECSS-E-10-02C.047796.pdf>.
- [50] Samuel Adam Schweighart. *Electromagnetic formation flight dipole solution planning*. PhD thesis, Massachusetts Institute of Technology, Department of Aeronautics and Astronautics, 2005.
- [51] S. Babic and et al. Magnetic force between inclined circular loops (lorentz approach). *Progress In Electromagnetics Research B*, 38:333–349, 2012.
- [52] Milton Abramowitz, Irene A Stegun, et al. Handbook of mathematical functions. *Applied mathematics series*, 55(62):39, 1966.
- [53] Z. Zhang. A flexible new technique for camera calibration. *IEEE Transactions on pattern analysis and machine intelligence*, 22(11):1330–1334, 2000.

- [54] Kneip L., Scaramuzza D., Siegwart R. *A Novel Parametrization of the Perspective-Three-Point Problem for a Direct Computation of Absolute Camera Position and Orientation*. IEEE, 2011.
- [55] M. A. Fischler and R. C. Bolles. Random sample consensus: a paradigm for model fitting with applications to image analysis and automated cartography. *Commun. ACM*, 24(6):381–395, 1981.
- [56] F. Gai. *NOVESPACe Experiment Design Requirements for Parabolic Flights*. 2016.
- [57] Lorenzo Olivieri and Alessandro Francesconi. Design and test of a semiandrogynous docking mechanism for small satellites. *Acta Astronautica*, 122:219–230, 2016.
- [58] Duncan Lee Miller. *Development of resource-constrained sensors and actuators for in-space satellite docking and servicing*. PhD thesis, Massachusetts Institute of Technology, 2015.
- [59] Steve Ulrich, Dustin Hayhurst, Alvar Saenz-Otero, David Miller, and Itzhak Barkana. Simple adaptive control for spacecraft proximity operations. In *AIAA Guidance, Navigation, and Control Conference*, page 1288, 2014.
- [60] Muriel Richard, L Kronig, Federico Belloni, S Rossi, V Gass, C Paccolat, JP Thiran, S Araomi, I Gavrilovich, and H Shea. Uncooperative rendezvous and docking for microsats. In *6th International Conference on Recent Advances in Space Technologies*, 2013.
- [61] H Clohessy and S Wiltshire. A terminal guidance system for satellite rendezvous. *Astro Science*, 27:563, 1960.
- [62] Hari B Hablani, Myron Tapper, and David Dana-Bashian. Guidance algorithms for autonomous rendezvous of spacecraft with a target vehicle in circular orbit. In *AIAA Guidance, Navigation, and control conference and Exhibit*, pages 6–9, 2001.
- [63] Don J Pearson. The glideslope approach. In *Orbital mechanics and mission design*, volume 1, pages 109–123, 1989.
- [64] Feng Wang, Xibin Cao, and Xueqin Chen. Guidance algorithms for the near-distance rendezvous of on-orbit-servicing spacecraft. *Transactions of the Japan Society for Aeronautical and Space Sciences*, 50(167):9–17, 2007.
- [65] Wim De Groot. Propulsion options for primary thrust and attitude control of microspacecraft. In *COSPAR Colloquia Series*, volume 10, pages 200–209. Elsevier, 1999.

- [66] Juergen Mueller, Richard Hofer, and John Ziemer. Survey of propulsion technologies applicable to cubesats. 2010.
- [67] M. Dobrowolny and N. H. Stone. A technical overview of tss-1: The first tethered-satellite system mission. *Il Nuovo Cimento C*, 17(1):1–12, Jan 1994. ISSN 0390-5551. doi: 10.1007/BF02506678. URL <https://doi.org/10.1007/BF02506678>.
- [68] Joseph A Carroll. Seds deployer design and flight performance. *AIAA paper*, pages 93–4764, 1993.
- [69] EC Lorenzini, SB Bortolami, CC Rupp, and F Angrilli. Control and flight performance of tethered satellite small expendable deployment system-ii. *Journal of guidance, control, and dynamics*, 19(5):1148–1156, 1996.
- [70] & Lorenzini E. C. Cosmo, M. L. *Tethers in space handbook*. 1997.
- [71] D Petrillo, M Gaino, M Duzzi, G Grassi, and A Francesconi. Tethered docking systems: advances from felds experiment. in: *Acta Astronautica*, 2017, forthcoming.
- [72] G. et al Grassi. Space tether automatic retrieval. *Drop Your Thesis! 2016, Final Report, European Space Agency Education Office*, 2017.
- [73] Kalyan K Mankala and Sunil K Agrawal. Dynamic modeling and simulation of satellite tethered systems. *Journal of vibration and acoustics*, 127(2):144–156, 2005.
- [74] Denis Zanutto, Enrico C Lorenzini, Riccardo Mantellato, Giacomo Colombatti, and Antonio Sánchez Torres. Orbital debris mitigation through deorbiting with passive electrodynamic drag. 2012.
- [75] Soon-Jo Chung, Edmund M Kong, and David W Miller. Spheres tethered formation flight testbed: Application to nasas specs mission. Society of Photo-Optical Instrumentation Engineers (SPIE), 2005.
- [76] SD Drell, HM Foley, and MA Ruderman. Drag and propulsion of large satellites in the ionosphere: An alfvén propulsion engine in space. *Journal of Geophysical Research*, 70(13):3131–3145, 1965.
- [77] JT Carter and M Greene. Deployment and retrieval simulation of a single tether satellite system. In *System Theory, 1988., Proceedings of the Twentieth Southeastern Symposium on*, pages 657–660. IEEE, 1988.
- [78] M Pascal, A Djebli, and L El Bakkali. A new deployment/retrieval scheme for a tethered satellite system, intermediate between the conventional scheme and the crawler scheme. *Journal of Applied Mathematics and Mechanics*, 65(4):689–696, 2001.

- [79] A Djebli, M Pascal, and L El Bakkali. Laws of deployment/retrieval in tether connected satellites systems. *Acta astronautica*, 45(2):61–73, 1999.
- [80] A Djebli, L El Bakkali, and M Pascal. On fast retrieval laws for tethered satellite systems. *Acta Astronautica*, 50(8):461–470, 2002.
- [81] L et al. Olivieri. Technologies to join spacecraft using a tethered electromagnetic probe. in: XXIV Italian Association of Aeronautics and Astronautics International Conference, Palermo-Enna, Italy, 18-22 September, 2017, forthcoming.
- [82] R Mantellato, A Valmorbida, and EC Lorenzini. Thrust-aided librating deployment of tape tethers. *Journal of Spacecraft and Rockets*, 52(5):1395–1406, 2015.
- [83] Joseph A Carroll. Tether applications in space transportation. *Acta Astronautica*, 13(4):165–174, 1986.
- [84] FL Chernous' ko. Dynamics of retrieval of a space tethered system. *Journal of Applied Mathematics and Mechanics*, 59(2):165–173, 1995.
- [85] Paul Williams. Optimal deployment/retrieval of tethered satellites. *Journal of Spacecraft and Rockets*, 45(2):324–343, 2008.